

# **NEW TRANSITION METAL OXIDES BY TOPOTACTIC ION EXCHANGE AND THEIR MAGNETIC PROPERTIES**

**Ph.D. THESIS**

*by*

**VANDANA MEENA**



**DEPARTMENT OF CHEMISTRY  
INDIAN INSTITUTE OF TECHNOLOGY ROORKEE  
ROORKEE 247 667, (INDIA)  
JUNE, 2019**

# **NEW TRANSITION METAL OXIDES BY TOPOTACTIC ION EXCHANGE AND THEIR MAGNETIC PROPERTIES**

**A THESIS**

*Submitted in partial fulfilment of the  
requirements for the award of the degree*

*of*

**DOCTOR OF PHILOSOPHY**

*in*

**CHEMISTRY**

*by*

**VANDANA MEENA**



**DEPARTMENT OF CHEMISTRY  
INDIAN INSTITUTE OF TECHNOLOGY ROORKEE  
ROORKEE 247 667, (INDIA)  
JUNE, 2019**



**©INDIAN INSTITUTE OF TECHNOLOGY ROORKEE, ROORKEE-2019  
ALL RIGHTS RESERVED**



# INDIAN INSTITUTE OF TECHNOLOGY ROORKEE ROORKEE

## CANDIDATE'S DECLARATION

I hereby certify that the work which is being presented in the thesis entitled “**NEW TRANSITION METAL OXIDES BY TOPOTACTIC ION EXCHANGE AND THEIR MAGNETIC PROPERTIES**” in partial fulfilment of the requirements for the award of the degree of Doctor of Philosophy and submitted in the Department of Chemistry of the Indian Institute of Technology Roorkee, Roorkee is an authentic record of my own work carried out during a period of July, 2013 to June, 2019 under the supervision of Dr. Tapas Kumar Mandal, Assistant Professor, Department of Chemistry, Indian Institute of Technology Roorkee, Roorkee.

The matter presented in the thesis has not been submitted by me for the award of any other degree of this or any other Institution.

(VANDANA MEENA)

This is to certify that the above statement made by the candidate is correct to the best of my knowledge.

(Tapas Kumar Mandal)  
Supervisor

The Ph.D. Viva-Voce Examination of Ms. **VANDANA MEENA**, Research Scholar, has been held on \_\_\_\_\_

Chairman, SRC

Signature of External Examiner

This is to certify that the student has made all the corrections in the thesis.

Supervisor

Head of the Department

Dated:

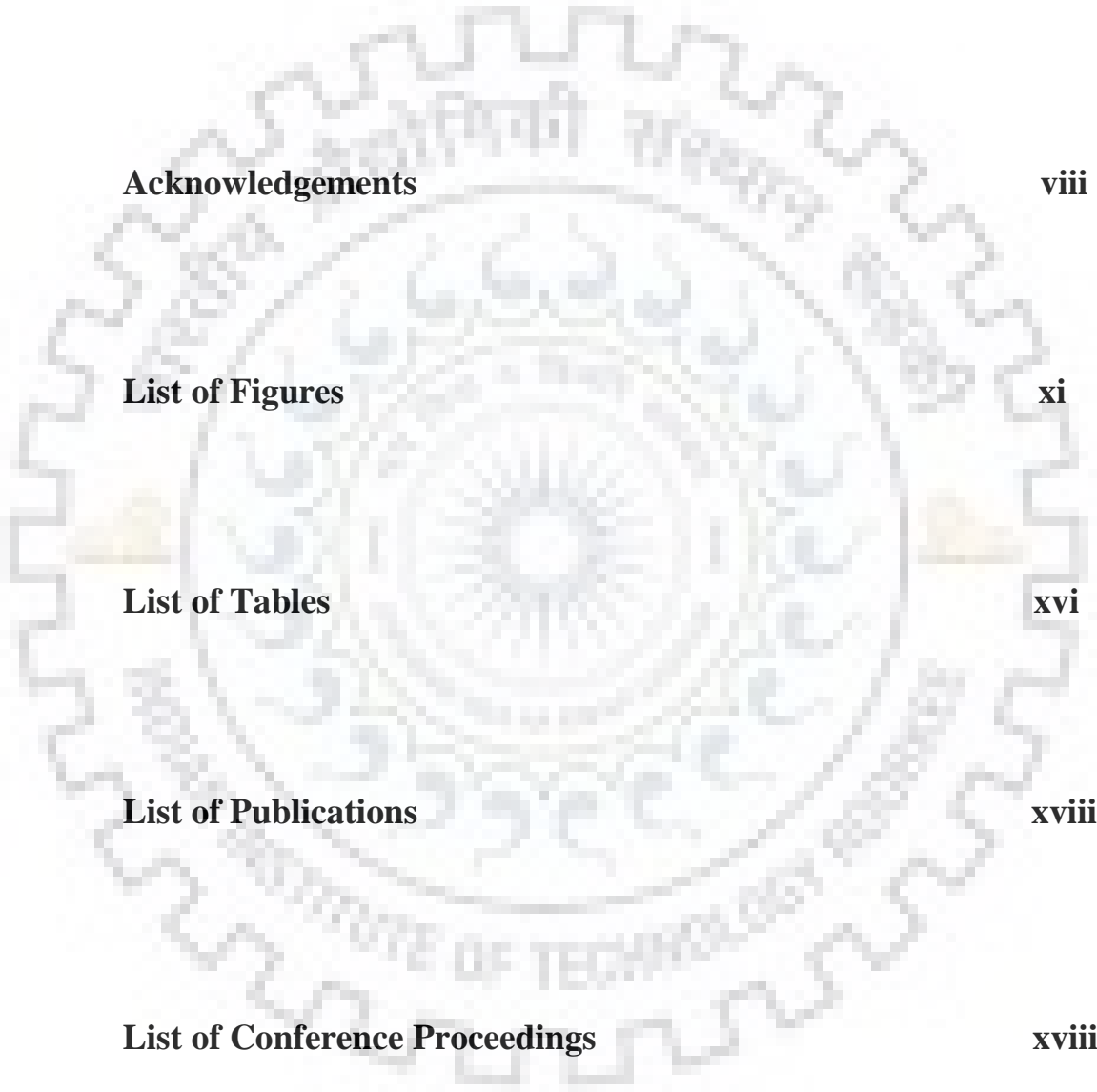




***Dedicated to my Family  
&  
Friends***

# CONTENTS

<b>Abstract</b>	<b>i</b>
<b>Acknowledgements</b>	<b>viii</b>
<b>List of Figures</b>	<b>xi</b>
<b>List of Tables</b>	<b>xvi</b>
<b>List of Publications</b>	<b>xviii</b>
<b>List of Conference Proceedings</b>	<b>xviii</b>



## ABSTRACT

Transition metal oxides continue to attract research attention owing to their various novel and exciting physical and chemical properties. The oxides may adopt structures ranging from rock salt, spinel to perovskites and its variants. Although a large variety of transition metal oxides are reported in the literature, a lot of possibility remains to be explored with new chemical compositions and structures that are not achievable by conventional high temperature synthetic route. Although, the routine solid-state synthesis is very convenient and widely employed to synthesize many functional oxides, but the range of compositions accessible are limited by the competition between thermodynamic and kinetic factors. The key limiting factor in solid-state synthesis is often the requirement for diffusion of individual atoms/ions that necessitates high temperature reaction condition and thus produces thermodynamically stable products or phases. On the other hand, low temperature syntheses methods enable one to access the so called metastable phases, while retaining part or all of the structural and bonding features of the precursor molecules/motifs. In this way, a thermodynamically stable precursor, typically made by a high temperature solid-state reaction, can be converted into a related metastable structure, which is not accessible by direct synthesis, through soft-chemical methods. These kinds of reactions, initially developed by French chemists, were called “*chimie douce*”, most commonly translated as “soft chemistry” to signify the gentle conversion of one structure into another with part or complete retention of chemical bonding and structural features of the precursor. Soft-chemical reactions have since been widely explored for the synthesis of layered oxides and include ion exchange, intercalation, reductive deintercalation, layer expansion, grafting, exfoliation, pillaring, and substitution reactions. The utilization of topochemical reactions has increased in recent years allowing access to a series of new compounds that are structurally varied and can exhibit significantly different properties, including those of fundamental and technological interest.

Topochemical manipulations include a number of methods, such as, substitution or ion exchange, intercalation and deintercalation, to name a few. The ion exchange simply involves the substitution or replacement of one type of cations or anions by another. While most of these types of reactions involve a one-to-one exchange of monovalent ions, in some instances aliovalent species may likewise take part in exchange (e.g. one divalent cation replacing two monovalent

cations) and in rare cases the co-exchange of cation/ anion combinations can also occur. Another topochemical method, namely intercalation occurs when species are inserted into a host compound. These reactions can involve reductive or oxidative processes that result in either the introduction of cationic or anionic species, respectively, or the insertion of neutral molecules (e.g. H<sub>2</sub>O). In the deintercalation process, cations or anions can be removed by oxidative or reductive means and these can be executed either chemically or electrochemically.

Ion exchange is one of the most popular soft-chemistry routes in preparing novel metastable phases of layered oxides and utilizes general chemistry principles of charge density and acid-base chemistry. Generally, an ion exchange reaction refers to a class of chemical reactions between two materials that involve an exchange of one or more ionic components. Certain inorganic crystalline materials can react with aqueous salt solutions to selectively remove one ionic component and replace it with other ions from the solution with the end result being new materials. The ion exchange process, based on topotactic reactions can result in a material crystallographically analogous to the parent phase but with a new chemical composition. Thus, it is a simple and versatile method for exploring new compositions of materials having a certain crystal framework and is used widely in various fields.

Ion exchange has been mostly limited to the layered oxides with the Dion-Jacobson (DJ) and Ruddlesden-Popper (RP) compounds, such as, NaLaTiO<sub>4</sub>, RbLaNb<sub>2</sub>O<sub>7</sub>, RbLa<sub>2</sub>Ti<sub>2</sub>NbO<sub>10</sub>, RbSrNb<sub>2</sub>O<sub>6</sub>F, K<sub>2</sub>SrTa<sub>2</sub>O<sub>7</sub> and Rb<sub>2</sub>La<sub>2</sub>Ti<sub>3</sub>O<sub>10</sub>. The DJ phases were the first reported examples of ion exchangeable layered perovskites, and the initial ion exchange reactions involved the replacement of larger interlayer cations such as Cs<sup>+</sup>, Rb<sup>+</sup>, and K<sup>+</sup> with smaller cations, such as Na<sup>+</sup>, Li<sup>+</sup>, NH<sub>4</sub><sup>+</sup>, and TI<sup>+</sup> using molten nitrate salts ( $T_m \sim 300$  °C) as the ion exchange medium. DJ phases containing small interlayer cations, such as, Li<sup>+</sup> or Na<sup>+</sup> are often difficult to synthesize as phase-pure materials at high reaction temperatures (> 1000 °C) where the three dimensional perovskite phases are usually more stable. RP phases also undergo similar ion exchange reactions. Like the DJ phases, the interlayer cations of RP phases (typically Na<sup>+</sup>, K<sup>+</sup>, and sometimes Rb<sup>+</sup>) can be replaced by smaller alkali cations, such as, Na<sup>+</sup>, Li<sup>+</sup>, NH<sub>4</sub><sup>+</sup>, and Ag<sup>+</sup> using molten salt ion exchange reactions. RP phases are especially amenable to divalent ion exchange because two interlayer monovalent alkali cations can be replaced with one divalent cation to transform a RP phase into a DJ phase. Hyeon *et al.* reported M<sup>II</sup>La<sub>2</sub>Ti<sub>3</sub>O<sub>10</sub> (M = Co, Cu, Zn) by exchanging 2Na<sup>+</sup>

for  $M^{2+}$  using molten nitrates, chlorides, or a eutectic mixture. Mallouk *et al.* used aqueous ion exchange to form  $A^{II}Eu_2Ti_3O_{10}$  ( $A = Ca, Sr$ ) and  $M^{II}Eu_2Ti_3O_{10}$  ( $M = Ni, Cu, Zn$ ). Gopalakrishnan *et al.* used a higher temperature metathesis reaction to form  $A^{II}La_2Ti_3O_{10}$  ( $A = Sr, Ba, Pb$ ). Additionally, protons can also replace the interlayer alkali cations, which opens up the interlayer gallery to subsequent acid/base reactions including the intercalation of long chain amines. Wiley *et al.* have described an extension of ion exchange reactions in the triple-layered RP series to obtain  $Li_{0.3}Ni_{0.85}La_2Ti_3O_{10}$  in aqueous solution.

While the topotactic ion exchange is common in oxides with the layered perovskite or in other tunnel and framework structures, but are rare in the 3D close packed structures based on all edge and/or corner shared polyhedra. An interesting type of exchange, namely, ‘intra-site exchange’, where perovskite A-site cations were exchanged with the interlayer A'-cations within a compound, was demonstrated in a layered perovskite. A cubooctahedral A-site ion exchange in  $NaTaO_3$  is the only report involving a three-dimensional perovskite structure with all octahedral corner connectivity. In the present investigation, topotactic ion exchange have been explored in three-dimensional structures based purely on corner/edge connected octahedral network in addition to a ribbon type and a framework titanate, also based on edge/corner shared  $TiO_6$  octahedra. The study has enabled transformation of a number of non-magnetic oxides into magnetic ones in addition to altering its optical property to a significant extent. **Chapter 1** gives a brief outline of ion exchange and other soft-chemistry reactions in layered and other oxides, in addition to various other soft-chemical manipulations that these compounds undergo. Syntheses of precursor oxides, their ion exchange, characterization and properties of the resulting compounds are described in subsequent chapters.

**Chapter 2** describes the synthetic methodologies and the details of all the characterization techniques used in the present study. The precursor oxides were synthesized by solid-state reactions starting from binary metal oxides and carbonates. The ion exchange reactions were carried out in aqueous metal nitrate or metal chloride solutions. The progress of the reaction and formation of final products were monitored by powder X-ray diffraction (P-XRD) and elemental analysis by Energy Dispersive X-ray Spectroscopy (EDX). Final morphological and compositional characterizations were carried out by Field Emission-Scanning Electron Microscopy (FE-SEM), Transmission-Electron Microcopy (TEM) and EDX analysis. Further,

the optical properties were studied by UV-vis diffuse reflectance spectroscopy (UV-vis DRS). Solid-state NMR technique was used as an additional probe to estimate the amount of exchanged Li by comparing the integrated intensities of the parent and its ion exchanged counterpart. X-Ray Photoelectron Spectroscopy (XPS) was used to ascertain the oxidation states of the redox active metals in the compounds. Magnetic measurements of the synthesized compounds were carried out by SQUID magnetometer and VSM. The details of P-XRD, FE-SEM, EDX, TEM, UV-vis DRS, ssNMR, XPS, SQUID/VSM instruments and characterization techniques are discussed in this chapter.

**Chapter 3** describes divalent iron-exchange in a three-dimensional close-packed trirutile oxide with all octahedral coordination. For the first time, the transition metal ion exchange in  $\alpha$ -LiNbWO<sub>6</sub> and characterization of the resulting trirutile oxide is reported here. The ion exchange with Fe<sup>II</sup> has been achieved by refluxing  $\alpha$ -LiNbWO<sub>6</sub> in an aqueous solution of FeCl<sub>2</sub>·4H<sub>2</sub>O under an argon atmosphere at 60 °C for 4 days. The close resemblance of the P-XRD pattern of the ion exchanged sample with that of the parent substantiated the topotactic nature of the exchange. An ICP-OES analysis of the Fe-exchanged LiNbWO<sub>6</sub> revealed the exchange of 90% of the Li, leaving behind 10% Li in the sample. Considering 90% exchange of Li, the ion-exchanged compound is formulated as Li<sub>0.1</sub>Fe<sub>0.45</sub>NbWO<sub>6</sub>. The FE-SEM analysis indicated retention of the particle morphology upon exchange and the EDX data confirmed the elemental ratio for Fe, Nb, and W in corroboration with the ICP-OES derived composition. The lattice fringes with 0.932 nm separation in the HR-TEM image conformed to the quasi-ordered trirutile phase akin to the periodicity of the (Li/Fe)O<sub>6</sub> octahedron connected to an NbO<sub>6</sub>–WO<sub>6</sub> bioctahedral unit along the *c* direction. The corresponding SAED pattern is consistent with the tetragonal crystal system and in agreement with the P-XRD data. While the <sup>7</sup>Li MAS NMR spectra of LiNbWO<sub>6</sub> clearly revealed the presence of only one type of Li site, the presence of a <sup>7</sup>Li peak in the Fe exchanged sample with the same chemical shift as that of the parent is supportive of the retention of a small amount of Li without any change to its coordination environment. The XPS data indicated Fe2p binding energies of 723.0 and 709.7 eV for spin–orbit coupled Fe2p<sub>1/2</sub> and Fe2p<sub>3/2</sub> states, respectively, corresponding largely to the presence of Fe<sup>2+</sup> in Li<sub>0.1</sub>Fe<sub>0.45</sub>NbWO<sub>6</sub>. As evidenced in the UV–vis DRS, Fe exchanged has clearly resulted in extension of the optical absorption edge deep into the visible region as compared to its parent, only a near-UV absorber. This amounts to a significant reduction of the indirect band gap of Li<sub>0.1</sub>Fe<sub>0.45</sub>NbWO<sub>6</sub> to 1.71 eV from 3.01 eV of



the parent, as estimated from the Tauc plots. The magnetic susceptibility data below 200 K indicates Curie-like paramagnetism, which arises due to the disorder of Fe at the 2*c* sites and the presence of random vacancies that keeps the Fe<sup>2+</sup> sites isolated from other neighboring Fe<sup>2+</sup> spins in the lattice. The paramagnetic moment corroborates well with the spin-only moment for high-spin Fe<sup>2+</sup>.

**Chapter 4** deals with the synthesis, characterization and magnetic properties of a new tri- $\alpha$ -PbO<sub>2</sub> type oxide, Li<sub>0.08</sub>Fe<sub>0.46</sub>SbWO<sub>6</sub>. The compound is synthesized for the first time by ion exchange reaction of LiSbWO<sub>6</sub> at 60 °C for 4 days under an argon atmosphere. The phase purity of the resulting compound and the topotactic nature of exchange are ascertained by P-XRD analysis. The morphological homogeneity upon ion exchange and the elemental composition are determined using FE-SEM and EDX studies. The UV-vis DRS data of the iron-antimony tungstate also showed a considerable reduction of the visible band gap to 2.06 eV from ~ 3.02 eV of the parent lithium-antimony tungstate. The reduction in the band gap is attributed to the formation of valence band (VB) states, primarily constituted by the overlap of Fe3d and O2p orbitals, which would be situated at higher energies in Li<sub>0.08</sub>Fe<sub>0.46</sub>SbWO<sub>6</sub> as compared to the VB states of the parent LiSbWO<sub>6</sub>. This upshift of VB edge and a consequent decrease in the band gap is ascribed to the extended optical absorption of Li<sub>0.08</sub>Fe<sub>0.46</sub>SbWO<sub>6</sub>. The Fe2p binding energies of 723.2 and 709.6 eV confirmed the presence of Fe<sup>2+</sup>. The observed lattice fringes in the HR-TEM image with a separation of 0.495 nm is in agreement with the periodicity in the *c*-direction. The SAED pattern is consistent with the orthorhombic crystal system and the indexed spots are in agreement with the P-XRD data. The ZFC magnetization data show antiferromagnetic transition at ~ 20 K. Unlike Li<sub>0.1</sub>Fe<sub>0.45</sub>NbWO<sub>6</sub>, where isolated Fe<sup>2+</sup> are present, Fe(II) dimers can exist in Li<sub>0.08</sub>Fe<sub>0.46</sub>SbWO<sub>6</sub> due to the presence of edge-shared chains of LiO<sub>6</sub> octahedra running along the *c*-direction in the tri- $\alpha$ -PbO<sub>2</sub> structure. This probably is responsible for the low-temperature antiferromagnetic transition in the compound. The high temperature paramagnetic moment, however, matches well with the spin-only moment of high spin Fe<sup>2+</sup>.

In **Chapter 5**, the synthesis, characterization and magnetic properties of transition metal exchanged ribbon-type layered titanates, Na<sub>2(1-x)</sub>M<sub>x</sub>Ti<sub>3</sub>O<sub>7</sub> (M = Mn, Fe, Co and Ni), are reported. The compounds are synthesized by ion exchange of Na<sub>2</sub>Ti<sub>3</sub>O<sub>7</sub> at 60 °C for 48 hours. The close similarity of the P-XRD patterns of the resulting compounds to that with the parent and a color

change over from white to orange-brown/brown/grey-green/light green confirmed the exchange of transition metals in a topotactic fashion. The morphological homogeneity and elemental composition is established with FE-SEM and EDX studies for all the compounds. The HR-TEM showed clear lattice fringes with interfringe spacing of 0.390 nm, which is consistent with the *b*-parameter of the monoclinic unit cell. The SAED pattern is also indexable in the monoclinic space group and consistent with the P-XRD data. UV-vis DRS study confirmed the presence of visible band gaps for all the compounds ranging from 1.99 - 2.86 eV. The Mn compound,  $\text{Na}_{0.02}\text{Mn}_{0.99}\text{Ti}_3\text{O}_7$ , shows antiferromagnetic transition at 32 K, while the rise in susceptibility at ~ 8 K is ascribed to a ferrimagnetic correlation between the  $\text{Mn}^{2+}$  and  $\text{Mn}^{3+}$  spins that may arise due to spin canting. Similar antiferromagnetic transition is also observed in the Ni compound but the low temperature feature is absent. The M-H data for Mn and Ni at low temperatures (5 and 30 K for Mn and 5 K for Ni) showed hysteretic behavior which is a signature of ferrimagnetism possibly arising out of the spin canting. On the contrary, the corresponding Fe and Co compounds showed paramagnetic behaviors throughout the entire temperature range (5 – 300 K).

**Chapter 6** describes the synthesis, characterization and magnetic properties of a new framework titanate,  $\text{Na}_{0.02}\text{Fe}_{0.99}\text{Ti}_6\text{O}_{13}$ . The compound is prepared by ion exchange reaction between  $\text{Na}_2\text{Ti}_6\text{O}_{13}$  and  $\text{FeCl}_2 \cdot 4\text{H}_2\text{O}$  in aqueous medium at 60 °C under continuous stirring for 4 days. The P-XRD pattern indicated that the ion-exchanged product retained the layered framework structure of the parent. The morphology and elemental ratios were characterized by FE-SEM and EDX analysis, respectively. As prepared  $\text{Na}_2\text{Ti}_6\text{O}_{13}$  and the ion-exchanged compound showed plate-like morphology, often seen and expected in layered type oxides. The elemental ratios obtained from EDX analysis, both on spot and area basis are in good agreement with the nominal compositions. UV-vis DRS data revealed  $\text{Na}_{0.02}\text{Fe}_{0.99}\text{Ti}_6\text{O}_{13}$  as a visible light active semiconductor with a band gap of 2.05 eV. The magnetization data indicates paramagnetic character of the compound.

**Chapter 7** provides overall conclusions and future prospects of the present investigation. Ion exchange method have been exploited to synthesize a series of metastable transition metal oxides with close-packed three-dimensional trirutile and tri  $\alpha$ - $\text{PbO}_2$  type structures, in addition to a ribbon-type and a framework layered structure. These results reveal that simple topotactic reactions can be applied for the construction of metal-anion arrays for a number of transition



metals and structures. The effectiveness of this approach is noteworthy as none of them could be prepared by a direct solid-state reaction method. It is expected that the continued development of such synthetic strategies will eventually result in a general set of methodologies for the conscious design and preparation of intricate structural arrangements.



## ACKNOWLEDGEMENTS

It is a milestone achieved with lifelong experiences at Department of Chemistry, IIT Roorkee specifically, my lab **D-305A**. This thesis is the result of many experiences, as pursuing Ph.D. is a painful as well as enjoyable experience. It gives me immense pleasure to express gratitude to all those people who had supported me throughout my Ph.D. and made this thesis possible. First and foremost, I must acknowledge and thank The Almighty God for blessing, protecting and guiding me throughout this period. I could never have accomplished this without the faith I have in the Almighty.

Firstly, I would like to express a deep sense of appreciation to my supervisor, **Dr. Tapas Kumar Mandal** who accepted me as his research student, when I approached him for Ph.D. He has been very supportive and guided me over for the past six years of Ph.D. studies. I couldn't make so much development without his invaluable guidance, immense help and various helpful discussions throughout this research work. I have learnt extensively from him, that includes designing of new materials and thinking of new possibilities to solve a research problem by systematic approach. He is that kind of honest and ethical person that he will do what is right, whatever may be the situation is. He has always taught me to never forget ethics of research which evolves me as a better researcher. I owe him a heavy debt of devoting so much time and efforts to me my entire life. I am also very thankful to **Dipanwita Mam** for providing so much love, care and a homely atmosphere for me in Roorkee.

I am very grateful and would like to thank, **Prof. K R Justin Thomas**, Head of the Department of Chemistry and all other faculty members for their assistance and support. I sincerely thank the members of my SRC, **Prof. Mala Nath** (Chairman), **Dr. P. Jeevanandam**. (Internal member), Department of Chemistry and **Dr. Davinder Kaur** (External member), Department of Physics, IIT Roorkee for their brilliant comments and suggestions to carry out this work.

I am very thankful to Head, Institute Instrumentation Centre (IIC) for providing all the necessary instrumental facilities. I appreciate the help provided by **Mr. Devender Sharma** and **Mr. Shiv Kumar**, in-charge of XRD and **Mr. Shiva** for his kind help during the FE-SEM measurements. I thank **Mr. Gaurav Malik** for XPS measurements and **Mr. D Prasad**, in-charge of SQUID and

XPS instruments. I should also thank **Mr. Subhaneet**, Department of Metallurgical and Materials Engineering for TEM measurements. I am extremely thankful to **Mr. Madan Pal**, Department of Chemistry, for his help in all kind of arrangements during my presentations in the department.

I gratefully acknowledge **University Grants Commission** (UGC), for providing me financial support and Director, IIT Roorkee for allowing me to carry out my research in this esteemed institute.

I thank very much to all the members of solid state chemistry Lab for creating healthy and friendly ambience in lab over all these years. I want to thank **Dr. Naresh** for his constant help during my Ph.D. Thank you **Dr. Nishant** for helping me during ssNMR measurements. Thanks to **Sonia Rani** and **Rita** for your love and care whenever my health deteriorated. Special thanks to **Ambikesh** for inspired me during a difficult time when I needed words of encouragement. I also thanks to the young and energetic team of our lab, **Lalit, Vijay, Jaideep, Shubham, Anil, Prachi, Preeti** and **Megha** for their kind help, support and fun filled discussions. All the best to you all for your future ahead. I thank rest of the lab members **Anowar, Poonam, Avnish** and **Vishal**.

The everlasting and evergreen friends cannot be forgotten. I would like to thanks my school friends **Abhijeet, Aditya, Anantmati, Dr. Dickson, Hitesh, Dr. Jaishree, Jaya, Kapil, Dr. Mohit, Narvada, Pratiksha, Priyanka, Rashmi, Shelly, Sudha, Sunita, Vikram** and **Yogita** for still connected with me and recalling those funny childhood memories. I would like to thank my college friends **Neha Katara, Neha Meena** and **Rajesh** from B.Sc. and **Anchal, Dr. Anshul, Naren, Pravin, Preeti, Rachna, Dr. Renu, Saroj, Seema, Shweta** and **Dr. Yogita** from M.Sc. whose chatting and company always kept my mood.

The list of acknowledgment incomplete if my departmental colleagues and IITR friends are not thanked. I thank **Aakansha di, Dr. Anjana di, Dr. Ankita, Dr. Iram, Dr. Joseph, Dr. Jyoti, Dr. Kiran, Dr. Lata Rana, Dr. Mandeep, Dr. Nitika, Dr. Preeti, Dr. Shweta, Dr. Tawseef, Dr. Urvashi** and **Dr. Zeeshan** for their wonderful co-operation and for providing a positive environment. I also don't want to forget to mention my juniors **Veenu, Chesta** and **Neha Antil** for the quality time they spent with me during their brief stay.

Special thanks from bottom of my heart to my dearest friends **Ankit, Dhapi** and **Meenakshi** for making me laugh at tough times, visiting me to cheer me up whenever I needed them and all those gossips we did in free time. I thank **Arshad, Faisal, Nanhi, Naveen, Ravi, Shahid, Tanweer bhaiya**, and **Tarique**.

Lastly, I would like to thank my family. I feel a deep sense of gratitude for my father **Sh. Mohan Lal Meena**, my mother **Smt. Dhankanwar Meena**, my grandfather Late **Sh. Laxminarayan Meena** and my grandmother **Sita Devi** who formed part of my vision and taught me good things that really matter in life. A special thanks to my elder sister **Meenu** and brother-in-law **Mahendra (jija ji)**, sister and brother-in-law: **Divya** and **Vikas**, brothers **Sonu** and **Nikki** and my niece **Pappu** and nephew **Kaanu** and our new family member **Kiran** for their love and affection. I owe thanks to all my relatives, Grandfather-Grandmother: **Hiralal (nana)-Kailash (nani)**, Uncles-Aunts: **Saraswati (chachi), Balkrishan (chacha)-and Santosh (chachi), Rambilas (mausa ji)-Laxmi (mausi)**, Cousins: **Sulekha, Rajkumar, Kavita, Sandhya, Sudha, Chanchal, Golu, Devan, Archi** and **Nishi**.

Last but not the least, I would like to thank someone very special to me. A huge thanks you for standing by my side whenever I had a hard phase. Without you this journey was incomplete and thank you for everything that you've done for me.

I am glad to interact with you all, you all are genuinely nice, supportive and helpful. I extend my apologies in advance if I forgot to mention anyone.

(VANDANA MEENA)

## List of Figures

- 1.1 Structural motifs of selected layered oxides which are suitable to soft-chemical changes: (a)  $\text{MoO}_3 \cdot 2\text{H}_2\text{O}$  and (b)  $\text{V}_2\text{O}_5$  (c)  $\text{LiCoO}_2$ ;  $\text{ABO}_2$ -type structure, (d) layered double hydroxide (LDH), (e)  $\text{Ca}_2\text{Fe}_2\text{O}_5$ ; Brownmillerite structure. Shear structures of (f)  $\text{KNb}_3\text{O}_8$ , (g)  $\text{K}_4\text{Nb}_6\text{O}_{17}$ , and (h)  $\text{Na}_2\text{Ti}_3\text{O}_7$ ; layered perovskite oxides: (i) Ruddlesden – Popper phase,  $\text{A}'_2[\text{A}_{n-1}\text{B}_n\text{O}_{3n+1}]$ , (j) Dion–Jacobson phase,  $\text{A}'[\text{A}_{n-1}\text{B}_n\text{O}_{3n+1}]$ , and (k) Aurivillius phase  $\text{Bi}_2\text{O}_2[\text{A}_{n-1}\text{B}_n\text{O}_{3n+1}]$ .
- 1.2 The topochemical reaction includes ion exchange, intercalation, layer extraction, reductive deintercalation, layer construction, grafting, exfoliation, pillaring and substitution reactions.
- 1.3 Ion exchange in the open framework chalcogenide  $\text{K}_6\text{Sn}[\text{Zn}_4\text{Sn}_4\text{S}_{17}]$  with  $\text{Cs}^+$ .
- 1.4 Ion exchange conversion of  $\text{RbLaNb}_2\text{O}_7$  to  $(\text{CuCl})\text{LaNb}_2\text{O}_7$ .
- 1.5 Ion exchange in Dion–Jacobson phase  $\text{A}'[\text{A}_{n-1}\text{B}_n\text{O}_{3n+1}]$  and Ruddlesden–Popper phase,  $\text{A}'_2[\text{A}_{n-1}\text{B}_n\text{O}_{3n+1}]$  with  $\text{Ag}^+$ .
- 1.6 Reaction of  $\text{NiCl}_2$  with  $\text{NaTaO}_3$  leads the formation of the perovskite phase  $\text{Ni}_{0.5}\text{TaO}_3$ , via a topochemical nickel-for-sodium cation exchange.
- 1.7 Ion exchange reaction in lamellar structure  $\text{CuNbO}_3$  from lithium cation.
- 1.8 Topotactic reaction of precursor  $\text{A}_2\text{IrO}_3$  ( $\text{A} = \text{Li}, \text{Na}$ ) and  $\text{CuCl}$  to form iridium containing honeycomb Delafossites  $\text{Cu}_3\text{A}\text{Ir}_2\text{O}_6$ .
- 1.9 Scheme showing reductive site-selective intercalation of  $\text{Y}_2\text{Ti}_2\text{O}_5\text{S}_2$  (1) by the intercalation of electropositive metals: (2) lithium intercalates,  $\text{Li}_x\text{Y}_2\text{Ti}_2\text{O}_5\text{S}_2$  ( $0 < x \leq 2$ ), (3) sodium intercalates,  $\alpha\text{-Na}_x\text{Y}_2\text{Ti}_2\text{O}_5\text{S}_2$  ( $0 < x \leq 1.0$ ) obtained at temperatures of around 500-600 °C. In contrast, (4) sodium intercalate,  $\beta\text{-NaY}_2\text{Ti}_2\text{O}_5\text{S}_2$  and (5) potassium intercalate,  $\text{KY}_2\text{Ti}_2\text{O}_5\text{S}_2$  were obtained at room temperature.

- 1.10  $A_2CuO_3$  ( $A = Ca, Sr$ ) fluorination with simultaneously anion lattice rearrangement, retaining the apexed  $CuO_4$  square plane sheets.
- 1.11 Topochemical fluorination of  $Sr_3Ru_2O_7$  to  $Sr_3Ru_2O_7F_2$  and oxidative insertion of fluorine and the formation of the  $A_3B_2O_7F_2$ .
- 1.12 An overview of the modification in the Layered Perovskite,  $H_2La_2Ti_3O_{10}$  with  $n$ -alkylamine and  $n$ -alcohol by ion-exchange reactions
- 1.13  $La_3Ni_2O_{7-x}$  and  $La_3Ni_2O_6$ , a single oxygen from the perovskite block moves into the rock-salt layer to produce a T' structure.
- 1.14 RP layered perovskite layer extraction treatment,  $K_2La_2Ti_3O_{10}$  (I); potassium oxide extraction with  $(PBU_4Br; PPh_4Br)$  salts, (II)  $KLa_2Ti_3O_{9.5}$  and (III)  $La_2Ti_3O_9$ .
- 1.15 Various structures accessible topochemically within layered perovskite hosts. (a)  $(MCl)LaNb_2O_7$  ( $M =$  transition metal), (b)  $(Li_2Cl)LaNb_2O_7$ , (c)  $(Rb_2Cl)LaNb_2O_7$ , and (d)  $(Rb_2OH)LaNb_2O_7$
- 3.1 P-XRD patterns of  $LiNbWO_6$  and  $Li_{0.1}Fe_{0.45}NbWO_6$ .
- 3.2 Rietveld refinement of P-XRD data for  $Li_{0.1}Fe_{0.45}NbWO_6$ . Observed (+), calculated (–) and difference (at the bottom) profiles are shown. Vertical bars below the profile mark the Bragg reflection positions.
- 3.3 Polyhedral representations of  $Li_{0.1}Fe_{0.45}NbWO_6$  in the  $ab$ -plane.
- 3.4 Polyhedral representations of the structure of  $Li_{0.1}Fe_{0.45}NbWO_6$  drawn with the refined atomic coordinates. The structure shown here presents Li/Fe vacancies in an ordered fashion.
- 3.5 FE-SEM and corresponding EDX data of  $Li_{0.1}Fe_{0.45}NbWO_6$  (a) after 24 h of ion exchange and (b) after 48 h of ion exchange.
- 3.6 FE-SEM and corresponding EDX data of (a)  $\alpha$ - $LiNbWO_6$  and (b)  $Li_{0.1}Fe_{0.45}NbWO_6$ .

- 3.7 EDX line scan of Fe, Nb and W for  $\text{Li}_{0.1}\text{Fe}_{0.45}\text{NbWO}_6$  along with the corresponding bright field SEM image.
- 3.8 (a) HR-TEM image and (b) SAED pattern of  $\text{Li}_{0.1}\text{Fe}_{0.45}\text{NbWO}_6$ .
- 3.9 Solid-state  $^7\text{Li}$  MAS NMR spectra of  $\text{LiNbWO}_6$  and  $\text{Li}_{0.1}\text{Fe}_{0.45}\text{NbWO}_6$ .
- 3.10 Fe-2p XPS of  $\text{Li}_{0.1}\text{Fe}_{0.45}\text{NbWO}_6$ .
- 3.11 XPS survey spectra for  $\text{Li}_{0.1}\text{Fe}_{0.45}\text{NbWO}_6$ .
- 3.12 P-XRD patterns of  $\text{Li}_{0.1}\text{Fe}_{0.45}\text{NbWO}_6$  after heating at 350 (in air), 550 and 800°C (in argon atmosphere).
- 3.13 UV-vis DRS data (a) and corresponding Tauc plots (b) for  $\text{Li}_{0.1}\text{Fe}_{0.45}\text{NbWO}_6$ .
- 3.14 (a) Magnetization vs temperature, (b) molar susceptibility and inverse molar susceptibility vs. temperature for  $\text{Li}_{0.1}\text{Fe}_{0.45}\text{NbWO}_6$ .
- 4.1 P-XRD patterns of  $\text{LiSbWO}_6$  and  $\text{Li}_{0.08}\text{Fe}_{0.46}\text{SbWO}_6$ .
- 4.2 Rietveld refinement of P-XRD data for  $\text{Li}_{0.08}\text{Fe}_{0.46}\text{SbWO}_6$ . Observed (+), calculated (–) and difference (at the bottom) profiles are shown. Vertical bars below the profile mark the Bragg reflection positions.
- 4.3 Polyhedral representation of  $\text{Li}_{0.08}\text{Fe}_{0.46}\text{SbWO}_6$  in the *ac*-plane.
- 4.4 Polyhedral representation of  $\text{Li}_{0.08}\text{Fe}_{0.46}\text{SbWO}_6$  in the *bc*-plane and *ab*-plane drawn with the refined atomic coordinates. Fe(II) dimers are seen in the *ab*-plane generated by selectively removing the Li sites that remain vacant on Fe exchange.
- 4.5 (a) FE-SEM image and (b) corresponding EDX data for  $\text{Li}_{0.08}\text{Fe}_{0.46}\text{SbWO}_6$  after 48 h of ion exchange.
- 4.6 (a, b) FE-SEM images and (a', b') corresponding EDX for  $\text{LiSbWO}_6$  and  $\text{Li}_{0.08}\text{Fe}_{0.46}\text{SbWO}_6$ .



- 4.7 EDX line scan of Fe, Sb and W for  $\text{Li}_{0.08}\text{Fe}_{0.46}\text{SbWO}_6$  along with the corresponding bright field SEM image.
- 4.8 (a) HR-TEM image and (b) selected SAED patterns for  $\text{Li}_{0.08}\text{Fe}_{0.46}\text{SbWO}_6$ .
- 4.9 (a) K-M plots and (b) Tauc plots of  $\text{LiSbWO}_6$  and  $\text{Li}_{0.08}\text{Fe}_{0.46}\text{SbWO}_6$ .
- 4.10 Fe 2p XPS of  $\text{Li}_{0.08}\text{Fe}_{0.46}\text{SbWO}_6$ .
- 4.11 XPS Survey spectra of  $\text{Li}_{0.08}\text{Fe}_{0.46}\text{SbWO}_6$ .
- 4.12 (a) Molar and inverse molar susceptibility vs. temperature and (b) magnetization vs field data for  $\text{Li}_{0.08}\text{Fe}_{0.46}\text{SbWO}_6$ .
- 5.1 Crystal Structure of  $\text{Na}_2\text{Ti}_3\text{O}_7$ .
- 5.2 P-XRD patterns of  $\text{Na}_2\text{Ti}_3\text{O}_7$ ,  $\text{Na}_{0.02}\text{Mn}_{0.99}\text{Ti}_3\text{O}_7$ ,  $\text{Na}_{0.16}\text{Fe}_{0.92}\text{Ti}_3\text{O}_7$ ,  $\text{Na}_{0.14}\text{Co}_{0.93}\text{Ti}_3\text{O}_7$  and  $\text{Na}_{0.02}\text{Ni}_{0.99}\text{Ti}_3\text{O}_7$ .
- 5.3 (a-e) FE-SEM and corresponding EDX data (a'-e') of (a, a')  $\text{Na}_2\text{Ti}_3\text{O}_7$ , (b, b')  $\text{Na}_{0.02}\text{Mn}_{0.99}\text{Ti}_3\text{O}_7$ , (c, c')  $\text{Na}_{0.16}\text{Fe}_{0.92}\text{Ti}_3\text{O}_7$ , (d, d')  $\text{Na}_{0.14}\text{Co}_{0.93}\text{Ti}_3\text{O}_7$  and (e, e')  $\text{Na}_{0.02}\text{Ni}_{0.99}\text{Ti}_3\text{O}_7$ .
- 5.4 EDX elemental mapping of Na, Ti, Mn, Fe, Co and Ni for  $\text{Na}_2\text{Ti}_3\text{O}_7$ ,  $\text{Na}_{0.02}\text{Mn}_{0.99}\text{Ti}_3\text{O}_7$ ,  $\text{Na}_{0.16}\text{Fe}_{0.92}\text{Ti}_3\text{O}_7$ ,  $\text{Na}_{0.14}\text{Co}_{0.93}\text{Ti}_3\text{O}_7$  and  $\text{Na}_{0.02}\text{Ni}_{0.99}\text{Ti}_3\text{O}_7$  along with the corresponding bright field SEM image.
- 5.5 (a) HR-TEM and (b) SAED pattern of  $\text{Na}_{0.02}\text{Ni}_{0.99}\text{Ti}_3\text{O}_7$ .
- 5.6 High resolution Mn-2p and survey XPS of  $\text{Na}_{0.02}\text{Mn}_{0.99}\text{Ti}_3\text{O}_7$ .
- 5.7 High resolution Fe-2p and survey XPS of  $\text{Na}_{0.02}\text{Fe}_{0.99}\text{Ti}_6\text{O}_{13}$ .
- 5.8 High resolution Co-2p and survey XPS of  $\text{Na}_{0.14}\text{Co}_{0.93}\text{Ti}_3\text{O}_7$ .
- 5.9 High resolution Ni-2p and survey XPS spectra of  $\text{Na}_{0.02}\text{Ni}_{0.99}\text{Ti}_3\text{O}_7$ .



- 5.10 (a) UV-vis DRS data and (b) Tauc plots for  $\text{Na}_2\text{Ti}_3\text{O}_7$ ,  $\text{Na}_{0.02}\text{Mn}_{0.99}\text{Ti}_3\text{O}_7$ ,  $\text{Na}_{0.16}\text{Fe}_{0.92}\text{Ti}_3\text{O}_7$ ,  $\text{Na}_{0.14}\text{Co}_{0.93}\text{Ti}_3\text{O}_7$  and  $\text{Na}_{0.02}\text{Ni}_{0.99}\text{Ti}_3\text{O}_7$ .
- 5.11 (a) ZFC and FC magnetization vs. temperature and (b) magnetization vs. field plot for  $\text{Na}_{0.02}\text{Mn}_{0.99}\text{Ti}_3\text{O}_7$ . Inset of (a) show the inverse molar susceptibility vs. temperature plot for the FC data.
- 5.12 (a) ZFC and FC magnetization vs. temperature and (b) molar susceptibility and inverse molar susceptibility vs. temperature plot for  $\text{Na}_{0.16}\text{Fe}_{0.92}\text{Ti}_3\text{O}_7$ .
- 5.13 (a) ZFC and FC magnetization vs. temperature. (b) Molar susceptibility and inverse molar susceptibility vs. temperature plot for  $\text{Na}_{0.14}\text{Co}_{0.93}\text{Ti}_3\text{O}_7$ .
- 5.14 (a) ZFC and FC magnetization vs. temperature and (b) magnetization vs. field plot for  $\text{Na}_{0.02}\text{Ni}_{0.99}\text{Ti}_3\text{O}_7$ . Inset of (a) show the inverse molar susceptibility vs. temperature plot for the FC data.
- 6.1 Crystal structure of  $\text{Na}_2\text{Ti}_6\text{O}_{13}$ .
- 6.2 P-XRD patterns of  $\text{Na}_2\text{Ti}_6\text{O}_{13}$  and  $\text{Na}_{0.02}\text{Fe}_{0.99}\text{Ti}_6\text{O}_{13}$ .
- 6.3 Rietveld refinement of P-XRD data for  $\text{Na}_{0.02}\text{Fe}_{0.99}\text{Ti}_6\text{O}_{13}$ . Observed (+), calculated (-) and difference (at the bottom) profiles are shown. Vertical bars below the profile mark the Bragg reflection positions.
- 6.4 Polyhedral representations of the structure of  $\text{Na}_{0.02}\text{Fe}_{0.99}\text{Ti}_6\text{O}_{13}$  drawn with the refined atomic coordinates. The structure shown here presents Li/Fe vacancies in an ordered fashion.
- 6.5 FE-SEM and corresponding EDX data of (a, a')  $\text{Na}_2\text{Ti}_6\text{O}_{13}$  and (b, b')  $\text{Na}_{0.02}\text{Fe}_{0.99}\text{Ti}_6\text{O}_{13}$ .
- 6.6 (a) HR-TEM and (b) SAED pattern of  $\text{Na}_{0.02}\text{Fe}_{0.99}\text{Ti}_6\text{O}_{13}$ .
- 6.7 Fe-2p XPS of  $\text{Na}_{0.02}\text{Fe}_{0.99}\text{Ti}_6\text{O}_{13}$ .
- 6.8 XPS survey spectra for  $\text{Na}_{0.02}\text{Fe}_{0.99}\text{Ti}_6\text{O}_{13}$ .

- 6.9 (a) UV-vis DRS data for  $\text{Na}_{0.02}\text{Fe}_{0.99}\text{Ti}_6\text{O}_{13}$ . (b) Corresponding Tauc plot for the calculation of band gap.
- 6.10 (a) Magnetization vs. temperature and (b) magnetization vs. field data for  $\text{Na}_{0.02}\text{Fe}_{0.99}\text{Ti}_6\text{O}_{13}$ . Inset show the inverse molar susceptibility vs. temperature plot for the FC data.

## List of Tables

- 3.1 Lattice Parameters and Band Gap of  $\text{LiNbWO}_6$  and  $\text{Li}_{0.1}\text{Fe}_{0.45}\text{NbWO}_6$
- 3.2 Indexed P-XRD Data for  $\text{Li}_{0.1}\text{Fe}_{0.45}\text{NbWO}_6$
- 3.3.1 Atomic Positions, Site Occupancy and Thermal Parameters of  $\text{Li}_{0.1}\text{Fe}_{0.45}\text{NbWO}_6$
- 3.3.2 Space group, Refined Cell Parameter and the Reliability Factor for  $\text{Li}_{0.1}\text{Fe}_{0.45}\text{NbWO}_6$
- 3.4 Selected Bond Lengths ( $\text{\AA}$ ) of  $\text{Li}_{0.1}\text{Fe}_{0.45}\text{NbWO}_6$
- 3.5 Magnetic Data for  $\text{Li}_{0.1}\text{Fe}_{0.45}\text{NbWO}_6$  Calculated from the Linear Fit of the  $\chi_m^{-1}$  vs. T Plot
- 4.1 Lattice Parameters and Band Gap Energy of  $\text{LiSbWO}_6$  and  $\text{Li}_{0.08}\text{Fe}_{0.46}\text{SbWO}_6$
- 4.2 Indexed P-XRD Data for  $\text{Li}_{0.08}\text{Fe}_{0.46}\text{SbWO}_6$
- 4.3 Refinement Parameters, Atomic Positions, Site Occupancy and Thermal Parameters of  $\text{Li}_{0.08}\text{Fe}_{0.46}\text{SbWO}_6$
- 4.4 Selected Bond Lengths ( $\text{\AA}$ ) of  $\text{Li}_{0.08}\text{Fe}_{0.46}\text{SbWO}_6$
- 4.5 Magnetic Data for  $\text{Li}_{0.08}\text{Fe}_{0.46}\text{SbWO}_6$  Calculated from the Linear Fit of the  $\chi_m^{-1}$  vs. T Plot

- 5.1 Lattice Parameters and Band gap of  $\text{Na}_2\text{Ti}_3\text{O}_7$  and  $\text{Na}_{0.02}\text{Mn}_{0.99}\text{Ti}_3\text{O}_7$ ,  $\text{Na}_{0.16}\text{Fe}_{0.92}\text{Ti}_3\text{O}_7$ ,  $\text{Na}_{0.14}\text{Co}_{0.93}\text{Ti}_3\text{O}_7$ ,  $\text{Na}_{0.02}\text{Ni}_{0.99}\text{Ti}_3\text{O}_7$
- 5.2 Indexed P-XRD Data for  $\text{Na}_{0.02}\text{Mn}_{0.99}\text{Ti}_3\text{O}_7$
- 5.3 Indexed P-XRD Data for  $\text{Na}_{0.16}\text{Fe}_{0.92}\text{Ti}_3\text{O}_7$
- 5.4 Indexed P-XRD Data for  $\text{Na}_{0.14}\text{Co}_{0.93}\text{Ti}_3\text{O}_7$
- 5.5 Indexed P-XRD Data for  $\text{Na}_{0.02}\text{Ni}_{0.99}\text{Ti}_3\text{O}_7$
- 5.6 Magnetic Data for  $\text{Na}_{0.02}\text{Mn}_{0.99}\text{Ti}_3\text{O}_7$ ,  $\text{Na}_{0.16}\text{Fe}_{0.92}\text{Ti}_3\text{O}_7$ ,  $\text{Na}_{0.14}\text{Co}_{0.93}\text{Ti}_3\text{O}_7$  and  $\text{Na}_{0.02}\text{Ni}_{0.99}\text{Ti}_3\text{O}_7$  Calculated from the Linear Fit of the  $\chi_m^{-1}$  vs. T Plot
- 6.1 Lattice Parameters and Band Gap of  $\text{Na}_2\text{Ti}_6\text{O}_{13}$  and  $\text{Na}_{0.02}\text{Fe}_{0.99}\text{Ti}_6\text{O}_{13}$
- 6.2 Indexed P-XRD Data for  $\text{Na}_{0.02}\text{Fe}_{0.99}\text{Ti}_6\text{O}_{13}$
- 6.3 Atomic Positions, Site Occupancy and Thermal Parameters of  $\text{Na}_{0.02}\text{Fe}_{0.99}\text{Ti}_6\text{O}_{13}$
- 6.4 Selected Bond Lengths (Å) of  $\text{Na}_{0.02}\text{Fe}_{0.99}\text{Ti}_6\text{O}_{13}$
- 6.5 Magnetic Data for  $\text{Na}_{0.02}\text{Fe}_{0.99}\text{Ti}_6\text{O}_{13}$  Calculated from the Linear Fit of the  $\chi_m^{-1}$  vs. T Plot

### List of Publications:

1. **Vandana Meena** and Tapas Kumar Mandal, Topotactic Ion Exchange in a Three-Dimensional Close-Packed Trirutile Structure with an Octahedral Network. *Inorg. Chem. (Communication)* **2019**, 58, 2921–2924.
2. **Vandana Meena** and Tapas Kumar Mandal,  $\text{Li}_{(1-2x)}\text{Fe}_x\text{SbWO}_6$ : A novel magnetic tri- $\alpha$ - $\text{PbO}_2$  type iron antimony tungstate through topotactic ion-exchange of  $\text{LiSbWO}_6$ . (manuscript under preparation)
3. **Vandana Meena** and Tapas Kumar Mandal, Topotactic transformation of non-magnetic ribbon-type titanates into magnetic analogs through soft-chemistry. (manuscript under preparation)
4. **Vandana Meena** and Tapas Kumar Mandal, New magnetic framework-type layered titanates,  $\text{Na}_{2(1-x)}\text{Fe}_x\text{Ti}_6\text{O}_{13}$ , by ion-exchange of  $\text{Na}_2\text{Ti}_6\text{O}_{13}$ . (manuscript under preparation)

### List of Conference Proceedings:

1. **Vandana Meena** and Tapas Kumar Mandal,  $\text{Li}_{(1-2x)}\text{Fe}_x\text{NbWO}_6$ : A Novel Layered Trirutile Oxide Obtained By Topotactic Ion-exchange And Its Magnetic Properties. Modern Trends in Inorganic Chemistry – XVII, *NCL Pune, IISER Pune, India*, December 11-14, 2017.
2. **Vandana Meena** and Tapas Kumar Mandal, Topotactic Transformation of Non-magnetic Layered Titanates into Magnetic Titanates through Soft-chemistry. 23<sup>rd</sup> CRSI, *IISER Bhopal, Bhopal, India*, July 13-15, 2018.
3. **Vandana Meena** and Tapas Kumar Mandal,  $\text{Li}_{0.08}\text{Fe}_{0.46}\text{SbWO}_6$ : A New tri- $\alpha$ - $\text{PbO}_2$  Type Fe-Sb-Tungstate by Topotactic Ion Exchange of  $\text{LiSbWO}_6$ . 47<sup>th</sup> IUPAC World Chemistry Congress, *Le Palais des Congrès Paris, France*. July 7 -12, 2019.

# Contents

<b>1</b>	<b>Introduction</b>	
<b>1.1</b>	<b>Introduction</b>	<b>1</b>
<b>1.2</b>	<b>Topochemical Manipulations</b>	<b>6</b>
1.2.1	Ion exchange	7
1.2.2	Intercalation	15
1.2.2.1	Reductive Intercalation	16
1.2.2.2	Oxidative Intercalation	18
1.2.2.3	Neutral Intercalation	22
1.2.3	Reductive Deintercalation	24
1.2.4	Layer Extraction	26
1.2.5	Metal-Nonmetal Layer Construction	27
1.2.6	Methods to Synthesize Metal Oxides	29
	References	31
<b>2</b>	<b>Characterization Techniques</b>	
<b>2.1</b>	<b>Powder X-ray Diffraction (P-XRD)</b>	<b>48</b>
<b>2.2</b>	<b>Field Emission Scanning Electron Microscopy and Energy Dispersive X ray Spectroscopy (FE-SEM and EDX)</b>	<b>49</b>
<b>2.3</b>	<b>High Resolution Transmission Electron Microscopy (HR-TEM)</b>	<b>50</b>
<b>2.4</b>	<b>UV-Visible Diffuse Reflectance Spectroscopy (UV-vis DRS)</b>	<b>51</b>
<b>2.5</b>	<b>X-Ray Photoelectron spectroscopy (XPS)</b>	<b>52</b>
<b>2.6</b>	<b>Inductively Couple Plasma Optical Emission Spectroscopy (ICP-OES)</b>	<b>52</b>

<b>2.7</b>	<b>Solid State Nuclear Magnetic Resonance (ssNMR)</b>	<b>53</b>
<b>2.8</b>	<b>Magnetic Measurements</b>	<b>54</b>
2.8.1	Classification of materials	55
2.8.2	Superconducting Quantum Interference Device (SQUID) Magnetometer	57
2.8.3	Vibrating sample Magnetometer (VSM)	57
	References	58
<b>3</b>	<b>Topotactic Ion Exchange in a Three-Dimensional Close-Packed Trirutile Structure with an Octahedral Network</b>	
3.1	Introduction	59
3.2	Experimental Section	61
3.2.1	Materials and Synthesis	61
3.3	Results and Discussion	61
3.3.1	Powder-XRD Analysis	61
3.3.2	FE-SEM and EDX Analysis	67
3.3.3	FE-SEM-EDX Line Scan Analysis	69
3.3.4	HR-TEM Analysis	70
3.3.5	Solid-State Nuclear Magnetic Resonance (ssNMR) Analysis	70
3.3.6	XPS Analysis	71
3.3.7	Thermal Stability	72
3.3.8	UV-vis DRS Analysis	73
3.3.9	Magnetic Measurement	74

<b>References</b>	<b>77</b>
<b>4 A New tri <math>\alpha</math>-PbO<sub>2</sub> Type Fe-Sb-Tungstate by Topotactic Ion Exchange of LiSbWO<sub>6</sub></b>	
4.1 Introduction	80
4.2 Experimental Section	82
4.2.1 Materials and Synthesis	82
4.3 Results and Discussion	82
4.3.1 Powder-XRD Analysis	82
4.3.2 FE-SEM and EDS Analysis	88
4.3.3 FE-SEM-EDX Line Scan Analysis	89
4.3.4 HR-TEM Analysis	90
4.3.5 UV-vis DRS Analysis	91
4.3.6 XPS Analysis	92
4.3.7 Magnetic Measurement	94
References	96
<b>5 Topotactic transformation of non-magnetic ribbon type layered titanates, Na<sub>2</sub>Ti<sub>3</sub>O<sub>7</sub> into magnetic analogs through ion exchange</b>	<b>99</b>
5.1 Introduction	99
5.2 Experimental Section	101
5.2.1 Materials and Synthesis	101
5.3 Results and Discussion	101
5.3.1 Powder-XRD Analysis	101
5.3.2 FE-SEM Analysis	107

5.3.3	FE-SEM-EDX Elemental Mapping Analysis	109
5.3.4	HR-TEM Analysis	110
5.3.5	XPS Analysis	110
5.3.6	UV-vis DRS Analysis	113
5.3.7	Magnetic Measurement	113
	References	118
<b>6</b>	<b>New paramagnetic framework titanate by topotactic Fe(II) exchange of Na<sub>2</sub>Ti<sub>6</sub>O<sub>13</sub></b>	
6.1	Introduction	121
6.2	Experimental Section	123
6.2.1	Materials and Synthesis	123
6.3	Results and Discussion	124
6.3.1	Powder-XRD Analysis	124
6.3.2	FE-SEM Analysis	131
6.3.3	HR-TEM Analysis	131
6.3.4	XPS Analysis	132
6.3.5	UV-vis DRS Analysis	134
6.3.6	Magnetic Measurement	134
	References	137
<b>7</b>	<b>Conclusions and Future Prospects</b>	<b>140</b>



*CHAPTER -1*

*Introduction*



**1.1 Introduction.**

Transition metal oxides continue to attract research attention because of their diverse and exciting physical and chemical characteristics. The oxides may adopt structures ranging from rock salt, spinel to perovskites and its variants. Although a large variety of transition metal oxides are reported in the literature, there remain a lot of possibility to explore new chemical compositions and structures that are not achievable by high temperature reactions. Although, conventional ceramic route (solid-state synthesis) is a convenient way to synthesize numerous functional oxides, both layered and three-dimensional, but the range of compositions that are accessible are limited by thermodynamic and kinetic factors. The key limiting factor in solid-state syntheses is often the requirement for diffusion of individual atoms that necessitates high temperatures and the most stable thermodynamic products are therefore produced. In contrast, low temperature material synthesis permits access to metastable kinetic phases, often while retaining some or all of the precursor molecular chemical bonds. Topochemical solid-state reactions transform extended solids of one form to another, usually retaining much of the precursor bonds. In this way, a thermodynamically stable precursor which is usually made through a high temperature solid-state reaction can be turned into a corresponding metastable structure which cannot be directly accessed through synthesis. Initially, such reactions were developed by French chemists, were most frequently referred to as “soft chemistry”, which means that the one structure is gently converted to another, while retaining most of its initial chemical bonding features. Since then, soft chemical reactions involving layered oxides have been extensively explored that includes ion exchange, intercalation, reductive deintercalation, layer expansion, grafting, exfoliation, pillaring, and substitution reactions.

It has long been the field of molecular synthetic chemists to effectively direct atomic connectivity in the synthesis of certain target compounds. The use of well-constructed consecutive reactions leads easily to complex structures with specific functionalities. In contrast, it is not easy to manipulate non-molecular compounds in large volume as the ability to direct connectivity homogeneously across a solid is very difficult with the extended structures, in fact, these manipulations are often not feasible without degrading its crystalline matrix. However, there are several methods that allowed the structures of non-molecular solids to be effectively manipulated once a crystalline lattice has been established. These

methodologies, known as topotactic or topochemical manipulations, allow the transformation of compounds while maintaining most of the structural characteristics of the parent.

Layered metal oxides are specific class of solids, which are capable of chemical transformation at low temperatures without disturbing the covalent bonding of the layers. These compounds may include stacks of electro-neutral metal oxide layers, but they are more often intergrowths of charged layers that are connected to cations or anions, or their sheets of metal oxides that alternate with covalently bonded interlayers. For example, uncharged layered oxides include  $\text{MoO}_3 \cdot 2\text{H}_2\text{O}$ , which contains distorted  $\text{MoO}_5(\text{H}_2\text{O})$ , octahedral layers with interspacing water molecules, and  $\text{V}_2\text{O}_5$  consisting of O atoms, which are cross related in a zig-zag pattern to form sheets with trigonal bipyramidal coordination around V atoms [1, 2]. The intergrowths in ionic material include  $\text{A}_x\text{MO}_2$  and  $\text{AMO}_3$  that have an octahedral edge-sharing  $\text{MO}_6$  layers with alkali metal ions between the layers [3]. In addition, they also include alkali metal niobates,  $\text{KNb}_3\text{O}_8$  [4] and  $\text{K}_4\text{Nb}_6\text{O}_{17}$  [5] and titanates, with general formula,  $\text{M}_2\text{Ti}_n\text{O}_{2n+1}$ , (M = Na, K) [6, 7] and  $\text{Na}_4\text{Ti}_n\text{O}_{2n+2}$  [8, 9]. The structure of titanates are layered with sheared sheets in the direction of each  $n^{\text{th}}$  octahedron that is perpendicular to the plane. Other transitional metals, including Mn, V, and W have also been prepared with ternary oxides and some of them are anion exchangers [10-12].

Layered perovskites are a special class of compounds containing layers with the fundamental components of  $\text{ABX}_3$  perovskite, where A refers to 12-coordinated alkali / alkaline earth or a rare earth cation and B refers to d or p block metal cation in octahedral (X = O, halogen, N, S, and / or H) coordination,  $\text{BX}_6$ . Dion-Jacobson (DJ),  $\text{A}'[\text{A}_{n-1}\text{B}_n\text{O}_{3n+1}]$ , and Ruddlesden-Popper (RP) phases,  $\text{A}'_2[\text{A}_{n-1}\text{B}_n\text{O}_{3n+1}]$ , are the two most frequently encountered structural classes of layered oxide perovskites containing ion-exchangeable cations [13], where A' and A are alkali, alkaline-earth, or rare-earth cations, B is a transition metal cation, and  $n$  represents the number of  $\text{BO}_6$  octahedral layers in between the A' cation layers. The main difference between these structural families is that the number of interlayer cations (alkali) in the DJ phase is half of that are present in the RP phases. (In Figure 1.1).

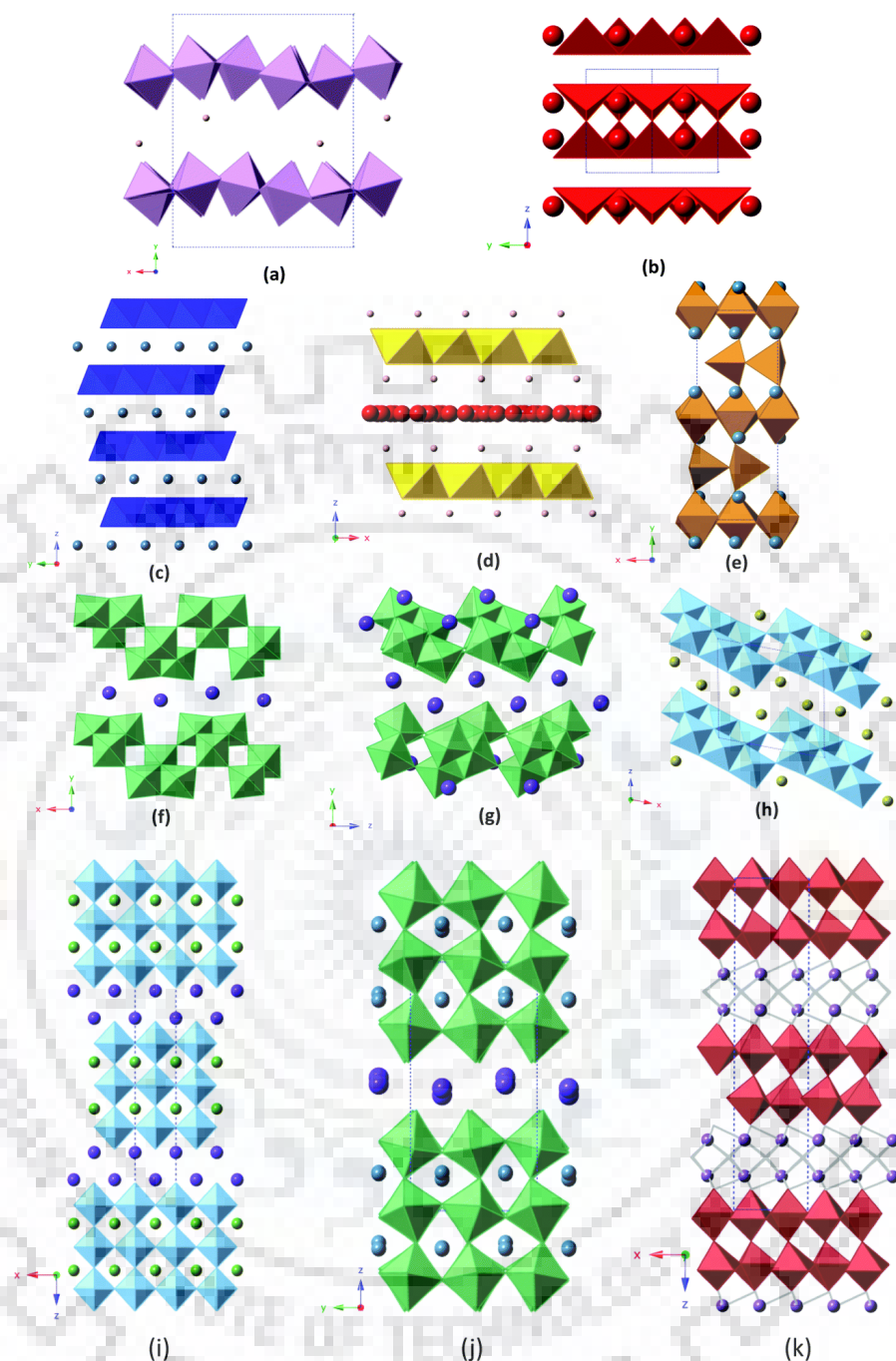


**Figure 1.1** Structural motifs of selected layered oxides which are suitable to soft-chemical changes: (a)  $\text{MoO}_3 \cdot 2\text{H}_2\text{O}$  and (b)  $\text{V}_2\text{O}_5$  (c)  $\text{LiCoO}_2$ ;  $\text{ABO}_2$ -type structure, (d) layered double hydroxide (LDH), (e)  $\text{Ca}_2\text{Fe}_2\text{O}_5$ ; Brownmillerite structure. Shear structures of (f)  $\text{KNb}_3\text{O}_8$ , (g)  $\text{K}_4\text{Nb}_6\text{O}_{17}$ , and (h)  $\text{Na}_2\text{Ti}_3\text{O}_7$ ; layered perovskite oxides: (i) Ruddlesden–Popper phase,  $\text{A}_2'[\text{A}_{n-1}\text{B}_n\text{O}_{3n+1}]$ , (j) Dion–Jacobson phase,  $\text{A}'[\text{A}_{n-1}\text{B}_n\text{O}_{3n+1}]$ , and (k) Aurivillius phase,  $\text{Bi}_2\text{O}_2[\text{A}_{n-1}\text{B}_n\text{O}_{3n+1}]$ .

Aurivillius (AV) phases,  $\text{Bi}_2\text{O}_2[\text{A}_{n-1}\text{B}_n\text{O}_{3n+1}]$ , are another class of layered perovskites, in which an interlayer gallery is occupied by  $[\text{Bi}_2\text{O}_2^{2+}]$  covalent network. The layered perovskites may have their layers based on the  $\text{BX}_6$  octahedral connectivity pattern and interlayer orientation along various crystallographic axes [14].

The layered anion exchangers are rather rare compared to the cation exchangers, which are very common among layered oxides. During the study of co-precipitation of alkali metal cations, Feitknecht was able to discover layered double hydroxides (LDHs), which contain positive metal hydroxide sheets interleaved by anions, in the 1940s [15]. The LDH have the general formula  $[\text{M}^{2+}_{(1-x)}\text{M}^{3+}_x(\text{OH})_2]\text{A}^{n-}_{x/n}.m\text{H}_2\text{O}$ , with divalent and trivalent cations representing the structures analogous to the brucite,  $\text{Mg}(\text{OH})_2$ , where  $x$  corresponds to the  $\text{M}^{3+}/(\text{M}^{2+} + \text{M}^{3+})$  ratio, and  $n$  represents the anionic charge. The choice of ions  $\text{M}^{2+}$  and  $\text{M}^{3+}$  is in the same size range as  $\text{Mg}^{2+}$  ions can be composed of a range of counter anions like carbonates, nitrates, and hydroxides.  $\text{Li}^+$  and  $\text{Al}^{3+}$  ions have also been used to develop LDHs with a hydrotalcite structure [15-17]. Another class of layered anion exchangers is the layered rare earth hydroxides of common formulas,  $\text{Ln}(\text{OH})_2\text{A}^{q-}_{1/q}.m\text{H}_2\text{O}$  [18] and  $\text{Ln}_8(\text{OH})_{20}\text{A}^{q-}_{4/q}.n\text{H}_2\text{O}$  [19, 20].

The Brownmillerites are oxygen deficient perovskites with the general formula,  $\text{A}_2\text{B}_2\text{O}_5$ , and with alternating layers of octahedral and tetrahedral oxygen coordination found in the 1920s. The oxides with a cation and anion ordering were investigated for different applications [21]. These structures can also have B-site cations ordered, which in the alternating layers can show tetrahedral and octahedral coordination. Oxyhydrides, oxychlorides, and oxyfluorides also exist as anionically ordered layered oxides, which have been investigated as ion conductors and antiferromagnets [22-24]. Figure 1.1. Illustrates the most common families of layered oxide structures.

In contrary to van der Waals solids where weak intermolecular forces exist between layers (e.g. graphite), most layered transition metal oxides consist of charged sheets with enhanced intersheet interaction. The presence of electric attraction between sheets makes them conducive to 'host-guest' chemistry, where the guest species is interchangeable or intercalant in the host metal oxide block. Due to electrostatic attractive forces layered oxides can be

pulled into double layer, monolayer nanosheets or the monolayers can also be stacked back into three-dimensional perovskites [25].

For various technological applications like photocatalysis [26], magnetic [27], ferroelectrics [28], solid state ion conduction [29], giant magnetoresistance [30], and superconductivity [31], layered oxides have been studied. This is reflected in the large number of review papers on this subject, ranging from new synthesis techniques to energy storage applications [32-40]. In the last few years, a large number of new compounds were synthesized using topotactic reactions that cannot be achieved earlier by conventional solid-state reaction methods. These reactions are structurally varied and can have interesting characteristics, including those of basic and technological interest.

While limited as compared to those used by molecular chemists, the synthetic tools used in topochemical manipulations can still be very effective. They include a number of methods, for example, substitution, intercalation, and deintercalation / extraction. The exchange of ions, simply involves replacement of one by similar anionic or cationic species. While the majority of these reactions involves the one-to-one exchange of monovalent ions, in some instance aliovalent species can also react (e.g., one divalent cation to replace two monovalent cations) and the cation / anion combinations can often co-exchange in rare cases. The intercalation occurs when species are inserted into a host compound as a further topochemical method. This can include reduction and oxidation processes leading either to the introduction of cationic or anionic species, by chemical or electrochemical means or insertion of neutral molecules (e.g. H<sub>2</sub>O). Another important method is deintercalation, the opposite of intercalation. Cations or anions can be removed or executed either chemically or electrochemically in oxidative or reductive manner.

Also other topochemical techniques of ion exchange and (de)intercalation are very useful involving specialized methods. This includes: (a) extraction from layers and removal of laminar features within the host, (b) grafting in the layers, by formation of the covalent bonds with the host (generally using organic molecules), (c) exfoliation of the layers within the host, by separation and solvation of a group or individual layers, (d) construction of a layer, generation of an expanded metal-nonmetal layer between the host interlayer, (e)



pillaring, development of columnary components in the host block, and (f) replacing of ions, often as a part of a redox process in the host block.

## 1.2 Topochemical Manipulations

In Figure 1.2, a variety of topochemical manipulations for the different perovskites are shown. The main emphasis here are different techniques such as ion exchange, intercalation (reductive, oxidative and neutral species), layer extraction, reductive deintercalation, layer construction, grafting, exfoliation, pillaring, and substitution reactions that are useful in creating new structural characteristics in a layered host structure.

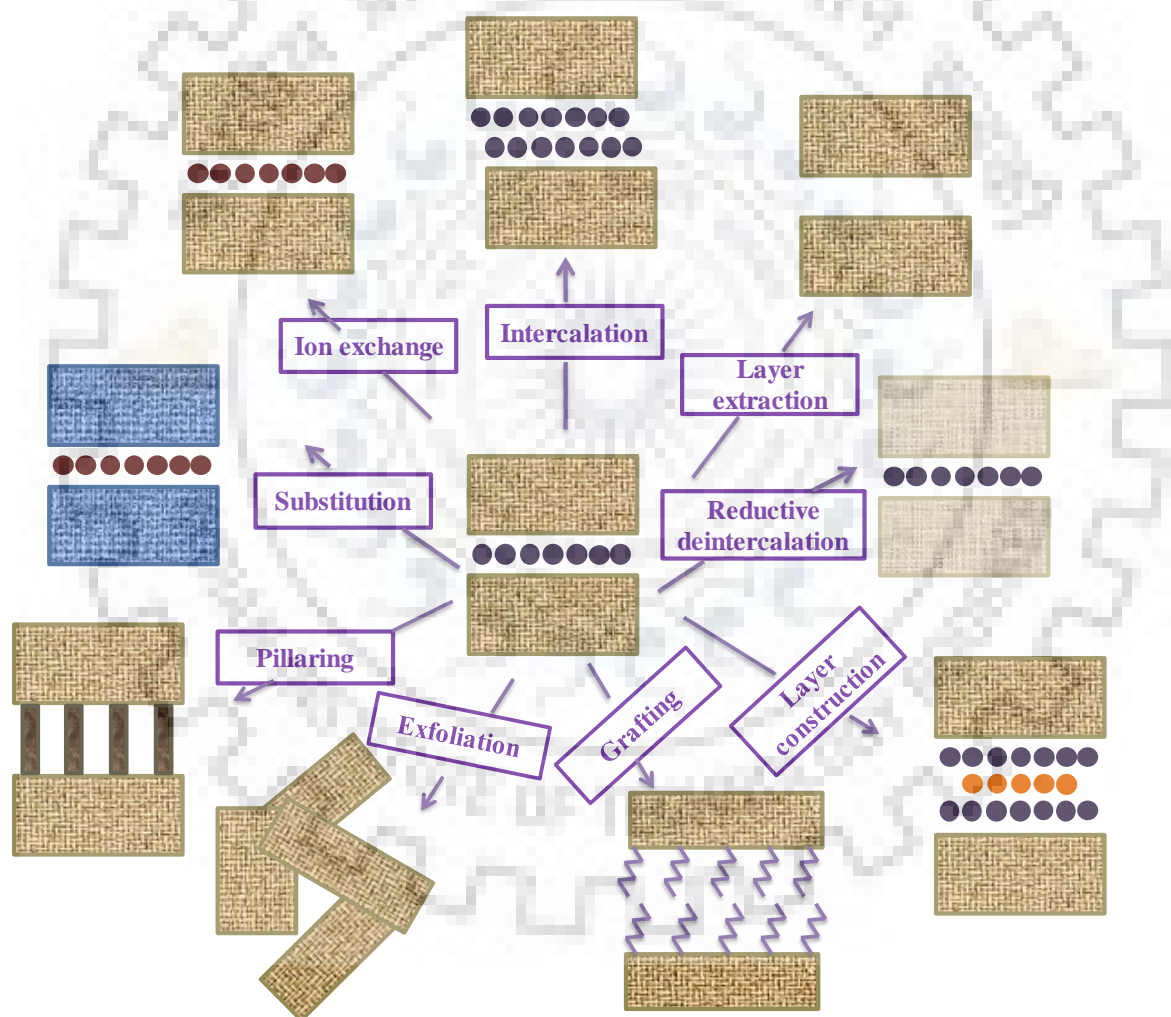


**Figure 1.2** The topochemical reaction includes ion exchange, intercalation, layer extraction, reductive deintercalation, layer construction, grafting, exfoliation, pillaring, and substitution reactions [32].

### 1.2.1 Ion exchange

Ion exchange is one of the most important routes in soft-chemical processes for the synthesis of new metastable phases of the layered oxides. In general, ion exchange is a class of chemical reaction that involves exchange of one or more ionic components between two materials. Some inorganic crystalline materials may react with ionic solutions of other ions to remove a single ionic component selectively from the host lattice and get replaced with others from the solution, resulting in new materials. Due to the topotactic nature, often the ion exchange process can produce a material with crystal structure similar to the parent compound but with a new composition. This makes it quite easy to investigate new chemical compositions with a certain crystal structure and is widely used in various areas. Ion exchange in the layered titanate,  $Tl_2Ti_4O_9$ , was first demonstrated with the molten  $KNO_3$ - $KCl$  flux to achieve isostructural  $K_2Ti_4O_9$  [41]. The ion exchange are usually limited to the structural genres described above, which offer opportunities to explore other structural types by ion exchange. Moreover, the ion exchange is exhaustive one among other soft-chemistry techniques, leading to the development of a wide variety of compounds with structures covering from open framework solids (e.g. MOFs) [42-44], faujasite zeolite [45-57], clays (e.g. montmorillonite) [58], layered double hydroxides (e.g. hydroxyapatites) [59, 60], and tunnel structure compounds [61-65] to layered compounds (e.g. layered perovskites) [66-74] both with the oxide and non-oxide compositions.

Chalcogenides may be a new kind of inorganic ion exchangers exhibiting unusual exchange properties due to special affinity of its non-oxidic framework with specific cations as well as due to variety in its pores and channels. With unique exchange properties not only because of their variety in pores and channel, but also because of the specific affinity of the non-oxidic framework for certain cationic species, the cations may also be a new kind of inorganic ion exchangers. Furthermore, crystalline chalcogenides can be an appropriate model to understand the mechanism of different types of ion exchange techniques based on their structure. Kanatzidis and co-workers [48] have reported high selectivity and exchange capacities in the open framework chalcogenide material  $K_6Sn[Zn_4Sn_4S_{17}]$  on ion exchange with  $Cs^+$  and  $NH_4^+$  ions (Figure 1.3). In  $K_6Sn[Zn_4Sn_4S_{17}]$ , there found to be mainly three types of microporous cavities. The largest one in the  $K_6Sn[Zn_4Sn_4S_{17}]$ , fits  $Cs^+$  accurately and is highly selective for this ion. The second biggest pore is able to accommodate  $NH_4^+$  ions, which



leads to high ammonium-exchange capacity (3.06 meq/g) in  $K_6Sn[Zn_4Sn_4S_{17}]$  that is close to the ammonium ion exchange capacities of natural zeolites.

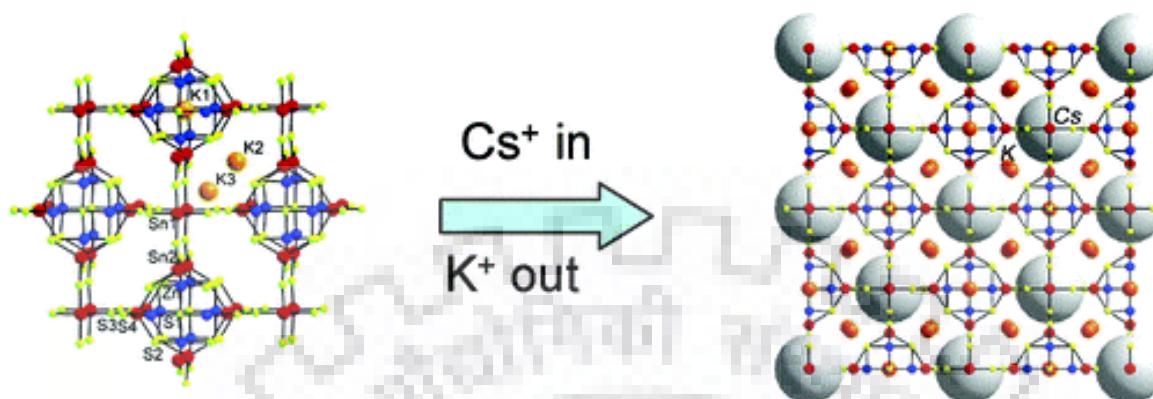


**Figure 1.3** Ion exchange in the open framework chalcogenide  $K_6Sn[Zn_4Sn_4S_{17}]$  with  $Cs^+$  [48].

Thallos ion exchange method (TIE) was first employed by Seff and co-workers [50] to incorporate  $Cu^+$  and  $Cu^{2+}$  in zeolite Y (FAU, Si/Al = 1.69) as the extraframework sites. They reported that  $|Cu^{+10.9}Cu^{2+10.7}Tl^{+3.92}| [Si_{121}Al_{71}O_{384}]$ -FAU can be prepared by reaction of dehydrated  $Tl^+$ -exchanged zeolite Y ( $Tl_{71}$ -Y) with  $CuCl_2(g)$  and its decomposition products,  $CuCl(g)$  and  $Cl_2(g)$  formed at 400 °C under anhydrous conditions. Yamashita and co-workers [53] have reported ion exchange in ZSM-5 and Y-zeolites ( $H^+$ ,  $Na^+$  and  $Cs^+$ ).  $NH_4$ -ZSM-5 and Na-Y were initial zeolites. The commercial form ( $NH_4$ -ZSM-5) when heated at 450 °C in air with heating rate of 5 °C/min for 6 hours, H-ZSM-5 was obtained as a product. Na-ZSM-5 was synthesized by ion exchange of H-ZSM-5 with 0.2 M solution of  $NaNO_3$  ( $Na^+$  precursor) and afterwards Cs-ZSM-5 by exchange of Na-ZSM-5 with 0.1 M solution of  $CsNO_3$  ( $Cs^+$  precursor) by stirring in a thermostatic bath for 1 hour at 60 °C. The analysis of these zeolite-based catalysts showed that both frameworks (MFI and FAU) play a significant role in catalytic behavior. Azambre and co-workers [55] have reported preparation of silver containing zeolites by ion exchange reaction; for this 23 wt % Ag / Y sorbent with Si / Al ratio of 2.5 was prepared using 3-fold silver nitrate exchanges. The exchange of ions revealed that Ag species are highly dispersed in the faujasite framework, with most of the silver available on the sites,  $S_{II}$  and  $S_{III}$  as  $Ag^+$  isolated cations and the rest as charged  $Ag_n^{\delta+}$  or metallic  $Ag_m^{\circ}$  clusters. This was studied in the context of a greivous nuclear accident, to discover the mechanism of trapping and degradation of methyl iodide by silver faujasite zeolite.

One well known class of anionic clays is known as layered double hydroxides (LDHs). LDHs have a hydroxide basal layer with a positive charge, which is electrically balanced in the interlayer space by anions. These anions, present in the interlayer can be interchanged or exchanged by various other anions to produce numerous new functional materials. The LDHs can be represented by the general formula,  $(M^{2+}_{1-x}M^{3+}_x)(OH)_2 (A^{n-})_{x/n} \cdot mH_2O$ , which contains  $M^{2+}$  and  $M^{3+}$  as metallic cations like  $Mg^{2+}$ ,  $Ni^{2+}$ ,  $Mn^{2+}$ , or  $Zn^{2+}$  and  $Al^{3+}$ ,  $Cr^{3+}$ , or  $Fe^{3+}$ , etc.  $A^{n-}$  is a replaceable anion such as  $CO_3^{2-}$ ,  $SO_4^{2-}$ ,  $Cl^-$ ,  $NO_3^-$ , or a different organic anion, where,  $x$  and  $m$  are the molar ratio of  $M^{3+}$  to  $(M^{2+} + M^{3+})$  ions and the count of water molecules found in the region of interlayer space with anions. Recently, LDHs have attracted considerable attention as catalysts, catalyst supports, electrodes, sensitizers, anionic exchangers, absorbents, and polymer additives [75-80].

Li and co-workers have reported that a large anionic UV absorbent with a solution of 2-naphthylamine-1,5-disulfonic acid in water was intercalated into a layered double hydroxide (LDH) host by ion exchange of a Zn-Al LDHs-nitrate precursor [81]. The distance between layers of intercalated LDHs expanded to 1.5 nm after intercalation of the UV absorber, while, 0.90 nm is the basic spacing between precursor LDHs. The interlayers in the double hydroxides or anionic clays are composed of brucite-type inorganic sheets with replaceable anions present in the interlamellar spacing. In order to ensure neutrality of charges, negatively charged moiety should be present in the interlamellar space due to which the host-guest chemistry in LDHs is limited only to ion exchange reactions. Vasudevan and co-workers [82] have investigated the insertion of neutral TCNQ (7,7,8,8-tetracyanoquinodimethane), into the lamellar spaces of LDH by charge-transfer interaction. They take advantage of the fact that TCNQ is an electron acceptor in nature and can form various donor-acceptor complexes with several electron donors. By ion exchange reaction, aniline (an electron donor) was interleaved as *p*-aminobenzoate (AB) into a Mg-Al LDH. They illustrated that TCNQ molecules with intercalated *p*-aminobenzoate anions can be transferred in the interlamellar space of the Mg-Al LDH by charge-transfer complex formation. Ion exchange in Co(II) / Al(III) layered double hydroxide has been reported by Ogawa and co-workers [83]. The ion exchange of carbonate ions ( $CO_3^{2-}$ ) from  $CO_3^{2-}$ -CoAl-LDH was carried out in aqueous media with dodecylsulfate ions by hydrothermal reaction. In comparison to the ratio of layer spacing (~3.4 times) with the ratio of average particle thickness (~3.1 times), both before and after the

exchange with dodecylsulfate, was consistent. This was the first example which correlates the layer spacing with the particle thickness, confirming the intercalation by topochemical reaction.

The ion exchange was mostly confined to the DJ and RP phases in the perovskite systems. Some of the widely investigated compounds are NaLaTiO<sub>4</sub> [84], RbLaNb<sub>2</sub>O<sub>7</sub> [85], RbLa<sub>2</sub>Ti<sub>2</sub>NbO<sub>10</sub> [86], RbSrNb<sub>2</sub>O<sub>6</sub>F [22], K<sub>2</sub>SrTa<sub>2</sub>O<sub>7</sub> [67] and Rb<sub>2</sub>La<sub>2</sub>Ti<sub>3</sub>O<sub>10</sub> [87]. In the initial ion exchange reactions, involved replacement of larger alkali metal cations, such as Cs<sup>+</sup>, Rb<sup>+</sup>, and K<sup>+</sup> from the interlayer and with the smaller cations, such as Na<sup>+</sup>, Li<sup>+</sup>, NH<sub>4</sub><sup>+</sup>, and Tl<sup>+</sup> using molten nitrate salts ( $T_m \sim 300$  °C) as reaction medium [86, 88-90]. DJ phases were among the first reported examples of layered perovskites studied for ion exchange [88]. Synthesis of DJ phases, as phase-pure materials with small size interlayer cations, such as, Li<sup>+</sup> or Na<sup>+</sup> is very challenging with conventional high temperature reactions ( $\geq 1000$  °C). The formation of layered perovskites is preferred with the larger cations, such as, Cs<sup>+</sup>, as large size cations fits better into large interlayer space of a layered perovskite than the smaller interlayer space of a 3D perovskite [91]. Presence of smaller cations between interlayers is desirable due to the enhanced ionic conductivity [92-97] and size of cations is also important for subsequent low-temperature reactions [98]. The alkali metal of the DJ phases can also be replaced by divalent ions [99, 100], although it leads to phases with less than half of the interlayer spaces filled. The alkali metal cations in the interlayer of the DJ phase can also be exchanged with protons [88, 101-103]. The protonated forms of most of the DJ phases, like many other layered solid acids, [104-106] intercalate a range of different organic bases [101, 107] and alcohols [108, 109]. Long-chain alkylamines like *n*-octylamine, in the interlayer gallery, usually arranged as paraffin-like bilayers [104] after intercalation.

Topotactic route for assembly of metal-anion arrays in a perovskite host was demonstrated by Wiley and co-workers [110]. They reported a new set of layered copper oxyhalide perovskites, (CuX)LaNb<sub>2</sub>O<sub>7</sub>, through an ion exchange reaction between DJ phase, RbLaNb<sub>2</sub>O<sub>7</sub> and CuX<sub>2</sub> (X = Cl, Br) (Figure 1.4). This new type of structure has unusual CuO<sub>2</sub>X<sub>4</sub> octahedra, corner-connected by NbO<sub>6</sub> octahedra in the perovskite slab and edge-shared with each other along the four equatorial edges. Antiferromagnetic transition under 40 K is exhibited by both the products (CuX)LaNb<sub>2</sub>O<sub>7</sub> (X = Cl, Br). Likewise, Maggard and co-workers [111] established rapid flux synthesis, in which various kinds of DJ perovskite hosts

exchanged with copper-halide layers. The insertion of halide layers and transition metal creates new valance bands with higher energy and consequently reduces the band gap.

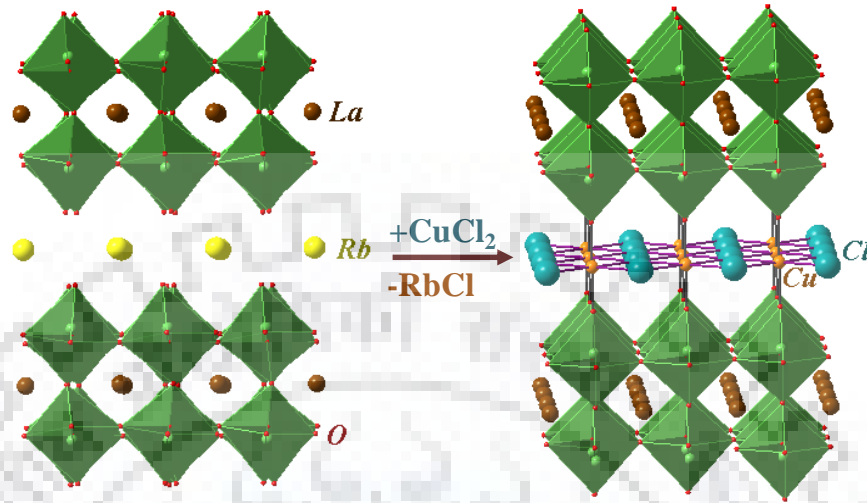


**Figure 1.4** Ion exchange conversion of RbLaNb<sub>2</sub>O<sub>7</sub> to (CuCl)LaNb<sub>2</sub>O<sub>7</sub> [110].

The ion exchange reactions are also common to RP phases [112, 113]. Like the DJ phases, smaller cations such as Na<sup>+</sup>, Li<sup>+</sup>, NH<sub>4</sub><sup>+</sup>, and Ag<sup>+</sup> may be replaced with the molten salt ion exchange reactions in place of larger interlayer cation species Na<sup>+</sup>, K<sup>+</sup>, and occasionally Rb<sup>+</sup> of RP phase. [95, 96, 113-116]. RP phases are particularly suitable for ion exchange of divalent cations, as two alkali cations can be replaced by a divalent cation resulting its conversion into a DJ phase. Hyeon *et al.* have prepared M<sup>II</sup>La<sub>2</sub>Ti<sub>3</sub>O<sub>10</sub> (M = Co, Cu, Zn) [69] by exchanging 2Na<sup>+</sup> for M<sup>2+</sup> with molten nitrates / chlorides / or a eutectic mixture. A<sup>II</sup>Eu<sub>2</sub>Ti<sub>3</sub>O<sub>10</sub> (A = Ca, Sr) and M<sup>II</sup>Eu<sub>2</sub>Ti<sub>3</sub>O<sub>10</sub> (M = Ni, Cu, Zn) were used by Mallouk and co-workers for aqueous ion exchange [98]. Gopalakrishnan and co-workers have synthesised, A<sup>II</sup>La<sub>2</sub>Ti<sub>3</sub>O<sub>10</sub> (A = Sr, Ba, Pb) by a higher temperature metathesis reaction [117]. The interlayer alkali cations can also be replaced by proton [67, 118-120], thus opening up this interlayer space for subsequent acid / base reactions. The extension of Li<sub>0.3</sub>Ni<sub>0.85</sub>La<sub>2</sub>Ti<sub>3</sub>O<sub>10</sub> by the aqueous-solution reactions in the RP triple-layered series is described by Wiley and co-workers [121]. To achieve this, they inserted a nickel layer in triple-layer Li<sub>2</sub>La<sub>2</sub>Ti<sub>3</sub>O<sub>10</sub> perovskite blocks by ion exchange to form Li<sub>0.3</sub>Ni<sub>0.85</sub>La<sub>2</sub>Ti<sub>3</sub>O<sub>10</sub>. Li<sub>0.3</sub>Ni<sub>0.85</sub>La<sub>2</sub>Ti<sub>3</sub>O<sub>10</sub> follows Curie-Weiss law at high temperatures and possess a magnetic moment in accordance with the presence of Ni<sup>2+</sup> in the compound. Two magnetic transitions, one is ferromagnetic and other is spin-glass type occurs at lower temperatures of 23 K and 10 K, respectively.



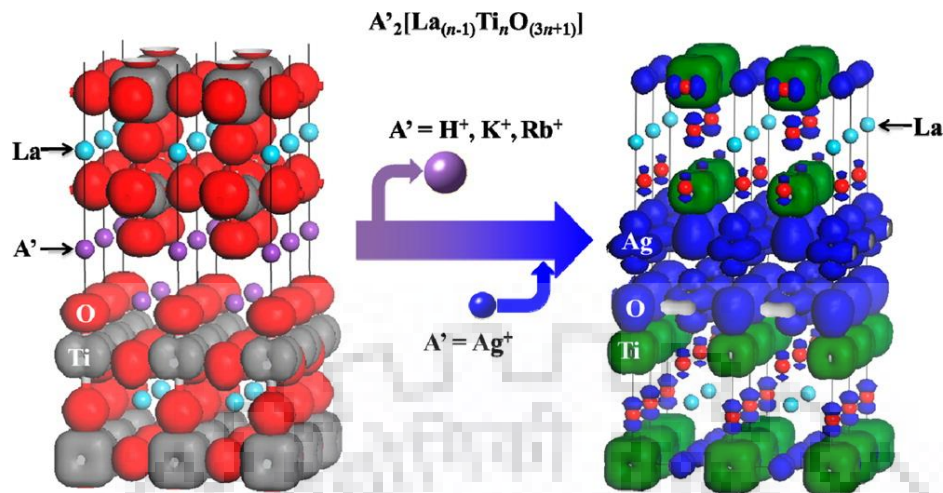


**Figure 1.5** Ion exchange in Dion–Jacobson phase  $A'[A_{n-1}B_nO_{3n+1}]$  and Ruddlesden–Popper phase,  $A'_2[A_{n-1}B_nO_{3n+1}]$  with  $Ag^+$  [72].

The ion exchange reported in the DJ layered phases,  $RbLaNb_2O_7$ ,  $RbA_2Nb_3O_{10}$ , ( $A = Ca, Sr$ ) and the RP phase,  $Rb_2La_2Ti_3O_{10}$  with excess  $AgNO_3$  was reported by Maggard and co-workers [72] (Figure 1.5). On irradiation with ultraviolet and visible light in presence of aqueous methanol, the silver-exchanged  $AgA_2Nb_3O_{10}$  layered perovskites exhibited high photocatalytic hydrogen formation ( $\sim 13,616 \mu\text{mol H}_2 \cdot \text{g}^{-1} \cdot \text{h}^{-1}$ ) in comparison with the parent ( $\sim 1,418 \mu\text{mol H}_2 \cdot \text{g}^{-1} \cdot \text{h}^{-1}$ ). Wiley and co-workers have recently reported the synthesis of a new DJ phase,  $FeLa_2Ti_3O_{10}$  and studied the modifications in structure, magnetic properties, and contraction in the DJ phase. While accessible easily via ion exchange, the compound has distorted tetrahedra of  $FeO_4$  in the interlayer gallery of  $La_2Ti_3O_{10}$  perovskite blocks. It shows paramagnetic behavior above 30 K, while a spin glass like transition is noticed below 30 K. Thermal studies have shown that  $Fe_{0.67}La_2Ti_3O_{10}$  is prepared by oxidative deintercalation, followed by a significant contraction in interlayer space, where  $FeO_4$  tetrahedra transformed to  $FeO_6$  octahedra [122].

The alkali form of a RP phase converted into Aurivillius phase by ion exchange of  $2K^+$  with  $Bi_2O_2^{2+}$  is reported by the Gopalakrishnan and co-workers [117]. The Aurivillius phase,  $Bi_2O_2[La_2Ti_3O_{10}]$ , for instance synthesized by solid-state metathesis reaction of  $K_2La_2Ti_3O_{10}$  and  $BiOCl$ . The  $PbBiO_2[LaNb_2O_7]$  related phase prepared from the  $KLaNb_2O_7$  by reaction with  $PbBiO_2Cl$  has also been reported. The new DJ phases,  $A^{II}La_2Ti_3O_{10}$  ( $A = Sr, Ba, Pb$ ) were prepared by reacting with  $ACl_2$  by the similar metathesis method. The low temperature

reaction of  $\text{K}_2\text{La}_2\text{Ti}_3\text{O}_{10}$  with  $\text{VOSO}_4$  in aqueous medium resulted in the formation of an interesting perovskite/vanadyl intergrowth structure.

Although the topochemical ion exchange is common in oxides with the layered perovskite structure, but rare in the 3D close packed structures based on all edge and/or corner shared polyhedra. Among few unique exchanges in layered oxides, mention may be made of the interesting ‘intra-site exchange’, where perovskite A-site cations were exchanged with the interlayer A'-cations within a compound [123]. A multivalent ion exchange in a lamellar  $\alpha$ - $\text{NaFeO}_2$  type structure was reported long ago [124]. A cubooctahedral A-site ion exchange in  $\text{NaTaO}_3$  is the only report involving a three-dimensional perovskite structure with all octahedral corner connectivity [125] (Figure 1.6).

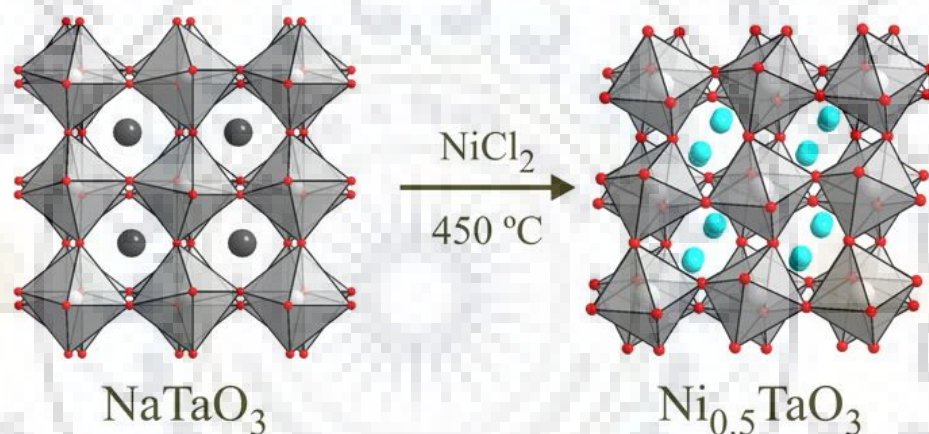


**Figure 1.6** Reaction of  $\text{NiCl}_2$  with  $\text{NaTaO}_3$  leads the formation of the perovskite phase  $\text{Ni}_{0.5}\text{TaO}_3$ , via a topochemical nickel-for-sodium cation exchange [125].

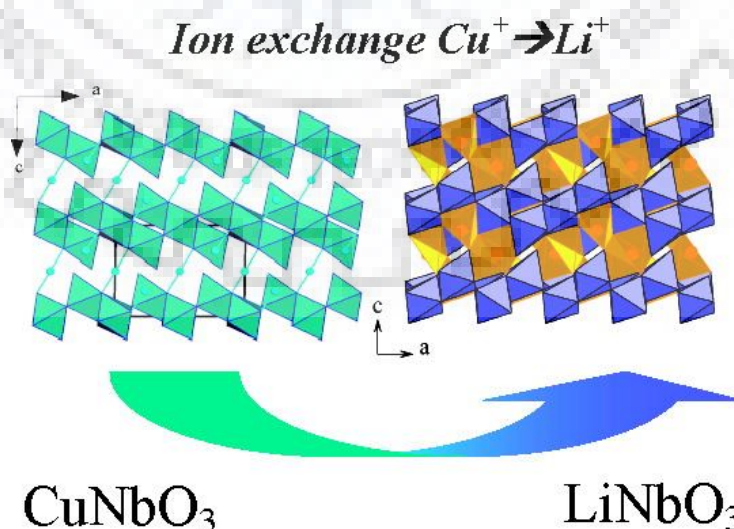


**Figure 1.7** Ion exchange reaction in lamellar structure  $\text{CuNbO}_3$  from lithium cation [126].

The exchange of lithium for univalent copper in  $\text{CuNbO}_3$  was investigated by Prolong *et al.* [126]. The topotactic reaction between  $\text{CuNbO}_3$  and the molten salt eutectic mixture “ $\text{LiCl}/\text{LiNO}_3$ ” resulted a new form of  $\text{LiNbO}_3$  with a lamellar structure (Figure 1.7).

Uma and co-workers [127] reported ion exchange in honeycomb ordered monoclinic layered structure  $\text{Na}_2\text{Cu}_2\text{TeO}_6$  with excess of  $\text{LiNO}_3$  at low temperature and produced  $\text{Li}_2\text{Cu}_2\text{TeO}_6$  as a product. After ion exchange, the resulting  $\text{Li}_2\text{Cu}_2\text{TeO}_6$  is isostructural with the parent  $\text{Na}_2\text{Cu}_2\text{TeO}_6$ .

The resulting properties are modified by ion exchange in both layered perovskites and non-perovskite oxides. The partial ion exchange in RP phase,  $\text{LiSrTa}_2\text{O}_7$ , leads to  $\text{LiHSrTa}_2\text{O}_7$ , as reported by Galven and co-workers [71]. This compound is prepared with either  $\text{NH}_4\text{Cl}$  or aqueous  $\text{HNO}_3$  solutions under strictly controlled reaction conditions. Another partial ion exchange route was reported by Cussen and co-worker, [73] who converted  $\text{HLaTiO}_4$  to the solid-state solution,  $\text{H}_{1-x}\text{Li}_x\text{LaTiO}_4$ . The RP phases,  $\text{H}_{1-x}\text{Li}_x\text{LaTiO}_4$ , comprises isostructural compounds with an arrangement of  $\text{H}^+$  and  $\text{Li}^+$  in the interlayer, that is distorted on the diffractive length scale. Hydroxyl groups formed by protons and oxide anions, projected outwards from the perovskite layer and the environment of  $\text{Li}^+$  is in-between the four coordinated square planar and tetrahedral geometry. Mitsuyama *et al.* [128] have reported use of mixed molten nitrate  $\text{A}'\text{NO}_3$  ( $\text{A}' = \text{K}, \text{Li}$ ) and  $\text{NaNO}_3$  for the ion exchange in triple-layered DJ phases  $\text{CsCa}_2\text{Ta}_3\text{O}_{10}$ . The Na content in the ion exchange compound  $\text{A}'_{1-x}\text{Na}_x\text{Ca}_2\text{Ta}_3\text{O}_{10} \cdot 2\text{H}_2\text{O}$  cause the variation in the interlayer hydration which greatly influence the photocatalytic activity and overall water splitting under UV light.

Roudebush *et al.* [74] have reported the synthesis of iridium-based honeycomb Delafossite compounds (Figure 1.8),  $\text{Cu}_3\text{NaIr}_2\text{O}_6$  and  $\text{Cu}_3\text{LiIr}_2\text{O}_6$ , respectively, by topotactic ion exchange method and studied their structural and magnetic properties. The compounds were prepared by heating the parent  $\text{Na}_2\text{IrO}_3$  and  $\text{Li}_2\text{IrO}_3$  with  $\text{CuCl}$  below  $450^\circ\text{C}$ . The parent compounds adopt a honeycomb type lattice in which octahedral layers of  $\text{IrO}_6$  are separated by layers of alkali cations. The new iridium-based compounds behave in a different way than their parent compound, as  $\text{Cu}_3\text{NaIr}_2\text{O}_6$  shows ferromagnetic behavior, while  $\text{Cu}_3\text{LiIr}_2\text{O}_6$  shows antiferromagnetic transition similar to its parent compound but exhibits stronger antiferromagnetic coupling.



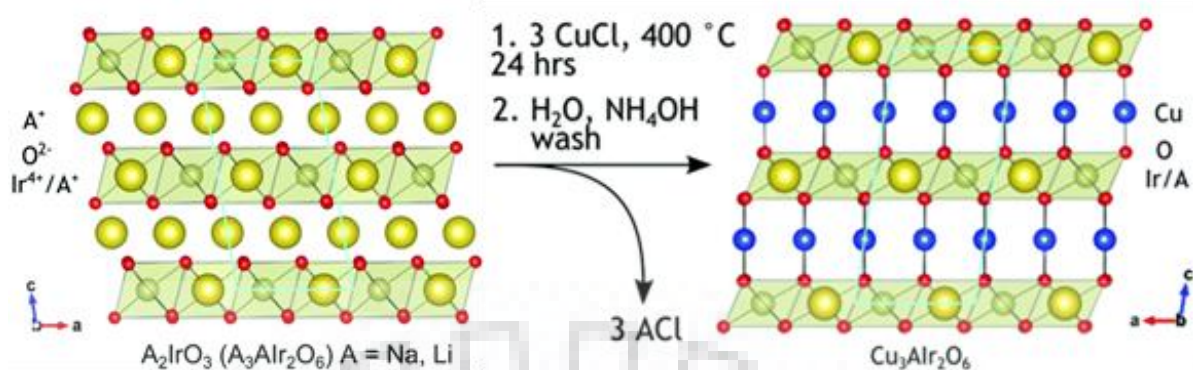


**Figure 1.8** Topotactic reaction of precursor  $A_2IrO_3$  ( $A = Li, Na$ ) and  $CuCl$  to form iridium containing honeycomb Delafossites  $Cu_3AlIr_2O_6$  [74].

In acid leaching, cations or other structural units are replaced with protons analogous to ion exchange. A major reaction developed by Sugahara and co-workers, transforms the Aurivillius phases into the protonated form of the RP phases by particularly dissolving the bismuth oxide layers from the perovskite block in acid [129, 130]. On treating the Aurivillius phase, such as  $Bi_2O_2[SrNaNb_3O_{10}]$  with  $HCl$ , layers of  $[Bi_2O_2^{2+}]$  in between the perovskite slabs is leached to form the RP phase,  $H_2SrNaNb_3O_{10}$ , after being replaced with two protons. Acid exchange in  $Na_2Ti_3O_7$  and  $K_2Ti_4O_9$  layers was also demonstrated in order to transform anhydrous  $H_2Ti_3O_7$  and hydrated  $H_2Ti_4O_9$  respectively [131]. A topotactic proton exchange in the layer of potassium ruthenate is replaced to result in the formation of layer ruthenic acid such as,  $H_{0.22}RuO_{2.11}.nH_2O$  [132]. In a similar acid exchange, a layered trivalent iridate,  $K_{0.75}Na_{0.25}IrO_2$ , was converted into  $IrOOH$ , a trivalent iridate with a concomitant shrinkage of the interlayer distance [133].

Vidyasagar and co-workers reported topotactic ion exchange in  $KInSnS_4$  and  $NaInSnS_4$  with monovalent  $Rb^+$ ,  $Cs^+$ ,  $NH_4^+$ ,  $Tl^+$  divalent  $Ca^{2+}$ ,  $Sr^{2+}$  as well as trivalent  $Ce^{3+}$  ions. Exchanged compounds are metastable in nature and show good potential application for nuclear waste removal [134]. They also described topotactic ion exchange in layered phosphates,  $K_3Sb_3P_2O_{14}.3H_2O$  [135].

### 1.2.2 Intercalation

In the interlayer gallery of layered oxides, intercalation represents another topochemical synthetic approach which introduces different species (cations, anions,

polymers, organic ligands). In this section, efforts are divided into three subsections with (1) reduction, (2) oxidation, and (3) neutral intercalation reaction in perovskite intercalation chemistry.

### 1.2.2.1 Reductive Intercalation

Reductive intercalation generally involves an intercalant site for the host that can either be a cuboctahedron site in the perovskite slab or a vacant space between these slabs. For instance, the simple  $\text{ReO}_3$  related compounds in which the lithium is chemically introduced to the structure is an example of intercalation at A-site. For example, one or two lithiums can be inserted into  $\text{ReO}_3$  itself [136]. The DJ phase,  $\text{RbLaNb}_2\text{O}_7$ , could be intercalated in order to make the RP-related phase,  $\text{Rb}_2\text{LaNb}_2\text{O}_7$  [66], as Armstrong and Anderson have shown. Subsequent studies have shown that DJ-layered perovskites including  $\text{ALaNb}_2\text{O}_7$  ( $A = \text{H, Li}$ ) [137-140],  $\text{ACa}_2\text{Ta}_3\text{O}_{10}$  ( $A = \text{H, Li}$ ),  $\text{LiLaTa}_2\text{O}_7$  [141], and  $\text{RbCa}_2\text{Nb}_3\text{O}_{10}$  [142] are suitable for the use of this chemistry. It is noteworthy, that superconductivity at high transition temperatures of 6 K was observed in the Li-intercalated three-layered niobates,  $\text{Li}_x\text{ACa}_2\text{Nb}_3\text{O}_{10}$  ( $A = \text{K, Rb}$ ), synthesized using reductive intercalation reactions [143-145]. As mentioned, RP compounds are usually not open to reduction. However, an aliovalent ion exchange step may precede the intercalation to create vacancies within the layer.  $\text{Na}_{0.5}\text{Ca}_{0.4}\text{TiO}_4$  [146] and  $\text{Na}_{1.1}\text{Ca}_{0.6}\text{La}_2\text{Ti}_3\text{O}_{10}$  [147] mixed valence compounds, produced by calcium exchange between  $\text{NaLaTiO}_4$  and  $\text{Na}_2\text{La}_2\text{Ti}_3\text{O}_{10}$ , respectively, accompanied by sodium reductive intercalation.

Early research has been carried out in chemical and electrochemical processes on reductive intercalation of lithium-based Aurivillius phases. Choy and co-workers [148] have shown for the first time, lithium intercalation in Aurivillius layered perovskite,  $\text{Bi}_4\text{Ti}_3\text{O}_{12}$ . X-ray absorption studies revealed that some of the bismuth and titanium cation amounts were reduced because of lithium intercalation. Similar lithium intercalation reactions were performed on  $\text{Ba}_{3.25}\text{La}_{0.75}\text{Ti}_3\text{O}_{12}$ , but it was not possible to insert more than one lithium in the host, to provide  $\text{LiBi}_{3.25}\text{La}_{0.75}\text{Ti}_3\text{O}_{12}$  [149]. The electrochemical intercalation of the Aurivillius phases of niobium, molybdenum, and tungsten have been carried out by Rodriguez *et al.* [150, 151]. They demonstrated that a high amount of lithium could be intercalated without any irreversible reactions but with a major destruction of the host. Clarke and colleagues described

a very convincing set of insertion reactions for the reductive intercalation of mixed-metal oxysulfides—(Figure 1.9). Lithium is intercalated into  $Y_2Ti_2O_5S_2$  resulting in  $LiY_2Ti_2O_5S_2$ , where lithium occupies the square planar gaps present in between vacant A-sites (Figure 1.9(2)) of the perovskite block [152].  $KY_2Ti_2O_5S_2$  is made from a similar intercalation chemistry with potassium [153], although the large  $K^+$  cation favors the cubic occupancy between the perovskite slabs with the  $Y_2Ti_2O_5S_2$  layers aligned (Figure 1.9(5)). Interestingly with sodium, one can regulate cation placement with reaction conditions [154, 155]. At or below 200 °C, the sodium cations insert into sites of the interlayer  $Y_2Ti_2O_5S_2$ ,  $\beta$ - $NaY_2Ti_2O_5S_2$  producing (Figure 1.9 (3)). Reaction with elemental sodium at high temperatures (600 °C) produce another polymorph,  $\alpha$ - $NaY_2Ti_2O_5S_2$ . The cations are then directed to the perovskite slab to occupy the vacant A-sites (Figure 1.9 (4)), under these conditions.  $\alpha$ - $NaY_2Ti_2O_5S_2$  can be formed by heating the  $\beta$ - $NaY_2Ti_2O_5S_2$  at 600 °C. The intercalation of the cations in the host structure largely depends on the size of cation and the temperature of the reaction as small size lithium cations can easily intercalate in the perovskite block, but large size sodium requires high temperatures. Preferential intercalation in interlayer sites takes place with sodium as well as with large size cations, like potassium at lower temperatures.

Oxysulfides,  $Sr_2MnO_2Cu_{2m-\delta}S_{m+1}$  ( $m = 1, 2, 3; \delta \approx 0.5$ ), have been studied by Clarke and co-workers, as possible battery materials [156, 157]. They discovered that lithium can be intercalated reversibly by displacing copper in the sulfide layer. Intercalation can be done by both chemical and electrochemical methods. Replacement of copper ions by lithium ions in the disulfide layer was confirmed by Rietveld refinement of neutron diffraction data, as elementary analysis and refinement shows that the amount of intercalated lithium is higher than the copper contents, so that some manganese is also reduced from  $Mn^{3+}$  to  $Mn^{2+}$  in addition to copper reduction. For  $Sr_2MnO_2Cu_{1.5}S_2$  and  $Sr_2MnO_2Cu_{3.5}S_3$  ( $m = 1, 2$ ) compounds,  $^6Li$  and  $^7Li$ -NMR mainly have a single strong lithium resonance. The  $m = 2$  parent, reportedly shows anti-ferromagnetism below 30 K and shows bulk ferromagnetism at an applied magnetic field of 1.2 T [156]. Magnetic ordering disappears when the copper is replaced with lithium which is attributed to the reduction of  $Mn^{3+}$  to  $Mn^{2+}$  and due to the loss of super-exchange routes that are based on the copper-sulfide layer.

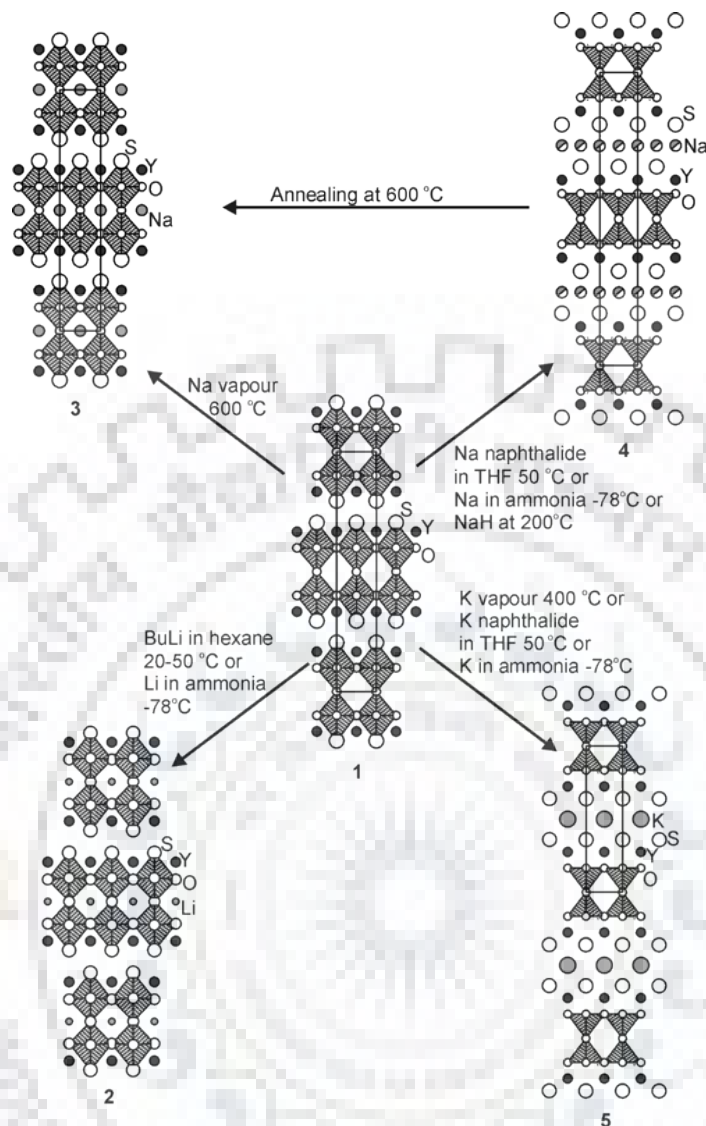


**Figure 1.9** Scheme showing reductive site-selective intercalation of  $\text{Y}_2\text{Ti}_2\text{O}_5\text{S}_2$  (1) by the intercalation of electropositive metals: (2) lithium intercalates,  $\text{Li}_x\text{Y}_2\text{Ti}_2\text{O}_5\text{S}_2$  ( $0 < x \leq 2$ ) [152], (3) sodium intercalates,  $\alpha\text{-Na}_x\text{Y}_2\text{Ti}_2\text{O}_5\text{S}_2$  ( $0 < x \leq 1.0$ ) [145,156] obtained at temperatures of around 500-600 °C. In contrast, (4) sodium intercalate,  $\beta\text{-NaY}_2\text{Ti}_2\text{O}_5\text{S}_2$  and (5) potassium intercalate,  $\text{KY}_2\text{Ti}_2\text{O}_5\text{S}_2$  [153] were obtained at room temperature.

### 1.2.2.2 Oxidative Intercalation

In manipulation of perovskites, intercalation by various oxidative methods is also noteworthy. There is oxidative intercalation when either the intercalant resides in the interlayer or within the perovskite block on a vacant anion site. A range of compounds, including  $\text{Sr}_{2-x}\text{Ae}_x\text{CuO}_3$  ( $\text{Ae} = \text{Ca}, \text{Ba}$ ), [158]  $\text{Ln}_{2-x}\text{Ae}_{1+x}\text{Cu}_2\text{O}_{6-\gamma}$  ( $\text{Ln} = \text{La}, \text{Nd}$ ;  $\text{Ae} = \text{Ca}, \text{Sr}$ ),



[158-160]  $\text{LaSrMnO}_4$ , [161]  $\text{La}_{1.2}\text{Sr}_{0.8}\text{Mn}_2\text{O}_7$ , [161] and  $\text{Sr}_3\text{Ru}_2\text{O}_7$  [162], were studied by various investigators. For instance, in  $\text{Sr}_{2-x}\text{Ae}_x\text{CuO}_3$ , equatorial oxygen vacancies are ordered that leads to corner-sharing  $\text{CuO}_4$  chains. A substitution and insertion combination leads to  $\text{Sr}_{2-x}\text{Ae}_x\text{CuO}_2\text{F}_{2+\delta}$  when reacted with fluorine. Corbel and his co-workers have initially deintercalated oxygen into  $\text{Nd}_2\text{CuO}_4$  [163] to obtain a distorted monoclinic structure,  $\text{NdCuO}_{3.5}$ , including oxygen vacancies in the Cu-O layer [164]. With fluorination of  $\text{XeF}_2$  at a temperature of 200 °C, the product regains its T' structure, and oxygen also relocated to the vacancies in the Cu-O layer as the fluorine moves into the Nd-O block. In the case of more fluorine content, compounds with additional F in the Nd-O block, can also be produced at 300 °C. These fluorinated samples have been found to be superconductor at temperatures between 6 and 11 K [165]. Another example is the reaction where anions are intercalated only in the layers of rock salt between the perovskite blocks. For example,  $\text{Sr}_3\text{Ru}_2\text{O}_7$  can easily accommodate double-layer of fluorine in its rock-salt layer [162]. The tetrahedral  $\text{FSr}_4$  occupy the fluorine and produce an extension layer of around 3.5 Å. Although the reports on the magnetic behavior of  $\text{Sr}_3\text{Ru}_2\text{O}_7$  vary [166,167]  $\text{Sr}_3\text{Ru}_2\text{O}_7\text{F}_2$  appears to have 2K and high temperature ferromagnetism (185 K). The occupation of alternating layer sets was induced in other layered perovskite systems. Greaves and co-workers [162] showed in an extremely new display of topochemical control that it is possible to do this in some layered manganese, where fluorine occupies each other. Both  $\text{La}_2\text{MnO}_4$  and  $\text{La}_{1.2}\text{Sr}_{0.8}\text{Mn}_2\text{O}_7$  can produce these stage compounds. The compounds are first fluorinated to  $\text{La}_2\text{MnO}_4$  and  $\text{La}_{1.2}\text{Sr}_{0.8}\text{Mn}_2\text{O}_7$  at their maximum and are then reacted to their respective  $\text{La}_2\text{MnO}_4\text{F}$  and  $\text{La}_{1.2}\text{Sr}_{0.8}\text{Mn}_2\text{O}_7\text{F}$  with appropriate parent ratios to the staged compounds.

The electronic behavior of complex copper oxides to induce superconductivity was also widely adjusted with low-temperature topochemical fluorination reactions [158]. A strong, energetic preference to preserve  $\text{CuO}_4$  square planar motifs appears to direct the structural selectivity of the anion insertion/substitution reactions of those phases. For instance,  $\text{Sr}_2\text{CuO}_3$  fluorination to  $\text{Sr}_2\text{CuO}_2\text{F}_{2+x}$  through an insertion-and anion exchange combination leads to a large rearrangement of the anion lattice in the host phase. The majority of fluoride ions in the product phase therefore lie within interlayer interstitial sites at the axial coordination sites with a small minority (Figure 1.10) [158, 168, 169].

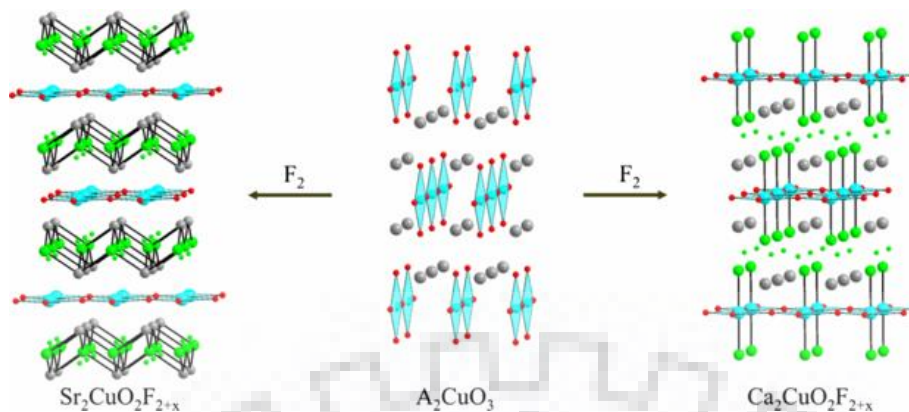


**Figure 1.10**  $A_2CuO_3$  ( $A = Ca, Sr$ ) fluorination with simultaneous anion lattice rearrangement, retaining the apexed  $CuO_4$  square plane sheets [158, 168, 169].

This converts the host phase of the  $SrO-SrO-CuO-SrO$ -stacking to  $SrF-Fx-SrF-CuO_2-SrF-Fx-SrF$ - in the product. Although it is difficult to determine the distribution of oxygen-fluoride to a mixed oxyfluoride by diffraction due to the similar x-ray and neutron dispersion lengths of anions, the Madelung energy calculations support the structure shown in Figure 1.10. The large-scale reorganization of the anion lattice also shows clearly all the anions are highly mobile in the system. The fluorination of  $Ca_2CuO_3$ , leads to a subtly different structure in the analogous calcium phase [169].  $CaCuO_3$  reacts with the fluorine gas giving  $Ca_2CuO_2F_{2+x}$ , in which most of the inserted fluoride ions are now located at interlayered sites with a small minority of fluoride ions located at sites axially placed to the copper centers (Figure 1.10). Consequently,  $Ca_2CuO_2F_{2+x}$  structure is closely linked to  $Nd_2CuO_4$   $T'$ -Structure rather than Ruddlesden-Popper parent phase. The difference in distribution of ions between the two coordinating sites in  $A_2Cu_2O_2F_{2+x}$  in order to produce a Ruddlesden-Popper phase depends on whether,  $A = Sr$  ( $T'$  phase) or,  $A = Ca$ , a smaller cation stabilizes the  $T'$  direct structure.

McCabe and co-workers reported  $LaSrFeO_4$  [170] fluorination. It seems that this reaction involves both intercalation and substitution reactions, in which intercalation of one interstitial anion and substitution of one oxygen by two fluorine (two-for-one substitution) are proposed for the final composition of  $LaSrFeO_3F_3$ . The  $La_2SrFe_2O_7$  is another compound that these authors examined and was used to produce,  $La_2SrFe_2O_7F_2$  by direct reaction with excess fluorine. A second stage compound,  $La_2SrFe_2O_7F$ , was developed by reaction of same amount of  $La_2SrFe_2O_7$  and  $La_2SrFe_2O_7F_2$  [170]. A series of  $Ln_{1.2}Sr_{0.8}Mn_2O_7F_2$ , where,  $Ln = Pr, Nd$ ,

Sm, Eu, Gd is also reported for the intercalation of fluorine [171]. Further oxidative intercalation reactions that includes layered perovskites involves manipulations of copper oxides, superconducting at high temperatures, such as AV. The AV superconductors [171-173], like  $\text{Bi}_2\text{Sr}_2\text{CaCuO}_y$ , shows insertion of intercalate in the  $[\text{Bi}_2\text{O}_2]^{2+}$  layer, and orientation of a parallel layer changes from staggered to an eclipsed one. In such systems as iodine occupies alternating layers of Bi-O, staging can also be carried out. The spectroscopic Raman and X-ray absorption near edge structure (XANES) techniques confirms the presence of iodine intercalant, as a triiodide ( $\text{I}_3^-$ ) ion in the interlayer. In terms of the effect of iodine intercalation on superconducting properties, the transition temperature decreases. For instance, there is a decrease of about 10 K in  $\text{Bi}_2\text{Sr}_2\text{CaCu}_2\text{O}_7$ . In another system that was studied by Clarke *et al.* [174], they found that the  $\text{XeF}_2$  can be oxidized by the use of fluorine with  $\text{Sr}_4\text{Mn}_3\text{O}_{7.5}\text{Cu}_2\text{Ch}_2$  (Ch = S, Se). The compounds resulted were antiferromagnetic as the parent, but the ordering temperature was higher.

Hayward and co-workers [175] found that the suitable two-layered RP phases,  $\text{Sr}_3(\text{M}_{0.5}\text{Ru}_{0.5})_2\text{O}_7$  (M = Ti, Mn, Fe) with  $\text{CuF}_2$  under flowing oxygen by the way of topochemical insertion / substitution method leads to the development of new phases,  $\text{Sr}_3(\text{M}_{0.5}\text{Ru}_{0.5})_2\text{O}_7\text{F}_2$  (M = Ti, Mn) and  $\text{Sr}_3(\text{Fe}_{0.5}\text{Ru}_{0.5})_2\text{O}_{5.5}\text{F}_{3.5}$ . The  $\text{Sr}_3(\text{M}_{0.5}\text{Ru}_{0.5})_2\text{O}_7\text{F}_2$  (M = Ti and, Mn) phases have  $\text{Ti}^{4+}$ ,  $\text{Ru}^{6+}$  and  $\text{Mn}^{4+}$ ,  $\text{Ru}^{6+}$  oxidation state (O.S.) combinations, respectively, while,  $\text{Sr}_3(\text{Fe}_{0.5}\text{Ru}_{0.5})_2\text{O}_{5.5}\text{F}_{3.5}$  have  $\text{Fe}^{3+}$ ,  $\text{Ru}^{5.5+}$  O.S. combination as indicated by the analysis of Mossbauer spectra. Thus, on fluorination by soft chemistry, O.S. of transition metal ions remains same while it causes development of highly oxidized  $\text{Ru}^{6+}$  in all the three phases. The fluorination of  $\text{Sr}_3(\text{Ti}_{0.5}\text{Ru}_{0.5})_2\text{O}_7$  into  $\text{Sr}_3(\text{Ti}_{0.5}\text{Ru}_{0.5})_2\text{O}_7\text{F}_2$  results in magnetic order suppression as metallic behavior is noticeable in the fluorinated material. The fluorination of  $\text{Sr}_3(\text{M}_{0.5}\text{Ru}_{0.5})_2\text{O}_7$  (M = Mn and, Fe), on the other hand, lifted the magnetic frustration observed in the oxide phases which results in the long range ordered anti-ferromagnetism at low temperatures in the corresponding fluorinated compounds.

The fluorination of  $n = 2$  RP phase,  $\text{La}_2\text{SrCr}_2\text{O}_7$  by insertion of fluorine via topochemical method at low temperature to produce  $\text{La}_2\text{SrCr}_2\text{O}_7\text{F}_2$  has also been reported (Figure 1.11). After fluorination reaction, chromium centers retain the octahedral geometry as found initially in the oxide phase because of structure conserving character of fluorination that results in a material containing a wide range of  $\text{Cr}^{4+}\text{O}_6$  units. The neutron diffraction,



magnetization and +SR data confirms, that  $\text{La}_2\text{SrCr}_2\text{O}_7\text{F}_2$  undergoes an anti-ferromagnetic transition below  $T_N \approx 140$  K [176].

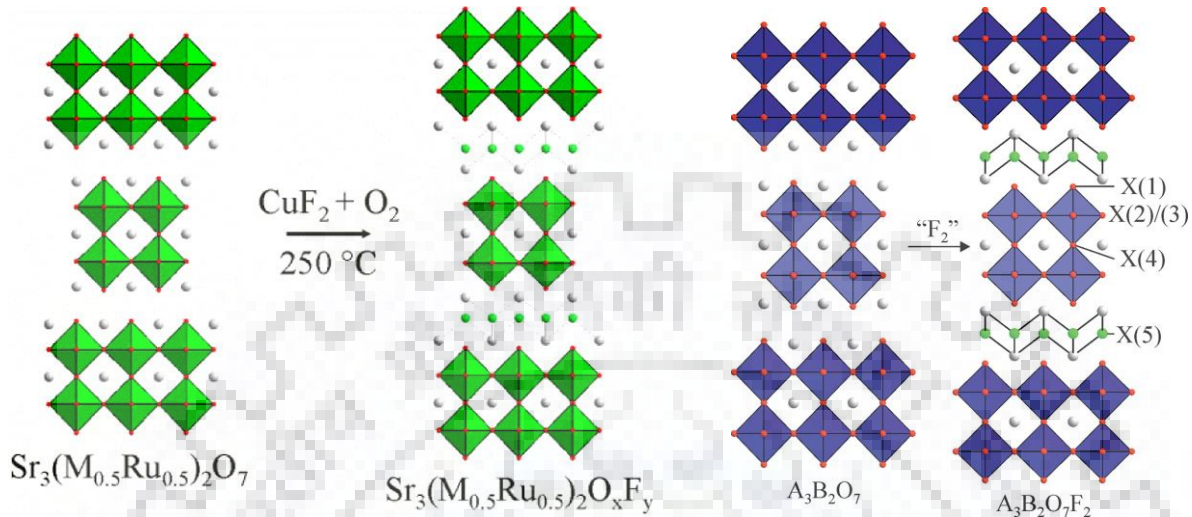


**Figure 1.11** Topochemical fluorination of  $\text{Sr}_3\text{Ru}_2\text{O}_7$  into  $\text{Sr}_3\text{Ru}_2\text{O}_7\text{F}_2$  [169] and oxidative insertion of fluorine and the formation of  $\text{A}_3\text{B}_2\text{O}_7\text{F}_2$  [176].

### 1.2.2.3 Neutral Intercalation

The insertion of full formula units including neutral species into a particular compound can also be observed by intercalation reactions, like water molecules inserted into several layered perovskites. The perovskites that are known to reversibly form the hydrates are  $\text{NaLaB}_2\text{O}_7$  ( $\text{B} = \text{Nb}$  or  $\text{Ta}$ ), [85, 177]  $\text{HLaNb}_2\text{O}_7$  [85]  $\text{K}_2\text{La}_2\text{Ti}_3\text{O}_{10}$ , [87]  $\text{NaEuTiO}_4$ , [178]  $\text{K}_2\text{La}_{0.67}\text{Ta}_2\text{O}_7$ , [179]  $\text{NaLa}_2\text{Ti}_2\text{TaO}_{10}$ , [180] and  $\text{K}_2\text{SrTa}_2\text{O}_7$  [181,182]. Two hydrates of the RP phase,  $\text{NaEuTiO}_4 \cdot n\text{H}_2\text{O}$  ( $n = 0.5, 0.8$ ), have been discovered by Toda *et al.* [178]. On hydration, configuration of perovskite slabs changes from staggered to the eclipsed one and gives the  $\alpha$ -phase,  $n = 0.5$ , where water molecules create a layer in between the sodium ions. While, the perovskite slab is in the staggered configuration in the  $\beta$ -form,  $n = 0.8$  and complete sodium ion hydration is available in a contracted square-planar-like coordination.

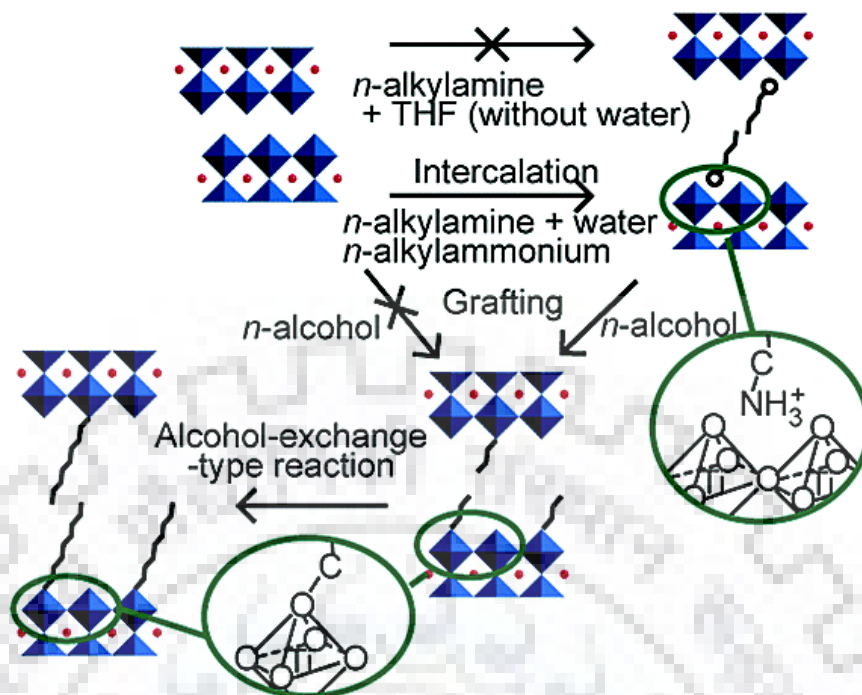


**Figure 1.12** An overview of the modification in the Layered Perovskite,  $H_2La_2Ti_3O_{10}$  with  $n$ -alkylamine and  $n$ -alcohol by ion-exchange reactions [186].

Long-chain alkyl amines,  $RNH_2$  ( $R = n$ -alkyl group), is another example of species that undergoes neutral intercalation. A number of perovskites were studied in which the acid form of the compounds easily intercalates these amines. Early work on DJ hosts was done by Jacobson and co-workers [102]. The intercalation of  $HCaNa_{n-3}Nb_nO_{3n+3}$  ( $3 \leq n \leq 7$ ), with alkyl amine is result of interaction of solid acid perovskite and basic amine in an acid-base reaction. The structure of the interlayer space is such that it consists of two amine layers that interact with the protons in the perovskite blocks with the  $NH_2$  groups. The orientation of zigzag alkali chains is in such a way that they are a little tilted to maximize interactions with the adjacent chains. Uma *et al.* [183] have synthesized polymer composites of perovskites by the above approach. First, they intercalated the aniline into the perovskite hosts,  $HCa_2Nb_3O_{10}$  and  $HCa_2Nb_2MO_9$  ( $M = Al, Fe$ ), and then polyaniline (PANi) was formed in the interlayer gallery on polymerization with 0.4 M solution of  $(NH_4)_2S_2O_8$ . They used this approach to prepare perovskite polymer composites; initially aniline was intercalated into both  $HCa_2Nb_3O_{10}$  and  $HCa_2Nb_2MO_9$  ( $M = Al, Fe$ ) and then on oxidation with ammonium persulfate, polyaniline (PANi) was formed within the hosts. Yang and co-workers [184] reported a simple acid base mechanism for the insertion of a number of long-chain amines into  $H_2W_2O_7$ . Similar amine

intercalated tungstates of  $\text{H}_2\text{W}_2\text{O}_7$  were also produced by Chen and Sugahara [185]; in a separate report by Sugahara and co-workers [186], intercalation of amine in the protonated RP phase,  $\text{H}_2\text{La}_2\text{Ti}_3\text{O}_{10}$ , was described (Figure 1.12). They revealed that  $\text{H}_2\text{La}_2\text{Ti}_3\text{O}_{10}$  perovskites, undergo intercalation by ion exchange in contrary to acid-base mechanisms followed by other hosts. They have shown that insertion of *n*-butylamine in the host structure cannot be possible in absence of water. After hydration, formation of *n*-butylammonium ions takes place which further believed to be exchanged with protons in the interlayer space. Intercalation can also be observed in the superconductors of AV-related copper-oxides with neutral species. Vapors of  $\text{HgBr}_2$  and  $\text{HgI}_2$  can be directly intercalated into the  $[\text{Bi}_2\text{O}_2]^{2+}$  layers of  $\text{Bi}_2\text{O}_2\text{Sr}_2\text{CaCu}_2\text{O}_7$  [187, 188]. The extended X-ray absorption fine structure (EXAFS) data reveals that the intercalants,  $\text{HgX}_2$  ( $\text{X} = \text{B}, \text{I}$ ) are stabilized in the interlayer as linear molecules.

### 1.2.3 Reductive Deintercalation

The RP phase oxides obtained from late transition metals, such as Mn, Fe and Co also undergoes redox topochemical reactions. The resulting compounds are not ion-exchangeable but show interesting properties for various applications, such as anti-ferromagnetism, high temperature superconductors, ferroelectrics and anode material for Li-ion batteries. When we aim for reducing the oxygen content of the transitional metal perovskite oxides, then reactions are usually carried out in reducing atmospheres, such as in  $\text{H}_2$  gas flow or in presence of oxygen acceptor metals, such as, Ti and Zr in an evacuated tube. These reactions generally take place far beyond 500 °C, however, in the year 1999, Rosseinsky and co-workers have reported a new low temperature method, which allows the formation of large quantities of oxygen vacancy [189]. The precursor  $\text{LaNiO}_3$  was reduced to  $\text{LaNiO}_2$  ( $\delta = 1$ ) by using a solid state reducing agent (NaH) without any decomposition of  $\text{LaNiO}_3$ .

It has been demonstrated by Greenblatt *et al.* that nickel perovskites of double or triple-layers, namely,  $\text{La}_3\text{Ni}_2\text{O}_{7-x}$  [190] and  $\text{La}_4\text{Ni}_3\text{O}_{10-x}$  [191] produce compounds with nickel in the mixed valence (1 +, or 2 +) states. When these compounds are reduced, perovskite sheets get transformed to an infinite number of square-planar Ni-O layers and fluorite-type layers generated from interlayers, which are similar to those observed in the T'-structures (Figure 1.13); this was achieved by the removal of oxygen from the perovskite slab as well as the migration of extra oxygen to the vacant tetrahedral sites in the layer.

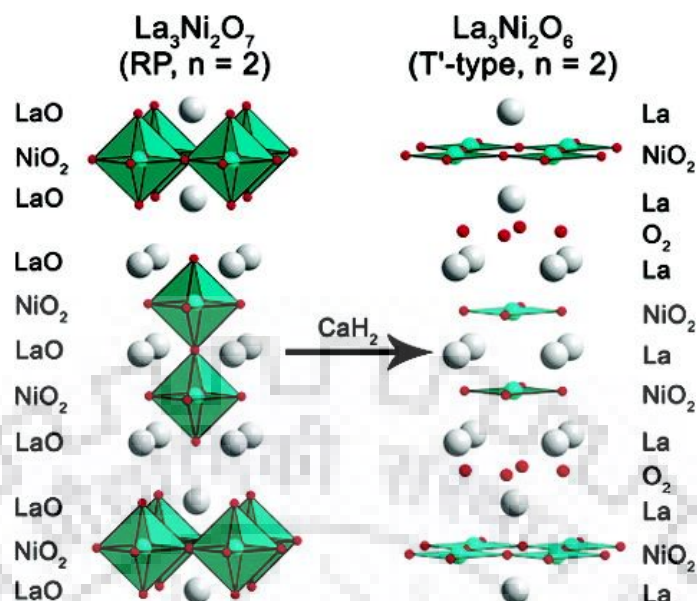


**Figure 1.13**  $\text{La}_3\text{Ni}_2\text{O}_{7-x}$  and  $\text{La}_3\text{Ni}_2\text{O}_6$ , a single oxygen from the perovskite block moves into the rock-salt layer to produce a T' structure [190].

Similarly, Kageyama *et al.* have reported several new iron compounds [192-194]. However, there are a number of previously known square-planar Ni-O layered compounds available but they reported the first ever compound with square-planar layers of iron oxide.  $\text{CaH}_2$  was used as the reducing agent to remove the oxide layers from the parent perovskite structures.  $\text{SrFeO}_3$  was reportedly converted to  $\text{SrFeO}_2$  in the initial studies [192]. The magnetic spin configuration of this compound is high and it exhibits antiferromagnetic transition at room temperature with coupling of spins oriented towards the plane. In the second system of iron oxides,  $\text{Sr}_3\text{Fe}_2\text{O}_{6.6}$  is reduced to  $\text{Sr}_3\text{Fe}_2\text{O}_5$  [193]. On topochemical treatment, 1D chains consisting of double  $\text{FeO}_4$  spin ladders were generated instead of infinite 2D iron-oxide layers. This compound also indicates long-range antiferromagnetic ordering.  $\text{CaFeO}_2$  can also be prepared similarly, [194] however, as opposed to  $\text{SrFeO}_2$ , the square planar  $\text{FeO}_4$  units show a slight distortion towards tetrahedral geometry.

Hadermann *et al.* [195] reported the topotactic reduction in anion deficient perovskite,  $4\text{H-BaMnO}_{2+x}$ , with  $\text{LiH}$  and resulted the sequence of oxygen vacancies changes from  $\text{Mn}_2\text{O}_9$  (face-sharing Mn – O octahedral unit) into  $\text{Mn}_2\text{O}_7$  (two corner-connected tetrahedral unit) and  $\text{Mn}_2\text{O}_6$  (two edge-connected tetrahedral unit). The compound exhibited antiferromagnetic transition below 350 K. Clarke and co-workers [174] have reported topotactic reductive



deintercalation in  $\text{Sr}_4\text{Mn}_3\text{O}_{7.5}\text{CuCh}_2$  ( $\text{Ch} = \text{S}, \text{Se}$ ) and after deintercalation long-range antiferromagnetic ordering was observed. Hayward and co-workers have shown topotactic reduction in the hexagonal perovskite,  $4\text{H-AMn}^{\text{IV}}\text{O}_3$ , ( $\text{A} = \text{Ba}$  and  $\text{Ba}_{0.5}\text{Se}_{0.2}$ ) with LiH as reducing agent and the structure changes into a vacancy-ordered perovskite,  $\text{AMn}^{\text{II}}\text{O}_2$ . The magnetic susceptibility data indicates canted antiferromagnetic ordering below 355 K [195, 196].

#### 1.2.4 Layer Extraction

Sugahara and co-workers reportedly treated Aurivillius phase,  $[\text{Bi}_2\text{O}_2]\text{SrNaNb}_3\text{O}_{10}$ , with acid solution and produced a protonated form of bismuth oxide [129]. Many other Aurivillius oxides were treated with this approach such as,  $[\text{Bi}_2\text{O}_2]\text{SrTa}_2\text{O}_7$  [130],  $[\text{Bi}_2\text{O}_2]\text{W}_2\text{O}_7$  [197] and  $[\text{Bi}_2\text{O}_2]\text{CaNaNb}_3\text{O}_{10}$  [198]. The uncommon mixed layer system,  $(\text{Bi}_2\text{O}_2)_2\text{BiNb}_3\text{O}_{11}$ , which contains both single and double-layered perovskite blocks, has been modified to remove Bi-O layers, resulting in  $\text{H}_4\text{BiNb}_3\text{O}_{11}$  [199]. Gonen *et al.* [200] have reported conversion of RP phase,  $\text{K}_2\text{La}_2\text{Ti}_3\text{O}_{10}$  with either tetraphenylphosphonium bromide ( $\text{PPh}_4\text{Br}$ ) or tetrabutylphosphonium bromide ( $\text{PBu}_4\text{Br}$ ) and allowed extraction of potassium oxide from the interlayer gallery of the host by topochemical method. They discovered that even one equivalent of  $\text{KO}_{0.5}$  can be extracted by regulating the quantity of phosphonium salt to produce  $\text{KL}_{0.5}\text{La}_2\text{Ti}_3\text{O}_{9.5}$ . When the first equivalent of potassium oxide, was removed from the parent RP phase, the structure transformed into a DJ phase. Then, on further removal of the second equivalent of potassium oxide, the structure reverts back to the staggered form. Another significant aspect of manipulation in the  $\text{K}_2\text{La}_2\text{Ti}_3\text{O}_9$ , compounds is that these layer extractions are reversible; in nature.  $\text{KL}_{0.5}\text{La}_2\text{Ti}_3\text{O}_{9.5}$  and  $\text{La}_2\text{Ti}_3\text{O}_9$  on treatment with  $\text{KNO}_3$  ( $\leq 600$  °C) allowed the reinsertion of the potassium oxide, by converting back the compounds to  $\text{K}_2\text{La}_2\text{Ti}_3\text{O}_{10}$  (Figure 1.14). Palacin and co-workers [139] reported a mixed-valence derivative of the layered perovskite,  $\text{HLaNb}_2\text{O}_7$ , which can be chemically reduced in air up to 650 °C to produce  $\text{LaNb}_2\text{O}_{6.5}$ , with retention of the perovskite structure.

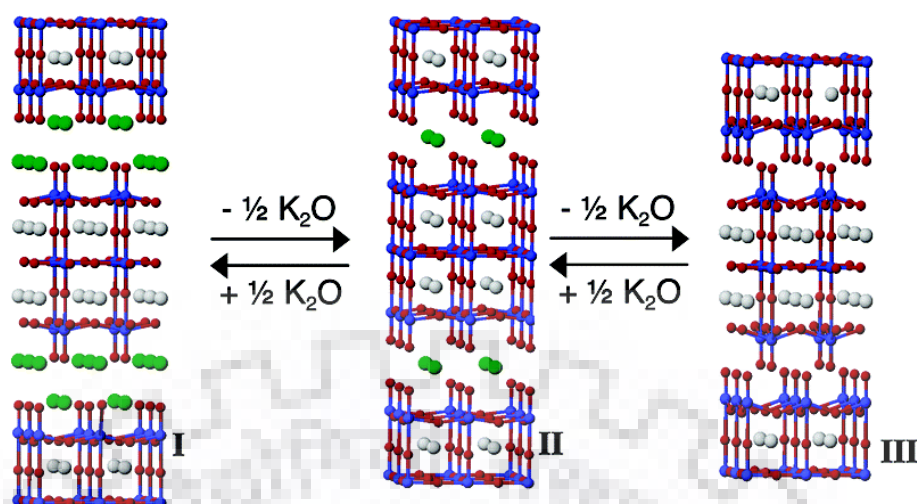


**Figure 1.14** RP layered perovskite layer extraction treatment,  $\text{K}_2\text{La}_2\text{Ti}_3\text{O}_{10}$  (I); potassium oxide extraction with ( $\text{PBU}_4\text{Br}$ ;  $\text{PPH}_4\text{Br}$ ) salts, (II)  $\text{KLa}_2\text{Ti}_3\text{O}_{9.5}$  and (III)  $\text{La}_2\text{Ti}_3\text{O}_9$  [200].

### 1.2.5 Metal-Nonmetal Layer Construction

Different methods were used in layered perovskites to construct metal-non-metal arrays. It has been found that a simple ion exchange route, starting with the DJ-layered perovskites, can lead to a series of transition metal halide arrays in the host. It is an unusual reaction in which both cationic and anionic species are simultaneously exchanged.

Kodenkandath *et al.* reported co-exchange reaction between the DJ phase,  $\text{RbLaNb}_2\text{O}_7$ , and transition metal-oxyhalide,  $\text{CuX}_2$  ( $\text{X} = \text{Cl}, \text{Br}$ ) at low temperature. After co-exchange both the obtained copper-oxyhalide products exhibit antiferromagnetic transition [110]. Similar transition metal halide co-exchange interactions with copper halide has been observed in the double- or triple-layered perovskites, such as,  $\text{ALa Nb}_2\text{O}_7$  ( $\text{A} = \text{H}, \text{Li}, \text{Na}, \text{K}, \text{Rb}, \text{NH}_4^+$ ),  $\text{RbLaTa}_2\text{O}_7$ ,  $\text{RbANb}_2\text{O}_7$ , ( $\text{A} = \text{La}, \text{Nd}, \text{Bi}$ ),  $\text{RbCa}_2\text{Nb}_3\text{O}_{10}$ ,  $\text{ACa}_2\text{Ta}_3\text{O}_{10}$  ( $\text{A} = \text{Li}, \text{Rb}$ ), and  $\text{RbLa}_2\text{Ti}_2\text{NbO}_{10}$  [201, 202]. Viciu *et al.* reported similar type of metal-oxyhalide co-exchange reaction in DJ host compound,  $\text{RbLaNb}_2\text{O}_7$ , to form  $(\text{MCl})\text{LaNb}_2\text{O}_7$ , ( $\text{M} = \text{Mn}, \text{Fe}$ ) [203-205]. The  $(\text{CuCl})\text{LaNb}_2\text{O}_7$  consists of  $\text{CuO}_2\text{Cl}_4$  octahedral layers and these copper-oxyhalide layers form bridge between two perovskite blocks [201, 206]. After co-exchange reaction with transition-metal oxyhalides, the host compounds exhibit interesting physical properties [207-210].

Kageyama and co-workers have reported topotactic ion exchange in double layered perovskite,  $\text{RbLaTa}_2\text{O}_7$ , with copper-bromide and then heated for several days to obtain  $(\text{CuBr})\text{LaNb}_2\text{O}_7$ , which show long range antiferromagnetic ordering at low temperature [211]. Tsujimoto and co-workers [212] also reported metal-nonmetal halide arrays in triple layered perovskite,  $(\text{CuBr})\text{A}_2\text{B}_3\text{O}_{10}$ , ( $\text{A} = \text{Ca}, \text{Sr}, \text{Ba}, \text{Pb}$  and,  $\text{B} = \text{Nb}, \text{Ta}$ ), by topotactic ion exchange. These metal-oxybromide compounds reportedly exhibit antiferromagnetic behavior [211-213].  $(\text{CuCl})\text{LaNb}_{2-\gamma}\text{Ta}_\gamma\text{O}_7$  also show complex antiferromagnetically ordered [213]. Uemura and co-workers established a solid solution system,  $(\text{CuCl}_{1-x}\text{Br}_x)\text{LaNb}_{2-\gamma}\text{Ta}_\gamma\text{O}_7$ , by low temperature ion exchange reaction and displayed evolution from the spin gap to an antiferromagnetically ordered state with magnetic phase separation and / or a first-order phase transition [213]. Wiley and co-workers have reported two step topotactic transformation in DJ perovskite,  $\text{RbLaTa}_2\text{O}_7$ . In the first step, topotactic ion exchange was performed between DJ host and copper-oxyhalide to produce  $(\text{CuCl})\text{LaNb}_2\text{O}_7$ , which in the second step underwent intercalation with  $n\text{-BuLi}$ . The  $(\text{Li}_x\text{Cl})\text{LaNb}_2\text{O}_7$  consists of a double layer of  $\text{LiO}_2\text{Cl}_2$  tetrahedra that is corner-connected with the perovskite slabs [214] (Figure 1.15).

Choi *et al.* reported construction of alkali metal halide layers in the perovskite host by two step intercalation reaction. In the first step reductive intercalation was performed in DJ host compounds,  $\text{ALaTa}_2\text{O}_7$  with alkali metal and heated at  $290^\circ\text{C}$  for 4 days. In the second step, oxidative intercalation was performed with the reduced products,  $\text{A}_2\text{LaTa}_2\text{O}_7$ , and chlorine gas, which results in formation of  $(\text{A}_2\text{Cl})\text{LaNb}_2\text{O}_7$  ( $\text{A} = \text{Rb}, \text{Cs}$ ) as the final products [215]. Wiley and co-workers [216] reported the formation of alkali-metal hydroxide layers in the layered perovskites by a two-step topotactic reaction method. Similarly,  $(\text{CuCl})\text{-PrNb}_2\text{O}_7$ , is also prepared by replacement of  $\text{Rb}^+ / \text{Cs}^+$  with  $\text{CuCl}^+$ . The parent compounds,  $\text{RbPrNb}_2\text{O}_7$  and  $\text{CsPrNb}_2\text{O}_7$ , both show paramagnetic behavior, while the  $(\text{CuCl})\text{PrNb}_2\text{O}_7$ , shows an antiferromagnetic transition below 20 K [217].



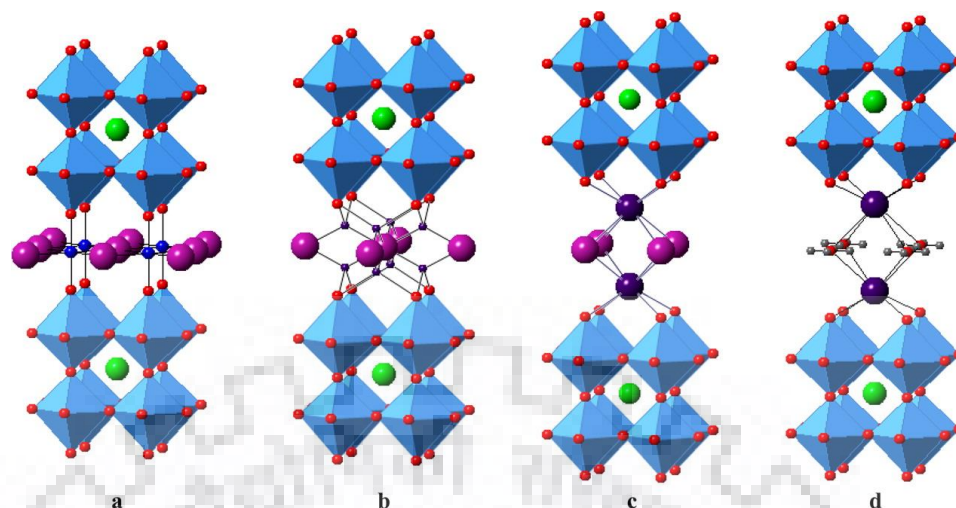


**Figure 1.15** Various structures accessible topochemically within layered perovskite hosts. (a)  $(MCl)LaNb_2O_7$  ( $M =$  transition metal), (b)  $(Li_2Cl)LaNb_2O_7$ , (c)  $(Rb_2Cl)LaNb_2O_7$ , and (d)  $(Rb_2OH)LaNb_2O_7$  [217].

### 1.2.6 Methods to Synthesize Metal Oxides

A diverse array of methods are available for the synthesis of mixed metal oxides. Some of the commonly used methods include the following.

- Ceramic
- Hydrothermal
- Sol-gel
- Microwave

The most popular technique for the synthesis of solids is a ceramic or conventional solid-state reaction (SSR) method. In this method, stoichiometric quantities of solid starting materials, such as, binary / simple metal oxides / carbonates / oxides/ oxalates are weighed and ground thoroughly in an agate mortar for nearly an hour. The ground mixture is then placed in a silica / platinum / alumina container (crucible / boat) and finally heated in a muffle / tube furnace at high temperatures for variable durations. The requirement of high temperatures is due to the fact that the reactions are diffusion controlled and the diffusion coefficients of the solids are very low (in the order of  $10^{-12} \text{ cm}^2\text{s}^{-1}$ ). If any starting component is either volatile or air sensitive, then the reaction is carried out in sealed tube or controlled gas atmospheres (argon/nitrogen) to avoid any contact with the  $O_2$  or moisture. The reaction

mixtures are ground thoroughly at each intermittent stage during the entire course of the reaction. The repeated grinding and heating steps involved in the ceramic method helps in bring down the diffusion barrier between the grains of starting reactants and products formed during the course of a reaction. The nucleation step in the ceramic method is slightly difficult due to the structural differences between the starting materials and product and a large amount of structural reorganization is required to get the final product by bond braking, reforming and migration of constituent elements.

While the ceramic method is a very common method for the preparation of various solid materials, it has some disadvantages, such as, complete homogenous mixing of the starting compounds is not possible, poor diffusion rate in reacting solids, and decomposition of the required product at elevated temperatures. There have been significant attempts in recent years to overcome the limitations of conventional synthetic methods, resulting in alternative routes for solid-state synthesis. Among these alternative strategies, the following three methods, which rely on the knowledge of structural chemistry and reactivity patterns of solids, have proved significant: (i) the solid-state precursor method, (ii) methods based on topochemical redox reactions and (iii) topochemical ion-exchange reactions. The three procedures focus on synthesis at low temperatures and the products should be finely divided with high surface areas, a feature essential for catalysis and other applications. More importantly, synthesis at temperatures considerably lower than the sintering temperatures of solids preserves the essential features of the parent structure with minimal structural reorganization. Due to this reason we have called methods (ii) and (iii) topochemical methods. Synthesis by topochemical methods often yields metastable phases that cannot be obtained by conventional methods.

## REFERENCES

- (1) Krebs, B. The Crystal Structure of  $\text{MoO}_3 \cdot 2\text{H}_2\text{O}$ : A Metal Aquoxide with Both Coordinated and Hydrate Water. *J. Chem. Soc. D Chem. Commun.* **1970**, 50–51.
- (2) Bachmann, H. G.; Ahmed, F. R.; Barnes, W. H. The Crystal Structure of Vanadium Pentoxide. *Z. Krist. – Cryst. Mater* **1961**, *115*, 110–131.
- (3) Delmas, C.; Fouassier, C.; Hagenmuller, P. Structural Classification and Properties of the Layered Oxides. *Phys. B + C* **1980**, *99*, 81–85.
- (4) Gasperin, M. P. Structure of Potassium Triniobate (V)  $\text{KNb}_3\text{O}_8$ , a Lamellar Niobate. *Acta Cryst. Chem.* **1982**, B38, 2024–2026.
- (5) Du, G.; Chen, Q.; Yu, Y.; Zhang, S.; Zhou, W.; Peng, L.-M. Synthesis, Modification and Characterization of  $\text{K}_4\text{Nb}_6\text{O}_{17}$ -type Nanotubes. *J. Mater. Chem.* **2004**, *14*, 1437–1442.
- (6) Inoue, Y.; Kubokawa, T.; Sato, K. Photocatalytic Activity of Alkali-Metal Titanates Combined with Ruthenium In the Decomposition of Water. *J. Phys. Chem.* **1991**, *95*, 4059–4063.
- (7) Kim, Y. I.; Atherton, S. J.; Brigham, E. S.; Mallouk, T. E. Sensitized Layered Metal Oxide Semiconductor Particles for Photochemical Hydrogen Evolution from Nonsacrificial Electron Donors. *J. Phys. Chem.* **1993**, *97*, 11802–11810.
- (8) Olazcuaga, R.; Reau, J.-M.; Devalette, M.; Flem, G. Le; Hagenmuller, P. The Phases  $\text{Na}_4\text{XO}_4$  (X = Si, Ti, Cr, Mn, Co, Ge, Sn, Pb) and  $\text{K}_4\text{XO}_4$ , (X = Ti, Cr, Mn, Ge, Zr, Sn, Hf, Pb). *J. Solid State Chem.* **1975**, *13*, 275–282.
- (9) Werthmann, R.; Hoppe, R. Zur Kenntnis von  $\text{Na}_4\text{Ti}_5\text{O}_{12}$ . *Z. anorg. allg. Chem.* **1984**, *519*, 117–133.
- (10) Chen, R.; Zavalij, P.; Wittingham, M. S. Hydrothermal Synthesis and Characterization of  $\text{K}_x\text{MnO}_2 \cdot y\text{H}_2\text{O}$ . *Chem. Mater.* **1996**, *8*, 1275–1280.
- (11) Wadsley, A. D. Crystal Chemistry of Non-stoichiometric Pentavalent Vanadium Oxides: Crystal Structure of  $\text{Li}_{1+x}\text{V}_3\text{O}_8$ . *Acta Crystallogr.* **1957**, *10*, 261–267.
- (12) Okada, K.; Marumo, F.; Iwai, S. The Crystal Structure of  $\text{Cs}_6\text{W}_{11}\text{O}_{36}$ . *Acta Cryst.* **1978**, B34, 50–54.
- (13) Mao, L.; Ke, W.; Pedesseau, L.; Wu, Y.; Katan, C.; Even, J.; Wasielewski, M. R.; Stoumpos, C. C.; Kanatzidis, M. G. Hybrid Dion–Jacobson 2D Lead Iodide Perovskites. *J. Am. Chem. Soc.* **2018**, 3775–3783.
- (14) Mandal, T. K.; Sivakumar, T.; Augustine, S.; Gopalakrishnan, J. Heterovalent Cation-Substituted Aurivillius Phases,  $\text{Bi}_2\text{SrNaNb}_2\text{TaO}_{12}$  and  $\text{Bi}_2\text{Sr}_2\text{Nb}_{3-x}\text{M}_x\text{O}_{12}$  (M = Zr, Hf, Fe, Zn). *Mater. Sci. Eng. B* **2005**, *121*, 112–119.
- (15) Serna, C. J.; White, J. L.; Hem, Stanley, L. Hydrolysis of Aluminum-Tri-(Sec-

- Butoxide) in Ionic and Nonionic Media. *Clays Clay Miner.* **1977**, *25*, 384–391.
- (16) Thiel, J. P.; Chiang, C. K.; Poeppelmeier, K. R. Structure of  $\text{LiAl}_2(\text{OH})_7 \cdot 2\text{H}_2\text{O}$ . *Chem. Mater.* **1993**, *5*, 297–304.
- (17) Besserguenev, A. V.; Fogg, A. M.; Francis, R. J.; Price, S. J.; O'Hare, D.; Isupov, V. P.; Tolochko, B. P. Synthesis and Structure of the Gibbsite Intercalation Compounds  $[\text{LiAl}_2(\text{OH})_6]\text{X}$  {X = Cl, Br,  $\text{NO}_3$ } and  $[\text{LiAl}_2(\text{OH})_6]\text{Cl} \cdot \text{H}_2\text{O}$  Using Synchrotron X-ray and Neutron Powder Diffraction. *Chem. Mater.* **1997**, *9*, 241–247.
- (18) Klevtsova, R. F.; Klevtsova, P. V. X-Ray Diffraction Study of a New Modification of Yttrium Hydroxychloride  $\text{Y}(\text{OH})_2\text{Cl}$ . *J. Struct. Chem.* **1967**, *7*, 524–527.
- (19) Geng, F.; Matsushita, Y.; Ma, R.; Xin, H.; Tanaka, M.; Izumi, F.; Iyi, N.; Sasaki, T. General Synthesis and Structural Evolution of a Layered Family of  $\text{Ln}_8(\text{OH})_{20}\text{Cl}_4 \cdot n\text{H}_2\text{O}$  (Ln = Nd, Sm, Eu, Gd, Tb, Dy, Ho, Er, Tm, and Y). *J. Am. Chem. Soc.* **2008**, *130*, 16344–16350.
- (20) Ma, R.; Sasaki, T. Two-Dimensional Oxide and Hydroxide Nanosheets: Controllable High-Quality Exfoliation, Molecular Assembly, and Exploration of Functionality. *Acc. Chem. Res.* **2015**, *48*, 136–143.
- (21) Hansen, W. C.; Brownmiller, L. T.; Bogue, R. H. Studies on the System Calcium Oxide-Alumina-Ferric Oxide. *J. Am. Chem. Soc.* **1928**, *50*, 396–406.
- (22) Choy, J. -H.; Kim, J. -Y.; Kim, S. -J.; Sohn, J. -S.; Han, C. H. New Dion-Jacobson-Type Layered Perovskite Oxyfluorides,  $\text{ASrNb}_2\text{O}_6\text{F}$  (A = Li, Na, and Rb). *Chem. Mater.* **2001**, *13*, 906–912.
- (23) Ida, S.; Okamoto, Y.; Matsuka, M.; Hagiwara, H.; Ishihara, T. Preparation of Tantalum-Based Oxynitride Nanosheets by Exfoliation of a Layered Oxynitride,  $\text{CsCa}_2\text{Ta}_3\text{O}_{10-x}\text{N}_y$ , and Their Photocatalytic Activity. *J. Am. Chem. Soc.* **2012**, *134*, 15773–15782.
- (24) Romero, F. D.; Leach, A.; Möller, J. S.; Foronda, F.; Blundell, S. J.; Hayward, M. A. Strontium Vanadium Oxide-Hydrides: “Square-Planar” Two-Electron Phases. *Angew. Chemie - Int. Ed.* **2014**, *53*, 7556–7559.
- (25) Schaak, R. E.; Mallouk, T. E. Perovskites by Design: A Toolbox of Solid-State Reactions. *Chem. Mater.* **2002**, *14*, 1455–1471.
- (26) Rakibuddin, M.; Mandal, S.; Ananthkrishnan, R. A Novel Ternary CuO Decorated  $\text{Ag}_3\text{AsO}_4/\text{GO}$  Hybrid as a Z-Scheme Photocatalyst for Enhanced Degradation of Phenol under Visible Light. *New J. Chem.* **2017**, *41*, 1380–1389.
- (27) Kumar, N., Jagadeesan, D.; Pillai, P. B.; Chacko, M.; P.; Eswaramoorthy, M.; Sundaresan, A. Ferromagnetism in Thin-Walled Hollow Spheres of Non-Magnetic Inorganic Materials. *Chem. Phys. Lett.* **2011**, *504*, 189–192.
- (28) Perez-Mato, J. M.; Aroyo, M.; García, A.; Blaha, P.; Schwarz, K.; Schweifer, J.; Parlinski, K. Competing Structural Instabilities In the Ferroelectric Aurivillius Compound  $\text{SrBi}_2\text{Ta}_2\text{O}_9$ . *Phys. Rev. B.* **2004**, *70*, 214111.

- (29) Boivin, J. C.; Mairesse, G. Recent Material Developments in Fast Oxide Ion Conductors. *Chem. Mater.* **1998**, *10*, 2870–2888.
- (30) Moritomo, Y.; Asamitsu, A.; Kuwahara, H.; Tokura, Y. Giant Magnetoresistance of Manganese Oxides with a Layered Perovskite Structure. *Nature* **1996**, *380*, 141–144.
- (31) Bednorz, J. G.; Müller, K. A. Possible High  $T_c$  Superconductivity in the Ba-La-Cu-O System. *Z. Phys. B Condens. Matter* **1986**, *64*, 189–193.
- (32) Ranmohotti, K. G. S.; Josepha, E.; Choi, J.; Zhang, J.; Wiley, J. B. Topochemical Manipulation of Perovskites: Low-Temperature Reaction Strategies for Directing Structure and Properties. *Adv. Mater.* **2011**, *23*, 442–460.
- (33) Takagaki, A.; Tagusagawa, C.; Hayashi, S.; Hara, M.; Domen, K. Nanosheets as Highly Active Solid Acid Catalysts for Green Chemical Syntheses. *Energy Environ. Sci.* **2010**, *3*, 82–93.
- (34) Miyamoto, N.; Nakato, T. Liquid Crystalline Inorganic Nanosheet Colloids Derived from Layered Materials. *Isr. J. Chem.* **2012**, *52*, 881–894.
- (35) Osada, M.; Sasaki, T. Two-Dimensional Dielectric Nanosheets: Novel Nanoelectronics from Nanocrystal Building Blocks. *Adv. Mater.* **2012**, *24*, 210–228.
- (36) Benedek, N. A.; Rondinelli, J. M.; Djani, H.; Ghosez, P.; Lightfoot, P. Understanding Ferroelectricity In Layered Perovskites: New Ideas and Insights from Theory and Experiments. *Dalt. Trans.* **2015**, *44*, 10543–10558.
- (37) Ma, R.; Sasaki, T. Organization of Artificial Superlattices Utilizing Nanosheets as a Building Block and Exploration of Their Advanced Functions. *Annu. Rev. Mater. Res.* **2015**, *45*, 111–127.
- (38) ten Elshof, J. E.; Yuan, H.; Rodriguez, P. G. Two-Dimensional Metal Oxide and Metal Hydroxide Nanosheets: Synthesis, Controlled Assembly and Applications in Energy Conversion and Storage. *Adv. Energy Mater.* **2016**, *6*, 1600355.
- (39) Kalantar-zadeh, K.; Ou, J. Z.; Daeneke, T.; Mitchell, A.; Sasaki, T.; Fuhrer, M. S. Two Dimensional and Layered Transition Metal Oxides. *Appl. Mater. Today* **2016**, *5*, 73–89.
- (40) Zhang, G.; Liu, G.; Wang, L.; Irvine, J. T. S. Inorganic Perovskite Photocatalysts for Solar Energy Utilization. *Chem. Soc. Rev.* **2016**, *45*, 5951–5984.
- (41) Dion, M.; Piffard, Y.; Tournoux, M. The Tetratitanates  $M_2Ti_4O_9$  ( $M = Li, Na, K, Rb, Cs, Tl, Ag$ ). *J. Inorg. Nucl. Chem.* **1978**, *40*, 917–918.
- (42) Nouar, F.; Eckert, J.; Eubank, J. F.; Forster, P.; Eddaoudi, M. Zeolite- like Metal–Organic Frameworks (ZMOFs) as Hydrogen Storage Platform: Lithium and Magnesium Ion-Exchange and  $H_2$ -(*rho*-ZMOF) Interaction Studies. *J. Am. Chem. Soc.* **2009**, *131*, 2864–2870.
- (43) Yang, S.; Martin, G. S. B.; Titman, J. J.; Blake, A. J.; Allan, D. R.; Champness, N. R.;



- Schröder, M. Pore with Gate: Enhancement of the Isosteric Heat of Adsorption of Dihydrogen via Postsynthetic Cation Exchange in Metal–Organic Frameworks. *Inorg. Chem.* **2011**, *50*, 9374–9384.
- (44) Evans, J. D.; Sumbly, C. J.; Doonan, C. J. Post-Synthetic Metalation of Metal–Organic Frameworks. *Chem. SoFarid Nouarc. Rev.* **2014**, *43*, 5933–5951.
- (45) Garcia, I.; Solache-Rios, M.; Bosch, P.; Bulbulian, S. Cobalt(2+) Ion Exchange with NaY. *J. Phys. Chem.* **1993**, *97*, 1249–1251.
- (46) Garcia, I.; Solache-Ríos, M.; Bosch, P.; Bulbulian, S. Effect of EDA on Co<sup>2+</sup> Ion Exchange In Zeolite 4A. *Langmuir* **1996**, *12*, 4474–4475.
- (47) Tang, Q.; Zhang, Q.; Wang, P.; Wang, Y.; Wan, H. Characterizations of Cobalt Oxide Nanoparticles within Faujasite Zeolites and the Formation of Metallic Cobalt. *Chem. Mater.* **2004**, *16*, 1967–1976.
- (48) Manos, M. J.; Chrissafis, K.; Kanatzidis, M. G. Unique Pore Selectivity for Cs<sup>+</sup> and Exceptionally High NH<sup>4+</sup> Exchange Capacity of the Chalcogenide Material K<sub>6</sub>Sn[Zn<sub>4</sub>Sn<sub>4</sub>S<sub>17</sub>]. *J. Am. Chem. Soc.* **2006**, *128*, 8875–8883.
- (49) Canfield, G. M.; Bizimis, M.; Lattur, S. E. Transition-Metal Ion Exchange Using Poly(Ethylene Glycol) Oligomers as Solvents. *Chem. Mater.* **2010**, *22*, 330–337.
- (50) Kim, H. S.; Bae, D.; Lim, W. T.; Seff, K. Li<sup>+</sup> Exchange into Zeolite Na–Y (FAU) from Aqueous Methanol. Single-Crystal Structures of Fully Dehydrated Li,Na–Y. *J. Phys. Chem. C* **2012**, *116*, 9009–9018.
- (51) Sen, D.; Kim, C. W.; Heo, N. H.; Seff, K. Introducing Copper Ions into Zeolite Y by the Thallous Ion Exchange Method: Single Crystal Structure of [Cu<sub>21.6</sub>Tl<sub>39.2</sub>][Si<sub>121</sub>Al<sub>171</sub>O<sub>384</sub>]–FAU. *J. Porous Mater.* **2014**, *21*, 321–330.
- (52) Zaarour, M.; Roz, M. E.; Dong, B.; Retoux, R.; Aad, R.; Cardin, J.; Dufour, C.; Gourbilleau, F.; Gilson, J. P.; Mintova, S. Photochemical Preparation of Silver Nanoparticles Supported on Zeolite Crystals. *Langmuir* **2014**, *30*, 6250–6256.
- (53) Navlani-García, M.; Miguel-García, I.; Berenguer-Murcia, Á.; Lozano-Castelló, D.; Cazorla-Amorós, D.; Yamashita, H. Pd/Zeolite-Based Catalysts for the Preferential CO Oxidation Reaction: Ion-Exchange, Si/Al and Structure Effect. *Catal. Sci. Technol.* **2016**, *6*, 2623–2632.
- (54) Seo, S. M.; Moon, D. J.; An, J.; Jeong, H. K.; Lim, W. T. Time-Dependent Ni<sup>2+</sup>-Ion Exchange in Zeolites Y (FAU, Si/Al = 1.56) and Their Single-Crystal Structures. *J. Phys. Chem. C* **2016**, *120*, 28563–28574.
- (55) Chebbi, M.; Azambre, B.; Cantrel, L.; Koch, A. A Combined DRIFTS and DR-UV–Vis Spectroscopic In Situ Study on the Trapping of CH<sub>3</sub>I by Silver-Exchanges Faujasite Zeolite. *J. Phys. Chem. C* **2016**, *120*, 18694–18706.
- (56) Samanta, S.; Bhunia, K.; Pradhan, D.; Satpati, B.; Srivastava, R. Ni and Cu Ion-Exchanged Nanostructured Mesoporous Zeolite: A Noble Metal Free, Efficient, and

- Durable Electrocatalyst for Alkaline Methanol Oxidation Reaction. *Mater Today Energy* **2018**, *8*, 45–56.
- (57) Samanta, S.; Bhunia, K.; Pradhan, D.; Satpati, B.; Srivastava, R. NiCuCo<sub>2</sub>O<sub>4</sub> Supported Ni–Cu Ion-Exchanged Mesoporous Zeolite Heteronano Architecture: An Efficient, Stable, and Economical Nonprecious Electrocatalyst for Methanol Oxidation. *ACS Sustainable Chem. Eng.* **2018**, *6*, 2023–2036.
- (58) Carrado, K. A.; Wasserman, S. R. Stability of Cu(II)- And Fe(III)-Porphyrins on Montmorillonite Clay: An X-Ray Absorption Study. *Chem. Mater.* **1996**, *8*, 219–225.
- (59) Sels, B.; Vos, D. D.; Buntinx, M.; Pierard, F.; Kirsch-De Mesmaeker, A.; Jacobs, P. Layered Double Hydroxides Exchanged with Tungstate as Biomimetic Catalysts for Mild Oxidative Bromination. *Nature* **1999**, *400*, 855–857.
- (60) Fei, H.; Oliver, S. R. J. Copper Hydroxide Ethanedisulfonate: A Cationic Inorganic Layered Material for High-Capacity Anion Exchange. *Angew. Chemie - Int. Ed.* **2011**, *50*, 9066–9070.
- (61) McCarthy, T. J.; Tanzer, T. A.; Kanatzidis, M. G. A New Metastable Three-Dimensional Bismuth Sulfide with Large Tunnels: Synthesis, Structural Characterization, Ion-Exchange Properties, and Reactivity of KBi<sub>3</sub>S<sub>5</sub>. *J. Am. Chem. Soc.* **1995**, *117*, 1294–1301.
- (62) Clearfield, A. Structure and Ion Exchange Properties of Tunnel Type Titanium Silicates. *Solid State Sci.* **2001**, *3*, 103–112.
- (63) Cai, J.; Liu, J.; Gao, Z.; Navrotsky, A.; Suib, S. L. Synthesis and Anion Exchange of Tunnel Structure Akaganeite. *Chem. Mater.* **2001**, *13*, 4595–4602.
- (64) Rowsell, J. L. C.; Taylor, N. J.; Nazar, L. F. Structure and Ion Exchange Properties of a New Cobalt Borate with a Tunnel Structure “Templated” by Na<sup>+</sup>. *J. Am. Chem. Soc.* **2002**, *124*, 6522–6523.
- (65) Sharma, R.; Mandal, T. K.; Ramesha, K.; Gopalakrishnan, J. Synthesis and Characterization of AgBiO<sub>3</sub> with the Cubic KSbO<sub>3</sub> Structure. *Indian J. Chem., Sect. A* **2004**, *43A*, 11–17.
- (66) Armstrong, A. R.; Anderson, P. A. Synthesis and Structure of a New Layered Niobium Blue Bronze: Rb<sub>2</sub>LaNb<sub>2</sub>O<sub>7</sub>. *Inorg. Chem.* **1994**, *33*, 4366–4369.
- (67) Ollivier, P. J.; Mallouk, T. E. A “Chimie Douce” Synthesis of Perovskite-Type SrTa<sub>2</sub>O<sub>6</sub> and SrTa<sub>2-x</sub>Nb<sub>x</sub>O<sub>6</sub>. *Chem. Mater.* **1998**, *10*, 2585–2587.
- (68) Kodenkandath, T. A.; Lalena, J. N.; Zhou, W. L.; Carpenter, E. E.; Sangregorio, C.; Falster, A. U.; Simmons, W. B.; Jr., C. J. O.; Wiley, J. B. Assembly of Metal–Anion Arrays within a Perovskite Host. Low-Temperature Synthesis of New Layered Copper–Oxyhalides, (CuX)LaNb<sub>2</sub>O<sub>7</sub>, X = Cl, Br. *J. Am. Chem. Soc.* **1999**, *121*, 10743–10746.
- (69) Hyeon, K.-A.; Byeon, S.-H. Synthesis and Structure of New Layered Oxides,



- $M^{II}La_2Ti_3O_{10}$  ( $M = Co, Cu, \text{ and } Zn$ ). *Chem. Mater.* **1999**, *11*, 352–357.
- (70) Kobayashi, Y.; Tian, M.; Eguchi, M.; Mallouk, T. E. Ion-Exchangeable, Electronically Conducting Layered Perovskite Oxyfluorides. *J. Am. Chem. Soc.* **2009**, *131*, 9849–9855.
- (71) Galven, C.; Fourquet, J. L.; Suard, E.; Crosnier-Lopez, M. P.; Le Berre, F. Structural Characterization of a New Acentric Ruddlesden-Popper Layered Perovskite Compound:  $LiHSrTa_2O_7$ . *Dalt. Trans.* **2010**, *39*, 3212–3218.
- (72) Boltersdorf, J.; Maggard, P. A. Silver Exchange of Layered Metal Oxides and Their Photocatalytic Activities. *ACS Catal.* **2013**, *3*, 2547–2555.
- (73) Yip, T. W. S.; Cussen, E. J. Ion Exchange and Structural Aging in the Layered Perovskite Phases  $H_{1-x}Li_xLaTiO_4$ . *Inorg. Chem.* **2013**, *52*, 6985–6993.
- (74) Roudebush, J. H.; Ross, K. A.; Cava, R. J. Iridium Containing Honeycomb Delafossites by Topotactic Cation Exchange. *Dalt. Trans.* **2016**, *45*, 8783–8789.
- (75) F. Cavani, F. Trifiro, A. V. Hydrotalcite-Type Anionic Clays: Preparation, Properties and Applications. *Catal. Today* **1991**, *11*, 173–301.
- (76) Narayanan, S.; Krishna, K. Highly Active Hydrotalcite Supported Palladium Catalyst for Selective Synthesis of Cyclohexanone from Phenol. *Appl. Catal. A Gen.* **1996**, *147*, L253–L258.
- (77) Kaneda, K.; Yamashita, T.; Matsushita, T.; Ebitani, K. Heterogeneous Oxidation of Allylic and Benzylic Alcohols Catalyzed by Ru-Al-Mg Hydrotalcites in the Presence of Molecular Oxygen. *J. Org. Chem.* **1998**, *63*, 1750–1751.
- (78) Pavan, P. C.; De A. Gomes, G.; Valim, J. B. Adsorption of Sodium Dodecyl Sulfate on Layered Double Hydroxides. *Microporous Mesoporous Mater.* **1998**, *21*, 659–665.
- (79) Roeffaers, M. B. J.; Sels, B. F.; Uji-i, H.; De Schryver, F. C.; Jacobs, P. A.; De Vos, D. E.; Hofkens, J. Spatially Resolved Observation of Crystal-Face-Dependent Catalysis by Single Turnover Counting. *Nature* **2006**, *439*, 572–575.
- (80) Grover, K.; Komarneni, S.; Katsuki, H. Uptake of Arsenite by Synthetic Layered Double Hydroxides. *Water Res.* **2009**, *43*, 3884–3890.
- (81) Chai, H.; Lin, Y.; Evans, D. G.; Li, D. Synthesis and UV Absorption Properties of 2-Naphthylamine-1,5-Disulfonic Acid Intercalated Zn-Al Layered Double Hydroxides. *Ind. Eng. Chem. Res.* **2008**, *47*, 2855–2860.
- (82) Dutta, D.; Tummanapelli, A. K.; Vasudevan, S. Charge-Transfer-Driven Inclusion of Neutral TCNQ Molecules in the Galleries of a Layered Double Hydroxide: An Experimental and Computational Study. *J. Phys. Chem. C* **2013**, *117*, 3930–3939.
- (83) Ogawa, M.; Hiramane, M. Direct Correlation between Nanostructure and Particle Morphology during Intercalation. *Cryst. Growth Des.* **2014**, *14*, 1516–1519.

- (84) Heuvel, Van Den G. P. M.; Blasse, G. Vibrational Spectra and Structural Considerations of Compounds  $\text{NaLnTiO}_4$ . *J. Solid State Chem.* **1974**, *10*, 206–210.
- (85) Gopalakrishnan, J.; Bhat, V.  $\text{A}^{\text{I}}\text{LaNb}_2\text{O}_7$ : A New Series of Layered Perovskites Exhibiting Ion Exchange and Intercalation Behaviour. *Mater. Res. Bull.* **1987**, *22*, 412–417.
- (86) Gopalakrishnan, J.; Uma, S.; Bhat, V. Synthesis of Layered Perovskite Oxides,  $\text{ACa}_{2-x}\text{La}_x\text{Nb}_{3-x}\text{Ti}_x\text{O}_{10}$  ( $\text{A} = \text{K, Rb, Cs}$ ), and Characterization of New Solid Acids,  $\text{HCA}_{2-x}\text{La}_x\text{Nb}_{3-x}\text{Ti}_x\text{O}_{10}$  ( $0 < x \leq 2$ ), Exhibiting Variable Bronsted Acidity. *Chem. Mater.* **1993**, *5*, 132–136.
- (87) Gopalakrishnan, J.; Bhat, V.  $\text{A}_2\text{Ln}_2\text{Ti}_3\text{O}_{10}$  ( $\text{A} = \text{K or Rb; Ln} = \text{La or Rare Earth}$ ): A New Series of Layered Perovskites Exhibiting Ion Exchange. *Inorg. Chem.* **1987**, *26*, 4299–4301.
- (88) Dion, M.; Ganne, M.; Tournoux, M. Nouvelles Familles Feuilletés De Phases  $\text{M}^{\text{I}}\text{M}_2^{\text{II}}\text{Nb}_3\text{O}_{10}$  A Feuilletés “Perovskites.” *Mater. Res. Bull.* **1981**, *16*, 1429–1435.
- (89) Sato, M.; Abo, J.; Jin, T. Solid State Structure Examination of  $\text{NaLaNb}_2\text{O}_7$  Synthesized by Soft Chemistry. *Solid State Ionics* **1992**, *57*, 285–293.
- (90) Toda, K.; Sato, M. Synthesis and Structure Determination of New Layered Perovskite Compounds,  $\text{ALaTa}_2\text{O}_7$  and  $\text{ACa}_2\text{Ta}_3\text{O}_{10}$  ( $\text{A} = \text{Rb, Li}$ ). *J. Mater. Chem.* **1996**, *6* (6), 1067–1071.
- (91) Gopalakrishnan, J.; Uma, S.; Vasanthacharya, N. Y.; Subbanna, G. N. Slicing the Perovskite Structure into Layers: Synthesis of Novel Three-Dimensional and Layered Perovskite Oxides,  $\text{ALaSrNb}_2\text{M}^{\text{II}}\text{O}_9$  ( $\text{A} = \text{Na, Cs}$ ). *J. Am. Chem. Soc.* **1995**, *117*, 2353–2354.
- (92) Thangadurai, V.; Shukla, A. K.; Gopalakrishnan, J. Proton Conduction in Layered Perovskite Oxides. *Solid State Ionics* **1994**, *73*, 9–14.
- (93) Byeon, S.-H.; Park, K.; Itoh, M. Structure and Ionic Conductivity of  $\text{NaLnTiO}_4$ ; Comparison with Those of  $\text{Na}_2\text{Ln}_2\text{Ti}_3\text{O}_{10}$  ( $\text{Ln} = \text{La, Nd, Sm, and Gd}$ ). *J. Solid State Chem.* **1996**, *121*, 430–436.
- (94) Toda, K.; Kameo, Y.; Kurita, S.; Sato, M. Crystal Structure Determination and Ionic Conductivity of Layered Perovskite Compounds  $\text{NaLnTiO}_4$  ( $\text{Ln} = \text{Rare Earth}$ ). *J. Alloys Compd.* **1996**, *234*, 19–25.
- (95) Toda, K.; Kurita, S.; Sato, M. New Layered Perovskite Compounds,  $\text{LiLaTiO}_4$  and  $\text{LiEuTiO}_4$ . *J. Ceram. Soc. Japan* **1996**, *104* (2), 140–142.
- (96) Thangadurai, V.; Shukla, A.; Gopalakrishnan, J.; Joubert, O.; Brohan, L.; Tournoux, M. X-Ray Powder Diffraction Study of  $\text{LiLnTiO}_4$  ( $\text{Ln} = \text{La, Nd}$ ): A Lithium-Ion Conductor. *Mater. Sci. Forum* **2000**, *321–324*, 965–970.
- (97) Thangadurai, V.; Weppner, W.  $\text{AA}'_2\text{M}_3\text{O}_{10}$  ( $\text{A} = \text{K, Rb, Cs; A}' = \text{Ca; M} = \text{Nb}$ ) Layered Perovskites: Low-Temperature Proton Conductors in Hydrogen Atmospheres. *J.*

*Mater. Chem.* **2001**, *11*, 636–639.

- (98) Schaak, R. E.; Mallouk, T. E. Topochemical Synthesis of Three-Dimensional Perovskites from Lamellar Precursors. *J. Am. Chem. Soc.* **2000**, *122*, 2798–2803.
- (99) Mahler, C. H.; Cushing, B. L.; Lalena, J. N.; Wiley, J. B. Divalent Ion Exchange of Alkaline-Earth Cations into the Triple-Layered Perovskite  $\text{RbCa}_2\text{Nb}_3\text{O}_{10}$ . *Mater. Res. Bull.* **1998**, *33* (11), 1581–1586.
- (100) Cushing, B. L.; Wiley, J. B. A Two-Step Ion Exchange Route To The New Metastable Double-Layered Perovskite,  $(\text{Rb,Na})_{1-x}\text{Ca}_{x/2}\text{LaNb}_2\text{O}_7$  ( $x \approx 0.9$ ). *Mater. Res. Bull.* **1999**, *34* (2), 271–278.
- (101) Jacobson, A. J.; Johnson, J. W.; Lewandowski, J. T. Interlayer Chemistry between Thick Transition-Metal Oxide Layers: Synthesis and Intercalation Reactions of  $\text{K}[\text{Ca}_2\text{Na}_{n-3}\text{Nb}_n\text{O}_{3n+1}]$  ( $3 \leq n \leq 7$ ). *Inorg. Chem.* **1985**, *24*, 3727–3729.
- (102) Treacy, M. M. J.; Rice, S. B.; Jacobson, A. J.; Lewandowski, J. T. Electron Microscopy Study of Delamination in Dispersions of the Perovskite-Related Layered Phases  $\text{K}[\text{Ca}_2\text{Na}_{n-3}\text{Nb}_n\text{O}_{3n+1}]$ : Evidence for Single-Layer Formation. *Chem. Mater.* **1990**, *2*, 279–286.
- (103) Uma, S.; Gopalakrishnan, J. Synthesis of Anion-Deficient Layered Perovskites,  $\text{ACa}_2\text{Nb}_{3-x}\text{M}_x\text{O}_{10-x}$  ( $\text{A} = \text{Rb}, \text{Cs}$ ;  $\text{M} = \text{Al}, \text{Fe}$ ), Exhibiting Ion-Exchange and Intercalation. Evidence for the Formation of Layered Brownmillerites,  $\text{ACa}_2\text{Nb}_2\text{AlO}_9$  ( $\text{A} = \text{Cs}, \text{H}$ ). *Chem. Mater.* **1994**, *6*, 907–912.
- (104) G., L. Interaction of Alkylamines with Different Types of Layered Compounds. *Solid State Ionics* **1986**, *22*, 43–51.
- (105) Hong, Y. S.; Kim, S. J.; Kim, S. J.; Choy, J. H. B-Site Cation Arrangement and Crystal Structure of Layered Perovskite Compounds  $\text{CsLn}_2\text{Ti}_2\text{NbO}_{10}$  ( $\text{Ln} = \text{La}, \text{Pr}, \text{Nd}, \text{Sm}$ ) and  $\text{CsCaLaTiNb}_2\text{O}_{10}$ . *J. Mater. Chem.* **2000**, *10*, 1209–1214.
- (106) Bhuvanesh, N. S. P.; Gopalakrishnan, J. Synthesis of Rutile-Related Oxides,  $\text{LiMMoO}_6$  ( $\text{M} = \text{Nb}, \text{Ta}$ ), and Their Proton Derivatives. Intercalation Chemistry of Novel Bronsted Acids,  $\text{HMMoO}_6 \cdot \text{H}_2\text{O}$ . *Inorg. Chem.* **1995**, *34*, 3760–3764.
- (107) Kinomura, N.; Kumada, N. Intercalation of Weak Lewis Bases into  $\text{HTaWO}_6 \cdot n\text{H}_2\text{O}$ . *Solid State Ionics* **1992**, *51*, 1–5.
- (108) Matsuda, T.; Miyamae, N.; Takeuchi, M. Intercalation of Various Alcohols in  $\text{HLaNb}_2\text{O}_7$ . *Bull. Chem. Soc. Jpn.* **1993**, *66*, 1551–1553.
- (109) Takahashi, S.; Nakato, T.; Hayashi, S.; Sugahara, Y.; Kuroda, K. Formation of a Methoxy-Modified Interlayer Surface via the Reaction between Methanol and Layered Perovskite  $\text{HLaNb}_2\text{O}_7 \cdot x\text{H}_2\text{O}$ . *Inorg. Chem.* **1995**, *34*, 5065–5069.
- (110) Kodenkandath, T. A.; Lalena, J. N.; Zhou, W. L.; Carpenter, E. E.; Sangregorio, C.; Falster, A. U.; Simmons, W. B.; O'Connor, C. J.; Wiley, J. B. Assembly of Metal-Anion Arrays within a Perovskite Host. Low-Temperature Synthesis of New Layered

- Copper-Oxyhalides,  $(\text{CuX})\text{LaNb}_2\text{O}_7$ ,  $\text{X} = \text{Cl, Br}$ . *J. Am. Chem. Soc.* **1999**, *121*, 10743–10746.
- (111) Porob, D. G.; Maggard, P. A. A Rapid Flux-Assisted Synthetic Approach towards the Bandgap Engineering of Layered Perovskites. *Chem. Mater.* **2007**, *19*, 970–972.
- (112) Ruddlesden, S. N.; Popper, P. New Compounds of the  $\text{K}_2\text{NiF}_4$  Type. *Acta Cryst.* **1957**, *10*, 538–539.
- (113) Ruddlesden, S. N.; Popper, P. The Compound  $\text{Sr}_3\text{Ti}_2\text{O}_7$  and Its Structure. *Acta Cryst.* **1958**, *11*, 54–55.
- (114) Toda, K. Synthesis and Ionic Conductivity of New Layered Perovskite Compound,  $\text{Ag}_2\text{La}_2\text{Ti}_3\text{O}_{10}$ . *Solid State Ionics* **1996**, *90*, 15–19.
- (115) Toda, K.; Watanabe, J.; Sato, M. Crystal Structure Determination of Ion-Exchangeable Layered Perovskite Compounds,  $\text{K}_2\text{La}_2\text{Ti}_3\text{O}_{10}$  and  $\text{Li}_2\text{La}_2\text{Ti}_5\text{O}_{10}$ . *Mater. Res. Bull.* **1996**, *31* (11), 1427–1435.
- (116) Schaak, R. E.; Afzal, D.; Schottenfeld, J. A.; Mallouk, T. E.  $\text{Na}_2\text{Ln}_2\text{Ti}_{3-x}\text{Mn}_x\text{O}_{10}$  ( $\text{Ln} = \text{Sm, Eu, Gd, and Dy}$ ;  $0 \leq x \leq 1$ ): A New Series of Ion-Exchangeable Layered Perovskites Containing B-Site Manganese. *Chem. Mater.* **2002**, *14*, 442–448.
- (117) Gopalakrishnan, J.; Sivakumar, T.; Ramesha, K.; Thangadurai, V.; Subbanna, G. N. Transformations of Ruddlesden - Popper Oxides to New Layered Perovskite Oxides by Metathesis Reactions. *J. Am. Chem. Soc.* **2000**, *122*, 6237–6241.
- (118) Richard, M.; Brohan, L.; Tournoux, M. Synthesis, Characterization, and Acid Exchange of the Layered Perovskites:  $\text{A}_2\text{Nd}_2\text{Ti}_3\text{O}_{10}$  ( $\text{A} = \text{Na, K}$ ). *J. Solid State Chem.* **1994**, *112*, 345–354.
- (119) Schaak, R. E.; Mallouk, T. E. Synthesis, Proton Exchange, and Topochemical Dehydration of New Ruddlesden-Popper Tantalates and Titanotantalates. *J. Solid State Chem.* **2000**, *155*, 46–54.
- (120) Bhuvanesh, N. S. P.; Crosnier-Lopez, M. P.; Duroy, H.; Fourquet, J.-L. Synthesis, Characterization and Dehydration Study of  $\text{H}_2\text{A}_{0.5n}\text{B}_n\text{O}_{3n+1} \cdot x\text{H}_2\text{O}$  ( $n = 2$  and  $3$ ,  $\text{A} = \text{Ca, Sr}$  and  $\text{B} = \text{Nb, Ta}$ ) Compounds Obtained by Ion-Exchange from the Layered  $\text{Li}_2\text{A}_{0.5n}\text{B}_n\text{O}_{3n+1}$  Perovskite Materials. *J. Mater. Chem.* **2000**, *10*, 1685–1692.
- (121) Neiner, D.; Spinu, L.; Golub, V.; Wiley, J. B. Ferromagnetism in Topochemically Prepared Layered Perovskite  $\text{Li}_{0.3}\text{Ni}_{0.85}\text{La}_2\text{Ti}_3\text{O}_{10}$ . *Chem. Mater.* **2006**, *18*, 518–524.
- (122) Gustin, L.; Hosaka, Y.; Tassel, C.; Aharen, T.; Shimakawa, Y.; Kageyama, H.; Wiley, J. B. From Tetrahedral to Octahedral Iron Coordination: Layer Compression in Topochemically Prepared  $\text{FeLa}_2\text{Ti}_3\text{O}_{10}$ . *Inorg. Chem.* **2016**, *55*, 11529–11537.
- (123) Bhuvanesh, N. S. P.; Woodward, P. M. Thermally Induced A' - A Site Exchange in Novel Layered Perovskites  $\text{Ag}_2[\text{Ca}_{1.5}\text{M}_3\text{O}_{10}]$  ( $\text{M} = \text{Nb, Ta}$ ). *J. Am. Chem. Soc.* **2002**, *124*, 14294–14295.



- (124) Cushing, B. L.; Falster, A. U.; Simmons, W. B.; Wiley, J. B. A Multivalent Ion Exchange Route to Lamellar Calcium Cobalt Oxides,  $\text{Ca}_x\text{CoO}_2$  ( $x \leq 0.5$ ). *Chem. Commun.*, **1996**, 2635–2636.
- (125) Patino, M. A.; Smith, T.; Zhang, W.; Halasyamani, P. S.; Hayward, M. A. Cation Exchange in a 3D Perovskite-Synthesis of  $\text{Ni}_{0.5}\text{TaO}_3$ . *Inorg. Chem.* **2014**, *53*, 8020–8024.
- (126) Pralong, V.; Reddy, M. A.; Caignaert, V.; Malo, S.; Lebedev, O. I.; Vardaraju, U.V.; Raveau, B. A New Form of  $\text{LiNbO}_3$  with a Lamellar Structure Showing Reversible Lithium Intercalation. *Chem. Mater.* **2011**, *23*, 1915–1922.
- (127) Kumar, V.; Gupta, A.; Uma, S. Formation of Honeycomb Ordered Monoclinic  $\text{Li}_2\text{M}_2\text{TeO}_6$  ( $\text{M} = \text{Cu}, \text{Ni}$ ) and Disordered Orthorhombic  $\text{Li}_2\text{Ni}_2\text{TeO}_6$  Oxides. *Dalt. Trans.* **2013**, *42*, 14992–14998.
- (128) Mitsuyama, T.; Tsutsumi, A.; Sato, S.; Ikeue, K.; Machida, M. Relationship between Interlayer Hydration and Photocatalytic Water Splitting of  $A'_{1-x}\text{Na}_x\text{Ca}_2\text{Ta}_3\text{O}_{10} \cdot n\text{H}_2\text{O}$  ( $A' = \text{K}$  and  $\text{Li}$ ). *J. Solid State Chem.* **2008**, *181*, 1419–1424.
- (129) Sugimoto, W.; Shirata, M.; Sugahara, Y.; Kuroda, K. New Conversion Reaction of an Aurivillius Phase into the Protonated Form of the Layered Perovskite by the Selective Leaching of the Bismuth Oxide Sheet. *J. Am. Chem. Soc.* **1999**, *121*, 11601–11602.
- (130) Tsunoda, Y.; Shirata, M.; Sugimoto, W.; Liu, Z.; Terasaki, O.; Kuroda, K.; Sugahara, Y. Preparation and HREM Characterization of a Protonated Form of a Layered Perovskite Tantalate from an Aurivillius Phase  $\text{Bi}_2\text{SrTa}_2\text{O}_9$  via Acid Treatment. *Inorg. Chem.* **2001**, *40*, 5768–5771.
- (131) Izawa, H.; Kikkawa, S.; Koizumi, M. Ion Exchange and Dehydration of Layered Titanates,  $\text{Na}_2\text{Ti}_3\text{O}_7$  and  $\text{K}_2\text{Ti}_4\text{O}_9$ . *J. Phys. Chem.* **1982**, *86*, 5023–5026.
- (132) Sugimoto, W.; Iwata, H.; Yasunaga, Y.; Murakami, Y.; Takasu, Y. Preparation of Ruthenic Acid Nanosheets and Utilization of Its Interlayer Surface for Electrochemical Energy Storage. *Angew. Chemie - Int. Ed.* **2003**, *42*, 4092–4096.
- (133) Weber, D.; Schoop, L. M.; Wurmbrand, D.; Nuss, J.; Seibel, E. M.; Tafti, F. F.; Ji, H.; Cava, R. J.; Dinnebier, R. E.; Lotsch, B. V. Trivalent Iridium Oxides: Layered Triangular Lattice Iridate  $\text{K}_{0.75}\text{Na}_{0.25}\text{IrO}_2$  and Oxyhydroxide  $\text{IrOOH}$ . *Chem. Mater.* **2017**, *29*, 8338–8345.
- (134) Yohannan, J. P.; Vidyasagarvidya, K. Syntheses, Structural Variants and Characterization of  $\text{AInM}'\text{S}_4$  ( $\text{A} = \text{alkali metals, Tl}$ ;  $\text{M}' = \text{Ge, Sn}$ ) Compounds; Facile Ion-Exchange Reactions of Layered  $\text{NaInSnS}_4$  and  $\text{KInSnS}_4$  Compounds. *J. Solid State Chem.* **2016**, *238*, 291–302.
- (135) Walko, P. S.; Paidi, A. K.; Vidyasagar, K. Syntheses and Structural Characterization of  $\text{A}_3\text{Sb}_3\text{P}_2\text{O}_{14} \cdot 3\text{H}_2\text{O}$  ( $\text{A} = \text{Rb, Cs, Tl}$  and  $\text{NH}_4$ ) Phosphates; Facile Aqueous Ion Exchange Reactions of  $\text{K}_3\text{Sb}_3\text{P}_2\text{O}_{14} \cdot 3\text{H}_2\text{O}$ . *Chemistry Select* **2017**, *2*, 11875–11879.
- (136) Cava, R. J.; Santoro, A.; Murphy, D. W.; Zahurak, S.; Roth, R. S. The Structures of

- Lithium-Inserted Metal Oxides:  $\text{LiReO}_3$  and  $\text{Li}_2\text{ReO}_3$ . *J. Solid State Chem.* **1982**, *42*, 251–262.
- (137) Gómez-Romero, P.; Palacín, M. R.; Casañ, N.; Fuertes, A. Synthesis of a Reduced Niobium “Blue” with a Layered Perovskite Structure. *Solid State Ionics* **1993**, *63–65*, 424–428.
- (138) Sato, M.; Jin, T.; Ueda, H. Structural Change in Lithium Intercalation of Layered Perovskite  $\text{LiLaNb}_2\text{O}_7$ . *Chem. Lett.* **1994**, 161–164.
- (139) Palacín, M. R.; Lira, M.; García, J. L.; Caldés, M. T.; Casafi-Pastor, N.; Fuertes, A.; Gómez-Romero, P. Synthesis Deintercalation And Transport Properties of a Mixed-Valence Derivative of the Layered Oxide  $\text{HLaNb}_2\text{O}_7$ . *Mater. Res. Bull.* **1996**, *31* (2), 217–225.
- (140) Bohnke, C.; Bohnke, O.; Fourquet, J. L. Electrochemical Intercalation of Lithium into  $\text{LiLaNb}_2\text{O}_7$  Perovskite. *J. Electrochem. Soc.* **1997**, *144* (4), 1151–1158.
- (141) Toda, K.; Takahashi, M.; Teranishi, T.; Ye, Z.-G; Sato, M.; Hinatsu, Y. Synthesis and Structure Determination of Reduced Tantalates,  $\text{Li}_2\text{LaTa}_2\text{O}_7$ ,  $\text{Li}_2\text{Ca}_2\text{Ta}_3\text{O}_{10}$  and  $\text{Na}_2\text{Ca}_2\text{Ta}_3\text{O}_{10}$ , with a Layered Perovskite Structure. *J. Mater. Chem.* **1999**, *9*, 799–803.
- (142) Byeon, S. H.; Kim, H. J.; Kim, D. K.; Hur, N. H. Synthesis, Structure, Magnetic Properties, and XANES Spectra of Reduced Niobate  $\text{RbNa}_x\text{Ca}_2\text{Nb}_3\text{O}_{10}$ . *Chem. Mater.* **2003**, *15*, 383–389.
- (143) Takano, Y.; Takayanagi, S.; Ogawa, S.; Yamadaya, T.; Mōri, N. Superconducting Properties of Layered Perovskite  $\text{KCa}_2\text{Nb}_3\text{O}_{10}$  and  $\text{KLaNb}_2\text{O}_7$ . *Solid State Commun.* **1997**, *103* (4), 215–217.
- (144) Nagai, I.; Abe, Y.; Kato, M.; Koike, Y.; Kakihana, M. Electrochemical Intercalation of Lithium in Layered Niobates  $\text{AB}_2\text{Nb}_3\text{O}_{10}$  ( $A = \text{K, Rb, Cs}$ ;  $B = \text{Ca, Sr}$ ) and Their Superconductivity. *Phys. C* **2001**, *357–360*, 393–396.
- (145) Kato, M.; Inoue, A.; Nagai, I.; Kakihana, M.; Sleight, A. W.; Koike, Y. Superconductivity in the Electrochemically Li-Intercalated Niobates with the Layered Perovskite Structure. *Phys. C* **2003**, *388–389*, 445–446.
- (146) McIntyre, R. A.; Falster, A. U.; Li, S.; Simmons, J.; O’Connor, C. J.; Wiley, J. B. Opening a Perovskite to Valence Manipulation: Two-Step Topotactic Route to a New Mixed-Valence Titanate,  $\text{Na}_{1-x+y}\text{Ca}_{x/2}\text{LaTiO}_4$ . *J. Am. Chem. Soc.* **1998**, *120*, 217–218.
- (147) Lalena, J. N.; Cushing, B. L.; Falster, A. U.; Simmons, W. B.; Seip, C. T.; Carpenter, E. E.; O’Connor, C. J.; Wiley, J. B. A Multistep Topotactic Route to the New Mixed-Valence Titanate,  $\text{Na}_{2-x+y}\text{Ca}_{x/2}\text{La}_2\text{Ti}_3\text{O}_{10}$ . Electron Localization Effects in a Triple-Layered Perovskite. *Inorg. Chem.* **1998**, *37*, 4484–4485.
- (148) Choy, J. H.; Kim, J. Y.; Chung, I. Neutron Diffraction and X-Ray Absorption Spectroscopic Analyses for Lithiated Aurivillius-Type Layered Perovskite Oxide,  $\text{Li}_2\text{Bi}_4\text{Ti}_3\text{O}_{12}$ . *J. Phys. Chem. B* **2001**, *105*, 7908–7912.



- (149) Chevallier, V.; Nihoul, G.; Madigou, V. Exfoliated Nanoplatelets of an Aurivillius Phase,  $\text{Bi}_{3.25}\text{La}_{0.75}\text{Ti}_3\text{O}_{12}$ : Characterisation by X-Ray Diffraction and by High-Resolution Electron Microscopy. *J. Solid State Chem.* **2008**, *181* (3), 439–449.
- (150) Longoria Rodríguez, F. E.; Martínez-de La Cruz, A. Electrochemical Study of the Reaction of Lithium with Aurivillius and Related Phases. *Mater. Res. Bull.* **2001**, *36* (7–8), 1195–1204.
- (151) Martínez-de la Cruz, A.; Longoria Rodríguez, F. E. Electrochemical Lithium Insertion in the Solid Solution  $\text{Bi}_2\text{WO}_6$ - $\text{Sb}_2\text{WO}_6$  with Aurivillius Framework. *Mater. Res. Bull.* **2007**, *42* (10), 1851–1855.
- (152) Hyett, G.; Rutt, O. J.; Gál, Z. A.; Denis, S. G.; Hayward, M. A.; Clarke, S. J. Electronically Driven Structural Distortions in Lithium Intercalates of the  $n = 2$  Ruddlesden-Popper-Type Host  $\text{Y}_2\text{Ti}_2\text{O}_5\text{S}_2$ : Synthesis, Structure, and Properties of  $\text{Li}_x\text{Y}_2\text{Ti}_2\text{O}_5\text{S}_2$  ( $0 < x < 2$ ). *J. Am. Chem. Soc.* **2004**, *126* (7), 1980–1991.
- (153) Rutt, O. J.; Hill, T. L.; L, Z. A. G.; Hayward, M. A.; Clarke, S. J. The Cation-Deficient Ruddlesden-Popper Oxysulfide  $\text{Y}_2\text{Ti}_2\text{O}_5\text{S}_2$  as a Layered Sulfide: Topotactic Potassium Intercalation To Form  $\text{KY}_2\text{Ti}_2\text{O}_5\text{S}_2$ . *Inorg. Chem.* **2003**, *42*, 7906–7911.
- (154) Denis, S. G.; Clarke, S. J. Two Alternative Products from the Intercalation of Alkali Metals into Cation-Defective Ruddlesden-Popper Oxysulfides. *Chem. Commun.* **2001**, *312*, 2356–2357.
- (155) Clarke, S. J.; Denis, S. G.; Rutt, O. J.; Hill, T. L.; Hayward, M. A.; Hyett, G.; Gál, Z. A. Sodium Intercalation into the  $n = 2$  Ruddlesden-Popper Type Host  $\text{Y}_2\text{Ti}_2\text{O}_5\text{S}_2$ : Synthesis, Structure, and Properties of  $\alpha$ - $\text{Na}_x\text{Y}_2\text{Ti}_2\text{O}_5\text{S}_2$  ( $0 < x \leq 1$ ). *Chem. Mater.* **2003**, *15* (26), 5065–5072.
- (156) Rutt, O. J.; Williams, G. R.; Clarke, S. J. Reversible Lithium Insertion and Copper Extrusion in Layered Oxysulfides. *Chem. Commun.* **2006**, *88*, 2869–2871.
- (157) Indris, S.; Cabana, J.; Rutt, O. J.; Clarke, S. J.; Grey, C. P. Layered Oxysulfides  $\text{Sr}_2\text{MnO}_2\text{Cu}_{2m-0.5}\text{S}_{m+1}$  ( $m = 1, 2, \text{ and } 3$ ) as Insertion Hosts for Li Ion Batteries. *J. Am. Chem. Soc.* **2006**, *128*, 13354–13355.
- (158) Slater, P. R.; Hodges, J. P.; Francesconi, M. G.; Greaves, C.; Slaski, M. Fluorination of the Ruddlesden-Popper Type Cuprates,  $\text{Ln}_{2-x}\text{A}_{1+x}\text{Cu}_2\text{O}_{6-y}$  ( $\text{Ln} = \text{La, Nd}$ ;  $\text{A} = \text{Ca, Sr}$ ). *J. Mater. Chem.* **1997**, *7* (10), 2077–2083.
- (159) Greaves, C.; Kissick, J. L.; Francesconi, M. G.; Aikens, L. D.; Gillie, L. J. Synthetic Strategies for New Inorganic Oxide Fluorides and Oxide Sulfates. *J. Mater. Chem.* **1999**, *9*, 111–116.
- (160) Kirbyshire, A. L.; Greaves, C.  $\text{PbY}_{1-x}\text{Ca}_x\text{Ba}_2\text{Cu}_3\text{O}_7\text{F}_2$ : Synthesis, Structure and Superconductivity. *Supercond. Sci. Technol.* **2004**, *17*, 963–970.
- (161) Aikens, L. D.; Gillie, L. J.; Li, R. K.; Greaves, C. Staged Fluorine Insertion into Manganese Oxides with Ruddlesden-Popper Structures:  $\text{LaSrMnO}_4\text{F}$  and  $\text{La}_{1.2}\text{Sr}_{1.8}\text{Mn}_2\text{O}_7\text{F}$ . *J. Mater. Chem.* **2002**, *12*, 264–267.

- (162) Li, R. K.; Greaves, C. Double-Layered Ruthenate  $\text{Sr}_3\text{Ru}_2\text{O}_7\text{F}_2$  Formed by Fluorine Insertion into  $\text{Sr}_3\text{Ru}_2\text{O}_7$ . *Phys. Rev. B* **2000**, *62* (6), 3811–3813.
- (163) Corbel, G.; Attfield, J. P.; Hadermann, J.; Abakumov, A. M.; Alekseeva, A. M.; Rozova, M. G.; Antipov, E. V. Anion Rearrangements in Fluorinated  $\text{Nd}_2\text{CuO}_{3.5}$ . *Chem. Mater.* **2003**, *15*, 189–195.
- (164) Pederzoli, D. R.; Attfield, J. P.  $\text{Nd}_4\text{Cu}_2\text{O}_7$ : A Copper(I) Oxide with a Novel Cooperatively Distorted T' Type Structure. *J. Solid State Chem.* **1998**, *136*, 137–140.
- (165) Cava, R. J.; Zandbergen, H. W.; Krajewski, J. J.; Peck, W. F.; Batlogg, B.; Carter, S.; Fleming, R. M.; Zhou, O.; Rupp, L. W.  $\text{Sr}_2\text{RuO}_4 \cdot 0.25\text{CO}_2$  and the Synthesis and Elementary Properties of  $\text{Sr}_3\text{Ru}_2\text{O}_7$ . *J. Solid State Chem.* **1995**, *116*, 141–145.
- (166) Cao, G.; McCall, S.; Crow, J. E. Observation of Itinerant Ferromagnetism in Layered  $\text{Sr}_3\text{Ru}_2\text{O}_7$  Single Crystals. *Phys. Rev. B* **1997**, *55* (2), R672–R675.
- (167) Al-Mamouri, M.; Edwards, P. P.; Greaves, C.; Slaski, M. Synthesis and Superconducting Properties of the Strontium Copper Oxy-Fluoride  $\text{Sr}_2\text{CuO}_2\text{F}_{2+\delta}$ . *Nature* **1994**, *369*, 382–384.
- (168) Slater, P. R.; Edwards, P. P.; Greaves, C.; Gameson, I.; Francesconi, M. G.; Hodges, J. P.; Al-Mamouri, M.; Slaski, M. Superconductivity up to 64 K in the Copper Oxyfluorides  $\text{Sr}_{2-x}\text{A}_x\text{CuO}_2\text{F}_{2+\delta}$  (A = Ca, Ba) Prepared Using  $\text{NH}_4\text{F}$  as a Fluorinating Reagent. *Phys. C* **1995**, *241*, 151–157.
- (169) Al-Mamouri, M.; Edwards, P. P.; Greaves, C.; Slater, P. R.; Slaski, M. Synthesis and Structure of the Calcium Copper Oxyfluoride,  $\text{Ca}_2\text{CuO}_2\text{F}_{2+\delta}$ . *J. Mater. Chem.* **1995**, *5* (6), 913–916.
- (170) McCabe, E. E.; Greaves, C. Fluorine Insertion Reactions into Pre-Formed Metal Oxides. *J. Fluor. Chem.* **2007**, *128*, 448–458.
- (171) Sivakumar, T.; Wiley, J. B. Topotactic Route for New Layered Perovskite Oxides Containing Fluorine:  $\text{Ln}_{1.2}\text{Sr}_{1.8}\text{Mn}_2\text{O}_7\text{F}_2$  (Ln = Pr, Nd, Sm, Eu, and Gd). *Mater. Res. Bull.* **2009**, *44*, 74–77.
- (172) Xiang, X.-D.; McKernan, S.; Vareka, W. A.; Zettl, A.; Corkill, J. L.; III, T. W. B.; Cohen, M. L. Iodine Intercalation of a High-Temperature Superconducting Oxide. *Nature* **1990**, *348*, 145–147.
- (173) Hwang, S.-J.; Park, N.-G.; Kim, D.-H.; Choy, J.-H. Charge Transfer– $T_c$  Relation in the Superconducting Intercalates  $\text{IBi}_2\text{Sr}_2\text{CaCu}_2\text{O}_y$ . *J. Solid State Chem.* **1998**, *138*, 66–73.
- (174) Hyett, G.; Barrier, N.; Clarke, S. J.; Hadermann, J. Topotactic Oxidative and Reductive Control of the Structures and Properties of Layered Manganese Oxychalcogenides. *J. Am. Chem. Soc.* **2007**, *129*, 11192–11201.
- (175) Romero, F. D.; Bingham, P. A.; Forder, S. D.; Hayward, M. A. Topochemical Fluorination of  $\text{Sr}_3(\text{M}_{0.5}\text{Ru}_{0.5})_2\text{O}_7$  (M = Ti, Mn, Fe),  $n = 2$ , Ruddlesden–Popper Phases. *Inorg. Chem.* **2013**, *52*, 3388–3398.

- (176) Zhang, R.; Read, G.; Lang, F.; Lancaster, T.; Blundell, S. J.; Hayward, M. A.  $\text{La}_2\text{SrCr}_2\text{O}_7\text{F}_2$ : A Ruddlesden–Popper Oxyfluoride Containing Octahedrally Coordinated  $\text{Cr}^{4+}$  Centers. *Inorg. Chem.* **2016**, *55*, 3169–3174.
- (177) Toda, K.; Uematsu, K.; Sato, M. Structure Determination of New Layered Perovskite Compound,  $\text{NaLaTa}_2\text{O}_7$ , Synthesized by Ion-Exchange Reaction. *J. Ceram. Soc. Japan* **1997**, *105* (6), 482–485.
- (178) Toda, K.; Kameo, Y.; Kurita, S.; Sato, M. Intercalation of Water in a Layered Perovskite Compound,  $\text{NaEuTiO}_4$ . *Bull. Chem. Soc. Jpn.* **1996**, *69*, 349–352.
- (179) Crosnier-Lopez, M. P.; Berre, F. Le; Fourquet, J. L. Synthesis and Crystal Structure of Two New Layered Perovskite Phases  $\text{K}_2\text{La}_{2/3}\text{Ta}_2\text{O}_7$  and  $\text{Li}_2\text{La}_{2/3}\text{Ta}_2\text{O}_7$ . *Z. Anorg. Allg. Chem.* **2002**, *628* (2049–2056).
- (180) Hong, Y.-S.; Han, C.-H.; Kim, K. Structural Characterization of New Layered Perovskites  $M\text{La}_2\text{Ti}_2\text{TaO}_{10}$  ( $M = \text{Cs}, \text{Rb}$ ) and  $\text{NaLa}_2\text{Ti}_2\text{TaO}_{10} \cdot x\text{H}_2\text{O}$  ( $x = 2, 0.9, 0$ ). *J. Solid State Chem.* **2001**, *158* (2), 290–298.
- (181) Kodenkandath, T. A.; Wiley, J. B. Synthesis and Structure of a Double-Layered Perovskite and Its Hydrate,  $\text{K}_2\text{SrTa}_2\text{O}_7 \cdot m\text{H}_2\text{O}$  ( $m = 0, 2$ ). *Mat. Res. Bull.* **2000**, *35*, 1737–1742.
- (182) Crosnier-Lopez, M.-P.; Berre, F. L.; Fourquet, J.-L. The Layered Perovskite  $\text{K}_2\text{SrTa}_2\text{O}_7$ : Hydration and  $\text{K}^+/\text{H}^+$  Ion Exchange. *J. Mater. Chem.* **2001**, *11* (4), 1146–1151.
- (183) Uma, S.; Gopalakrishnan, J. Polymerization of Aniline in Layered Perovskites. *Mater. Sci. Eng. B* **1995**, *34*, 175–179.
- (184) Wang, B.; Dong, X.; Pan, Q.; Cheng, Z.; Yang, Y. Intercalation Behavior of *n*-Alkylamines into an A-Site Defective Layered Perovskite  $\text{H}_2\text{W}_2\text{O}_7$ . *J. Solid State Chem.* **2007**, *180*, 1125–1129.
- (185) Chen, D.; Sugahara, Y. Tungstate-Based Inorganic-Organic Hybrid Nanobelts/Nanotubes with Lamellar Mesosstructures: Synthesis, Characterization, and Formation Mechanism. *Chem. Mater.* **2007**, *19*, 1808–1815.
- (186) Tahara, S.; Ichikawa, T.; Kajiwara, G.; Sugahara, Y. Reactivity of the Ruddlesden–Popper Phase  $\text{H}_2\text{La}_2\text{Ti}_3\text{O}_{10}$  with Organic Compounds: Intercalation and Grafting Reactions. *Chem. Mater.* **2007**, *19*, 2352–2358.
- (187) Rose, K. Facile Synthesis of Homogeneous Artificial Proteins. *J. Am. Chem. Soc.* **1994**, *116*, 30–33.
- (188) Choy, J. H.; Hwang, S. J.; Park, N. G. Intracrystalline Structure of Molecular Mercury Halide Intercalated in High- $T_c$  Superconducting Lattice of  $\text{Bi}_2\text{Sr}_2\text{CaCu}_2\text{O}_y$ . *J. Am. Chem. Soc.* **1997**, *119*, 1624–1633.
- (189) Hayward, M. A.; Green, M. A.; Rosseinsky, M. J.; Sloan, J. Sodium Hydride as a Powerful Reducing Agent for Topotactic Oxide Deintercalation: Synthesis and

- Characterization of the Nickel(I) Oxide  $\text{LaNiO}_2$ . *J. Am. Chem. Soc.* **1999**, *121*, 8843–8854.
- (190) Poltavets, V. V.; Lokshin, K. A.; Dikmen, S.; Croft, M.; Egami, T.; Greenblatt, M.  $\text{La}_3\text{Ni}_2\text{O}_6$ : A New Double T'-Type Nickelate with Infinite  $\text{Ni}^{1+/2+}\text{O}_2$  Layers. *J. Am. Chem. Soc.* **2006**, *128*, 9050–9051.
- (191) Poltavets, V. V.; Lokshin, K. A.; Croft, M.; Mandal, T. K.; Egami, T.; Greenblatt, M. Crystal Structures of  $\text{Ln}_4\text{Ni}_3\text{O}_8$  (Ln = La, Nd) Triple Layer T'-Type Nickelates. *Inorg. Chem.* **2007**, *46*, 10887–10891.
- (192) Tsujimoto, Y.; Tassel, C.; Hayashi, N.; Watanabe, T.; Kageyama, H.; Yoshimura, K.; Takano, M.; Ceretti, M.; Ritter, C.; Paulus, W. Infinite-Layer Iron Oxide with a Square-Planar Coordination. *Nature* **2007**, *450*, 1062–1065.
- (193) Kageyama, H.; Watanabe, T.; Tsujimoto, Y.; Kitada, A.; Sumida, Y.; Kanamori, K.; Yoshimura, K.; Hayashi, N.; Muranaka, S.; Takano, M.; Ceretti, M.; Paulus, W.; Ritter, C.; André, G. Spin-Ladder Iron Oxide:  $\text{Sr}_3\text{Fe}_2\text{O}_5$ . *Angew. Chemie - Int. Ed.* **2008**, *47*, 5740–5745.
- (194) Tassel, C.; Pruneda, J. M.; Hayashi, N.; Watanabe, T.; Kitada, A.; Tsujimoto, Y.; Kageyama, H.; Yoshimura, K.; Takano, M.; Nishi, M.; Ohoyama, K.; Mizumaki, M.; Kawamura, N.; Íñiguez, J.; Canadell, E.  $\text{CaFeO}_2$ : A New Type of Layered Structure with Iron in a Distorted Square Planar Coordination. *J. Am. Chem. Soc.* **2009**, *131*, 221–229.
- (195) Hadermann, J.; Abakumov, A. M.; Adkin, J. J.; Hayward, M. A. Topotactic Reduction as a Route to New Close-Packed Anion Deficient Perovskites: Structure and Magnetism of  $4\text{H-BaMnO}_{2+x}$ . *J. Am. Chem. Soc.* **2009**, *131*, 10598–10604.
- (196) Adkin, J. J.; Hayward, M. A. Room Temperature Antiferromagnetic Order in the Mn(II) Oxide  $4\text{H-Ba}_{0.5}\text{Sr}_{0.5}\text{MnO}_{2+\delta}$ . *Inorg. Chem.* **2008**, *47*, 10959–10964.
- (197) Kudo, M.; Ohkawa, H.; Sugimoto, W.; Kumada, N.; Liu, Z.; Terasaki, O.; Sugahara, Y. A Layered Tungstic Acid  $\text{H}_2\text{W}_2\text{O}_7 \cdot n\text{H}_2\text{O}$  with a Double-Octahedral Sheet Structure: Conversion Process from an Aurivillius Phase  $\text{Bi}_2\text{W}_2\text{O}_9$  and Structural Characterization. *Inorg. Chem.* **2003**, *42*, 4479–4484.
- (198) Sugimoto, W.; Shirata, M.; Kuroda, K.; Sugahara, Y. Conversion of Aurivillius Phases  $\text{Bi}_2\text{ANa}\text{Nb}_3\text{O}_{12}$  (A = Sr or Ca) into the Protonated Forms of Layered Perovskite via Acid Treatment. *Chem. Mater.* **2002**, *14*, 2946–2952.
- (199) Tahara, S.; Shimada, A.; Kumada, N.; Sugahara, Y. Characterization of  $\text{Bi}_5\text{Nb}_3\text{O}_{15}$  by Refinement of Neutron Diffraction Pattern, Acid Treatment and Reaction of the Acid-Treated Product with *n*-Alkylamines. *J. Solid State Chem.* **2007**, *180*, 2517–2524.
- (200) Gönen, Z. S.; Paluchowski, D.; Zavalij, P.; Eichhorn, B. W.; Gopalakrishnan, J. Reversible Cation/Anion Extraction from  $\text{K}_2\text{La}_2\text{Ti}_3\text{O}_{10}$ : Formation of New Layered Titanates,  $\text{KLa}_2\text{Ti}_3\text{O}_{9.5}$  and  $\text{La}_2\text{Ti}_3\text{O}_9$ . *Inorg. Chem.* **2006**, *45*, 8736–8742.
- (201) Kodenkandath, T. A.; Kumbhar, A. S.; Zhou, W. L.; Wiley, J. B. Construction of



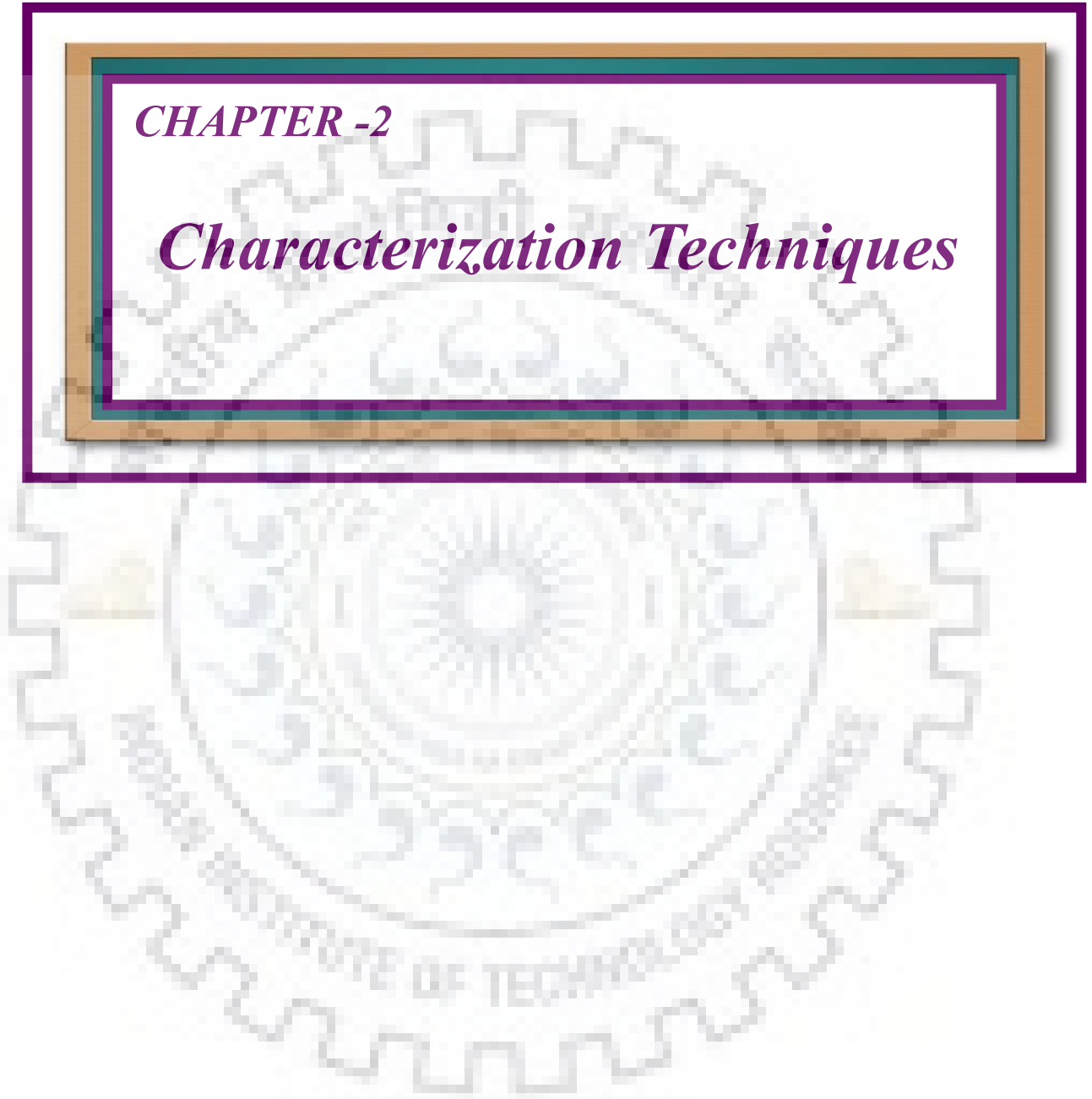
- Copper Halide Networks within Layered Perovskites. Syntheses and Characterization of New Low-Temperature Copper Oxyhalides. *Inorg. Chem.* **2001**, *40*, 710–714.
- (202) Kageyama, H.; Viciu, L.; Caruntu, G.; Ueda, Y.; Wiley, J. B. New Magnetic Materials Obtained by Ion-Exchange Reactions from Non-Magnetic Layered Perovskites. *J. Phys. Condens. Matter* **2004**, *16*, S585–S590.
- (203) Viciu, L.; Caruntu, G.; Royant, N.; Koenig, J.; Zhou, W. L.; Kodenkandath, T. A.; Wiley, J. B. Formation of Metal-Anion Arrays within Layered Perovskite Hosts. Preparation of a Series of New Metastable Transition-Metal Oxyhalides, (MCl)LaNb<sub>2</sub>O<sub>7</sub> (M = Cr, Mn, Fe, Co). *Inorg. Chem.* **2002**, *41*, 3385–3388.
- (204) Viciu, L.; Golub, V. O.; Wiley, J. B. Structural, Thermal and Magnetic Characterization of the Manganese Oxyhalide Layered Perovskite, (MnCl)LaNb<sub>2</sub>O<sub>7</sub>. *J. Solid State Chem.* **2003**, *175*, 88–93.
- (205) Viciu, L.; Koenig, J.; Spinu, L.; Zhou, W. L.; Wiley, J. B. Insertion of a Two-Dimensional Iron-Chloride Network between Perovskite Blocks. Synthesis and Characterization of the Layered Oxyhalide, (FeCl)LaNb<sub>2</sub>O<sub>7</sub>. *Chem. Mater.* **2003**, *15*, 1480–1485.
- (206) Caruntu, G.; Kodenkandath, T. A.; Wiley, J. B. Neutron Diffraction Study of the Oxychloride Layered Perovskite, (CuCl)LaNb<sub>2</sub>O<sub>7</sub>. *Mater. Res. Bull.* **2002**, *37*, 593–598.
- (207) Kageyama, H.; Kitano, T.; Oba, N.; Nishi, M.; Nagai, S.; Hirota, K.; Viciu, L.; Wiley, J. B.; Yasuda, J.; Baba, Y.; Ajiro, Y.; Yoshimura, K. Spin-Singlet Ground State in Two-Dimensional S = 1/2 Frustrated Square Lattice: (CuCl)LaNb<sub>2</sub>O<sub>7</sub>. *J. Phys. Soc. Japan* **2005**, *74* (6), 1702–1705.
- (208) Whangbo, M.-H.; Dadi, D. On the Disorder of the Cl Atom Position in and Its Probable Effect on the Magnetic Properties of (CuCl)LaNb<sub>2</sub>O<sub>7</sub>. *Inorg. Chem.* **2006**, *45*, 6227–6234.
- (209) Oba, N.; Kageyama, H.; Kitano, T.; Yasuda, J.; Baba, Y.; Nishi, M.; Hirota, K.; Narumi, Y.; Hagiwara, M.; Kindo, K.; Saito, T.; Ajiro, Y.; Yoshimura, K. Collinear Order in Frustrated Quantum Antiferromagnet on Square Lattice (CuBr)LaNb<sub>2</sub>O<sub>7</sub>. *J. Phys. Soc. Japan* **2006**, *75* (11), 113601–113605.
- (210) Tsujimoto, Y.; Baba, Y.; Oba, N.; Kageyama, H.; Fukui, T.; Narumi, Y.; Kindo, K.; Saito, T.; Takano, M.; Ajiro, Y.; Yoshimura, K. 1/3 Magnetization Plateau in Spin-1/2 Square Lattice Antiferromagnet (CuBr)Sr<sub>2</sub>Nb<sub>3</sub>O<sub>10</sub>. *J. Phys. Soc. Japan* **2007**, *76* (6), 063711.
- (211) Tsujimoto, Y.; Kageyama, H.; Baba, Y.; Kitada, A.; Yamamoto, T.; Narumi, Y.; Kindo, K.; Nishi, M.; Carlo, J. P.; Aczel, A. A.; Williams, T. J.; Goko, T.; Luke, G. M.; Uemura, Y. J.; Ueda, Y.; Ajiro, Y.; Yoshimura, K. Synthesis, Structure, and Magnetic Properties of the Two-Dimensional Quantum Antiferromagnets (CuBr)A<sub>2</sub>B<sub>3</sub>O<sub>10</sub> (A = Ca, Sr, Ba, Pb; B=Nb, Ta) with the 1/3 Magnetization Plateau. *Phys. Rev. B* **2008**, *78*, 214410.

- (212) Kitada, A.; Tsujimoto, Y.; Kageyama, H.; Ajiro, Y.; Nishi, M.; Narumi, Y.; Kindo, K.; Ichihara, M.; Ueda, Y.; Uemura, Y. J.; Yoshimura, K. Quantum Phase Transition in  $(\text{CuCl})\text{La}(\text{Nb}_{1-x}\text{Ta}_x)_2\text{O}_7$ . *Phys. Rev. B* **2009**, *80*, 174409.
- (213) Uemura, Y. J.; Aczel, A. A.; Ajiro, Y.; Carlo, J. P.; Goko, T.; Goldfeld, D. A.; Kitada, A.; Luke, G. M.; MacDougall, G. J.; Mihailescu, I. G.; Rodriguez, J. A.; Russo, P. L.; Tsujimoto, Y.; Wiebe, C. R.; Williams, T. J.; Yamamoto, T.; Yoshimura, K.; Kageyama, H. Muon Spin Relaxation Studies of the Frustrated Quasi-Two-Dimensional Square-Lattice Spin System  $\text{Cu}(\text{Cl},\text{Br})\text{La}(\text{Nb},\text{Ta})_2\text{O}_7$ : Evolution from Spin-Gap to Antiferromagnetic State. *Phys. Rev. B* **2009**, *80* (17), 174408.
- (214) Viciu, L.; Kodankandath, T. A.; Wiley, J. B. Construction of a Double-Layered Tetrahedral Network within a Perovskite Host: Two-Step Route to the Alkali-Metal-Halide Layered Perovskite,  $(\text{Li}_x\text{Cl})\text{LaNb}_2\text{O}_7$ . *J. Solid State Chem.* **2007**, *180*, 583–588.
- (215) Choi, J.; Zhang, X.; Wiley, J. B. Building Alkali-Metal-Halide Layers within a Perovskite Host by Sequential Intercalation:  $(\text{A}_2\text{Cl})\text{LaNb}_2\text{O}_7$  ( $\text{A} = \text{Rb}, \text{Cs}$ ). *Inorg. Chem.* **2009**, *48*, 4811–4816.
- (216) Montasserasadi, D.; Mohanty, D.; Huq, A.; Heroux, L.; Payzant, E. A.; Wiley, J. B. Topochemical Synthesis of Alkali-Metal Hydroxide Layers within Double- and Triple-Layered Perovskites. *Inorg. Chem.* **2014**, *53*, 1773–1778.
- (217) Montasserasadi, D.; Granier, M. W.; Spinu, L.; Rai, S. C.; Zhou, W.; Wiley, J. B. Synthesis and Characterization of the Rare-Earth Dion-Jacobson Layered Perovskites,  $\text{APrNb}_2\text{O}_7$  ( $\text{A} = \text{Rb}, \text{Cs}$  and  $\text{CuCl}$ ). *Dalt. Trans.* **2015**, *44*, 10654–10660.



*CHAPTER -2*

*Characterization Techniques*



## Characterization Techniques

All the synthesized precursor oxides with the trirutile, tri  $\alpha$ -PbO<sub>2</sub> oxide, ribbon-type layered and framework structures and their ion exchange products are being of intercalated with an array of state-of the art characterization techniques. The techniques include Powder X-ray diffraction (P-XRD), Field-emission scanning electron microscopy (FE-SEM), Energy dispersive X-ray spectroscopy (EDX), High resolution transmission electron microscopy (HR-TEM), Selected area electron diffraction (SAED), Inductively coupled plasma optical emission spectroscopy (ICP-OES), UV-visible diffuse reflectance spectroscopy (UV-vis DRS), Solid state nuclear magnetic resonance (ss-NMR) spectroscopy, X-ray photoelectron spectroscopy (XPS). Magnetic measurements of all the synthesized compounds were carried out by Superconducting quantum interference devices (SQUID) magnetometer or VSM.

### 2.1 Powder X-ray Diffraction (P-XRD)

P-XRD is the most commonly used technique for the characterization of crystalline inorganic solids it is a non-destructive technique for the distinction of crystalline and amorphous compounds, this is also helpful in the identification of crystal structure, lattice symmetry and their phase purity as different crystalline structures have their own characteristics set of peaks corresponding to their structure and crystal symmetry. For this constructive interference the path difference ( $d$ ) should be equal to a whole number integer ( $n$ ) and given by Bragg's as:

$$n\lambda = 2d\sin\theta \quad (2.1)$$

where,  $n$  is an integer known as the order of diffraction,  $\lambda$  refers to the wavelength of X-ray,  $d$  stands for the interplanar distance and  $\theta$  is the diffraction angle [1].

The P-XRD measurements were carried out by a Bruker AXS D8 Advance diffractometer using graphite monochromatized CuK $\alpha$  (1.5406 Å) radiation operating at 40 kV and 40 mA. The P-XRD data were collected in the angular  $2\theta$  range of 5–90° with a step size of 0.02°. DIFFRAC<sup>plus</sup> software was used to input the instrumental parameters for a scan

and EVA<sup>®</sup> for the evaluation of the data. For each scan, approximately 0.5g of sample was loaded on the sample holder and then pressed with a glass slide to make the surface smooth for uniform diffraction to take place.

The progress of reactions and phase purity of the compounds at each steps of synthesis were confirmed by comparing the P-XRD patterns with that of the standard powder diffraction files (PDF) present within the JCPDS (Joint Committee on Powder Diffraction Standards) database. PROSZKI program [2] was used for indexing of peaks and least-squares refinement of the lattice parameters. The refined lattice parameters were used to carry out simulations of the P-XRD patterns by POWDER CELL program [3]. The input parameters such as, space group, atom position, temperature factor, occupancy factor etc, required for the simulation were taken from reference structural model.

The FULLPROOF program suite [4] was used for the Rietveld structure refinements of the compounds. Slow scan P-XRD data were used for the Rietveld refinements. For this data were collected over an angular range of 5-90° over a duration of 6-8 hours with a step size of 0.018° and with 4.9 s/step scan speed. In the initial runs of the refinement, the scale and the cell parameters were refined, followed by the background coefficients and zero-shift. In the subsequent runs, the profile and shape parameters were refined. After the initial refinement of profile, background, scale and lattice parameters, the positional and thermal parameters were refined. In this step, first, the position of heavier elements were refined followed by the lighter ones. In certain circumstances the position and thermal parameters of the atom were refined together to achieve convergence and then they were kept fixed while refinement the same for other elements. However, in some cases thermal parameters of oxygen atoms were kept unchanged to achieve convergence.

## **2.2 Field-Emission Scanning Electron Microscopy and Energy Dispersive X-ray Spectroscopy (FE-SEM and EDX)**

To ascertain the surface morphology and determine the chemical composition of the compounds, FE-SEM was utilized [5, 6]. In this technique, sample surface is bombarded with a narrow beam of high energy electrons and the interaction of solids with the e<sup>-</sup> beam, generates various signals like X-rays, secondary electrons, backscattered electrons and auger

electrons. The generated secondary electrons are basically used to produce the signal and further transformed to an image. The magnification and resolution of these images is very high due to the utilization of high energy electron beams. The emitted x-rays have different energies and intensities depending on the nature of the elements present in the sample and these relative proportion in the sample were further utilized to get elemental ratio and chemical composition of the samples.

In this work, a Carl Zeiss FE-SEM, Ultra plus55, operating at an accelerating voltage of 20 kV was used for morphological studies of the samples. The elemental composition and mapping analysis of the compounds were investigated by energy dispersive X-ray spectroscopy (EDX) facility (Oxford Instruments) attached with the instrument. At first, a large area of the sample was scanned for analysis. Then the scan area was narrowed down to obtain elemental composition on individual crystallites. Various areas spots and crystalline sample were analyzed thoroughly to find out the local and overall chemical compositions. Moreover, to ascertain the compositional homogeneity of a crystallite, a number of spots within the crystallite were also investigated. The uniform distribution of all the elements present in a sample were determined with by elemental mapping analysis of a scanned area or line scan elemental mapping. Samples for SEM and EDX analysis were prepared by smearing powder samples on a carbon tape pasted on an aluminium stub, which was cleaned properly with isopropyl alcohol and dried prior to pasting carbon tape on it. Then, the stubs were gold sputtered in an inert atmosphere (argon) to make their surface electrically conductive.

### **2.3 High Resolution Transmission Electron Microscopy (HR-TEM)**

This technique of electron microscopy was utilized to the high resolution lattice images of the compounds. In TEM, a high energy beam of electrons emerged from the electron gun, with an accelerating voltage of 50-300 kV, is allowed to transmit through an ultrathin section of sample deposited on carbon coated copper grids [7]. The beam is regulated by many electromagnetic lenses present in microscope column into a small, thin and coherent beam before being focused on the sample. The transmitted electrons form an image depending on their interaction with the sample on transmission. Selected area electron diffraction (SAED) patterns were recorded to ascertain the crystallinity of the sample. The diffraction spots were analyzed and lattice planes were indexed to confirm the crystal structure and symmetry as

ascertained by PXRD analysis. Lattice periodicity was determined by calculating the spacing between observed lattice fringes.

In the present work, TEM images and SAED patterns were recorded with JEM-3200FS electron microscope fitted with an electron gun of 300 kV accelerating voltage (available at Department of Metallurgical and Materials Engineering, IIT Roorkee). Sample for TEM analysis was prepared by dispersing ~ 0.1 mg of powdered sample in 1 mL of ethanol in a pestle mortar and ground thoroughly for 5 - 10 minutes to prepare homogeneous suspension. A drop of the homogeneous suspension was dispensed on a carbon coated copper grid and allowed to dry overnight in air.

#### 2.4 UV-Visible Diffuse Reflectance Spectroscopy (UV-vis DRS)

UV-vis DRS is a widely employed technique to characterize the optical properties of solid materials. In this technique, relative change in reflected diffuse light in all possible directions with respect to the incident light wavelength from the particles oriented in all directions were measured. For present measurements, a Shimadzu UV-2450 UV-vis spectrophotometer was used to record UV-vis DRS of the samples within the wavelength range of 200-800 nm. BaSO<sub>4</sub> was used as a standard for baseline correction in all the measurements. For the sample preparation, 1:100 sample BaSO<sub>4</sub> was used. For this purpose, approximately 30 mg of the powder sample were mixed it well with about 3 g of BaSO<sub>4</sub> in a pestle mortar for 10-20 minutes. Then, the sample mixture was loaded in the furrow of the sample holder and its surface was flattened by pressing with a glass cylinder. The sample holder was positioned in the spectrophotometer along with the reference holder to measure the diffused reflectance spectrum. The reflectance data were converted into absorption form according to the Kubelka-Munk (K-M) theory [8]:

$$F(R_{\infty}) = (1 - R_{\infty})^2 / 2R_{\infty} \quad (2.2)$$

where,  $F(R_{\infty})$  is the K-M function and  $R_{\infty}$  is the observed reflectance of the sample. The band gap of the samples were determined using the following equation given by Tauc [9]:

$$(ah\nu)^n = A(h\nu - E_g) \quad (2.3)$$

Where,  $A$  is constant of proportionality,  $\alpha$  is the coefficient of absorption,  $h\nu$  is the energy of incident photons and  $E_g$  is the band gap of the compound. The nature of electronic transition between the valence band (VB) and conduction band (CB) is decided by the value of exponent,  $n$ ; for a direct transition,  $n = 2$  and for an indirect transition,  $n = \frac{1}{2}$  were used [10, 11]. The linear extrapolation of  $(\alpha h\nu)^{1/n}$  to the energy axis gave the band gap energies of the samples.

### 2.5 X-Ray Photoelectron spectroscopy (XPS)

XPS is a classical quantitative technique used for the analysis of surface composition of solid samples being studied. In this technique, surface of material under analysis was bombarded with a monochromatic X-ray from an Al- $K_\alpha$  radiation source of 1486.6 eV or from a Mg- $K_\alpha$  radiation source of 1253.3 eV to emit photoelectrons from the surface of samples. Then, the energy of these emitted photoelectrons were measured using a hemispherical electron energy analyzer. The binding energies and intensity of photoelectron peaks gave information about the elements and their chemical state present on the surface of the material.

In the work reported here all the samples were investigated by XPS to ascertain the oxidation state of the transition elements present in the compounds. For these investigations, a Physical Electronics make PHI-5000 Versa Probe III XPS spectrometer equipped with a hemispherical analyzer and a multichannel detector. For the analysis, a very small amount of sample was loaded in the sample holder and chamber under high vacuum for nearly 12 h. Then, the sample was targeted with a monochromatic Al- $K_\alpha$  radiation source ( $h\nu = 1486.6$  eV) under ultra-high vacuum conditions. The instrument can analyze the composition and chemical state of the elements up to a depth of 5 nm. The data reduction and fitting of various peaks obtained for different elements present were completed using MultiPak software. The binding energies of these elements were referenced with respect to that of C 1s peak at 284.8 eV before deconvoluting the data.

### 2.6 Inductively Couple Plasma Optical Emission Spectroscopy (ICP-OES)

Inductively coupled plasma-optical emissions spectrometry (ICP-OES) is extensively used analytical technique for the determination of elements. The analyzing atoms or elements



are excited when plasma energy has been provided from outside. After excitation elements or atoms come back to its low energy, emissions spectra are observed. On the basis of photon or emission rays position the type of element is defined and these elements are determined by the intensity of emission rays.

The ICP-OES analysis on an Agilent 720ICP-OES instrument has been carried out during the current work. For this purpose, samples have been dissolved in concentrated hydrofluoric acid. A 1000 ppm lithium nitrate solution (bought from SRL chemicals) was used as a calibration solution within a range of 200 to 600 ppb. Li was estimated in the compounds and the compositions were determined accordingly.

### **2.7 Solid State Nuclear Magnetic Resonance (ssNMR)**

The NMR has been used as a modern spectroscopic technology in various disciplines, from chemistry to biochemistry to materials and geoscience. The main focus of NMR spectroscopy is the interaction of isolated spin pairs. Dependent on the state of the matter, NMR spectroscopy may be classified into two main classes: solution and solid-state NMR (ssNMR). In the NMR solution compounds with a low viscosity and high-resolution NMR spectrum have been dissolved, the main advantage of this technology compared with ssNMR, are usually studied. Averaging multiple NMR interactions due to the rapid molecular tumbling is responsible for the high-resolution NMR spectra in solution. The absence of fast molecular movement for solid samples, however, results in broad peaks, which often contain spectral characteristics. However, by developing the spinning magic-angle (MAS) technique, the spectroscopists can produce "soluble" NMR spectrums of solid samples which can be used for extracting information similar to that from a solution NMR. Besides, ssNMR spectroscopy also offers various other advantages, such as, that for insoluble samples. Moreover, many compounds are not stable or unstable when dissolved within a solvent. ssNMR spectroscopy, therefore, provides structural and dynamic data that cannot be obtained by solution NMR or other techniques like single-crystal X-ray diffraction because of difficulties in producing suitable single crystals for XRD examination [12].

In the present work, a JEOL 400 MHz NMR spectrometer (model ECX 400 II) was used to as recorded  $^7\text{Li}$  ssNMR spectra using a 4 mm rotor sample holder.  $^7\text{Li}$  spectra were

averaged for 32 scans using a 90° pulse length of 3.7  $\mu$ s and a recycle delay of 8s. The  $^7\text{Li}$  spectra were referenced to aq. 1M LiCl at 0 ppm.

## 2.8 Magnetic Measurements

Magnetism, is a phenomenon in which materials can feel attraction or repulsion in the presence of magnetic field. Many of our advanced technological devices depend on magnetism and magnetic materials: such as electrical generators and transformers, electric movers, radio, TV, telephones, sound and video reproduction systems and components [13].

The medium is magnetized when a material is placed in a magnetic field. The dipole moment per unit of volume described is the magnetization vector,  $M$ . As the field induces the magnetization, we can assume that  $M$  is proportionate to  $H$ . That is,

$$\chi = M B. \quad (2.4)$$

where,  $\chi$  is known as the magnetic susceptibility of the medium.

In Eq. (2.4), we assumed that  $M$  is proportional to  $B$ , the external field, and thus we ignored the things that were included in the electric case, such as, the demagnetization field. For paramagnetic and diamagnetic materials, the neglect of these factors is justified, as  $M$  is very small, in comparison with  $B$  (typically  $\chi = B/M \sim 10^{-5}$ ), as opposed to electric case, in which  $\chi \sim 1$ . However, this omission cannot be sustained if we deal with ferromagnetic materials, where  $M$  is very large, and the above consequences must be included. We will not differentiate between the magnetic field and magnetic induction is not differentiate because of the low value of the magnetic susceptibility.

$\chi$  in Eq.(1) can be dependent on the applied magnetic field. In this case, we can define the magnetic susceptibility as follows

$$\chi = \partial M / \partial B \quad (2.5)$$

The magnetization can be defined as

$$M = \partial E / \partial B \quad (2.6)$$

where,  $E$  is the total energy of the system. Definitions (2.5) and (2.6) are more general and can be used in calculations.

### 2.8.1 Classification of materials

Magnetic materials are categorized into five classes such as, diamagnetic, paramagnetic, ferromagnetic, ferrimagnetic and antiferromagnetic on the basis of magnetic ordering, sign, magnitude and temperature dependent magnetic susceptibility. In diamagnetic and paramagnetic materials no magnetic ordering is present at any temperature, whereas in ferromagnetic, anti-ferromagnetic and ferromagnetic material, there are magnetic orders at low temperatures.

The magnetic susceptibility is negative in diamagnetic materials. It is usually the order of  $-10^{-6}$  to  $-10^{-5}$ . The negative value of the susceptibility implies that the diamagnetic materials obtain magnetization in the magnetic field applied that is directed opposite to the applied field. The susceptibility in diamagnetic materials is almost temperature-independent. Ionic crystals and inert gas atoms are examples of diamagnetic substances. These substances have completely filled shell atoms or ions and the diamagnetism of these substances depends on the magnetic field acting distort the orbital movement.

There is a positive susceptibility to all other material classes. The magnitude of the susceptibility varies over a wide range in these classes. However, susceptibility for all materials in such classes decreases with a sufficiently high temperature. All these materials were found to be more or less exactly in accordance with the relation for sufficiently high  $T$ .

$$\chi = C/T \pm T_c \quad (2.7)$$

$C$  and  $T_c$  here are positive and temperature-independent constants for characteristics of each material.

In certain materials,  $T_c = 0$  was found and this equation was observed at the lowest temperature at which measurements were carried out. This class is known as paramagnetic. In paramagnetic materials  $\chi$  is positive - that is, for which  $M$  is parallel to  $B$ . However, there is a very small susceptibility:  $10^{-4}$  to  $10^{-5}$ . The ions of transition and the rare earth metals are the best-known paramagnetic material. Their paramagnetic behavior lies in the fact that these ions

have incomplete atomic orbitals. Equation (2.7) breaks down when the temperature decreases for all other materials. All the materials exhibit a critical temperature below and above this temperatures variation in susceptibility changes with temperature.

The critical temperature  $T_C$  is called the Curie temperature in ferromagnetic materials. The susceptibility is followed by relation (2.7) with a negative sign above the Curie temperature. The magnetic susceptibility is infinite when the temperature approaches  $T_C$ . An infinite susceptibility implies that even in zero-applied fields, such as permanent magnets, a finite magnetization exists. The problem is that the magnetization of the zero field ferromagnetic materials can have a range of different values and cannot therefore be considered as a materials property. However, the magnetization of these materials tends to have a constant effect, which is known as  $M_S$  or spontaneous magnetization, where a relatively small magnetic field is applied to these materials. The magnetization disappears at the Curie temperature.

The non-zero magnetization of ferrimagnetic materials is similar to that of ferromagnetism below the Curie temperature. However, significant variations over a range of temperatures are occur according equation (2.7). This conduct only takes place at higher temperatures as compared to the Curie temperature. An additional difference between ferrimagnets and ferromagnets is that saturation magnetization against temperature have a more complicated effect in the case of ferrimagnetic materials. For instance, some ferrimagnets may show increase magnetization and then decrease at a higher temperature.

At all temperatures, the antiferromagnetic materials have low positive susceptibilities. They follow the same eq. (2.7) at high temperatures normally with a positive sign for  $T_C$ . In this case, the critical temperature is called the Néel temperature. The susceptibility decreases with decreasing temperature below the Néel temperature. In antiferromagnetic materials there is no spontaneous magnetization.

In the current work, a SQUID magnetometer or VSM is used to record the magnetization data for all the ion-exchanged compounds.

### **2.8.2 Superconducting Quantum Interference Device (SQUID) Magnetometer**

Magnetization (zero field cooled and field cooled) data of exchanged compounds were performed on a superconducting quantum interference device (SQUID) magnetometer (Quantum Design MPMS XL Ever Cool) in the temperature range of 4 – 300 K in a magnetic field of 1000 Oe.

### **2.8.3 Vibrating sample Magnetometer (VSM)**

Magnetization data of exchanged compounds under zero field cooled (ZFC) and field cooled (FC) conditions were performed on 3 Tesla cryogen free mini Vibrating Sample Magnetometer (VSM) (CRYOGENICS Ltd, UK) in the temperature range 4 - 300 K at a magnetic field strength of 1000 Oe.



## REFERENCES

- (1) West, A. R. *Solid State Chemistry and Its Applications*. Wiley Publishers, **2011**.
- (2) Losocha, W.; Lewinski, K. PROSZKI- A System of Programs for Powder Diffraction Data Analysis. *J. Appl. Crystallogr.* **1994**, *27*, 437-438.
- (3) Kraus, W.; Nolze, G. *POWDER CELL* - A Program for the Representation and Manipulation of Crystal Structures and Calculation of the Resulting X-ray Powder Patterns. *J. Appl. Crystallogr.* **1996**, *29*, 301-303.
- (4) Rodríguez-Carvajal, J. Recent advances in magnetic structure determination by neutron powder diffraction. *Phys. B* **1993**, *192*, 55-69.
- (5) Wetzig, K.; Schulze, D. *In Situ Scanning Electron Microscopy in Materials Research*. AkademieVerlag **1995**.
- (6) Chandler, G. W.; Seraphin, S.; Ed. Kaufmann, E. N. *Scanning Electron Microscopy. Characterization of Materials* **2003**, *2*, 1050-1063.
- (7) Pennycook, S. J.; Eds. Williams, D. B.; Carter, C. B. *Transmission Electron Microscopy: A Text Book for Materials Science. Microscopy and Microanalysis* **2010**, *16*, 111-111.
- (8) Kubelka, P.; Munk, F. Ein Beitrag zur Optik der Farbanstriche. *Z. Tech. Phys.* **1931**, *12*, 593-601.
- (9) Tauc, J.; Grigorovic, R.; Vancu, A. Optical Properties and Electronic Structure of Amorphous Germanium. *Phys. Status Solidi* **1966**, *15*, 627-637.
- (10) Kim, M. R.; Kang, Y.; Jang, D. Synthesis and Characterization of Highly Luminescent CdS@ZnS Core-Shell Nanorods. *J. Phys. Chem. C* **2007**, *111*, 18507-18511.
- (11) Joshi, U. A.; Maggard, P. A. CuNb<sub>3</sub>O<sub>8</sub>: A p-Type Semiconducting Metal Oxide Photoelectrode. *J. Phys. Chem. Lett.* **2012**, *3*, 1577-1581.
- (12) Chen, F. Basic Principles and Applications of Solid-State NMR in Catalysis. *J Thermodyn Catal* **2014**, *5*(2), 1000e127.
- (13) Callister, W. D.; Rethwisch, D. G. *Materials Science and Engineering: An Introduction* 9E. Wiley Publishers, **2014**.





**CHAPTER -3**

***Topotactic Ion Exchange in a Three-Dimensional Close-Packed Trirutile Structure with an Octahedral Network***



## **Topotactic Ion Exchange in a Three-Dimensional Close-Packed Trirutile Structure with an Octahedral Network**

### **3.1 INTRODUCTION**

Transition metal oxides continue to attract research attention owing to the emergence of exciting and often unusual physical and chemical properties in them. Most of the time, if the emergent compound is metastable, it gets arrested in a local minima of its potential energy landscape [1] and thus is not achievable under harsh reaction conditions (i.e. at high temperatures). Soft-chemistry synthetic techniques have been proven to work at its best in achieving metastable phases [2]. Ion-exchange is one among many soft-chemistry techniques that has been exhaustively employed for the synthesis of a large number of compounds with structures ranging from open framework solids (e.g. MOFs) [3-5], clays (e.g. montmorillonite) [6], layered double hydroxides (e.g. hydroxyapatites) [7, 8] tunnel structured [9-14] to layered compounds (e.g. layered perovskites) [15-24]. Despite numerous such reports, the ion exchange is usually limited to the above structural genres, leaving vast majority of close-packed three-dimensional structures outside the scope of ion-exchange reactions.

The lability of the exchangeable species (e.g. simple and complex ions or a structural motif) and consequently their facile exchange in the above mentioned category of solids can be directly mapped to their structural characteristics. For example, in MOFs ions residing at the channels and inter-connecting cavities of the open three-dimensional frameworks are loosely held or rattle and mostly act as framework charge compensating counter ions (both cationic and anionic) ensuing easy exchangeability with other ions by topotactic means [5]. In mineral clays, layered double hydroxides or layered perovskites, the structure may be considered to be weakly held along the stack direction, in a sense that the chemical binding force is stronger within the layers and relatively weaker in-between the layers due to changing bonding patterns and coordination environments. This periodic variation in the bonding pattern and differences in coordination environments set one of the layer forming units relatively loose and susceptible to ion exchange with respect to the other and the entirety of the structure. This property of the interlayer ions or species has been exploited in developing a large number of functional inorganic solids [2, 18, 21].

In recent years, the structural manipulation of layered perovskites have gained a lot of popularity in building different types of structural units and coordination environments within the interlayer galleries leading to the emergence of new layered structures [18, 21]. A variety of soft-chemical reactions including ion exchange have given rise to the genesis of various archetypes of layered perovskites, artificial hetero-interfaces and structures [25-29]. Moreover, in recent times ion exchange in colloidal nanocrystals has witnessed renewed interest and lately being utilized in structure selective cation exchange in zinc blende nanocrystals [30, 31].

While the topotactic ion exchange is common in oxides with the layered perovskite structure, rare in the 3D close packed structures based on all edge and/or corner shared polyhedra. An interesting type of exchange, namely, ‘intra-site exchange’, where perovskite A-site cations were exchanged with the interlayer A'-cations within a compound, was demonstrated in a layered perovskite [32]. A cubooctahedral A-site ion exchange in  $\text{NaTaO}_3$  is the only report involving a three-dimensional perovskite structure with all octahedral corner connectivity [33]. Here in, we demonstrate Li-ion exchange by Fe(II) in the trirutile,  $\text{LiNbWO}_6$ , where the Li is part of the corner and edge connected octahedral network of the rutile structure. The exchange has enabled the transformation of a near ultra-violet absorbing diamagnetic insulating oxide into a visible-light active paramagnetic semiconductor.

$\text{LiNbWO}_6$  was first reported as a Li-ion conductor [34] by Ohtsuka *et al.* and later on two of the structural variants ( $\alpha$  and  $\beta$ ) were established by Fourquet *et al.* While the  $\alpha$ - $\text{LiNbWO}_6$  adopted a quasi-ordered trirutile structure, the  $\beta$ -form crystallized in the  $\text{LiNbO}_3$ -type structure with completely disordered cation arrangement of Nb and W [35]. Moreover, due to the lability of the Li-ions, topotactic proton exchange was possible in the quasi-ordered form under milder acidic conditions [36], while structural transformation occurred during proton exchange under relatively harsh acidic conditions [37].

## 3.2 EXPERIMENTAL SECTION

### 3.2.1 Materials and Synthesis

The white colored  $\alpha$ -LiNbWO<sub>6</sub> was synthesized by a solid-state reaction as reported in the literature [37]. For this purpose, stoichiometric quantities of Li<sub>2</sub>CO<sub>3</sub> (Sigma Aldrich,  $\geq 98.0\%$ ), Nb<sub>2</sub>O<sub>5</sub> (Sigma Aldrich,  $\geq 99.9\%$ ) and WO<sub>3</sub> (Sigma Aldrich,  $\geq 99.0\%$ ) were first weighed along with 10 mole % of Li<sub>2</sub>CO<sub>3</sub> and 20 mole % of WO<sub>3</sub> in excess (to compensate the loss due to volatilization of the components at higher temperatures). The constituents were then ground thoroughly in an agate mortar for 1 h and calcined at 780 °C for 24 h in a high quality alumina ( $\geq 99.8\%$  Al<sub>2</sub>O<sub>3</sub>) boat.

The ion exchange reaction was performed by taking 1 g of  $\alpha$ -LiNbWO<sub>6</sub> powder in 100 mL of 0.2 M aqueous solution of FeCl<sub>2</sub>·4H<sub>2</sub>O (Sigma Aldrich,  $\geq 99.0\%$ ) and stirring at 60 °C in Argon atmosphere for 4 days. During the ion exchange, the aged aqueous FeCl<sub>2</sub>·4H<sub>2</sub>O solution was replaced with a fresh solution intermittently after 2 days. Finally, the product was washed with distilled water for several times and dried at room temperature in a desiccator. The dried sample after ion exchange was mustard-yellow in color.

## 3.3 RESULTS AND DISCUSSION

### 3.3.1 P-XRD Analysis

The P-XRD patterns of the as prepared compounds are shown in Figure 3.1. A comparison of the observed P-XRD data with that of the standard JCPDS data of the parent LiNbWO<sub>6</sub> (JCPDS PDF #41-0378) confirmed the topotactic nature of the exchange. All the peaks observed in the P-XRD pattern of Li<sub>0.1</sub>Fe<sub>0.45</sub>NbWO<sub>6</sub> are indexable in the tetragonal  $P-42_1m$  space group. The least-square refined lattice parameters for compounds are given in Table 3.1. The lattice parameters for the parent LiNbWO<sub>6</sub> are in good agreement with the literature data. Crystal structure of Li<sub>0.1</sub>Fe<sub>0.45</sub>NbWO<sub>6</sub> is refined by the Rietveld method using P-XRD data with the aid of FULLPROF program suite. The initial model for the structure refinement of Li<sub>0.1</sub>Fe<sub>0.45</sub>NbWO<sub>6</sub> was constructed using the atomic coordinates of LiNbWO<sub>6</sub> ( $P\bar{4}2_1m$  space group). The observed, calculated and difference profiles of Rietveld refinement are shown in Figure 3.2.



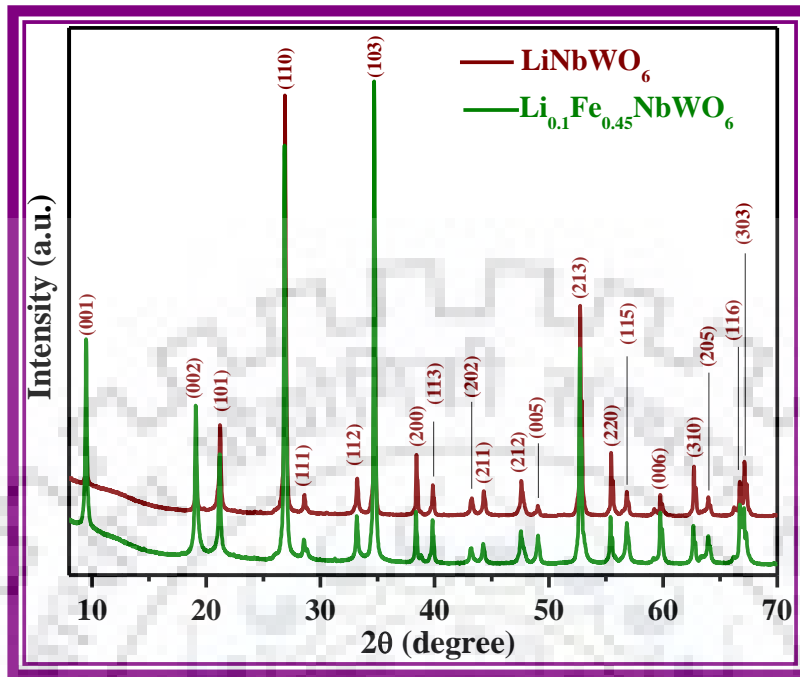


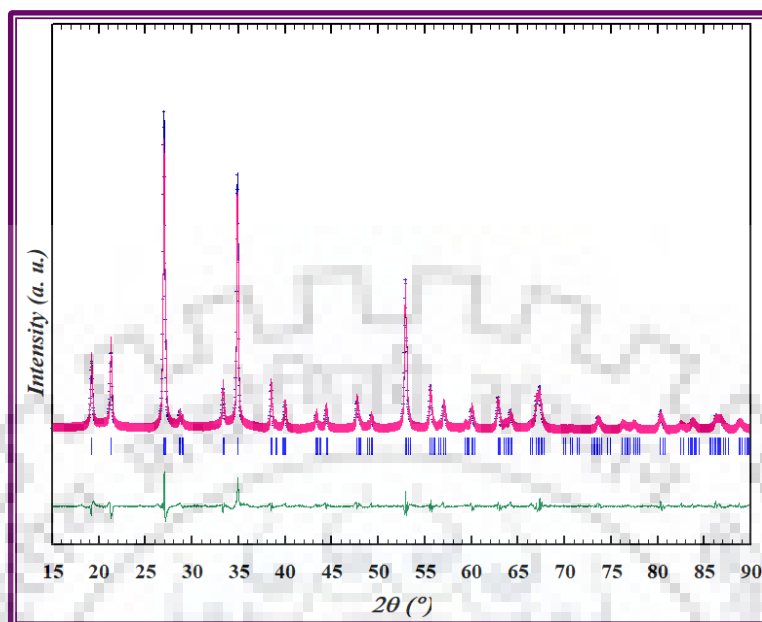
Figure 3.1 P-XRD patterns of  $\text{LiNbWO}_6$  and  $\text{Li}_{0.1}\text{Fe}_{0.45}\text{NbWO}_6$ .

Table 3.1 Lattice Parameters and Band Gap of  $\text{LiNbWO}_6$  and  $\text{Li}_{0.1}\text{Fe}_{0.45}\text{NbWO}_6$

Compound	Lattice Parameters (Å)		Band gap ( $E_g$ ) (eV)
	$a$	$c$	
$\text{LiNbWO}_6$	4.6818(2)	9.2754(5)	3.01
$\text{Li}_{0.1}\text{Fe}_{0.45}\text{NbWO}_6$	4.6737(1)	9.2411(3)	1.71

Table 3.2 Indexed P-XRD Data for  $\text{Li}_{0.1}\text{Fe}_{0.45}\text{NbWO}_6$ 

<i>h k l</i>	$d_{\text{obs}}$ (Å)	$d_{\text{calc}}$ (Å)	$I_{\text{obs}}$
0 0 1	9.319	9.274	37
0 0 2	4.646	4.637	23
1 0 1	4.189	4.182	49
1 1 0	3.316	3.313	100
1 1 1	3.123	3.119	9
0 0 3	3.095	3.091	18
1 1 2	2.697	2.695	70
1 0 3	2.582	2.580	18
2 0 0	2.344	2.342	7
1 1 3	2.262	2.260	7
2 0 2	2.091	2.091	13
2 1 1	2.045	2.043	16
2 1 2	1.910	1.909	4
0 0 5	1.855	1.854	57
2 1 3	1.735	1.734	16
2 2 0	1.657	1.656	10
1 1 5	1.618	1.618	6
0 0 6	1.546	1.545	5
3 1 0	1.481	1.481	14
1 0 6	1.467	1.467	1
2 0 5	1.454	1.454	8
1 1 6	1.400	1.400	10
3 0 3	1.393	1.394	9
2 0 6	1.290	1.290	16



**Figure 3.2** Rietveld refinement of P-XRD data for  $\text{Li}_{0.1}\text{Fe}_{0.45}\text{NbWO}_6$ . Observed (+), calculated (–) and difference (at the bottom) profiles are shown. Vertical bars below the profile mark the Bragg reflection positions.

The Rietveld refinement of the P-XRD data using initial structural parameters of  $\alpha$ - $\text{LiNbWO}_6$  in  $P-42_1m$  space group resulted in a good profile fitting (Figure 3.2) with the distributed Li and Fe occupancy (10% by Li; 45% by Fe) at the  $2c$  site akin to the composition,  $\text{Li}_{0.1}\text{Fe}_{0.45}\text{NbWO}_6$ . In the refinement, Li and Fe are collectively considered to occupy 55% of the  $2c$  sites, leaving behind 45% of the sites vacant at random. The representative structure of  $\text{Li}_{0.1}\text{Fe}_{0.45}\text{NbWO}_6$  drawn from the refined atomic coordinates displays the ordered arrangement of Nb and W in the  $a$ - $b$  plane (Figure 3.3), while Figure 3.4 represents edge-shared ordered octahedral chains, which are further interconnected through corners, running parallel to the  $c$ -direction. The Li/Fe vacancies seen in the structure (created in an ordered fashion) are in fact random rendering an occupied Li/Fe site mostly isolated from the neighboring Li/Fe, thus diminishing the possibility of any long range  $\text{Fe}^{2+}\text{-O-Fe}^{2+}$  magnetic interactions.

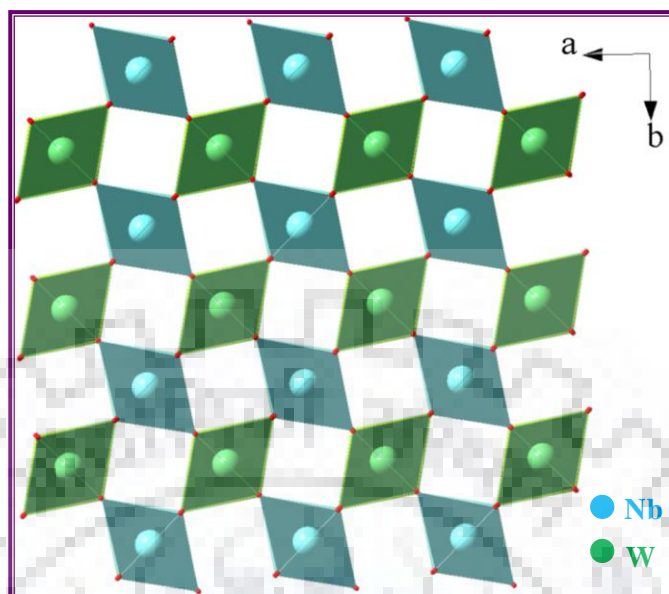


**Figure 3.3** Polyhedral representation of  $\text{Li}_{0.1}\text{Fe}_{0.45}\text{NbWO}_6$  in the  $ab$ -plane.

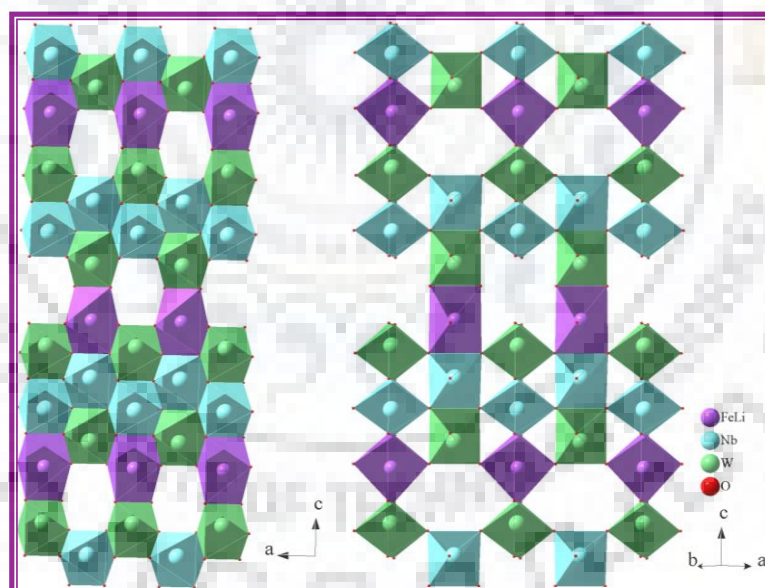


**Figure 3.4** Polyhedral representations of the structure of  $\text{Li}_{0.1}\text{Fe}_{0.45}\text{NbWO}_6$  drawn with the refined atomic coordinates. The structure shown here presents Li/Fe vacancies in an ordered fashion.

**Table 3.3.1 Atomic Positions, Site Occupancy and Thermal Parameters of  $\text{Li}_{0.1}\text{Fe}_{0.45}\text{NbWO}_6$**

Atom	<i>x</i>	<i>y</i>	<i>z</i>	B <sub>iso</sub>	Occ.
Li	0	0.5	0.4159(1)	2.70(1)	0.10
Fe	0	0.5	0.4159(1)	2.70(1)	0.45
Nb	0	0.5	0.0893(2)	0.24(1)	1
W	0	0.5	0.7305(1)	3.23(1)	1
O1	0.29	0.791	0.7712	2.55(1)	2
O2	0.3032	0.8032	0.0809	2.16(1)	2
O3	0.2993	0.7993	0.3939	3.49(1)	2

**Table 3.3.2 Space group, Refined Cell Parameter and the Reliability Factor for  $\text{Li}_{0.1}\text{Fe}_{0.45}\text{NbWO}_6$**

Parameter	value
space group	$P-42_1m$
<i>a</i>	4.6737(1) Å
<i>c</i>	9.2411 (3) Å
<i>V</i>	201.87(1) Å <sup>3</sup>
$R_{\text{Bragg}}$ (%)	4.1
$R_{\text{F}}$ (%)	2.5
$R_{\text{p}}$ (%)	4.8
$R_{\text{wp}}$ (%)	6.1
$\chi^2$	6.8

Table 3.4 Selected Bond Lengths (Å) of  $\text{Li}_{0.1}\text{Fe}_{0.45}\text{NbWO}_6$ 

Fe – O1 (×2)	2.213(6)
Fe – O3 (×2)	2.201(6)
Fe – O3 (×2)	1.988(6)
< Fe – O >	2.134
Nb – O1 (×2)	1.889(5)
Nb – O2 (×2)	2.005(6)
Nb – O2 (×2)	2.041(5)
< Nb – O >	1.978
W – O1 (×2)	1.959(6)
W – O3 (×2)	2.174(6)
W – O2 (×2)	1.755(4)
< W – O >	1.962

### 3.3.2 FE-SEM and EDX Analysis

The morphology and elemental composition of  $\text{LiNbWO}_6$  and  $\text{Li}_{0.1}\text{Fe}_{0.45}\text{NbWO}_6$  were investigated by FE-SEM and EDX analysis, respectively. Figure 3.5 indicated higher atomic percentages of Fe in the samples with longer reaction times. The final product purity is 100% since the ion exchange occurs in the entire sample as evidenced by the overall elemental composition and homogeneity observed in the EDX area and spot analyses at several locations of the sample. Figure 3.6 shows FE-SEM images and corresponding EDX spectra of the as synthesized compounds. FE-SEM images taken at several locations of the samples show morphological homogeneity all through the analyzed areas. The parent compound,  $\text{LiNbWO}_6$  shows homogenous plate like morphology, often observed for layered compounds throughout the imaging area. The ion-exchanged product,  $\text{Li}_{0.1}\text{Fe}_{0.45}\text{NbWO}_6$  was also shown plate like morphology indicated retention of layered structure. Both the compounds show morphological homogeneity of the crystallites in the entire region of image prevailing plate



like microstructures throughout with a fairly large variation in the size of crystallites ranging from several hundred nanometers to few micrometers. The elemental composition as obtained from EDX analysis, both on spot and area bases, are in good agreement with the nominal composition. The EDX data (Figure 3.6) confirmed the expected elemental ratio for Fe, Nb and W in corroboration with the ICP-OES derived composition.

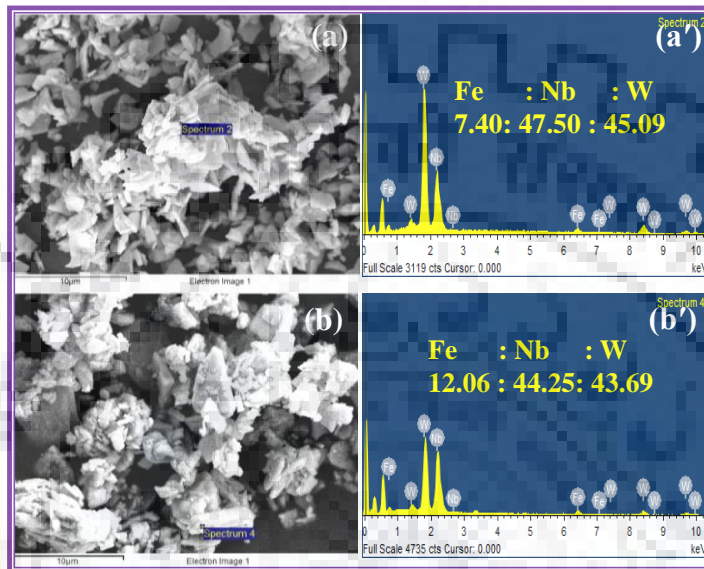


**Figure 3.5** FE-SEM and corresponding EDX data of  $\text{Li}_{0.1}\text{Fe}_{0.45}\text{NbWO}_6$  (a) after 24 h of ion exchange and (b) after 48 h of ion exchange.

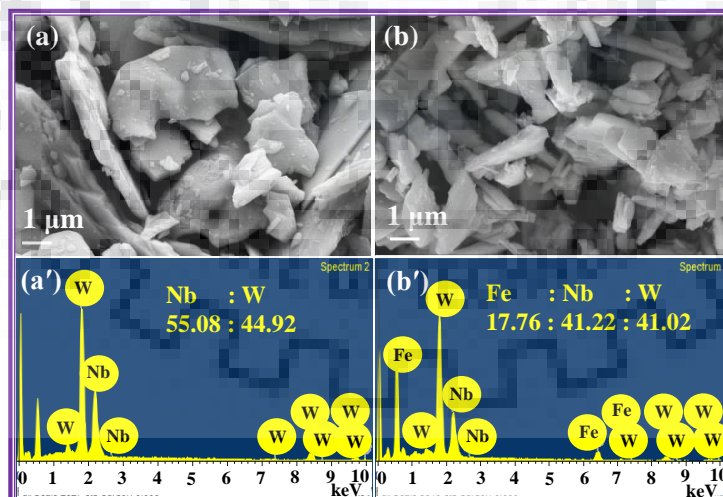


**Figure 3.6** FE-SEM and corresponding EDX data of (a)  $\alpha\text{-LiNbWO}_6$  and (b)  $\text{Li}_{0.1}\text{Fe}_{0.45}\text{NbWO}_6$ .

### 3.3.3 FE-SEM-EDX Line Scan Analysis

An elemental mapping analysis was carried out to examine the elemental distribution in the synthesized sample. The FE-SEM-EDX elemental line scans are shown in Figure 3.7. The results of elemental mapping line scan indicate that all the elements (iron, niobium and tungsten) scanned across the SEM image are homogeneously distributed in all the scanned crystallites.

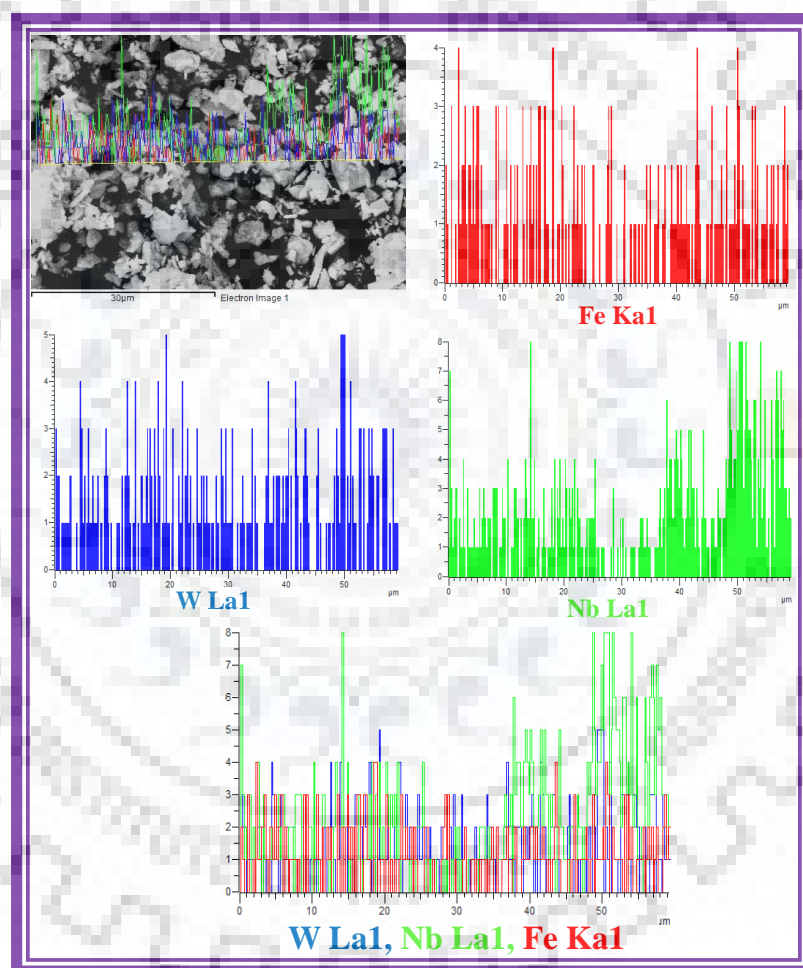


**Figure 3.7** EDX line scan of Fe, Nb and W for  $\text{Li}_{0.1}\text{Fe}_{0.45}\text{NbWO}_6$  along with the corresponding bright field SEM image.

### 3.3.4 HR-TEM Analysis

The HR-TEM images and ED pattern of  $\text{Li}_{0.1}\text{Fe}_{0.45}\text{NbWO}_6$  are shown in Figure 3.7. In the HR-TEM image (Figure 3.8a), the observed lattice fringes with a periodicity of 0.932 nm is representative of the ordered trirutile phase conforming to the periodicity of  $(\text{Li}/\text{Fe})\text{O}_6$  octahedron connected to  $\text{NbO}_6$ - $\text{WO}_6$  bi-octahedral unit along the  $c$ -direction. The selected area electron diffraction (SAED) image shows bright diffraction spots confirming its highly crystalline nature as well. This SAED pattern (Figure 3.8b) is consistent with the tetragonal crystal system and the indexed spots are in agreement with the P-XRD data.

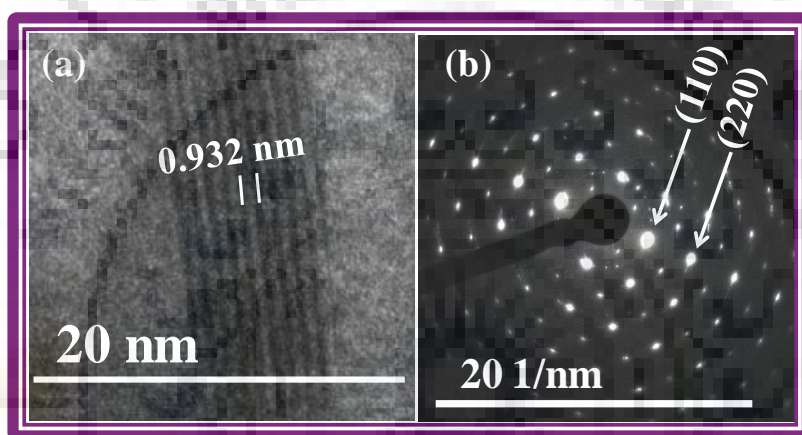


**Figure 3.8** (a) HR-TEM image and (b) SAED pattern of  $\text{Li}_{0.1}\text{Fe}_{0.45}\text{NbWO}_6$ .

### 3.3.5 Solid-State Nuclear Magnetic Resonance (ssNMR) Analysis

The  $^7\text{Li}$  MAS NMR spectra of  $\text{LiNbWO}_6$  shown in Figure 3.9 clearly reveal the presence of only one type of Li-site as expected. The presence of  $^7\text{Li}$  peak in the Fe-exchanged sample with the same chemical shift to that of the parent is supportive of the retention of small amount of Li without any change to its coordination environment. Moreover, a ratio of the integrated intensities of the  $^7\text{Li}$  peaks for  $\text{Li}_{0.1}\text{Fe}_{0.45}\text{NbWO}_6$  to  $\text{LiNbWO}_6$  supports retention of nearly 10 % of the Li, in agreement with the ICP-OES data.

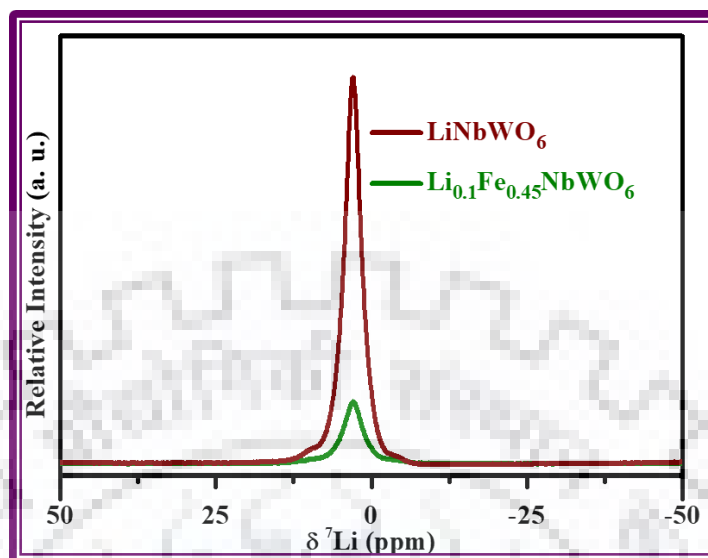


Figure 3.9 Solid-state  $^7\text{Li}$  MAS NMR spectra of  $\text{LiNbWO}_6$  and  $\text{Li}_{0.1}\text{Fe}_{0.45}\text{NbWO}_6$ .

### 3.3.6 XPS Analysis

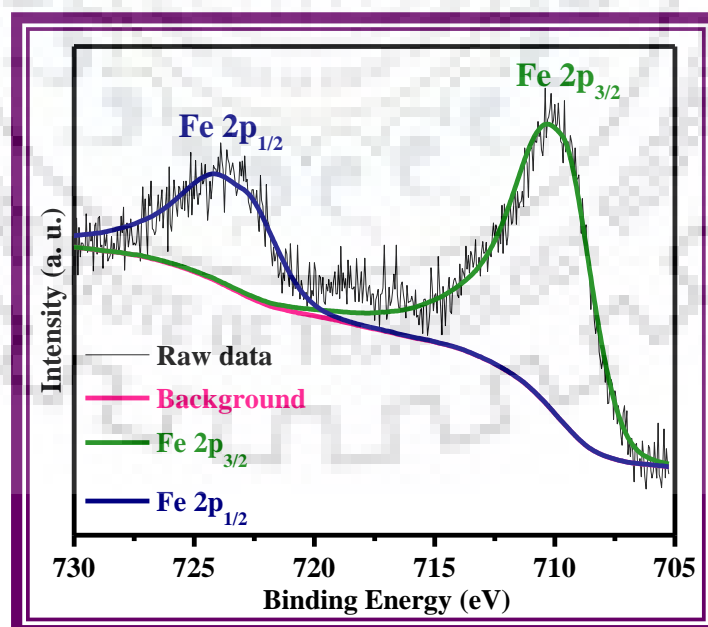
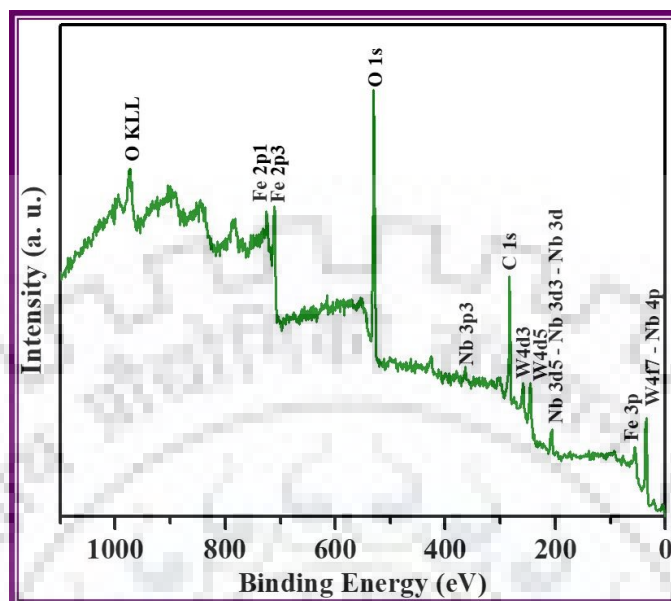


Figure 3.10 Fe-2p XPS of  $\text{Li}_{0.1}\text{Fe}_{0.45}\text{NbWO}_6$ .



**Figure 3.11** XPS survey spectra of  $\text{Li}_{0.1}\text{Fe}_{0.45}\text{NbWO}_6$ .

The high-resolution XPS spectra of Fe-2p<sub>1/2</sub> and Fe-2p<sub>3/2</sub> are shown in Figure 3.10. The XPS data calibrated with respect to C 1s binding energy of 284.8 eV indicated Fe-2p binding energies of 723.0 and 709.7 eV for spin-orbit coupled Fe-2p<sub>1/2</sub> and Fe-2p<sub>3/2</sub> states, respectively, corresponding largely to the presence of Fe<sup>2+</sup> in  $\text{Li}_{0.1}\text{Fe}_{0.45}\text{NbWO}_6$ . The survey spectra of  $\text{Li}_{0.1}\text{Fe}_{0.45}\text{NbWO}_6$  in Figure 3.11 are shown Nb 3d peak at 207.4 eV, Fe-2p<sub>1/2</sub> 723.0 eV, Fe-2p<sub>3/2</sub> 709.7 eV and W 4f peak 36.4 eV and these are the characteristic peaks for Nb (V) and Fe (II) and W(VI) oxidation state respectively.

### 3.3.7 Thermal Stability

The compound,  $\text{Li}_{0.1}\text{Fe}_{0.45}\text{NbWO}_6$ , was stable in air up to 350°C and up to 550°C in argon atmosphere as evidenced in the P-XRD patterns recorded after heating the samples in air and argon atmosphere (Figure 3.12). However, the fact that the compound decomposed at 800°C in argon atmosphere and it cannot be prepared by conventional solid-state reaction starting from its constituent oxides/oxalates under argon at similar reaction temperatures to that of  $\text{LiNbWO}_6$  indicated its true metastable nature.

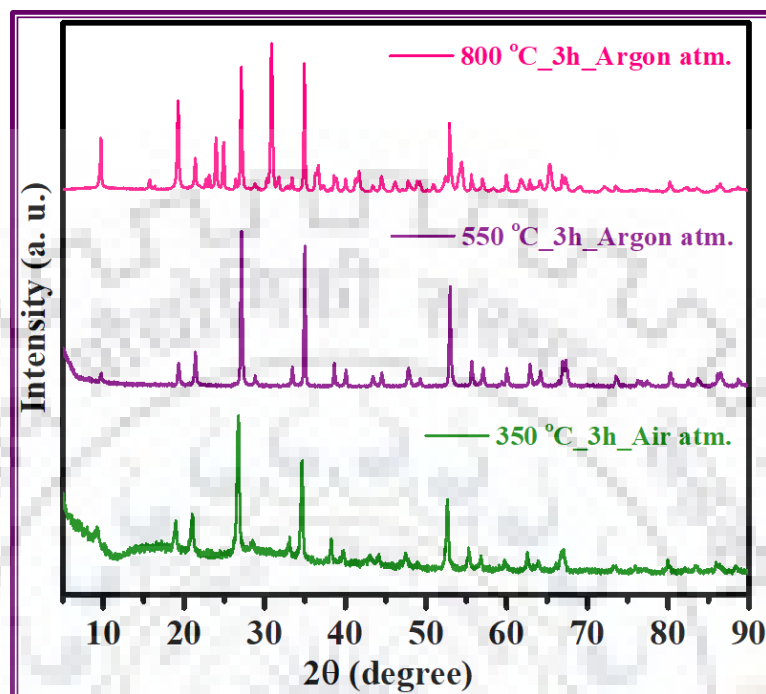


**Figure 3.12** P-XRD patterns of  $\text{Li}_{0.1}\text{Fe}_{0.45}\text{NbWO}_6$  after heating at 350 (in air), 550 and 800°C (in argon atmosphere).

### 3.3.8 UV-vis DRS Analysis

The band gaps of  $\text{LiNbWO}_6$  and  $\text{Li}_{0.1}\text{Fe}_{0.45}\text{NbWO}_6$  were determined by UV-vis DRS. As evidenced in the UV-vis DRS (Figure 3.13a), the Fe-exchange has clearly resulted in the extension of the optical absorption edge deep into the visible region (up to  $\sim 700$  nm) as compared to its parent, only a near UV absorber ( $\lambda_{\text{abs}} < 400$  nm). This amounts to a significant reduction of the indirect band gap of  $\text{Li}_{0.1}\text{Fe}_{0.45}\text{NbWO}_6$  to 1.71 eV from 3.01 eV of the parent, as estimated from the Tauc plot [38] (Figure 3.13b). The reduction in the band gap is due to the formation of valence band (VB) states, primarily constituted by the overlap of Fe-3d and O-2p orbitals, which would be situated at higher energies in  $\text{Li}_{0.1}\text{Fe}_{0.45}\text{NbWO}_6$  as compared to the VB states of  $\text{LiNbWO}_6$ . This upshift of VB edge and a consequent decrease in the band gap is ascribed to the extended optical absorption of  $\text{Li}_{0.1}\text{Fe}_{0.45}\text{NbWO}_6$ .



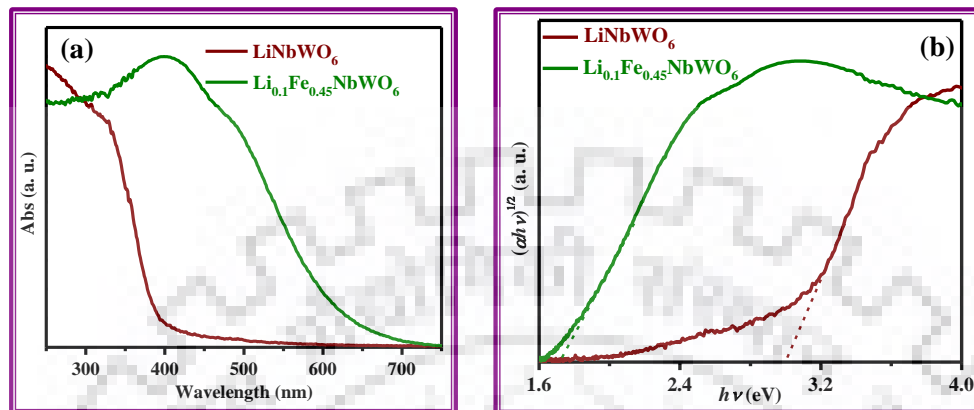


**Figure 3.13** UV-vis DRS data (a) and corresponding Tauc plots (b) for  $\text{Li}_{0.1}\text{Fe}_{0.45}\text{NbWO}_6$ .

### 3.3.9 Magnetic Measurement

Temperature-dependent magnetic susceptibility data in a 1000 Oe field were collected on  $\text{Li}_{0.1}\text{Fe}_{0.45}\text{NbWO}_6$  and are shown in Figure 3.14. It is certain that the Fe-exchange would transform the diamagnetic  $\text{LiNbWO}_6$  into at least a paramagnetic compound in absence of any long-range magnetic correlations at room temperature. In fact, inverse susceptibility data (Figures 3.14b) support pure Curie-like paramagnetism at temperatures below 200 K, as expected due to the disorder of Fe in the  $2c$  sites and the presence of random vacancies that perhaps leave the  $\text{Fe}^{2+}$  moments isolated from other neighboring moments in the lattice. The magnetic data for  $\text{Li}_{0.1}\text{Fe}_{0.45}\text{NbWO}_6$  are calculated from the linear fit of the  $\chi_m^{-1}$  vs. T plot and tabulated in Table 3.6. The observed magnetic moment ( $\mu_{\text{obs}} = 4.4 \mu_B$  per f. u.) corroborates well with the expected spin-only moment for high-spin  $\text{Fe}^{2+}$ .

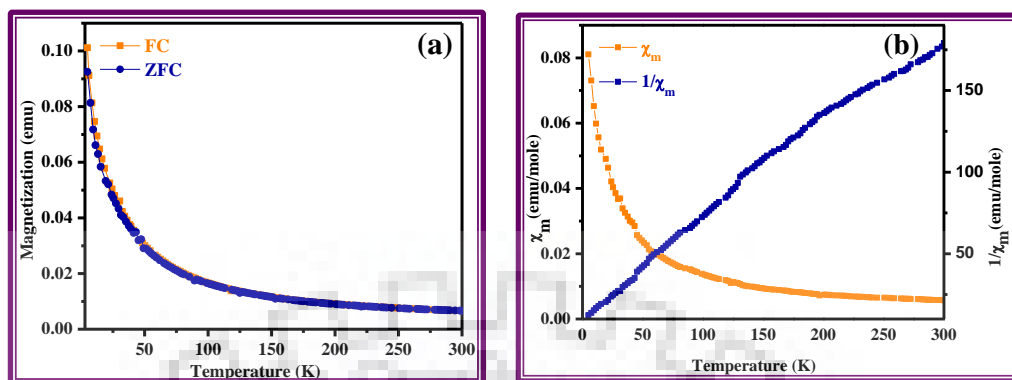
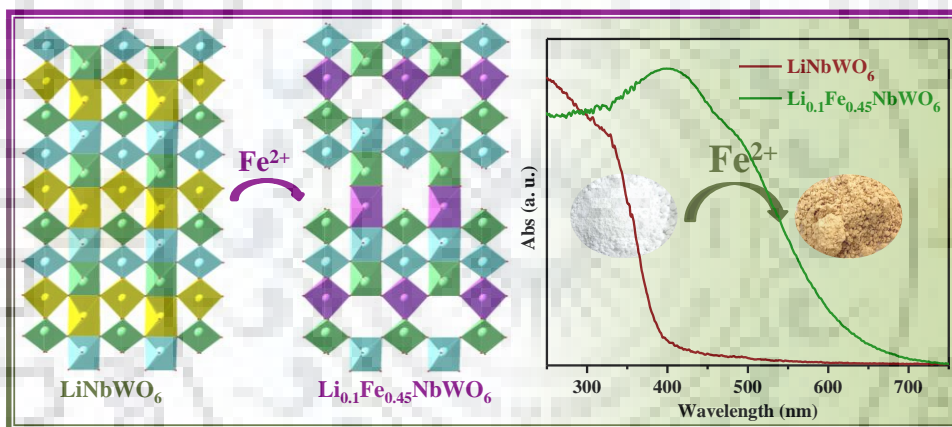


**Figure 3.14** (a) Magnetization vs temperature, (b) molar susceptibility and inverse molar susceptibility vs. temperature for  $\text{Li}_{0.1}\text{Fe}_{0.45}\text{NbWO}_6$ .

**Table 3.6** Magnetic Data for  $\text{Li}_{0.1}\text{Fe}_{0.45}\text{NbWO}_6$  Calculated from the Linear Fit of the  $\chi_m^{-1}$  vs. T Plot

Compound	C (emu/mole)	$\theta$ (K)	$\mu_{\text{eff}}$ (B.M.)
$\text{Li}_{0.1}\text{Fe}_{0.45}\text{NbWO}_6$	2.4	115.6	4.4

In summary, the topotactic ion exchange reported here is unique of its kind to happen in a close-packed three-dimensional structure containing cations of same polyhedral connectivity. It is believed that the scope of the exchange reported here would extend beyond the trirutile family and will open up ways for the development of a variety of metastable functional oxides with unprecedented structural diversity and properties. Realizing the importance of recent works on layered oxide hetero-interfaces and their architectures [26-29, 39] for various technological applications, and ion exchange in colloidal nanocrystals, the present work may offer opportunities in building novel architectures of three-dimensional close packed ordered or quasi-ordered oxides in the bulk, nanocrystals as well as in thin films through ion exchange.



## REFERENCES

- (1) Jansen, M.; Pentin, I. V.; Schön, J. C. A. Universal Representation of the States of Chemical Matter Including Metastable Configurations in Phase Diagrams. *Angew. Chem. Int. Ed.* **2012**, *51*, 132–135.
- (2) Gopalakrishnan, J. Chimie Douce Approaches to the Synthesis of Metastable Oxide Materials. *Chem. Mater.* **1995**, *7*, 1265–1275.
- (3) Nouar, F.; Eckert, J.; Eubank, J. F.; Forster, P.; Eddaoudi, M. Zeolite-like Metal-Organic Frameworks (ZMOFs) as Hydrogen Storage Platform: Lithium and Magnesium Ion-Exchange and H<sub>2</sub>-(rho-ZMOF) Interaction Studies. *J. Am. Chem. Soc.* **2009**, *131*, 2864–2870.
- (4) Yang, S.; Martin, G. S. B.; Titman, J. J.; Blake, A. J.; Allan, D. R.; Champness, N. R.; Schröder, M. Pore with Gate: Enhancement of the Isosteric Heat of Adsorption of Dihydrogen via Postsynthetic Cation Exchange in Metal–Organic Frameworks. *Inorg. Chem.* **2011**, *50*, 9374–9384.
- (5) Evans, J. D.; Sumbly, C. J.; Doonan, C. J. Post-Synthetic Metalation of Metal–Organic Frameworks. *Chem. Soc. Rev.* **2014**, *43*, 5933–5951.
- (6) Carrado, K. A.; Wasserman, S. R. Stability of Cu(II)-and Fe(III)-Porphyrins on Montmorillonite Clay: An X-ray Absorption Study. *Chem. Mater.* **1996**, *8*, 219–225.
- (7) Sels, B.; Vos, D. De.; Buntinx, M.; Pierard, F.; Kirsch-De Mesmaeker, A.; Jacobs, P. Layered Double Hydroxides Exchanged with Tungstate as Biomimetic Catalysts for Mild Oxidative Bromination. *Nature* **1999**, *400*, 855–857.
- (8) Fei, H. H.; Oliver, S. R. J. Copper Hydroxide Ethanedisulfonate: A Cationic Inorganic Layered Material for High-Capacity Anion Exchange. *Angew. Chem. Int. Ed.* **2011**, *50*, 9066–9070.
- (9) Dion, M.; Piffard, Y.; Tournoux, M. The tetratitanates  $M_2Ti_4O_9$  ( $M = Li, Na, K, Rb, Cs, Tl, Ag$ ). *J. Inorg. Nucl. Chem.* **1978**, *40*, 917–918.
- (10) McCarthy, T. J.; Tanzer, T. A.; Kanatzidis, M. G. A New Metastable Three-Dimensional Bismuth Sulfide with Large Tunnels: Synthesis, Structural Characterization, Ion-Exchange Properties, and Reactivity of  $KBi_3S_5$ . *J. Am. Chem. Soc.* **1995**, *117*, 1294–1301.
- (11) Clearfield, A. Structure and Ion Exchange Properties of Tunnel Type Titanium Silicates. *Solid State Sci.* **2001**, *3*, 103–112.
- (12) Cai, J.; Liu, J.; Gao, Z.; Navrotsky, A.; Suib, S. L. Synthesis and Anion Exchange of Tunnel Structure Akaganeite. *Chem. Mater.* **2001**, *13*, 4595–4602.

- (13) Rowsell, J. L. C.; Taylor, N. J.; Nazar, L. F. Structure and Ion Exchange Properties of a New Cobalt Borate with a Tunnel Structure “Templated” by Na<sup>+</sup>. *J. Am. Chem. Soc.* **2002**, *124*, 6522–6523.
- (14) Sharma, R.; Mandal, T. K.; Ramesha, K.; Gopalakrishnan, J. Synthesis and Characterization of AgBiO<sub>3</sub> with the Cubic KSbO<sub>3</sub> Structure. *Indian J. Chem., Sect. A* **2004**, *43A*, 11–17.
- (15) Ollivier, P. J.; Mallouk, T. E. A “Chimie Douce” Synthesis of Perovskite-Type SrTa<sub>2</sub>O<sub>6</sub> and SrTa<sub>2-x</sub>Nb<sub>x</sub>O<sub>6</sub>. *Chem. Mater.* **1998**, *10*, 2585–2587.
- (16) Kodenkandath, T. A.; Lalena, J. N.; Zhou, W. L.; Carpenter, E.E.; Sangregorio, C.; Falster, A. U.; Simmons, W. B.; O’Connor, C. J.; Wiley, J. B. Assembly of Metal-Anion Arrays within a Perovskite Host. Low-Temperature Synthesis of New Layered Copper-Oxyhalides, (CuX)LaNb<sub>2</sub>O<sub>7</sub> (X = Cl, Br). *J. Am. Chem. Soc.* **1999**, *121*, 10743–10746.
- (17) Hyeon, K.-A.; Byeon, S.-H. Synthesis and Structure of New Layered Oxides, M<sup>II</sup>La<sub>2</sub>Ti<sub>3</sub>O<sub>10</sub> (M = Co, Cu, and Zn). *Chem. Mater.* **1999**, *11*, 352–357.
- (18) Schaak R. E.; Mallouk, T. E. Perovskites by Design: A Toolbox of Solid-State Reactions. *Chem. Mater.* **2002**, *14*, 1455–1471.
- (19) Kobayashi, Y.; Tian, M.; Eguchi, M.; Mallouk, T. E. Ion-Exchangeable, Electronically Conducting Layered Perovskite Oxyfluorides. *J. Am. Chem. Soc.* **2009**, *131*, 9849–9855.
- (20) Galven, C.; Fourquet, J. L.; Suard, E.; Crosnier-Lopez, M. P.; Le Berre, F. Structural characterization of a New Acentric Ruddlesden–Popper Layered Perovskite Compound: LiHSrTa<sub>2</sub>O<sub>7</sub>. *Dalton Trans.* **2010**, *39*, 3212–3218.
- (21) Ranmohotti, K. G. S.; Josepha, E.; Choi, J.; Zhang, J.; Wiley, J. B. Topochemical Manipulation of Perovskites: Low Temperature Reaction Strategies for Directing Structure and Properties. *Adv. Mater.* **2011**, *23*, 442–460.
- (22) Boltersdorf, J.; Maggard, P. A. Silver Exchange of Layered Metal Oxides and Their Photocatalytic Activities. *ACS Catal.* **2013**, *3*, 2547–2555.
- (23) Yip, T. W. S.; Cussen, E. J. Ion Exchange and Structural Aging in the Layered Perovskite Phases H<sub>1-x</sub>Li<sub>x</sub>LaTiO<sub>4</sub>. *Inorg. Chem.* **2013**, *52*, 6985–6993.
- (24) Roudebush, J. H., Ross, K. A.; Cava, R. J. Iridium Containing Honeycomb Delafossites by Topotactic Cation Exchange. *Dalton Trans.* **2016**, *45*, 8783–8789.
- (25) Hayward. M. A. Topochemical Reactions of Layered Transition Metal Oxides. *Semicond. Sci. Technol.* **2014**, *29*, 064010.
- (26) Li, B. W.; Osada, M.; Ebina, Y.; Ueda, S.; Sasaki, T. Coexistence of Magnetic Order and Ferroelectricity at 2D Nanosheet Interfaces. *J. Am. Chem. Soc.* **2016**, *138*, 7621–7625.

- (27) Li, B. W.; Osada, M.; Kim, Y. H.; Ebina, Y.; Akatsuka, K.; Sasaki, T. Atomic Layer Engineering of High- $\kappa$  Ferroelectricity in 2D Perovskites. *J. Am. Chem. Soc.* **2017**, *139*, 10868–10874.
- (28) Osada, M.; Sasaki, T. Nanoarchitectonics in Dielectric/Ferroelectric Layered Perovskites: from Bulk 3D Systems to 2D Nanosheets. *Dalton Trans.* **2018**, *47*, 2841–2851.
- (29) Uppuluri, R.; Gupta, A. S.; Rosas, A. S.; Mallouk, T. E. Soft-Chemistry of Ion-Exchangeable Layered Metal Oxides. *Chem. Soc. Rev.* **2018**, *47*, 2401–2430.
- (30) Gupta, S.; Kershaw, S. V.; Rogach, A. L. 25th Anniversary Article: Ion Exchange in Colloidal Nanocrystals. *Adv. Mater.* **2013**, *25*, 6923–6944.
- (31) Fenton, J. L.; Schaak, R. E. Structure-Selective Cation Exchange in the Synthesis of Zincblende MnS and CoS Nanocrystals. *Angew. Chem. Int. Ed.* **2017**, *56*, 6464–6467.
- (32) Bhuvanesh, N. S. P.; Woodward, P. M. Thermally Induced A'-A Site Exchange in Novel Layered Perovskites  $\text{Ag}_2[\text{Ca}_{1.5}\text{M}_3\text{O}_{10}]$  (M = Nb, Ta). *J. Am. Chem. Soc.* **2002**, *124*, 14294–14295.
- (33) Patino, M. A.; Smith, T.; Zhang, W.; Halasyamani, P. S.; Hayward, M. A. Cation Exchange in a 3D Perovskite—Synthesis of  $\text{Ni}_{0.5}\text{TaO}_3$ . *Inorg. Chem.* **2014**, *53*, 8020–8024.
- (34) Okada, T.; Yamaji, A.; Ohtsuka, H. Electrical Conductivity of  $\text{LiNbWO}_6$ . *Solid State Ionics* **1984**, *14*, 283–288.
- (35) Fourquet, J. L.; Bail, A. L.; Gillet, P. A.  $\text{LiNbWO}_6$ : Crystal Structure of Its Two Allotropic Forms. *Mater. Res. Bull.* **1988**, *23*, 1163–1170.
- (36) He, J.; Li, Q. J.; Tang, Y.; Yang, P.; Li, A.; Li, R.; Li, H. Z. Characterization of  $\text{HNbMoO}_6$ ,  $\text{HNbWO}_6$  and  $\text{HTiNbO}_5$  as Solid Acids and their Catalytic Properties for Esterification Reaction. *Applied Catalysis A: General.* **2012**, *443-444*, 145–152.
- (37) Gopalakrishnan, J.; Bhat, V.  $\text{HNbWO}_6$  and  $\text{HTaWO}_6$ : Novel Oxides Related to  $\text{ReO}_3$  Formed by Ion Exchange of Rutile-Type  $\text{LiNbWO}_6$  and  $\text{LiTaWO}_6$ . *J. Solid State Chem.* **1986**, *63*, 278–283.
- (38) Tauc, J.; Grigorovic, R.; Vancu, A. Optical Properties and Electronic Structure of Amorphous Germanium. *Phys. Status Solidi* **1966**, *15*, 627–637.
- (39) Liu, G.; Zhen, C.; Kang, Y.; Wang, L.; Cheng, H. M. Unique Physicochemical Properties of Two-Dimensional Light Absorbers Facilitating Photocatalysis. *Chem. Soc. Rev.* **2018**, *47*, 6410–6444





*CHAPTER -4*

*A New tri- $\alpha$ -PbO<sub>2</sub> Type Fe-Sb-Tungstate  
by Topotactic Ion Exchange of LiSbWO<sub>6</sub>*



## A New tri $\alpha$ - $\text{PbO}_2$ Type Fe-Sb-Tungstate by Topotactic Ion Exchange of $\text{LiSbWO}_6$

### 4.1 INTRODUCTION

Transition metal oxides continue to attract research attention because they exhibit many exciting physical and chemical properties. Although a large variety of transition metal oxides are reported in the literature, a lot of possibility remains to be explored with new chemical compositions and structures that are not achievable by conventional high temperature synthetic route. While the conventional solid-state synthesis is very useful and widely employed for the syntheses of many functional oxides, the range of compositions accessible are limited due to the competition between thermodynamic and kinetic factors. This often leads to the formation of thermodynamically stable products leaving many envisioned composition out of reach due to its metastable nature. On the other hand, low temperature ‘*chimie douce*’ methods enable one to access the so-called metastable phases. Topotactic ion exchange is one such ‘soft chemistry’ based method where a new chemical compound emerges after exchange keeping all or a part of the structural and bonding features of the precursor solids intact. Such type of topotactic reactions often provides additional advantages in transforming one structural family to another. These types of transformations have opened up new possibilities to create library of reactions that can help structural engineering among several families of layered oxides.

Layered perovskites have been extensively used to formation of new compounds at relatively low temperatures by topochemical reactions. DJ and RP phases were display more interest in ion exchange for interlayer alkali metal cation exchange. Exchange reactions can be done in aqueous, molten salts or in the solid state. Ion-exchanged compounds have been shown huge attention due to their diverse properties such as physical and chemical. A number of DJ compounds were used to replace small alkali metals ( $\text{H}^+$ ,  $\text{Li}^+$ ,  $\text{Na}^+$ ) [1], transition metals [2, 3], and metallic chlorides [4-7] in monovalent, divalent ion exchange and co-exchange reactions. Monovalent ion exchange has been carried out in RP phase,  $\text{Na}_2\text{La}_2\text{Ti}_3\text{O}_{10}$ , via acidic exchange [8] or a molten mixture  $\text{LiNO}_3$  [9] and produced protonated  $\text{H}_2\text{La}_2\text{Ti}_3\text{O}_{10}$ , and  $\text{Li}_2\text{La}_2\text{Ti}_3\text{O}_{10}$ , as a product. Divalent ion exchange in RP phases,  $\text{M}_2\text{La}_2\text{Ti}_3\text{O}_{10}$ ,  $\text{M}_2\text{Eu}_2\text{Ti}_3\text{O}_{10}$ ,

(M = Na, K) by diamagnetic metal cations (Ca<sup>2+</sup>, VO<sup>2+</sup>) [10-12] and paramagnetic metal cations Co, Cu, Ni and Zn [13-17] either by aqueous ion exchange or by low temperature solid state reactions with eutectic mixtures of alkali metal / transition metal chlorides in sealed tubes.

While the topotactic ion exchange is common in oxides with the layered perovskite [18, 19] or other tunnel [20-22] and framework structures [23, 24], but are uncommon in the 3D close packed structures with all octahedral connectivity. Among few unique exchanges in layered oxides, mention may be made of the interesting ‘intra-site exchange’, where perovskite A-site cations were exchanged with the interlayer A'-cations within a compound [25]. A multivalent ion exchange in a lamellar  $\alpha$ -NaFeO<sub>2</sub> structure type was reported long ago [26]. A cubooctahedral A-site ion exchange in NaTaO<sub>3</sub> is the only report involving a three-dimensional perovskite structure with all octahedral corner connectivity [27]. Recently we have reported a topotactic ion exchange in a 3D close packed trirutile oxide, LiNbWO<sub>6</sub>. The structure is made up of all octahedral corner and edge connected network where the Li ions occupy the part of the octahedral network of the rutile structure in a quasi-ordered fashion. The Li exchange by Fe(II) has enabled the transformation of a near ultra-violet absorbing diamagnetic insulating oxide into a visible-light active paramagnetic semiconductor [28].

The analogous composition, LiSbWO<sub>6</sub>, obtained by replacing Nb of trirutile LiNbWO<sub>6</sub> with a p-block element like Sb, however, do not stabilize in the same structure. Initially, LiSbWO<sub>6</sub> was reported by Blasse and de Pauw with an ordered columbite structure [29]. Later on, Le Bail *et al* [30] have shown it by *ab-initio* structure determination of P-XRD data to adopt a superstructure obtained by tripling of the *b*-axis of  $\alpha$ -PbO<sub>2</sub> structure, unlike the columbite structure where the cation ordering was considered along the *a*-axis by the authors [29]. In this chapter, we undertook a systematic study of topotactic ion exchange in tri- $\alpha$ -PbO<sub>2</sub>-type LiSbWO<sub>6</sub>. Topotactic exchange of Fe(II) readily occurs in the aqueous medium resulting in the formation of a new tri- $\alpha$ -PbO<sub>2</sub>-type compound, Li<sub>0.08</sub>Fe<sub>0.46</sub>SbWO<sub>6</sub>. The compound show visible band gap and an antiferromagnetic ordering due to presence of ‘Fe<sub>2</sub>O<sub>10</sub>’ dimers, in contrary to the creation of isolated spin centers in trirutile Li<sub>0.1</sub>Fe<sub>0.45</sub>NbWO<sub>6</sub> that showed low temperature Curie paramagnetism.

## 4.2 EXPERIMENTAL SECTION

### 4.2.1 Materials and Synthesis

The  $LiSbWO_6$  was synthesized by a solid-state reaction between stoichiometric quantities of  $Li_2CO_3$  (Sigma Aldrich,  $\geq 98.0\%$ ),  $Sb_2O_5$  (Sigma Aldrich,  $\geq 99.9\%$ ) and  $WO_3$  (Sigma Aldrich,  $\geq 99.0\%$ ). The pellets were first heated at  $700\text{ }^\circ\text{C}$  for 12 h in air followed by intermittent grinding and reheating the mixture at  $900\text{ }^\circ\text{C}$  for 12 h in a high quality ( $\geq 99.8\%$   $Al_2O_3$ ) alumina boat [30].

The ion exchange reaction was performed by taking 1 g of  $LiSbWO_6$  powder in 100 mL of 0.2 M aqueous solution of  $FeCl_2 \cdot 4H_2O$  (Sigma Aldrich,  $\geq 99.0\%$ ) and stirring at  $60\text{ }^\circ\text{C}$  in Argon atmosphere for 4 days. During the ion exchange, the aged aqueous  $FeCl_2 \cdot 4H_2O$  solution was replaced with a fresh solution intermittently after 2 days. Finally, the product was washed with distilled water for several times and dried at room temperature in a desiccator. The dried sample after ion exchange was yellow in color.

## 4.3 RESULTS AND DISCUSSION

### 4.3.1 P-XRD Analysis

The P-XRD patterns of the parent  $LiSbWO_6$  and Fe(II) exchanged product are shown in Figure 4.1. The color changeover of the sample from white to yellow was indicative of Fe(II) exchange and retention of the X-ray diffraction peaks like that of the parent with slight changes of intensity was a signature of the topotactic nature of exchange. All the peaks observed in the P-XRD pattern of the Fe exchanged compound,  $Li_{1-2x}Fe_xSbWO_6$ , are indexable in the orthorhombic  $Pbcn$  space group. The least squares refined lattice parameters for the parent and the Fe-exchanged compounds are given in Table 4.1. The lattice parameters of the parent  $LiSbWO_6$  are in good agreement with the literature data. The Rietveld refinement of the crystal structure for  $Li_{1-2x}Fe_xSbWO_6$  is carried out using the P-XRD data in the FULLPROF program suite. The initial model for the structure refinement was constructed using the atomic coordinates of  $LiSbWO_6$  ( $Pbcn$  space group) and the occupancies are adjusted with the composition,  $Li_{0.08}Fe_{0.46}SbWO_6$ , as derived from the combined ICP-OES

and EDX analysis. The observed, calculated and difference profiles of Rietveld refinement are shown in Figure 4.2.

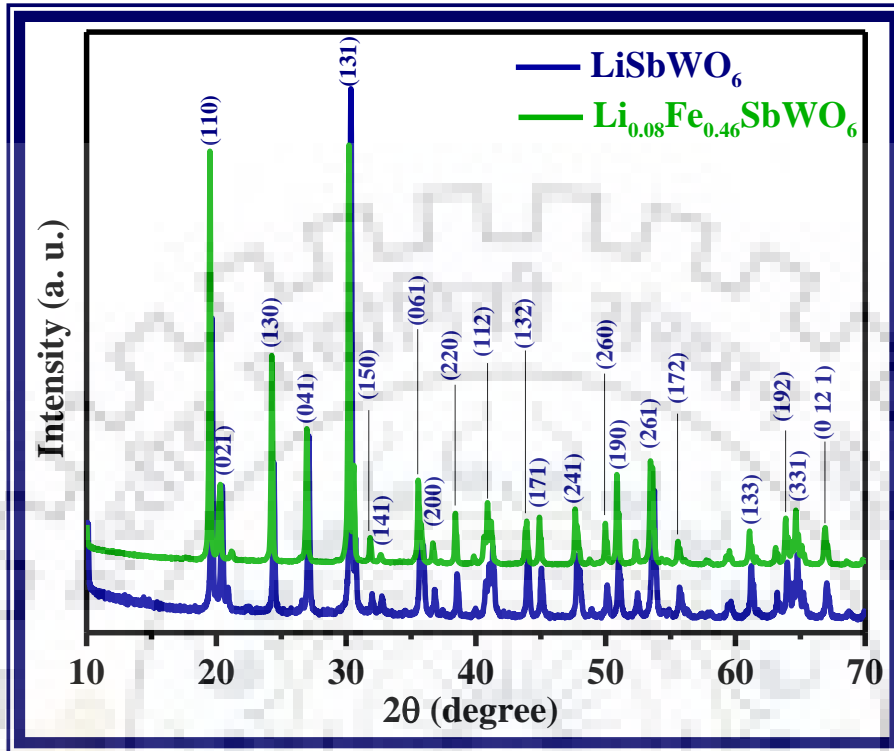


Figure 4.1 P-XRD patterns of  $\text{LiSbWO}_6$  and  $\text{Li}_{0.08}\text{Fe}_{0.46}\text{SbWO}_6$ .

Table 4.1 Lattice Parameters and Band Gap Energy of  $\text{LiSbWO}_6$  and  $\text{Li}_{0.08}\text{Fe}_{0.46}\text{SbWO}_6$

Compound	Lattice Parameters ( $\text{\AA}$ )			Band gap ( $E_g$ ) (eV)
	$a$	$b$	$c$	
$\text{LiSbWO}_6$	4.66(4)	17.43(1)	4.98(5)	3.05
$\text{Li}_{0.08}\text{Fe}_{0.46}\text{SbWO}_6$	4.64(9)	17.36(3)	4.97(1)	2.06



Table 4.2 Indexed P-XRD Data for  $\text{Li}_{0.08}\text{Fe}_{0.46}\text{SbWO}_6$ 

$h k l$	$d_{\text{obs}}$ (Å)	$d_{\text{calc}}$ (Å)	$I_{\text{obs}}$
0 2 0	8.580	8.613	27
1 1 0	4.467	4.468	60
0 2 1	4.320	4.331	30
1 3 0	3.610	3.602	26
0 4 1	3.263	3.266	34
1 3 1	2.924	2.925	100
0 6 0	2.879	2.871	11
0 0 2	2.500	2.505	15
2 0 0	2.317	2.313	8
1 1 2	2.188	2.185	14
2 2 1	2.044	2.040	11
1 9 0	1.783	1.768	11
2 0 2	1.702	1.768	22
1 9 2	1.450	1.451	10
3 3 1	1.435	1.435	10
0 12 1	1.392	1.394	5

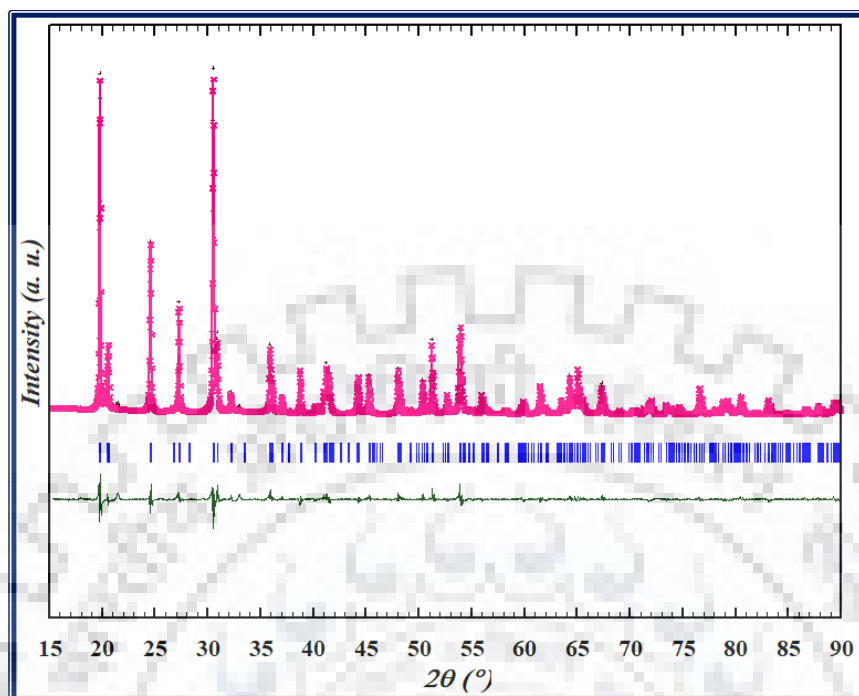


**Figure 4.2** Rietveld refinement of P-XRD data for  $\text{Li}_{0.08}\text{Fe}_{0.46}\text{SbWO}_6$ . Observed (+), calculated (–) and difference (at the bottom) profiles are shown. Vertical bars below the profile mark the Bragg reflection positions.

The representative structure in Figure 4.3 drawn from the refined atomic coordinates (Table 4.2) displays the zigzag chains of edge-shared octahedra of Sb and W ordered alternately in the  $a$ -direction. The structural depiction in Figure 4.4 shows Fe(II) dimer formation by exchange of four  $\text{Li}^+$  with two  $\text{Fe}^{2+}$  occupying adjacent sites. The magnetic data (see later) is in support of the presence of Fe(II) dimers in the structure, which is different from the isolated  $\text{Fe}^{2+}$  spin centers that were present in the trirutile  $\text{Li}_{0.1}\text{Fe}_{0.45}\text{NbWO}_6$ . The ‘ $\text{Fe}_2\text{O}_{10}$ ’ dimer formation might have originated due to the presence of edge-shared chains of  $\text{LiO}_6$  octahedra running along the  $c$ -direction in the tri- $\alpha$ - $\text{PbO}_2$  structure of  $\text{LiSbWO}_6$  in contrary to the presence of corner-connected  $\text{LiO}_6$  octahedra in the  $a/b$ -direction of the trirutile  $\text{LiNbWO}_6$ .

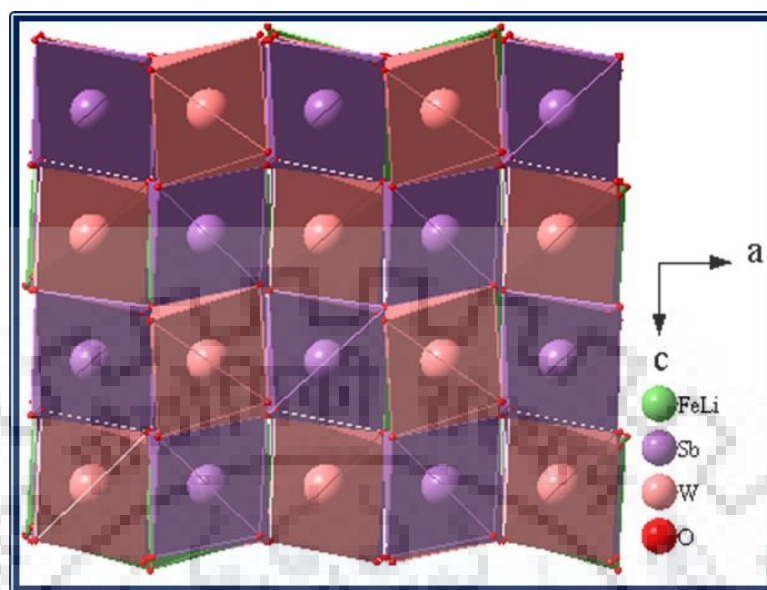


**Figure 4.3** Polyhedral representation of  $\text{Li}_{0.08}\text{Fe}_{0.46}\text{SbWO}_6$  in the  $ac$ -plane.

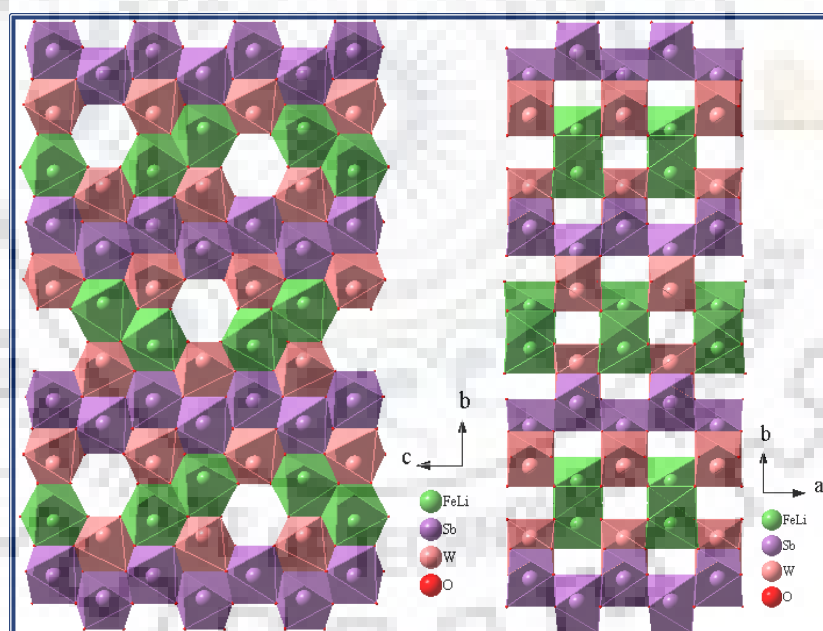


**Figure 4.4** Polyhedral representation of  $\text{Li}_{0.08}\text{Fe}_{0.46}\text{SbWO}_6$  in the  $bc$ -plane and  $ab$ -plane drawn with the refined atomic coordinates. Fe(II) dimers are seen in the  $ab$ -plane generated by selectively removing the Li sites that remain vacant on Fe exchange.

**Table 4.3 Refinement Parameters, Atomic Positions, Site Occupancy and Thermal Parameters of  $\text{Li}_{0.08}\text{Fe}_{0.46}\text{SbWO}_6$** 

Parameter	value
space group	<i>Pbcn</i>
<i>a</i>	4.6453(8) Å
<i>b</i>	17.3636(2) Å
<i>c</i>	4.9721(1) Å
<i>V</i>	401.06(1) Å <sup>3</sup>
$R_{\text{Bragg}}$ (%)	3.5
$R_{\text{F}}$ (%)	3.1
$R_{\text{p}}$ (%)	5.4
$R_{\text{wp}}$ (%)	7.1
$\chi^2$	7.2

**Table 4.3 Refinement Parameters, Atomic Positions, Site Occupancy and Thermal Parameters of  $\text{Li}_{0.08}\text{Fe}_{0.46}\text{SbWO}_6$  (contd.)**

Atom	<i>x</i>	<i>y</i>	<i>z</i>	$B_{\text{iso}}$	Occ.
Li	0	0.5	0.25	41.11(1)	0.08
Fe	0	0.5	0.25	41.11(1)	0.46
Sb	0	0.5	0.25	0.2581(7)	1
W	0	0.5	0.25	0.5941(7)	1
O1	0.2164(2)	0.3690(7)	0.5533(3)	1.8058(3)	2
O2	0.2489(1)	0.0471(7)	0.5865(3)	0.5101(3)	2
O3	0.2579(2)	0.2041(7)	0.5331(3)	0.3301(3)	2

**Table 4.4 Selected Bond Lengths ( $\text{\AA}$ ) of  $\text{Li}_{0.08}\text{Fe}_{0.46}\text{SbWO}_6$** 

Fe – O1 ( $\times 2$ )	2.037(3)
Fe – O2 ( $\times 2$ )	2.048(4)
Fe – O2 ( $\times 2$ )	2.354(3)
< Fe – O >	2.146
Sb – O1 ( $\times 2$ )	2.059(3)
Sb – O3 ( $\times 2$ )	1.817(3)
Sb – O3 ( $\times 2$ )	2.106(3)
< Sb – O >	1.994
W – O1 ( $\times 2$ )	1.880(3)
W – O3 ( $\times 2$ )	1.712(0)
W – O2 ( $\times 2$ )	2.359(3)
< W – O >	1.983

### 4.3.2 FE-SEM and EDX Analysis

The morphology and elemental composition of  $\text{LiSbWO}_6$  and  $\text{Li}_{0.08}\text{Fe}_{0.46}\text{SbWO}_6$  are investigated by FE-SEM and EDX analysis, respectively. Figure 4.5 and Figure 4.6 shows FE-SEM images and corresponding EDX spectra of the as synthesized compounds. The parent compound,  $\text{LiSbWO}_6$  shows rounded rectangular bar-like morphology throughout the imaging area. The morphology remains intact after the ion exchange as well. The retention of morphology on ion exchange is indicative of its topotactic nature with preservation of the parent crystal structure [19]. The width of the bar-like crystallites vary in the range of 1-2  $\mu\text{m}$  while they are sub-micrometer to few micrometers long. The elemental compositions as obtained from the EDX analyses, on both spot and area basis, are in good agreement with the nominal compositions.

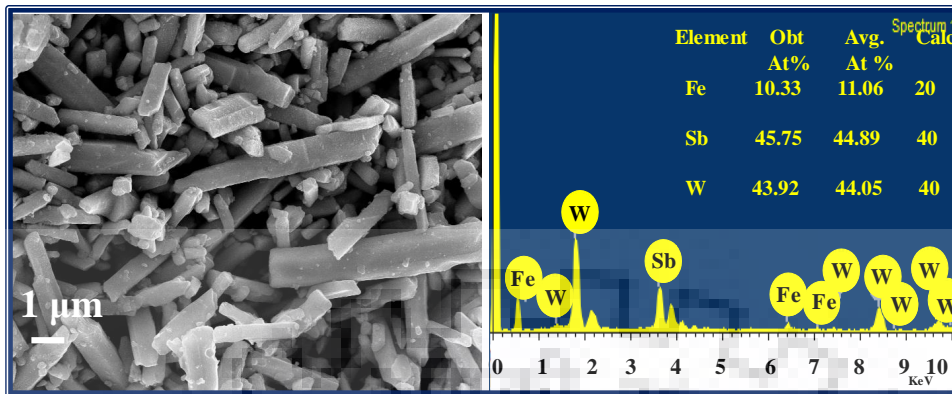


**Figure 4.5** (a) FE-SEM image and (b) corresponding EDX data for  $\text{Li}_{0.08}\text{Fe}_{0.46}\text{SbWO}_6$  after 48 h of ion exchange.

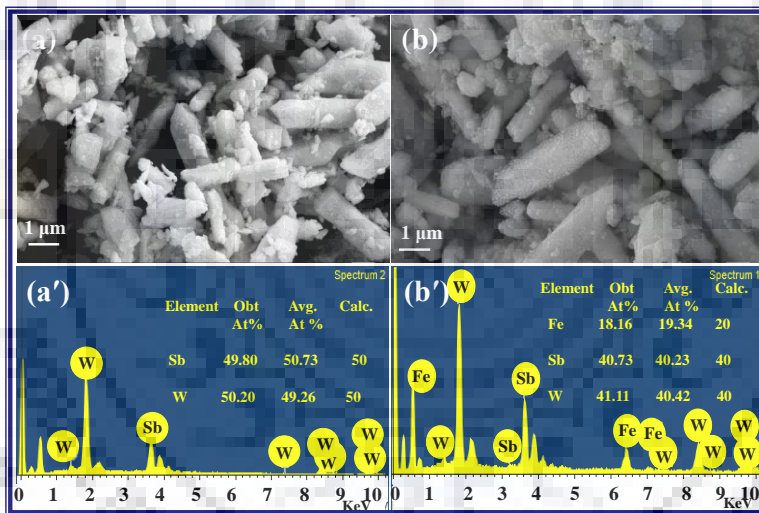


**Figure 4.6** (a, b) FE-SEM images and (a', b') corresponding EDX for  $\text{LiSbWO}_6$  and  $\text{Li}_{0.08}\text{Fe}_{0.46}\text{SbWO}_6$ .

### 4.3.3 FE-SEM-EDX Line Scan Analysis

An EDX line scan analysis was carried out at a selected rectangular area to examine the elemental distribution in the synthesized sample. The FE-SEM-EDX line scan images are shown in Figure 4.7. The results of elemental scanning shows that all the elements (iron,



antimony and tungsten) are homogeneously distributed along the line of the scan covering all the crystallites that are present along the line of the image.

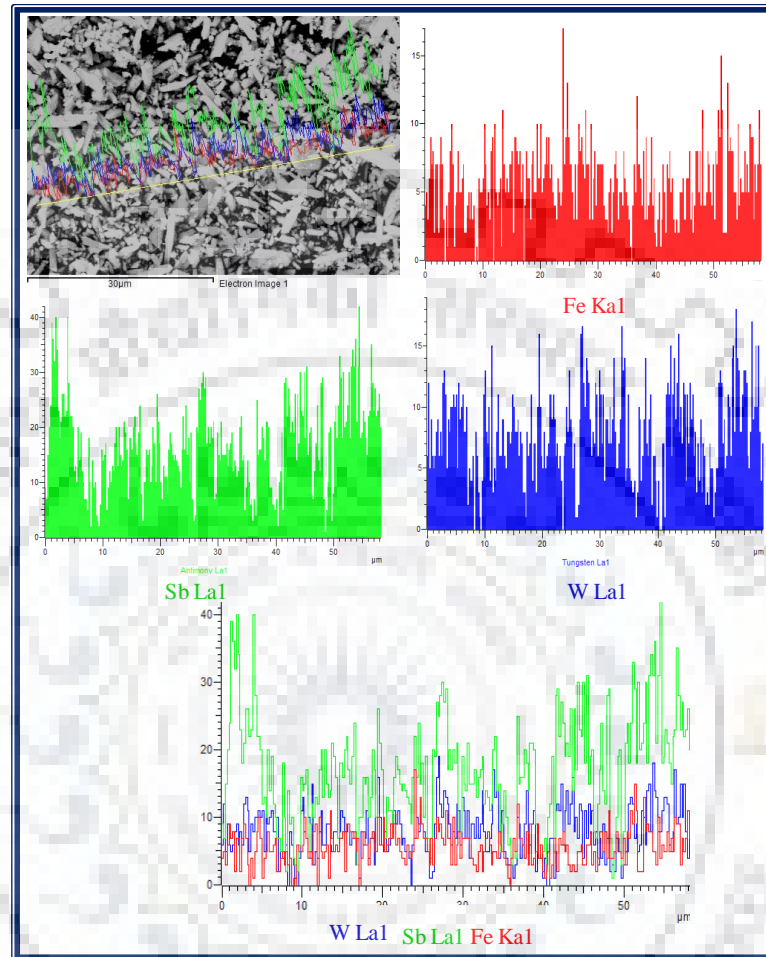


**Figure 4.7** EDX line scan of Fe, Sb and W for  $\text{Li}_{0.08}\text{Fe}_{0.46}\text{SbWO}_6$  along with the corresponding bright field SEM image.

#### 4.3.4 HR-TEM Analysis

The crystalline nature of  $\text{Li}_{0.08}\text{Fe}_{0.46}\text{SbWO}_6$  is confirmed by HR-TEM and SAED studies. The HR-TEM displayed in Figure 4.8(a) clearly shows the lattice fringes with a repetitive distance of 0.495 nm, which is consistent with the  $c$ -parameter of the unit cell. Indexed representative diffraction spots in the SAED pattern are shown in Figure 4.8(b). The

indexed SAED spots are consistent with the orthorhombic system and are in good agreement with the data obtained from P-XRD analysis.

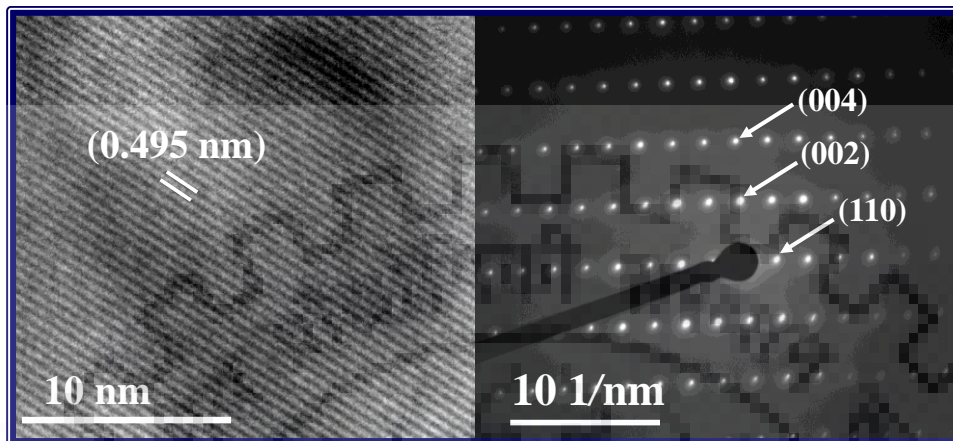


**Figure 4.8** (a) HR-TEM image and (b) selected SAED patterns for  $\text{Li}_{0.08}\text{Fe}_{0.46}\text{SbWO}_6$ .

#### 4.3.5 UV-vis DRS Analysis

The UV-vis DRS data (Figure. 4.9a), show absorption edge of the parent  $\text{LiSbWO}_6$  compound to lie in the UV region ( $\lambda_{\text{abs}} < 400$  nm) while for ion-exchanged  $\text{Li}_{0.08}\text{Fe}_{0.46}\text{SbWO}_6$  compound to lie in the visible region (up to  $\sim 700$  nm). This amounts to a significant reduction of the indirect band gap of  $\text{Li}_{0.08}\text{Fe}_{0.46}\text{SbWO}_6$  to 2.06 eV from 3.05 eV of the parent, as estimated from the Tauc plot [31, 32] (Figure. 4.9b).

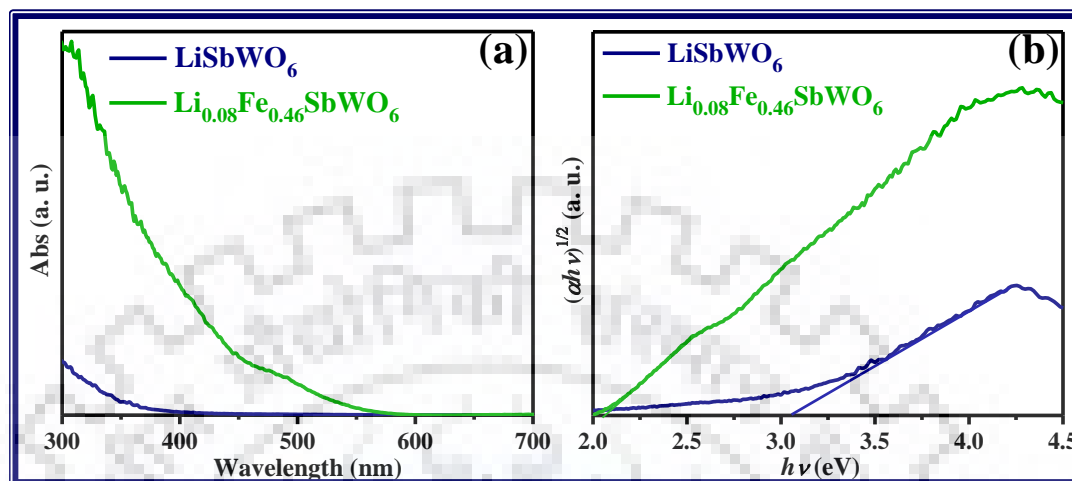


**Figure 4.9** (a) K-M plots and (b) Tauc plots for  $\text{LiSbWO}_6$  and  $\text{Li}_{0.08}\text{Fe}_{0.46}\text{SbWO}_6$ .

#### 4.3.6 XPS Analysis

To determine the oxidation state of Fe in the ion exchanged compound XPS spectra of Fe 2p is recorded. Figure 4.10 show Fe2p binding energies of 723.2 and 709.6 eV correspond to the spin-orbit coupled Fe  $2p_{1/2}$  and Fe  $2p_{3/2}$  states, respectively corresponding largely to the presence of  $\text{Fe}^{2+}$  in  $\text{Li}_{0.08}\text{Fe}_{0.46}\text{SbWO}_6$ . The survey spectra of  $\text{Li}_{0.1}\text{Fe}_{0.45}\text{NbWO}_6$  in Figure 4.11 are shown Sb  $3d^5$  peak at 530.7 eV, Fe- $2p_{1/2}$  723.2 eV, Fe- $2p_{3/2}$  709.6 eV and W 4f peak 35.9 eV and these are the characteristic peaks for Sb (V) and Fe (II) and W(VI) oxidation state respectively.

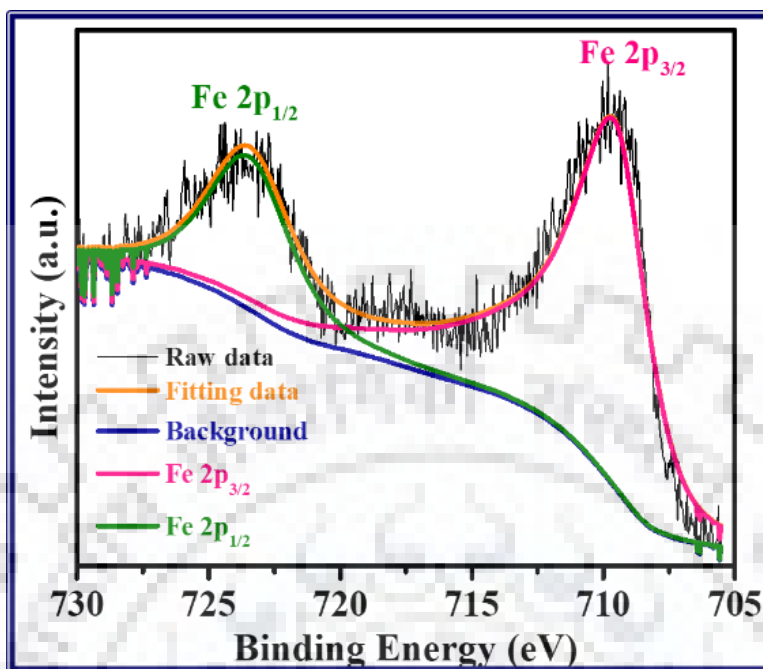


Figure 4.10 Fe 2p XPS of  $\text{Li}_{0.08}\text{Fe}_{0.46}\text{SbWO}_6$ .

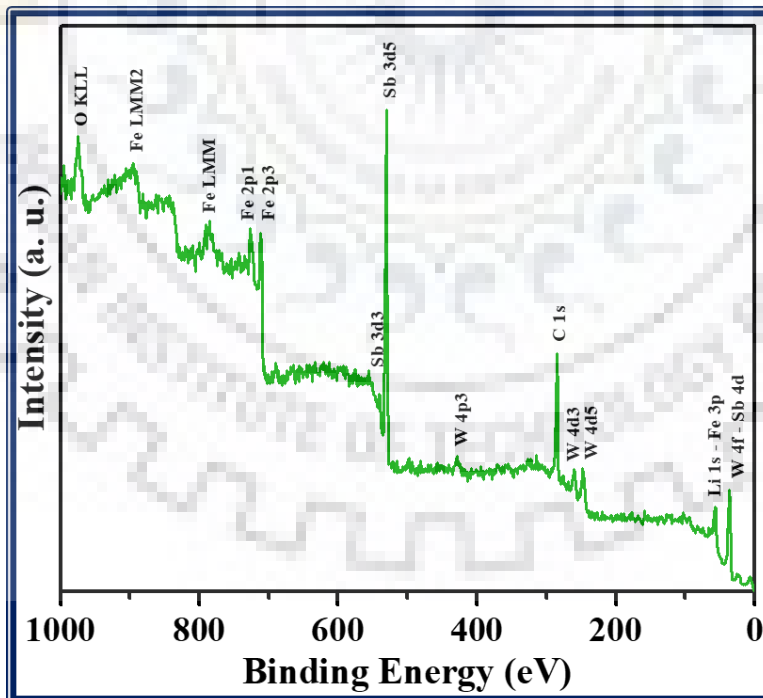
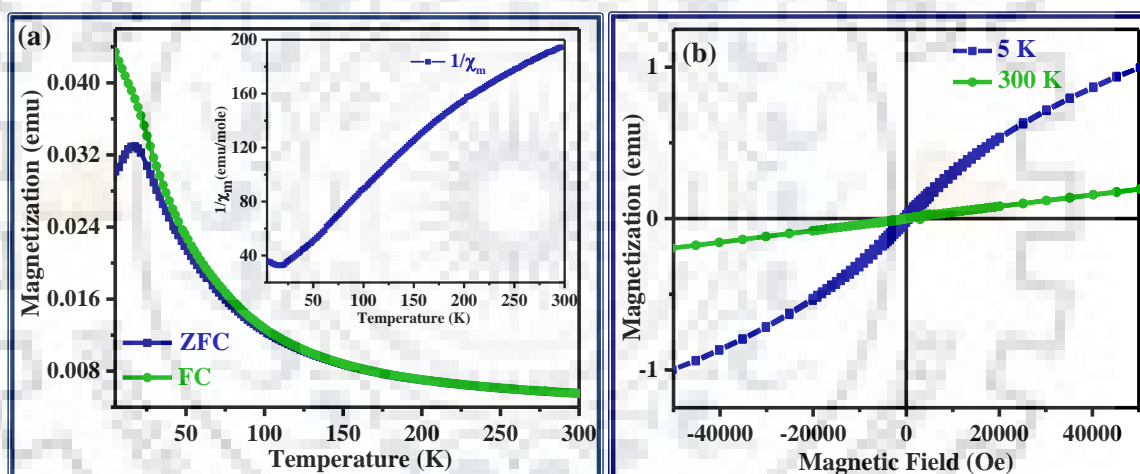


Figure 4.11 XPS Survey spectra of  $\text{Li}_{0.08}\text{Fe}_{0.46}\text{SbWO}_6$ .

## 4.3.7 Magnetic Measurements

Temperature-dependent magnetization data in a 1000 Oe applied magnetic field are collected for  $\text{Li}_{0.08}\text{Fe}_{0.46}\text{SbWO}_6$  and are shown in Figure 4.12. The molar susceptibility data (ZFC) show antiferromagnetic transition at  $\sim 20$  K (inset). Magnetization vs Field data indicates weak hysteresis loop at 5 K due to some spin canting. At 300 K it shows paramagnetic behavior. Unlike  $\text{Li}_{0.1}\text{Fe}_{0.45}\text{NbWO}_6$ , where isolated  $\text{Fe}^{2+}$  are present, Fe(II) dimers can exist in  $\text{Li}_{0.08}\text{Fe}_{0.46}\text{SbWO}_6$  due to the presence of edge-shared chains of  $\text{LiO}_6$  octahedra running along the  $c$ -direction in the tri- $\alpha$ - $\text{PbO}_2$  structure. This probably is responsible for the low-temperature antiferromagnetic transition in the compound. The high temperature paramagnetic moment, ( $\mu_{\text{obs}} = 4.4 \mu_{\text{B}}$  per f. u.), however, matches well with the spin-only moment of high spin  $\text{Fe}^{2+}$ .



**Figure 4.12** (a) Molar and inverse molar susceptibility vs. temperature and (b) magnetization vs field data for  $\text{Li}_{0.08}\text{Fe}_{0.46}\text{SbWO}_6$ .

**Table 4.5** Magnetic Data for  $\text{Li}_{0.08}\text{Fe}_{0.46}\text{SbWO}_6$  Calculated from the Linear Fit of the  $\chi_{\text{m}}^{-1}$  vs. T Plot

Compound	C (emu/mole)	$\theta$ (K)	$\mu_{\text{eff}}$ (B.M.)
$\text{Li}_{0.08}\text{Fe}_{0.46}\text{SbWO}_6$	2.38	167.6	4.4

In summary, the ion exchange of LiSbWO<sub>6</sub> with Fe(II) has been achieved by refluxing an aqueous solution of FeCl<sub>2</sub>·4H<sub>2</sub>O under argon atmosphere at 60 °C for 4 days. The close resemblance of the P-XRD pattern of the ion exchanged sample with that of the parent substantiated the topotactic nature of the exchange. The retention of particle morphology upon exchange was established by FE-SEM studies while the elemental compositions were determined by EDX analysis. The crystal structure of Li<sub>0.08</sub>Fe<sub>0.46</sub>SbWO<sub>6</sub> was refined by Rietveld refinement of P-XRD data. The HR-TEM and SAED analyses further lend support on the topotactic nature of exchange by the fact that the distance between lattice fringes and indexed diffraction spots are consistent with the P-XRD data. The low-temperature antiferromagnetic transition observed in Li<sub>0.08</sub>Fe<sub>0.46</sub>SbWO<sub>6</sub> is supportive of Fe(II) dimer formation. This can possibly occur in Li<sub>0.08</sub>Fe<sub>0.46</sub>SbWO<sub>6</sub> due to the presence of edge-shared chains of LiO<sub>6</sub> octahedra running along the *c*-direction of the tri- $\alpha$ -PbO<sub>2</sub> structure, in contrary to the presence of corner shared LiO<sub>6</sub> octahedra in the trirutile structure. The topotactic ion exchange described here offers new possibilities to synthesize metastable phases with three-dimensional structures with corner and/or edge shared polyhedral connectivity, and hitherto explore interesting optical, electronic and magnetic properties.



## REFERENCES

- (1) Gopalakrishnan, J.; Bhat, V.; Raveau, B.  $\text{A}'\text{LaNb}_2\text{O}_7$ : A New Series of Layered Perovskites Exhibiting Ion exchange and Intercalation Behavior. *Mater. Res. Bull.* **1987**, *22*, 413-417.
- (2) Viciu, L.; Liziard, N.; Golub, V.; Kodenkandath, T. A.; Wiley, J. B. Transition-Metal Dion-Jacobson Layered Perovskites,  $\text{M}_{0.5}\text{LaNb}_2\text{O}_7$ . *Mater. Res. Bull.* **2004**, *39*, 2147-2154.
- (3) Schaak, R. E.; Mallouk, T. E.; Topochemical Synthesis of Three Dimensional Perovskites from Lamellar Precursors. *J. Am. Chem. Soc.* **2000**, *122*, 2798-2803.
- (4) Viciu, L.; Caruntu, G.; Royant, N.; Koenig, J.; Zhou, W. L.; Kodenkandath, T. A.; Wiley, J. B. Formation of Metal-Anion Arrays Within Layered Perovskite Hosts. Preparation of a Series of New Metastable Transition-Metal Oxyhalides,  $(\text{MCl})\text{LaNb}_2\text{O}_7$  ( $\text{M} = \text{Cr}, \text{Mn}, \text{Fe}, \text{Co}$ ). *Inorg. Chem.* **2002**, *41*, 3385-3388.
- (5) Kodenkandath, T. A.; Lalena, J. N.; Zhou, W. L.; Carpenter, E. E.; Sangregorio, C.; Falster, A. U.; Simmons, W. B.; O'Connor, C. J.; Wiley, J. B. Assembly of Metal-Anion Arrays within a Perovskite Host. Low-Temperature synthesis of New Layered Copper-Oxyhalides,  $(\text{CuX})\text{LaNb}_2\text{O}_7$ ,  $\text{X} = \text{Cl}, \text{Br}$ . *J. Am. Chem. Soc.* **1999**, *121*, 10743-10746.
- (6) Josepha, E. A.; Farooq, S.; Mitchell, C. M.; Wiley, J. B. Synthesis and Thermal Stability Studies of a Metastable Dion-Jacobson Double-Layered Neodymium – Niobate Perovskite. *J. Solid State Chem.* **2014**, *216*, 85-90.
- (7) Tsujimoto, Y.; Kitada, A.; Uemura, Y. J.; Goko, T.; Aczel, A.A.; Williams, T. J.; Luke, G. M.; Narumi, Y.; Kindo, K.; Nishi, M.; Aijiro, Y.; Yoshimura, K.; Kageyama, H. Two-Dimensional  $S = 1$  Quantum Antiferromagnet  $(\text{NiCl})\text{Sr}_2\text{Ta}_3\text{O}_{10}$ . *Chem. Mater.* **2010**, *22*, 4625- 4631.
- (8) Gopalakrishnan, J.; Bhat, V.  $\text{A}_2\text{Ln}_2\text{Ti}_3\text{O}_{10}$  ( $\text{A} = \text{Potassium or Rubidium}; \text{Ln} = \text{Lanthanum or Rare Earth}$ ): A New Series of Layered Perovskites Exhibiting Ion Exchange. *Inorg. Chem.* **1987**, *26*, 4299-4301.
- (9) Toda, K.; Watanabe, J.; Sato, M. Crystal Structure Determination of Ion-Exchangeable Layered Perovskite Compounds,  $\text{K}_2\text{La}_2\text{Ti}_3\text{O}_{10}$  and  $\text{Li}_2\text{La}_2\text{Ti}_3\text{O}_{10}$ . *Mater. Res. Bull.* **1996**, *31*, 1427-1435.
- (10) McIntyre, R. A.; Falster, A. U.; Li, S.; Simmons, W. B.; O'Connor, C. J.; Wiley, J. B. Opening a Perovskite to Valence Manipulation: Two-Step Topotactic Route to a New Mixed-Valence Titanate,  $\text{Na}_{1+x}\text{Ca}_{x/2}\text{LaTiO}_4$ . *J. Am. Chem. Soc.* **1998**, *120*, 217-218.
- (11) Gopalakrishnan, J.; Shivakumar, T.; Ramesha, K.; Thangadurai, V.; Subbanna, G. N. Transformations of Ruddlesden-Popper Oxides to New Layered Perovskite Oxides by Metathesis Reactions. *J. Am. Chem. Soc.* **2000**, *122*, 6237-6241.

- (12) Neiner, D.; Golub, V.; Wiley, J. B. Synthesis and Characterization of the New Layered Perovskite,  $\text{Na}_{0.10}(\text{VO})_{0.45}\text{LaTiO}_{4.n}\text{H}_2\text{O}$ . *Mater. Res. Bull.* **2004**, *39*, 1385-1392.
- (13) Neiner, D.; Spinu, L.; Golub, V.; Wiley, J. B. Ferromagnetism in Topochemically Prepared Layered Perovskite  $\text{Li}_{0.3}\text{Ni}_{0.85}\text{La}_2\text{Ti}_3\text{O}_{10}$ . *Chem. Mater.* **2006**, *18*, 518-524.
- (14) Hyeon, K.-A.; Byeon, S.-H. Synthesis and Structure of New Layered Oxides,  $\text{M}^{\text{II}}\text{La}_2\text{Ti}_3\text{O}_{10}$  ( $\text{M} = \text{Co}, \text{Cu}, \text{and Zn}$ ). *Chem. Mater.* **1999**, *11*, 352-357.
- (15) Schaak, R.; Mallouk, T. E. Topochemical Synthesis of Three-Dimensional Perovskites from Lamellar Precursors. *J. Am. Chem. Soc.* **2000**, *122*, 2798.
- (16) Schaak, R. E.; Mallouk, T. E. Perovskites by Design: A Toolbox of Solid-State Reactions. *Chem. Mater.* **2002**, *14*, 1455-1471.
- (17) Ranmohotti, K. G. S.; Josepha, E.; Choi, J.; Zhang, J.; Wiley, J. B. Topochemical Manipulation of Perovskites: Low Temperature Reaction Strategies for Directing Structure and Properties. *Adv. Mater.* **2011**, *23*, 442-460.
- (18) Boltersdorf, J.; Maggard, P. A. Silver Exchange of Layered Metal Oxides and Their Photocatalytic Activities. *ACS Catal.* **2013**, *3*, 2547-2555.
- (19) Gustin, L.; Hosaka, Y.; Tassel, C.; Aharen, T.; Shimakawa, Y.; Kageyama, H.; Wiley, J. B. From Tetrahedral to Octahedral Iron Coordination: Layer Compression in Topochemically Prepared  $\text{FeLa}_2\text{Ti}_3\text{O}_{10}$ . *Inorg. Chem.* **2016**, *55*, 11529-11537.
- (20) Clearfield, A. Structure and Ion Exchange Properties of Tunnel Type Titanium Silicates. *Solid State Sci.* **2001**, *3*, 103-112.
- (21) Cai, J.; Liu, J.; Gao, Z.; Navrotsky, A.; Suib, S. L. Synthesis and Anion Exchange of Tunnel Structure Akaganeite. *Chem. Mater.* **2001**, *13*, 4595-4602.
- (22) Rowsell, J. L. C.; Taylor, N. J.; Nazar, L. F. Structure and Ion Exchange Properties of a New Cobalt Borate with a Tunnel Structure "Templated" by  $\text{Na}^+$ . *J. Am. Chem. Soc.* **2002**, *124*, 6522-6523.
- (23) Kataoka, K.; Awaka, J.; Kijima, N.; Hayakawa, H.; Ohshima, K.; Akimoto, J. Ion-Exchange Synthesis, Crystal Structure, and Electrochemical Properties of  $\text{Li}_2\text{Ti}_6\text{O}_{13}$ . *Chem. Mater.* **2011**, *23*, 2344-2352.
- (24) Pérez-Flores, J. C.; Baetz, C.; Hoelzel, M.; Kuhn, A.; García-Alvarado, F.  $\text{H}_2\text{Ti}_6\text{O}_{13}$ , A New Protonated Titanate Prepared by  $\text{Li}^+/\text{H}^+$  Ion Exchange: Synthesis, Crystal Structure and Electrochemical Li Insertion Properties. *RSC Adv.* **2012**, *2*, 3530-3540.
- (25) Bhuvanesh, N. S. P.; Woodward, P. M. Thermally Induced A'-A Site Exchange in Novel Layered Perovskites  $\text{Ag}_2[\text{Ca}_{1.5}\text{M}_3\text{O}_{10}]$  ( $\text{M} = \text{Nb}, \text{Ta}$ ). *J. Am. Chem. Soc.* **2002**, *124*, 14294-14295.
- (26) Cushing, B. L.; Falster, A. U.; Simmons, W. B.; Wiley, J. B. A Multivalent Ion Exchange Route to Lamellar Calcium Cobalt Oxides,  $\text{Ca}_x\text{CoO}_2$  ( $x \leq 0.5$ ). *Chem. Commun.* **1996**, 2635-2636.

- (27) Patino, M. A.; Smith, T.; Zhang, W.; Halasyamani, P. S.; Hayward, M. A. Cation Exchange in a 3D Perovskite— Synthesis of Ni<sub>0.5</sub>TaO<sub>3</sub>. *Inorg. Chem.* **2014**, *53*, 8020–8024.
- (28) Meena, V.; Mandal, T. K. Topotactic Ion Exchange in a Three-Dimensional Close-Packed Trirutile Structure with an Octahedral Network. *Inorg. Chem.* **2019**, *58*, 2921–2924.
- (29) Blasse, G.; dePauw, A. D. M. Crystal Structure of Some LiMe<sup>5+</sup>Me<sup>6+</sup>O<sub>6</sub> Compounds. *J. inorg. nucl. Chem.* **1970**, *32*, 3960–3961.
- (30) Bail, A. Le.; Duroy, H.; Fourquet, J. L. Ab-Initio Structure Determination of LiSbWO<sub>6</sub> by X-Ray Powder Diffraction. *Mater. Res. Bull.* **1988**, *23*, 447–452.
- (31) Tauc, J.; Grigorovic, R.; Vancu, A. Optical Properties and Electronic Structure of Amorphous Germanium. *Phys. Status Solidi* **1966**, *15*, 627–637.
- (32) Joshi, U. A.; Maggard, P. A. CuNb<sub>3</sub>O<sub>8</sub>: A p-Type Semiconducting Metal Oxide Photoelectrode. *J. Phys. Chem. Lett.* **2012**, *3*, 1577–1581.

## ***CHAPTER -5***

***Topotactic transformation of a non-magnetic ribbon type layered titanate,  $\text{Na}_2\text{Ti}_3\text{O}_7$ , into magnetic analogs through ion exchange***



## Topotactic Transformation of Non-Magnetic Ribbon Type Layered Titanates, $\text{Na}_2\text{Ti}_3\text{O}_7$ into Magnetic Analogs through Ion Exchange

### 5.1 INTRODUCTION

Titanium ( $\text{TiO}_2$ ) has been the most studied oxide material in the last 30 years due to its wider applications range and biocompatibility [1, 2]. In addition, to its traditional use as a pigment, it has improved the effectiveness of dye-sensitized solar cells [3], it has unique activity in photocatalysis [4-7] and it's the central element of the perovskite solar cell blocking layer [8-10]. It is also used extensively in sensors [11, 12], memory gages [13], supercapacitors [14, 15] and batteries [16]. There have been considerable attention in the layered titanates with interlayer alkali metals due to its potential use as ion exchangers, adsorbents as well as photocatalysts and catalysts in various technologies [17-20].  $\text{Na}_2\text{Ti}_3\text{O}_7$  belongs to the alkali titanates family with the general formula,  $\text{A}_2\text{Ti}_n\text{O}_{2n+1}$  ( $n = 3$ ). Akimoto and co-workers [21] reported ion exchange in  $\text{Na}_2\text{Ti}_3\text{O}_7$  by  $\text{Na}^+/\text{H}^+$  in the acidic solution at 333 K to produce hydrogen titanium oxide,  $\text{H}_2\text{Ti}_3\text{O}_7$ , as a product. By ion exchange and hydrothermal techniques two kinds of  $\text{H}_2\text{Ti}_3\text{O}_7$  powder were developed by Kim *et al.* and they examined the  $\text{H}_2$  sensing properties of the  $\text{TiO}_2$  sensors derived from  $\text{H}_2\text{Ti}_3\text{O}_7$  [22]. Chiba *et al.* reported ion exchange in  $\text{Na}_2\text{Ti}_3\text{O}_7$  through molten salt  $\text{LiNO}_3/\text{LiCl}$  at 260-280 °C and formed layered lithium titanate,  $\text{Li}_2\text{Ti}_3\text{O}_7$ , as a product [23]. Szirmai *et al.* have synthesized homogenous  $\text{Mn}^{2+}$  and  $\text{Gd}^{3+}$  co-doped titanate nanotubes through ionic exchange of scroll type trititanate nanotubes prepared by the hydrothermal synthesis method [24]. The alkaline and acidic ion exchange capacity for the sulfate of Co, Ni and Cu(II) have been studied and the copper cations have been verified to have the highest ion exchange capacities as the general behavior [25]. Nunes and co-workers [26] reported the ion exchange in layered alkali titanates by Cu(II) and concluded that  $\text{Na}_2\text{Ti}_3\text{O}_7$  shows the highest ion exchange capacity of  $3.0 \text{ mmol g}^{-1}$ . Vithal and co-workers have prepared nano-sized  $\text{Ag}^+$  and  $\text{Cu}^{2+}$  doped titanate by the acid free ion exchange reaction in  $\text{Na}_2\text{Ti}_3\text{O}_7$  at room temperature [27]. Sirinakorn *et al.* investigated ion exchange in  $\text{Na}_2\text{Ti}_3\text{O}_7$  by the aqueous solution of indium (III) chloride [28].



The crystal structure of  $\text{Na}_2\text{Ti}_3\text{O}_7$ , built on an octahedra of  $\text{TiO}_6$  connected by the edges, to form a zigzag  $3 \times 2 \times \infty$  ribbons (Figure 5.1). These ribbons are linked through vertices and create a layered framework. Sodium ions are distributed among two separate crystallographic sites, Na1 and Na2, between the octahedral layers within this framework. In the  $P2_1/m$  monoclinic space group, all atoms of the crystal structure,  $\text{Na}_2\text{Ti}_3\text{O}_7$  occupy special positions [29-31].

In the present study, new magnetic titanates,  $\text{Na}_{2(1-x)}\text{M}_x\text{Ti}_3\text{O}_7$  ( $\text{M} = \text{Mn}, \text{Fe}, \text{Co}, \text{Ni}$ ) were synthesized for the first time from non-magnetic  $\text{Na}_2\text{Ti}_3\text{O}_7$  host material by topotactic ion exchange reaction. The optical and magnetic properties after the topotactic ion exchange have been investigated.

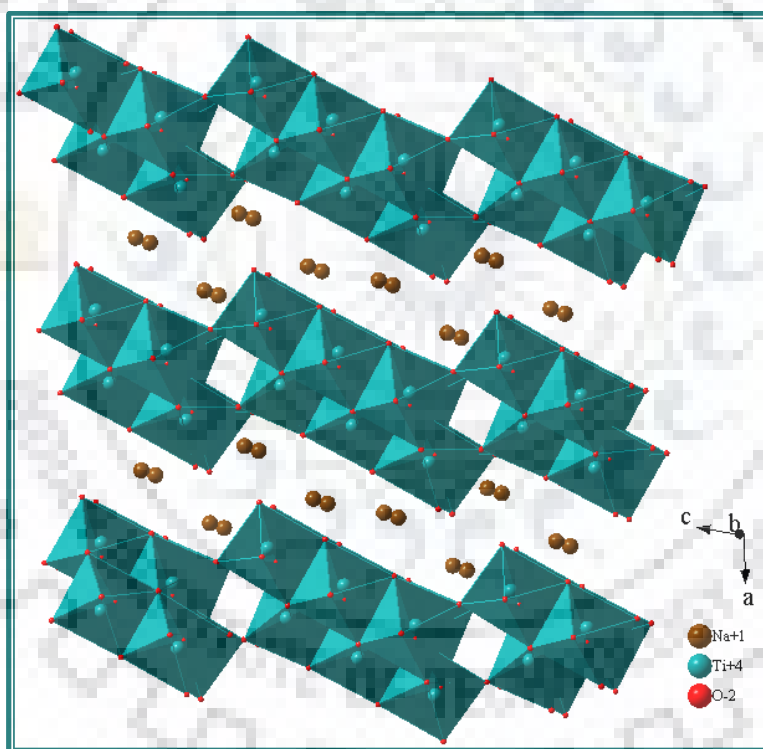


**Figure 5.1** Crystal Structure of  $\text{Na}_2\text{Ti}_3\text{O}_7$ .

## 5.2 EXPERIMENTAL SECTION

### 5.2.1 Materials and Synthesis

Pure  $\text{Na}_2\text{Ti}_3\text{O}_7$  was prepared by a solid-state reactions as reported in the literature [31]. For this purpose, stoichiometric quantities of anhydrous  $\text{Na}_2\text{CO}_3$  (Alfa Aesar,  $\geq 95.0\%$ ), anatase  $\text{TiO}_2$  (Sigma Aldrich,  $\geq 99.8\%$ ) were first weighed along with 10% excess of  $\text{Na}_2\text{CO}_3$  (to compensate the loss due to volatilization). These mixtures were ground thoroughly in an agate mortar for 1 hour and heated at  $800\text{ }^\circ\text{C}$  for 40 h with intermediate regrinding in a high quality alumina ( $\geq 99.8\% \text{ Al}_2\text{O}_3$ ) boat.

The ion exchange of  $\text{Na}_2\text{Ti}_3\text{O}_7$  (ca. 1 g) was performed in 100 mL of 0.2 M aqueous solution of  $\text{Mn}(\text{NO}_3)_2 \cdot 4\text{H}_2\text{O}$  (Sigma Aldrich,  $\geq 98.0\%$ ),  $\text{FeCl}_2 \cdot 4\text{H}_2\text{O}$  (Sigma Aldrich,  $\geq 99.0\%$ ),  $\text{Co}(\text{NO}_3)_2 \cdot 6\text{H}_2\text{O}$  (Sigma Aldrich,  $\geq 98.0\%$ ) and  $\text{Ni}(\text{NO}_3)_2 \cdot 6\text{H}_2\text{O}$  (SRL extra pure AR grade 99%) by stirring at  $60\text{ }^\circ\text{C}$  in Argon atmosphere for 2 days. Finally, the product was washed with distilled water for several times and dried at room temperature in a desiccator. The dried sample after ion exchange was orange-brown/brown/grey-green/light green in color for Mn, Fe, Co, and Ni, respectively.

## 5.3 RESULTS AND DISCUSSION

### 5.3.1 P-XRD Analysis

The P-XRD patterns of the as prepared compounds,  $\text{Na}_{2(1-x)}\text{M}_x\text{Ti}_3\text{O}_7$  ( $\text{M} = \text{Mn, Fe, Co and Ni}$ ) are shown in Figure 5.2. A comparison of the observed P-XRD data with that of the standard JCPDS data of the parent  $\text{Na}_2\text{Ti}_3\text{O}_7$  (JCPDS PDF # 31-1329) indicated the formation of single phase ribbon type layered titanate and the color change over from white was an indication for the exchange of transition metals in a topotactic fashion. All the peaks observed in the P-XRD pattern of the Mn, Fe, Co and Ni compounds, are indexable in the monoclinic  $P2_1/m$  space group. The least-squares refined lattice parameters for the parent and the Mn, Fe, Co and Ni-exchanged compounds are given in Table 5.1. The lattice parameters for the parent  $\text{Na}_2\text{Ti}_3\text{O}_7$  are in good agreement with the literature data. The indexed P-XRD data for  $\text{Na}_{0.02}\text{Mn}_{0.99}\text{Ti}_3\text{O}_7$ ,

$\text{Na}_{0.16}\text{Fe}_{0.92}\text{Ti}_3\text{O}_7$ ,  $\text{Na}_{0.14}\text{Co}_{0.93}\text{Ti}_3\text{O}_7$  and  $\text{Na}_{0.02}\text{Ni}_{0.99}\text{Ti}_3\text{O}_7$  are given in Tables 5.2, 5.3, 5.4 and 5.5, respectively.

A closer look at the lattice parameters (Table 5.1) of  $\text{Na}_{2(1-x)}\text{M}_x\text{Ti}_3\text{O}_7$  series shows a slight decrease in the  $b$  and  $c$ -parameter, while the  $a$  parameter slightly increased as compared to the parent  $\text{Na}_2\text{Ti}_3\text{O}_7$ , excepting in case of the Co-compound, where a slight contraction was observed.

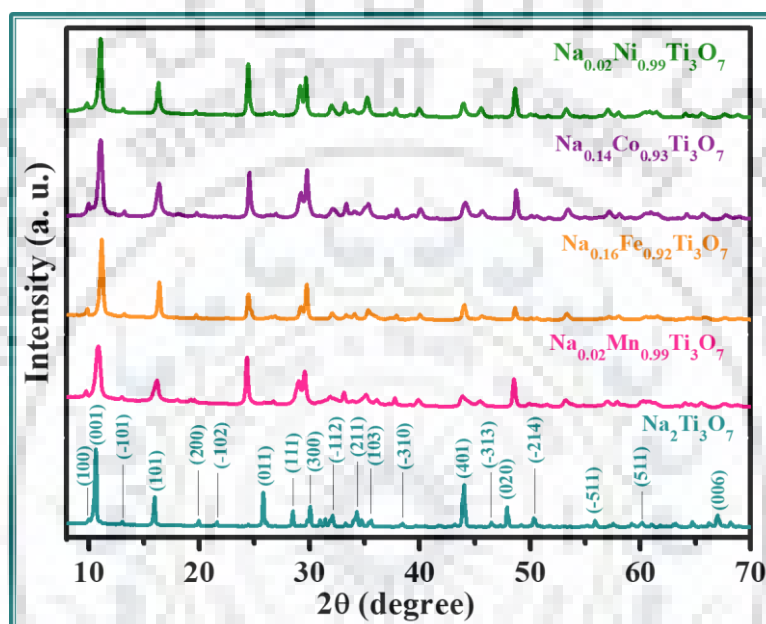


**Figure 5.2** P-XRD patterns of  $\text{Na}_2\text{Ti}_3\text{O}_7$ ,  $\text{Na}_{0.02}\text{Mn}_{0.99}\text{Ti}_3\text{O}_7$ ,  $\text{Na}_{0.16}\text{Fe}_{0.92}\text{Ti}_3\text{O}_7$ ,  $\text{Na}_{0.14}\text{Co}_{0.93}\text{Ti}_3\text{O}_7$  and  $\text{Na}_{0.02}\text{Ni}_{0.99}\text{Ti}_3\text{O}_7$ .

**Table 5.1** Lattice Parameters and Band Gap of  $\text{Na}_2\text{Ti}_3\text{O}_7$ ,  $\text{Na}_{0.02}\text{Mn}_{0.99}\text{Ti}_3\text{O}_7$ ,  $\text{Na}_{0.16}\text{Fe}_{0.92}\text{Ti}_3\text{O}_7$ ,  $\text{Na}_{0.14}\text{Co}_{0.93}\text{Ti}_3\text{O}_7$ , and  $\text{Na}_{0.02}\text{Ni}_{0.99}\text{Ti}_3\text{O}_7$

Compound	Lattice Parameters (Å)				Band gap ( $E_g$ ) (eV)
	$a$	$b$	$c$	$\beta$	
$\text{Na}_2\text{Ti}_3\text{O}_7$	9.117(1)	3.797(7)	8.555(1)	101.58(1)	3.47
$\text{Na}_{0.02}\text{Mn}_{0.99}\text{Ti}_3\text{O}_7$	9.248(9)	3.746(2)	8.326(1)	101.65(7)	2.15

$\text{Na}_{0.16}\text{Fe}_{0.92}\text{Ti}_3\text{O}_7$	9.184(6)	3.739(2)	8.092(9)	101.78(9)	1.99
$\text{Na}_{0.14}\text{Co}_{0.93}\text{Ti}_3\text{O}_7$	9.041(8)	3.730(3)	8.151(5)	101.40(9)	2.56
$\text{Na}_{0.02}\text{Ni}_{0.99}\text{Ti}_3\text{O}_7$	9.202(8)	3.739(2)	8.154(5)	101.82(1)	2.86

Table 5.2. Indexed P-XRD Data for  $\text{Na}_{0.02}\text{Mn}_{0.99}\text{Ti}_3\text{O}_7$ 

$h\ k\ l$	$d_{\text{obs}} (\text{Å})$	$d_{\text{calc}} (\text{Å})$	$I_{\text{obs}}$
1 0 0	9.073	9.058	7
0 0 1	8.154	8.154	100
$\bar{1}$ 0 1	6.803	6.779	4
1 0 1	5.498	5.530	30
2 0 1	3.653	3.658	2
1 1 1	3.097	3.101	18
$\bar{3}$ 0 1	3.010	3.011	7
3 0 0	3.017	3.019	20
2 0 2	2.770	2.765	7
$\bar{3}$ 0 2	2.701	2.701	5
$\bar{2}$ 1 2	2.549	2.544	6
$\bar{3}$ 1 1	2.362	2.359	3
2 1 2	2.258	2.259	1
$\bar{2}$ 0 4	2.060	2.090	35
4 0 1	2.052	2.062	40
0 2 0	1.874	1.873	20
4 1 3	1.719	1.720	1

$$a = 9.248 (9) \text{ Å}, b = 3.746 (2) \text{ Å}, c = 8.326 (1) \text{ Å}, \beta = 101.65 (7) \text{ Å}$$

Table 5.3 Indexed P-XRD Data for  $\text{Na}_{0.16}\text{Fe}_{0.92}\text{Ti}_3\text{O}_7$ 

$h k l$	$d_{\text{obs}} (\text{\AA})$	$d_{\text{calc}} (\text{\AA})$	$I_{\text{obs}}$
1 0 0	8.963	8.991	7
0 0 1	7.921	7.921	100
$\bar{1}$ 0 1	6.687	6.656	4
1 0 1	5.400	5.420	30
2 0 1	4.493	4.495	2
1 1 1	3.614	3.606	18
$\bar{3}$ 0 1	3.071	3.077	7
3 0 0	3.009	3.014	20
2 0 2	2.816	2.823	7
$\bar{3}$ 0 2	2.686	2.686	5
$\bar{2}$ 1 2	2.628	2.630	6
$\bar{3}$ 1 1	2.507	2.507	3
2 1 2	2.347	2.346	1
$\bar{2}$ 0 4	2.251	2.247	35
4 0 1	2.055	2.055	40
0 2 0	1.870	1.869	20
4 1 3	1.716	1.714	1
4 0 3	1.588	1.588	2

$$a = 9.184 (6) \text{ \AA}, b = 3.739 (2) \text{ \AA}, c = 8.092 (1) \text{ \AA}, \beta = 101.78 (9) \text{ \AA}$$

Table 5.4 Indexed P-XRD Data for  $\text{Na}_{0.14}\text{Co}_{0.93}\text{Ti}_3\text{O}_7$ 

$h k l$	$d_{\text{obs}} (\text{\AA})$	$d_{\text{calc}} (\text{\AA})$	$I_{\text{obs}}$
1 0 0	8.856	8.863	7
0 0 1	7.993	7.990	100
$\bar{1}$ 0 1	6.661	6.621	4
1 0 1	5.407	5.425	30
2 0 1	3.591	3.586	2
1 1 1	3.067	3.073	18
$\bar{3}$ 0 1	2.971	2.968	7
3 0 0	2.795	2.803	20
2 0 2	2.696	2.702	7
$\bar{3}$ 0 2	2.510	2.512	5
$\bar{2}$ 1 2	2.327	2.322	6
$\bar{3}$ 1 1	2.250	2.252	3
2 1 2	2.040	2.037	1
$\bar{2}$ 0 4	1.970	1.973	35
4 0 1	1.866	1.865	40
0 2 0	1.793	1.793	20
4 1 3	1.609	1.608	1

$$a = 9.041 (8) \text{ \AA}, b = 3.730 (3) \text{ \AA}, c = 8.151 (5) \text{ \AA}, \beta = 101.40 (9) \text{ \AA}$$



Table 5.5 Indexed P-XRD Data for  $\text{Na}_{0.02}\text{Ni}_{0.99}\text{Ti}_3\text{O}_7$ 

$h k l$	$d_{\text{obs}} (\text{\AA})$	$d_{\text{calc}} (\text{\AA})$	$I_{\text{obs}}$
1 0 0	8.981	9.007	7
0 0 1	7.993	7.980	100
$\bar{1}$ 0 1	6.714	6.693	4
1 0 1	5.434	5.444	30
2 0 1	3.628	3.617	2
1 1 1	3.075	3.082	18
$\bar{3}$ 0 1	3.016	3.021	7
3 0 0	2.819	2.827	20
2 0 2	2.700	2.706	7
$\bar{3}$ 0 2	2.530	2.528	5
$\bar{2}$ 1 2	2.351	2.350	6
$\bar{3}$ 1 1	2.253	2.251	3
2 1 2	2.058	2.059	1
$\bar{2}$ 0 4	1.982	1.980	35
4 0 1	1.869	1.869	40
0 2 0	1.717	1.716	20
4 1 3	1.612	1.612	1

$$a = 9.202 (8) \text{ \AA}, b = 3.739 (2) \text{ \AA}, c = 8.154 (1) \text{ \AA}, \beta = 101.82 (1) \text{ \AA}$$

### 5.3.2 FE-SEM and EDX Analysis

The morphology and elemental composition of  $\text{Na}_2\text{Ti}_3\text{O}_7$  and ion-exchanged compounds,  $\text{Na}_{0.01}\text{Mn}_{0.99}\text{Ti}_3\text{O}_7$ ,  $\text{Na}_{0.16}\text{Fe}_{0.92}\text{Ti}_3\text{O}_7$ ,  $\text{Na}_{0.14}\text{Co}_{0.93}\text{Ti}_3\text{O}_7$  and  $\text{Na}_{0.01}\text{Ni}_{0.99}\text{Ti}_3\text{O}_7$  were investigated by FE-SEM and EDX analysis, respectively. Figure 5.3 shows FE-SEM images and corresponding EDX spectra of the as synthesized compounds. The morphological homogeneity in all the analyzed areas is shown by FE-SEM images taken at several location of the sample. The parent  $\text{Na}_2\text{Ti}_3\text{O}_7$  shows uniform rod type morphology, which may be a reflection of the ribbon type structure of the titanates. The ion-exchanged products,  $\text{Na}_{0.02}\text{Mn}_{0.99}\text{Ti}_3\text{O}_7$ ,  $\text{Na}_{0.16}\text{Fe}_{0.92}\text{Ti}_3\text{O}_7$ ,  $\text{Na}_{0.14}\text{Co}_{0.93}\text{Ti}_3\text{O}_7$  and  $\text{Na}_{0.02}\text{Ni}_{0.99}\text{Ti}_3\text{O}_7$  were also shown rod like morphology indicating retention of the layered structure. All these compounds demonstrate the morphological consistency throughout the imaging region. The microstructures are quite uniform, though there is a substantial variation in crystallites size spanning from several hundred nanometers to few micrometers. The elemental composition is derived from the EDX analysis of the sample and the average composition is used to derive the final composition of the compounds.

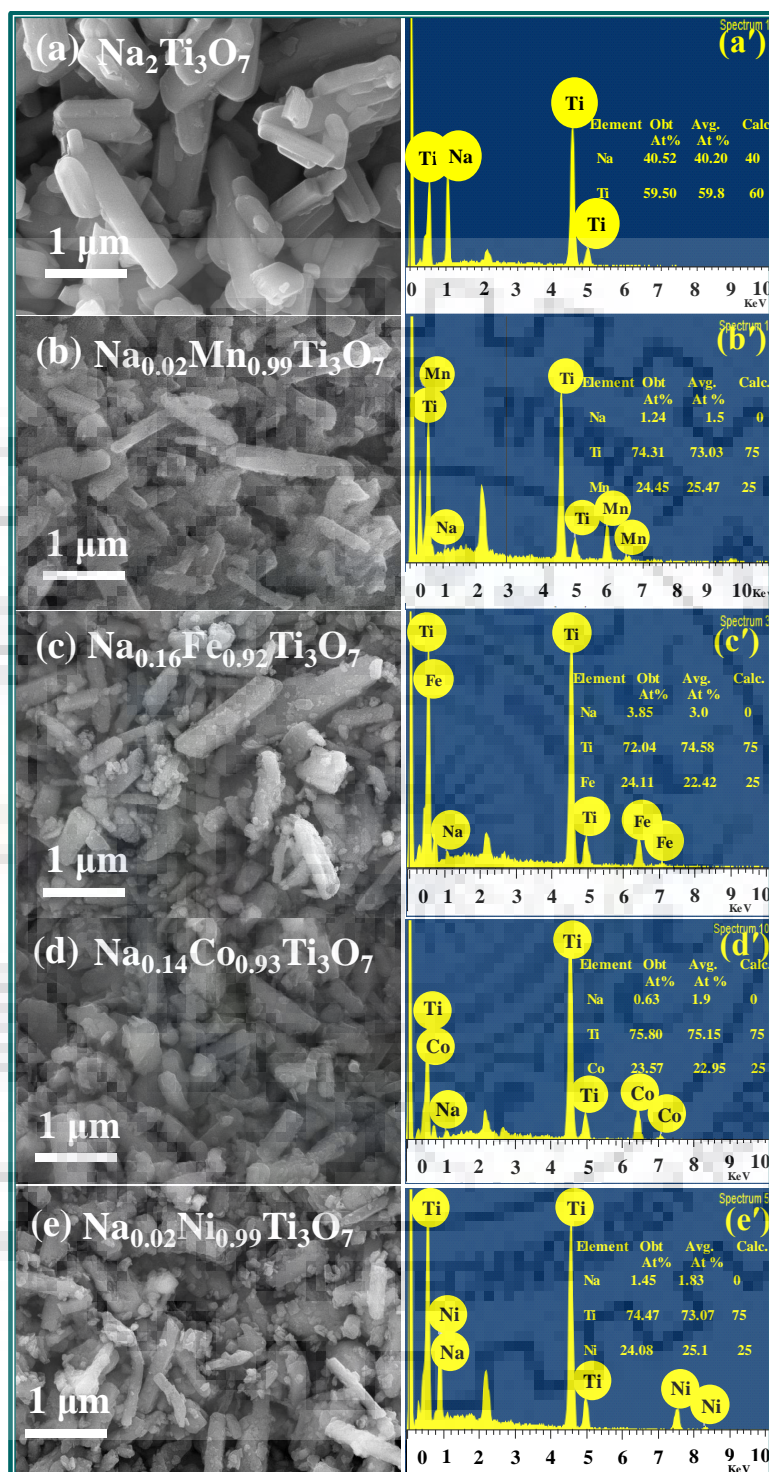


**Figure 5.3** (a-e) FE-SEM and corresponding EDX data (a'-e') of (a, a')  $\text{Na}_2\text{Ti}_3\text{O}_7$ , (b, b')  $\text{Na}_{0.02}\text{Mn}_{0.99}\text{Ti}_3\text{O}_7$ , (c, c')  $\text{Na}_{0.16}\text{Fe}_{0.92}\text{Ti}_3\text{O}_7$ , (d, d')  $\text{Na}_{0.14}\text{Co}_{0.93}\text{Ti}_3\text{O}_7$  and (e, e')  $\text{Na}_{0.02}\text{Ni}_{0.99}\text{Ti}_3\text{O}_7$ .

### 5.3.3 FE-SEM-EDX Elemental Mapping Analysis

In order to investigate the elemental distribution in  $\text{Na}_2\text{Ti}_3\text{O}_7$  and in the ion-exchanged compounds,  $\text{Na}_{0.02}\text{Mn}_{0.99}\text{Ti}_3\text{O}_7$ ,  $\text{Na}_{0.16}\text{Fe}_{0.92}\text{Ti}_3\text{O}_7$ ,  $\text{Na}_{0.14}\text{Co}_{0.93}\text{Ti}_3\text{O}_7$  and  $\text{Na}_{0.02}\text{Ni}_{0.99}\text{Ti}_3\text{O}_7$ , EDX elemental mapping was performed in a selected rectangular area of the sample as shown in the bright field SEM image. The results (Figure 5.4) indicate that all the elements in the selected rectangular area of the FE-SEM image are distributed homogeneously and consistently.

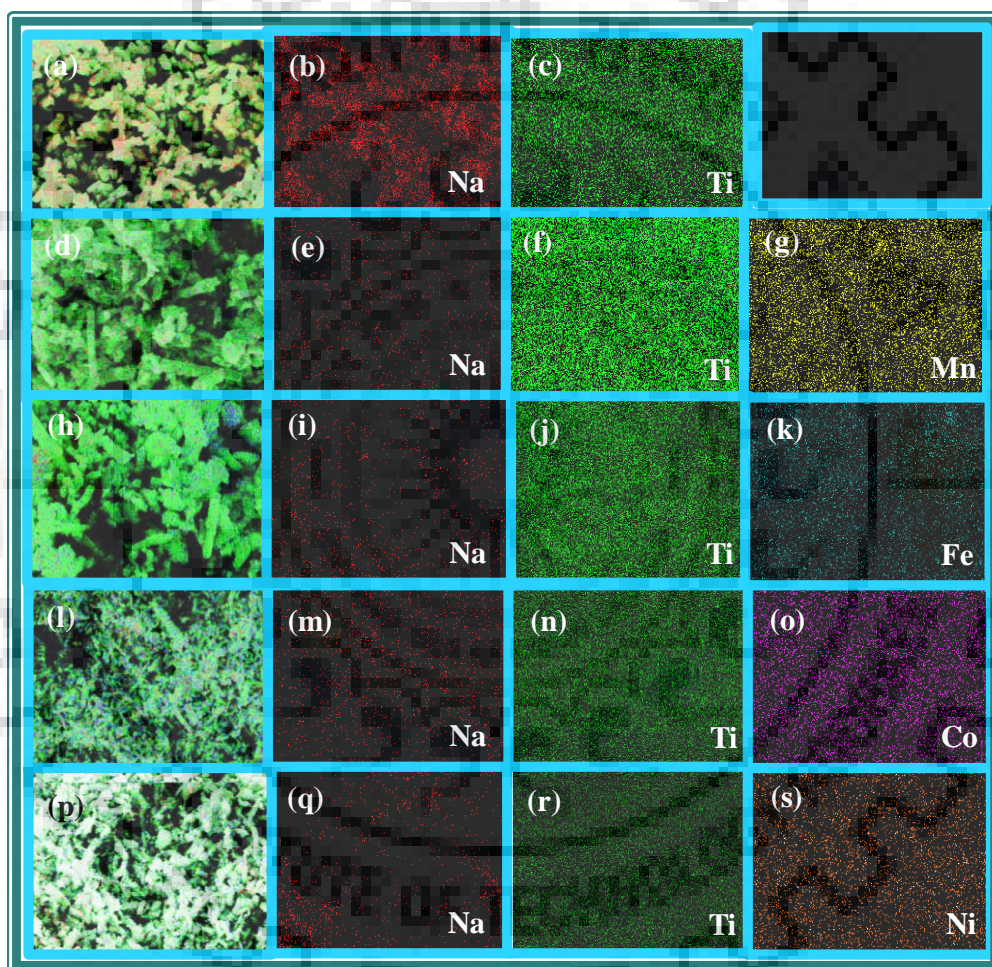


**Figure 5.4** EDX elemental mapping of Na, Ti, Mn, Fe, Co and Ni for  $\text{Na}_2\text{Ti}_3\text{O}_7$ ,  $\text{Na}_{0.02}\text{Mn}_{0.99}\text{Ti}_3\text{O}_7$ ,  $\text{Na}_{0.16}\text{Fe}_{0.92}\text{Ti}_3\text{O}_7$ ,  $\text{Na}_{0.14}\text{Co}_{0.93}\text{Ti}_3\text{O}_7$  and  $\text{Na}_{0.02}\text{Ni}_{0.99}\text{Ti}_3\text{O}_7$  along with the corresponding bright field SEM image.



### 5.3.4 HR-TEM Analysis

The high-resolution TEM study was carried out with one of the representative sample of ion-exchanged compound,  $\text{Na}_{0.02}\text{Ni}_{0.99}\text{Ti}_3\text{O}_7$ . The HR-TEM image (Figure 5.5 (a)) clearly revealed the lattice fringes and the distance between the fringes indicated is calculated to be 0.39 nm, which is consistent with the  $b$ -parameter of the unit cell. The SAED pattern is indexable in the monoclinic space group and consistent with the lattice parameters obtained from the P-XRD data analysis. Indexing of few representative spots in the SAED pattern are shown in Figure 5.5 (b). While the SAED pattern indicates polycrystalline nature of the sample, the HR-TEM confirms high crystallinity often compounds even after ion exchange.

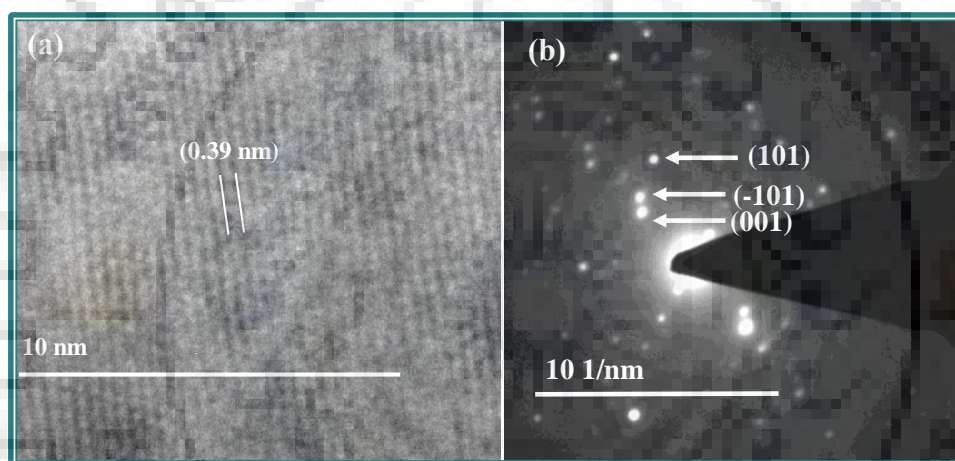


**Figure 5.5** (a) HR-TEM and (b) SAED pattern of  $\text{Na}_{0.02}\text{Ni}_{0.99}\text{Ti}_3\text{O}_7$ .

### 5.3.5 XPS Analysis

XPS measurements have carried out to evaluate the oxidation state of the transition metals present in  $\text{Na}_{0.02}\text{Mn}_{0.99}\text{Ti}_3\text{O}_7$ ,  $\text{Na}_{0.16}\text{Fe}_{0.92}\text{Ti}_3\text{O}_7$ ,  $\text{Na}_{0.14}\text{Co}_{0.93}\text{Ti}_3\text{O}_7$  and  $\text{Na}_{0.02}\text{Ni}_{0.99}\text{Ti}_3\text{O}_7$ . The XPS data was calibrated with respect to C-1s binding energy of 284.8 eV. XPS spectra of Mn, Fe, Co and Ni are shown in Figures 5.6, 5.7, 5.8 and 5.9.

The high-resolution XPS spectra of Mn 2p as shown in Figure 5.6, indicating Mn 2p<sub>1/2</sub> and Mn 2p<sub>3/2</sub> binding energies of 654.7 and 640.7 eV, respectively confirming Mn<sup>2+</sup> state and some Mn seems to be partly oxidized in Mn<sup>3+</sup> state. Figure 5.7 show the Fe 2p binding energies of 723.0 and 709.7 eV corresponds to the spin-orbit coupled Fe 2p<sub>1/2</sub> and Fe 2p<sub>3/2</sub> states,

respectively, corresponding largely to the presence of  $\text{Fe}^{2+}$  in  $\text{Na}_{0.16}\text{Fe}_{0.92}\text{Ti}_3\text{O}_7$ . Similarly, Co  $2p_{1/2}$  and Co- $2p_{3/2}$  spectra (Figure 5.8) shows peaks at binding energies of 796.2 and 780.7 eV, respectively conforming to the presence of  $\text{Co}^{2+}$  in  $\text{Na}_{0.14}\text{Co}_{0.93}\text{Ti}_3\text{O}_7$ . Symmetrical peaks at binding energies of 872.5 and 854.8 eV, due to Ni- $2p_{1/2}$  and Ni- $2p_{3/2}$ , respectively (Figure 5.9) also confirm nickel as  $\text{Ni}^{2+}$  in  $\text{Na}_{0.02}\text{Ni}_{0.99}\text{Ti}_3\text{O}_7$ .

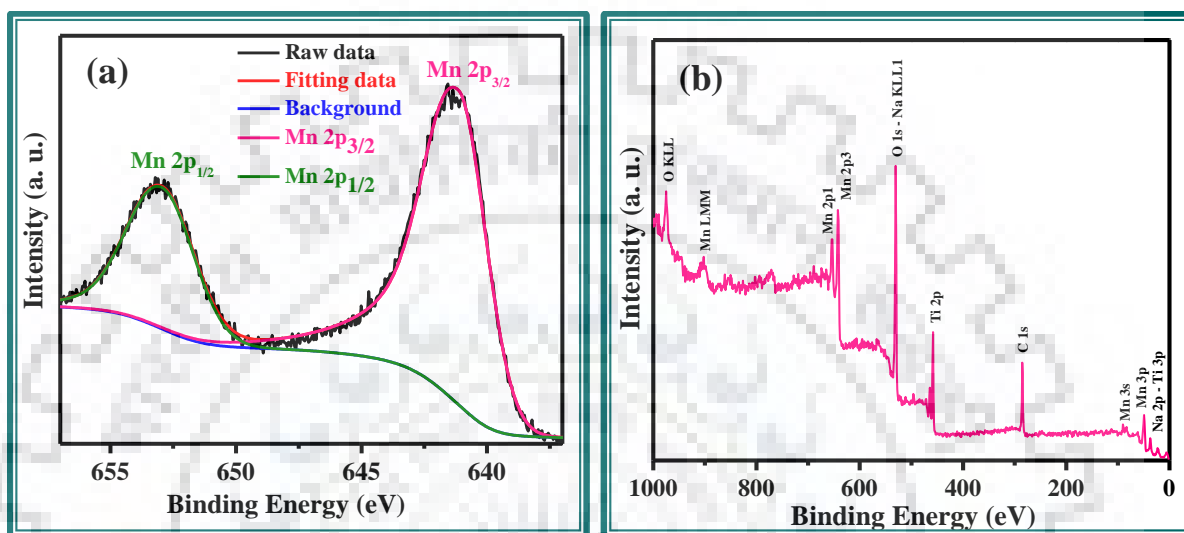


Figure 5.6 High resolution Mn-2p and survey XPS of  $\text{Na}_{0.02}\text{Mn}_{0.99}\text{Ti}_3\text{O}_7$ .

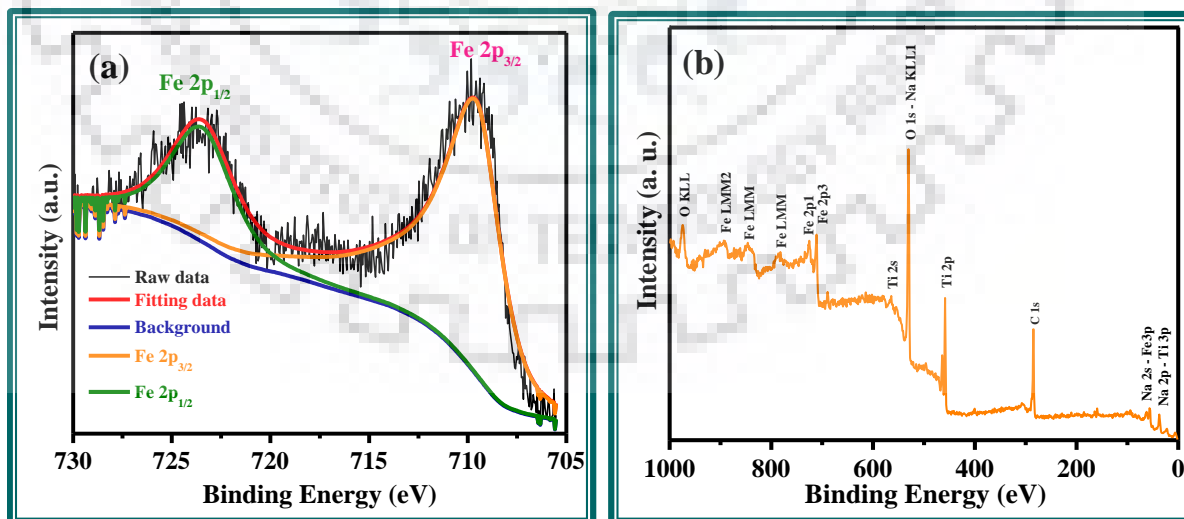


Figure 5.7 High resolution Fe-2p and survey XPS of  $\text{Na}_{0.02}\text{Fe}_{0.99}\text{Ti}_6\text{O}_{13}$ .



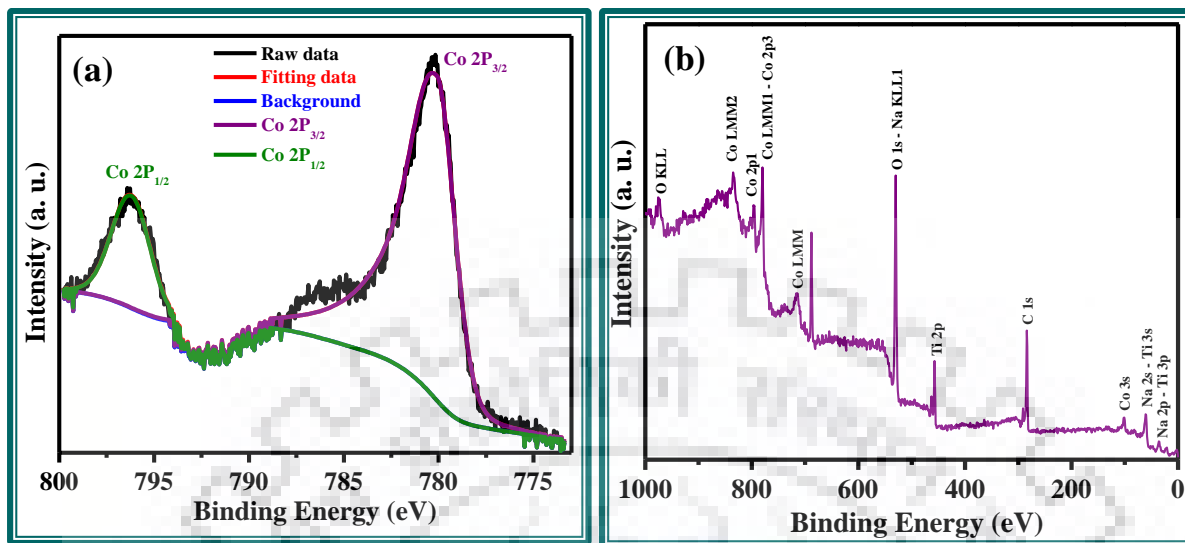


Figure 5.8 High resolution Co-2p and survey XPS of  $\text{Na}_{0.14}\text{Co}_{0.93}\text{Ti}_3\text{O}_7$ .

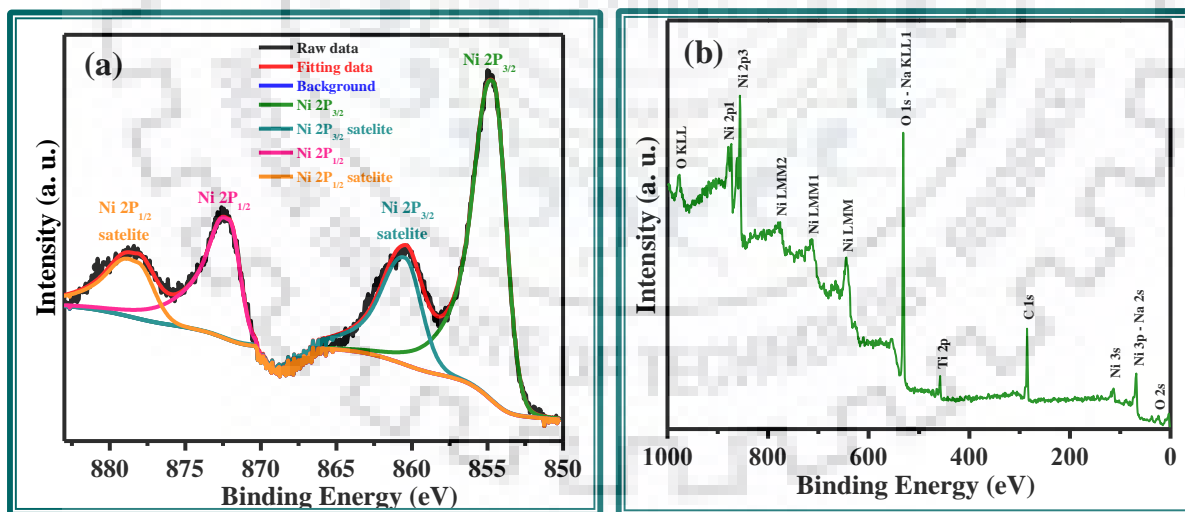
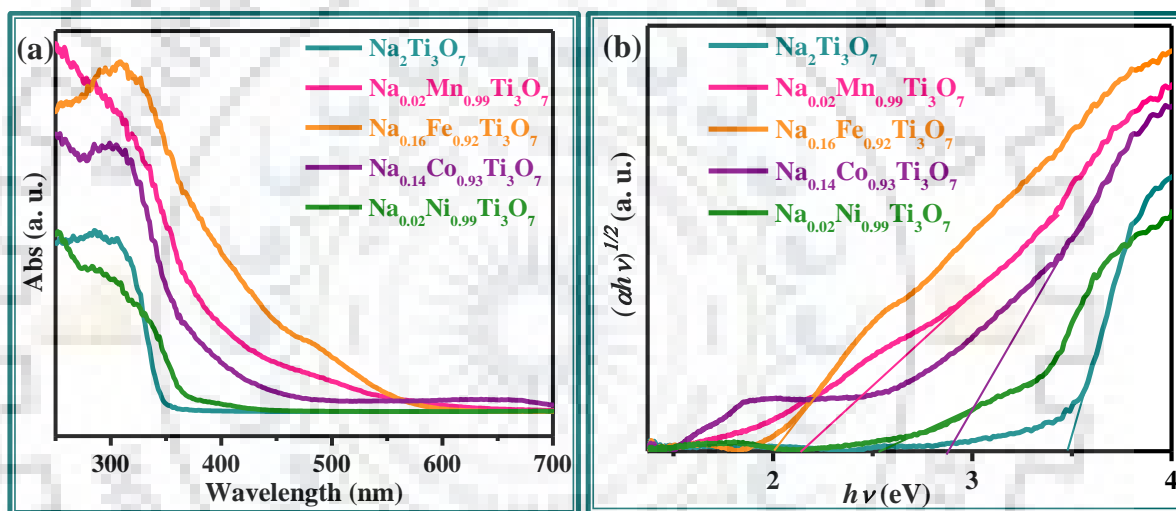


Figure 5.9 High resolution Ni-2p and survey XPS spectra of  $\text{Na}_{0.02}\text{Ni}_{0.99}\text{Ti}_3\text{O}_7$ .

### 6.3.6 UV-vis DRS Analysis

The UV-vis DRS data (Figure 5.10(a)) show absorption edge of the parent  $\text{Na}_2\text{Ti}_3\text{O}_7$  compound to lie in the UV region ( $\lambda < 400$  nm) while for all the ion exchanged compounds the absorption edges lie in the visible region ( $\lambda > 400$  nm). The band gap energies ( $E_g$ ) for all the oxides were estimated from the plot of  $(\alpha h\nu)^{1/2}$  versus  $h\nu$  (Figure 5.10(b)) [32,33]. The  $E_g$  for the compounds are given in Table 5.1. Because all the ion exchanged compounds reported here are visible light absorbers with band gaps ranging from  $\sim 1.99$  - 2.86 eV, the compounds may find their potential use in visible-light-driven photocatalysis.

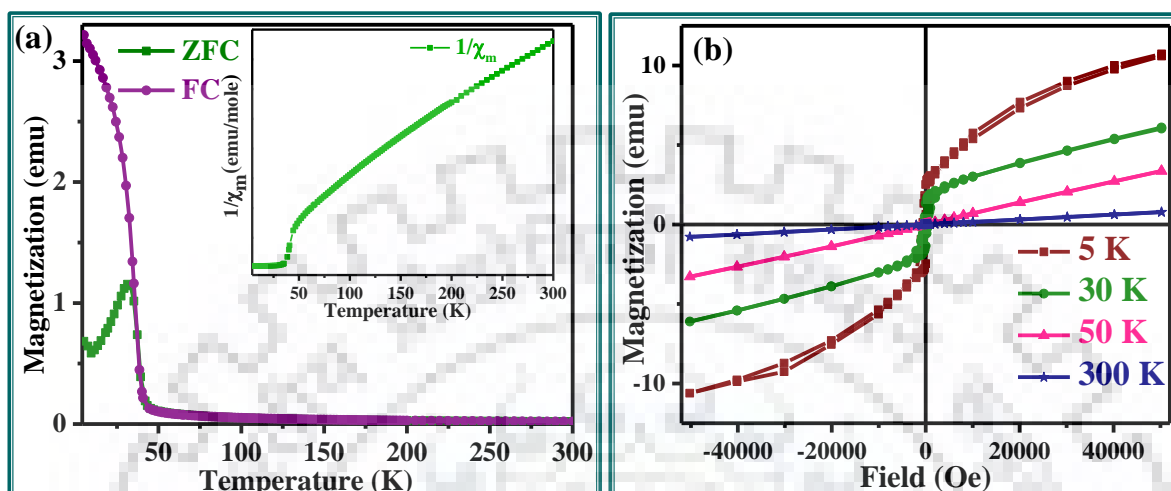


**Figure 5.10** (a) UV-vis DRS data and (b) Tauc plots for  $\text{Na}_2\text{Ti}_3\text{O}_7$ ,  $\text{Na}_{0.02}\text{Mn}_{0.99}\text{Ti}_3\text{O}_7$ ,  $\text{Na}_{0.16}\text{Fe}_{0.92}\text{Ti}_3\text{O}_7$ ,  $\text{Na}_{0.14}\text{Co}_{0.93}\text{Ti}_3\text{O}_7$  and  $\text{Na}_{0.02}\text{Ni}_{0.99}\text{Ti}_3\text{O}_7$ .

### 5.3.7 Magnetic Measurement

The magnetization vs temperature curve of  $\text{Na}_{0.02}\text{Mn}_{0.99}\text{Ti}_3\text{O}_7$  is shown in Figure 5.11. Two anomalies are noticed in the low temperature region. The transition at 32 K is attributed to an antiferromagnetic one, while the transition at  $T = 8$  K is associated with a ferrimagnetic like correlation between the  $\text{Mn}^{2+}$  and  $\text{Mn}^{3+}$  spins that may arise due to spin canting. The sudden increase in magnetic susceptibility and the change in slope observed on  $\chi_m^{-1} = f(T)$  at

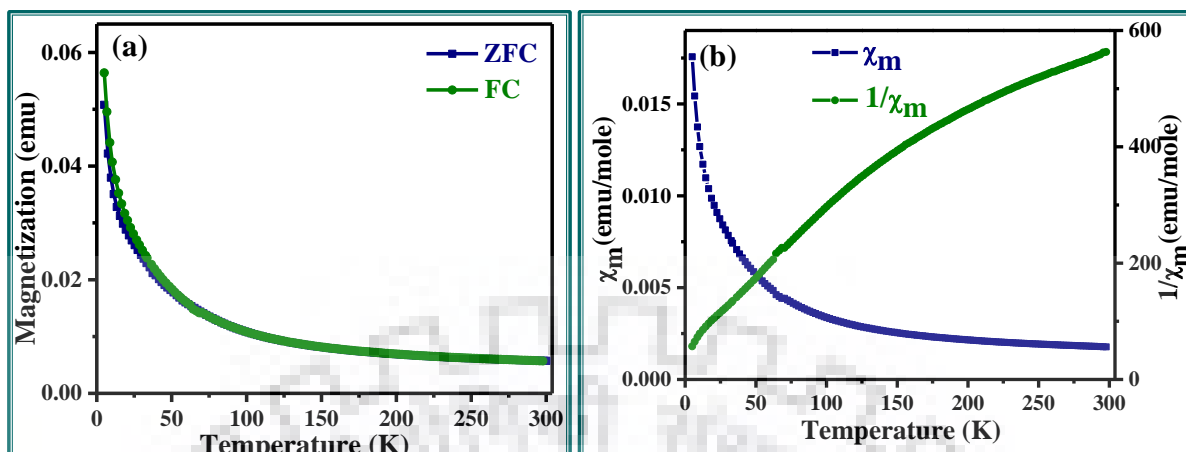
32 K can be attributed to the Curie temperature. The magnetization data clearly show pure paramagnetic behavior above 50 K while the magnetization at below 30 K is indicative of ferromagnetic like behavior.



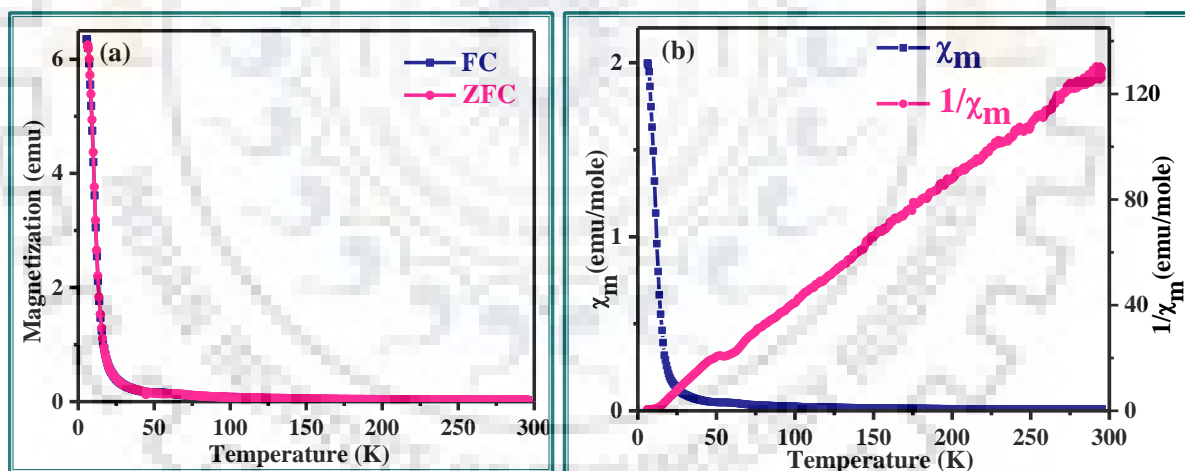
**Figure 5.11** (a) ZFC and FC magnetization vs. temperature and (b) magnetization vs. field plot for  $\text{Na}_{0.02}\text{Mn}_{0.99}\text{Ti}_3\text{O}_7$ . Inset of (a) show the inverse molar susceptibility vs. temperature plot for the FC data.

Figure 5.12 and 5.13 show the thermal evolution of magnetic susceptibility ( $\chi_m$ ) and its inverse ( $\chi_m^{-1}$ ) for the Fe and Co analogs, respectively. The variation of the inverse susceptibility ( $\chi^{-1}$ ) as a function of temperature follows the Curie-Weiss law. The linearity observed throughout the measured temperature range for  $\text{Na}_{0.14}\text{Co}_{0.93}\text{Ti}_3\text{O}_7$  can be assigned to nearly pure paramagnetic behaviour. In case of  $\text{Na}_{0.16}\text{Fe}_{0.92}\text{Ti}_3\text{O}_7$  a change in slope in the  $\chi_m^{-1}$  vs. T plot is observed with prevalent antiferromagnetic correlations.

In Figure 5.14, the magnetization vs temperature curve of  $\text{Na}_{0.02}\text{Ni}_{0.99}\text{Ti}_3\text{O}_7$  exhibit antiferromagnetism at  $\sim 8$  K. The magnetization data at 5 K, shows hysteresis loop indicating weak ferromagnetic interactions possibly due to the canting of the spin but at RT pure paramagnetic behavior was observed.



**Figure 5.12** (a) ZFC and FC magnetization vs. temperature and (b) molar susceptibility and inverse molar susceptibility vs. temperature plot for  $\text{Na}_{0.16}\text{Fe}_{0.92}\text{Ti}_3\text{O}_7$ .



**Figure 5.13** (a) ZFC and FC magnetization vs. temperature and (b) molar susceptibility and inverse molar susceptibility vs. temperature plot for  $\text{Na}_{0.14}\text{Co}_{0.93}\text{Ti}_3\text{O}_7$ .

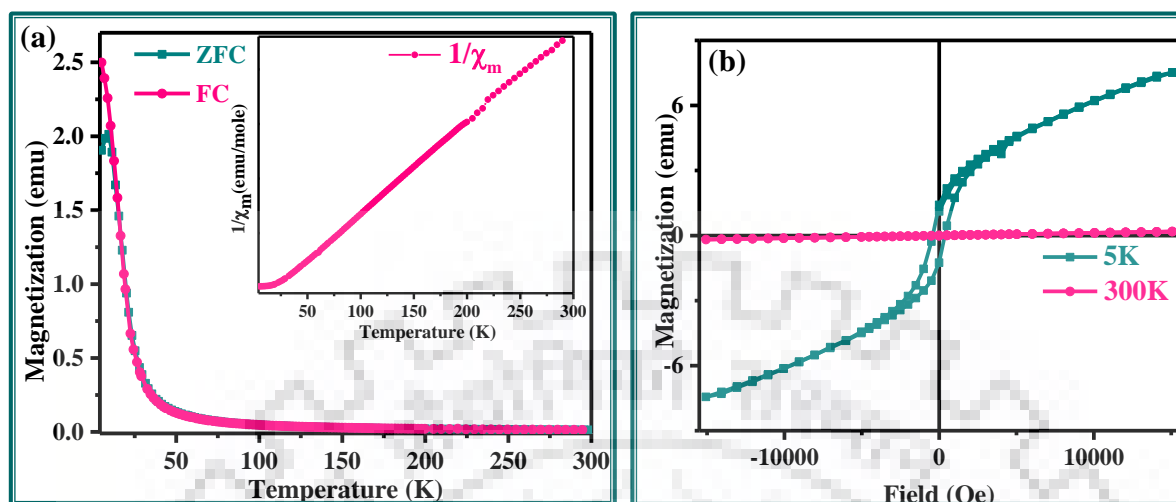


**Figure 5.14** (a) ZFC and FC magnetization vs. temperature and (b) magnetization vs. field plot for  $\text{Na}_{0.02}\text{Ni}_{0.99}\text{Ti}_3\text{O}_7$ . Inset of (a) show the inverse molar susceptibility vs. temperature plot for the FC data.

**Table 5.6** Magnetic Data for  $\text{Na}_{0.02}\text{Mn}_{0.99}\text{Ti}_3\text{O}_7$ ,  $\text{Na}_{0.16}\text{Fe}_{0.92}\text{Ti}_3\text{O}_7$ ,  $\text{Na}_{0.14}\text{Co}_{0.93}\text{Ti}_3\text{O}_7$  and  $\text{Na}_{0.02}\text{Ni}_{0.99}\text{Ti}_3\text{O}_7$  Calculated from the Linear Fit of the  $\chi_m^{-1}$  vs. T Plot

Compound	C (emu/mole)	$\theta$ (K)	$\mu_{\text{eff}}$ (cal.) (B. M.)	$\mu_{\text{eff}}$ (obs) (B. M.)
$\text{Na}_{0.02}\text{Mn}_{0.99}\text{Ti}_3\text{O}_7$	2.8	73.25	4.8	5.9
$\text{Na}_{0.16}\text{Fe}_{0.92}\text{Ti}_3\text{O}_7$	1.0	274.02	2.8	4.9
$\text{Na}_{0.14}\text{Co}_{0.93}\text{Ti}_3\text{O}_7$	2.3	3.16	4.3	4.3-5.9
$\text{Na}_{0.02}\text{Ni}_{0.99}\text{Ti}_3\text{O}_7$	1.1	-16.88	3.2	2.9-3.9

In summary, ribbon-type layered titanates, such as  $\text{Na}_{0.02}\text{Mn}_{0.99}\text{Ti}_3\text{O}_7$ ,  $\text{Na}_{0.16}\text{Fe}_{0.92}\text{Ti}_3\text{O}_7$ ,  $\text{Na}_{0.14}\text{Co}_{0.93}\text{Ti}_3\text{O}_7$  and  $\text{Na}_{0.02}\text{Ni}_{0.99}\text{Ti}_3\text{O}_7$  was prepared by topotactic ion exchange. The P-XRD patterns shows close resemblance with parent compound and a color change over from white to orange-brown/brown/grey-green/light green confirmed the exchange of transition metals in a topotactic fashion. The morphological homogeneity and elemental composition is established with FE-SEM and EDX studies for all the compounds. For  $\text{Na}_{0.02}\text{Ni}_{0.99}\text{Ti}_3\text{O}_7$ , in addition to the FE-SEM imaging, the TEM analysis also revealed rod-like morphology that are generally observed for oxides with ribbon-type/layered structures. The HR-TEM showed clear lattice fringes with interfringe spacing of 0.390 nm, which is consistent with the *b*-parameter of the monoclinic unit cell. The SAED pattern is also indexable in the monoclinic space group and consistent with the lattice parameters obtained from the P-XRD data. UV-vis DRS study confirmed the presence of visible band gaps for all the compounds ranging from 1.99 - 2.86 eV. XPS spectra revealed that after ion exchange Mn, Fe, Co and Ni exist in the +2 states. Magnetic measurements for  $\text{Na}_{0.02}\text{Mn}_{0.99}\text{Ti}_3\text{O}_7$  compound shows antiferromagnetic transition at 32 K, and at ~ 8 K it shows ferrimagnetic correlation, which may be arising due to spin canting. The corresponding Fe and Co compounds showed paramagnetic behaviors throughout the entire temperature range (5 – 300 K).  $\text{Na}_{0.02}\text{Ni}_{0.99}\text{Ti}_3\text{O}_7$  show antiferromagnetic transition. M vs H data for Mn and Ni at low temperatures (5 and 30 K for Mn and 5 K for Ni) showed hysteretic behavior which is a signature of ferrimagnetism possibly arising out of the spin canting.



## REFERENCES

- (1) Hashimoto, K.; Irie, H.; Fujishima, A. TiO<sub>2</sub> Photocatalysis: A Historical Overview and Future Prospects. *Jpn. J. Appl. Phys.* **2005**, *44*(12), 8269–8285.
- (2) Osterloh, F. E. Inorganic Materials as Catalysts for Photochemical Splitting of Water *Chem. Mater.* **2008**, *20*, 35–54.
- (3) O'Regan, B.; Grätzel, M. A Low-Cost, High-Efficiency Solar Cell Based on Dye-Sensitized Colloidal TiO<sub>2</sub> Films. *Nature* **1991**, *353*, 737–740.
- (4) Chen, X.; Mao, S. S. Titanium Dioxide Nanomaterials: Synthesis, Properties, Modifications, and Applications. *Chem. Rev.* **2007**, *107*, 2891–2959.
- (5) Nakata, K.; Fujishima, A. TiO<sub>2</sub> Photocatalysis: Design and Applications. *J. Photochem. Photobiol. C* **2012**, *13*, 169–189.
- (6) Fujishima, A.; Zhang, X.; Tryk, D. TiO<sub>2</sub> Photocatalysis and Related Surface Phenomena. *Surf. Sci. Rep.* **2008**, *63*, 515–582.
- (7) Malato, S.; Fernández-Ibáñez, P.; Maldonado, M.; Blanco, J.; Gernjak, W. Decontamination and Disinfection of Water by Solar Photocatalysis: Recent Overview and Trends. *Catal. Today* **2009**, *147*, 1–59.
- (8) Lee, M. M.; Teuscher, J.; Miyasaka, T.; Murakami, T. N.; Snaith, H. J. Efficient Hybrid Solar Cells Based on Meso-Superstructured Organometal Halide Perovskites. *Science* **2012**, *338*, 643–647.
- (9) Kim, H.-S.; Lee, C.-R.; Im, J.-H.; Lee, K.-B.; Moehl, T.; Marchioro, A.; Moon, S.-J.; Humphry-Baker, R.; Yum, J.-H.; Moser, J. E.; Grätzel, M.; Park, N. G. Lead Iodide Perovskite Sensitized All-Solid-State Submicron Thin Film Mesoscopic Solar Cell with Efficiency Exceeding 9%. *Sci. Rep.* **2012**, *2*, 591.
- (10) Stranks, S. D.; Eperon, G. E.; Grancini, G.; Menelaou, C.; Alcocer, M. J. P.; Leijtens, T.; Herz, L. M.; Petrozza, A.; Snaith, H. J. Electron-Hole Diffusion Lengths Exceeding 1 Micrometer in an Organometal Trihalide Perovskite Absorber. *Science* **2013**, *342*, 341–344.
- (11) Dutta, P. K.; Ginwalla, A.; Hogg, B.; Patton, B. R.; Chwieroth, B.; Liang, Z.; Gouma, P.; Mills, M.; Akbar, S. Interaction of Carbon Monoxide with Anatase Surfaces at High Temperatures: Optimization of a Carbon Monoxide Sensor. *J. Phys. Chem. B* **1999**, *103*, 4412–4422.
- (12) Arafat, M. M.; Dinan, B.; Akbar, S. A.; Haseeb, A. S. M. A. Gas Sensors Based on One Dimensional Nanostructured Metal-Oxides: A Review. *Sensors* **2012**, *12*, 7207–7258.
- (13) Strukov, D. B.; Snider, G. S.; Stewart, D. R.; Williams, R. S. The Missing Memristor Found. *Nature* **2008**, *453*, 80–83.

- (14) Wu, H.; Xu, C.; Xu, J.; Lu, L.; Fan, Z.; Chen, X.; Song, Y.; Li, D. Enhanced Supercapacitance in Anodic TiO<sub>2</sub> Nanotube Films by Hydrogen Plasma Treatment. *Nanotechnology* **2013**, *24*, 455401.
- (15) Salari, M.; Konstantinov, K.; Liu, H. K. Enhancement of the Capacitance in TiO<sub>2</sub> Nanotubes through Controlled Introduction of Oxygen Vacancies *J. Mater. Chem.* **2011**, *21*, 5128–5133.
- (16) Xu, J.; Jia, C.; Cao, B.; Zhang, W. Electrochemical Properties of Anatase TiO<sub>2</sub> Nanotubes as an Anode Material for Lithium-Ion Batteries. *Electrochim. Acta* **2007**, *52*, 8044–8047.
- (17) Izawa, H.; Kikkawa, S.; Koizumi, M. Ion Exchange and Dehydration of Layered Titanates, Na<sub>2</sub>Ti<sub>3</sub>O<sub>7</sub> and K<sub>2</sub>Ti<sub>4</sub>O<sub>9</sub>. *J. Phys. Chem.* **1982**, *86*, 5023–5026.
- (18) Sasaki, T.; Watanabe, M.; Komatsu, Y.; Fujiki, Y. Layered Hydrated Titanium Dioxide: Potassium Ion Exchange and Structural Characterization. *Inorg. Chem.* **1985**, *24*, 2265–2271.
- (19) Kim, Y.; Atherton, S. J.; Brigham, E. S.; Mallouk, T. E. Sensitized Layered Metal Oxide Semiconductor Particles for Photochemical Hydrogen Evolution from Nonsacrificial Electron Donors. *J. Phys. Chem.* **1993**, *97*, 11802–11810.
- (20) Yahya, R. B.; Hayashi, H.; Nagase, T.; Ebina, T.; Onodera, Y.; Saitoh, N. Hydrothermal Synthesis of Potassium Hexatitanates under Subcritical and Supercritical Water Conditions and Its Application in Photocatalysis. *Chem. Mater.* **2001**, *13*, 842–847.
- (21) Kataoka, K.; Kijima, N.; Akimoto, J. Ion-Exchange Synthesis, Crystal Structure, and Physical Properties of Hydrogen Titanium Oxide H<sub>2</sub>Ti<sub>3</sub>O<sub>7</sub>. *Inorg. Chem.* **2013**, *52*, 13861–13864.
- (22) Kim, H.-S.; Moon, W.-T.; Jun, Y.-K.; Hong, S.-H. High H<sub>2</sub> Sensing Performance in Hydrogen Trititanate-Derived TiO<sub>2</sub>. *Sensors and Actuators B* **2006**, *120*, 63–68.
- (23) Chiba, K.; Kijima, N.; Takahashi, Y.; Idemoto, Y.; Akimoto, J. Synthesis, Structure, and Electrochemical Li-Ion Intercalation Properties of Li<sub>2</sub>Ti<sub>3</sub>O<sub>7</sub> with Na<sub>2</sub>Ti<sub>3</sub>O<sub>7</sub>-type Layered Structure. *Solid State Ionics* **2008**, *178*, 1725–1730.
- (24) Szirmai, P.; Stevens, J.; Horváth, E.; Ćirić, L.; Kollár, M.; Forró, L.; Náfrádi, B. Competitive Ion-Exchange of Manganese and Gadolinium in Titanate Nanotubes. *Catal Today* **2017**, *284*, 146–152.
- (25) Cardoso, V de. A.; de Souza, A. G.; Sartoratto, P. P. C.; Nunes, L. M. The ionic Exchange Process of Cobalt, Nickel and Copper (II) in Alkaline and Acid-Layered Titanates. *Colloids and Surfaces A: Physicochem. Eng. Aspects* **2004**, *248*, 145–149.

- (26) Nunes, L. M.; de Souza, A. G.; de Farias, R. F. Synthesis of New Compounds Involving Layered Titanates and Niobates with Copper (II). *Journal of Alloys and Compounds* **2001**, *319*, 94–99.
- (27) Vithal, M.; Krishna, S. R.; Ravi, G.; Palla, S.; Velchuri, R.; Pola, S. Synthesis of Cu<sup>2+</sup> and Ag<sup>+</sup> doped Na<sub>2</sub>Ti<sub>3</sub>O<sub>7</sub> by a Facile Ion-Exchange Method as Visible-Light-Driven Photocatalysts. *Ceramics International* **2013**, *39*, 8429–8439.
- (28) Sirinakorn, T.; Bureekaew, S.; Ogawa, M. Highly Efficient Indium (III) Collection from Water by a Reaction with a Layered Titanate (Na<sub>2</sub>Ti<sub>3</sub>O<sub>7</sub>). *Eur. J. Inorg. Chem.* **2018**, 3835–3839.
- (29) Andersson, S.; Wadsley, A. D. The Crystal Structure of Na<sub>2</sub>Ti<sub>3</sub>O<sub>7</sub>. *Acta Cryst.* **1961**, *14*, 1245–1249.
- (30) Yakubovich, O. V.; Kireev, V. V. Refinement of the Crystal Structure of Na<sub>2</sub>Ti<sub>3</sub>O<sub>7</sub>. *Crystallography Reports* **2003**, *48*, 24–28.
- (31) Gwenaelle Rouse, G.; Dompablo, M. E. A.; Senguttuvan, P.; Ponrouch, A.; Tarascon, J.-M.; Palacín, M. R. Rationalization of Intercalation Potential and Redox Mechanism for A<sub>2</sub>Ti<sub>3</sub>O<sub>7</sub> (A = Li, Na). *Chem. Mater.* **2013**, *25*, 4946–4956.
- (32) Tauc, J.; Grigorovic, R.; Vancu, A. Optical Properties and Electronic Structure of Amorphous Germanium. *Phys. Status Solidi* **1966**, *15*, 627–637.
- (33) Joshi, U. A.; Maggard, P. A. CuNb<sub>3</sub>O<sub>8</sub>: A p-Type Semiconducting Metal Oxide Photoelectrode. *J. Phys. Chem. Lett.* **2012**, *3*, 1577–1581.

*CHAPTER -6*

*New paramagnetic framework titanate  
by topotactic Fe(II) exchange of  
 $\text{Na}_2\text{Ti}_6\text{O}_{13}$*



## New Paramagnetic Framework Titanate by Topotactic Fe(II) Exchange of $\text{Na}_2\text{Ti}_6\text{O}_{13}$

### 6.1 INTRODUCTION

Topotactic ion exchange reactions provide an important and straight forward route to metastable materials while allowing the retention of some of the structural and physical properties [1]. For certain chemical composition and structural functionalization, which cannot be prepared with traditional high temperature ceramic techniques, one required to use soft chemistry (*chimie douce method*). Direct synthesis from simple precursors is thermodynamically unfavorable for many such compounds. In such cases, topotactic soft chemical routes, such as ion exchange and intercalation can be used to maintain the resilient structural characteristics of a precursor. These methodologies can help to develop new materials of interesting structural, magnetic and electronic properties [2-7]. The objective of this work is to develop a methodology, which can be used to directly construct the new active structural features. This capability could help researchers in designing new, technically important materials, such as, semiconductor photocatalysts, catalysts, magnetic and multiferroric materials.

As discussed in the previous chapter, recently, the layered titanates have received a lot of attention because of their interesting interlayer chemistry, their ability to undergo ion exchange/intercalation reactions etc. In addition, they can be exfoliated or delaminated by intercalating bulky organic molecules, creating single sheets of distinct 2D morphology, that are highly attractive building blocks to produce artificial, hybrid, or microporous materials [8]. The potential uses of titanium oxide materials, in lithium ion battery electrodes, as photocatalysts or semiconducting devices have intensively been investigated [9-13]. The alkali metal titanates  $\text{A}_2\text{Ti}_n\text{O}_{2n+1}$  ( $\text{A} = \text{Li}, \text{Na}, \text{K}$  and  $n = 1-9$ ), are important materials for their use in reinforcements, dye sensitized solar cells, cation exchangers, photocatalysers, and sensors [14-16] etc. The physical and chemical properties of titanates,  $\text{A}_2\text{Ti}_n\text{O}_{2n+1}$ , change with the value of 'n'. Titanates with a high alkali content ( $n = 2-4$ ) generally have an open layered structure and wide cation exchange characteristics, so they can become ion exchangers. In contrast, titanates of low alkali metal content ( $n = 6-8$ ) have a tunnel structure



with high chemical stability and a high insulating capacity. It can therefore be used as reinforcement materials and as adiabatics [17].

The family of alkali metal titanates with the general chemical formula,  $\text{A}_2\text{Ti}_6\text{O}_{13}$  (A = Na, Li, H), have attracted a great deal of attention in contrast due to their interesting chemical properties.  $\text{Na}_2\text{Ti}_6\text{O}_{13}$  was specifically tested as photocatalyst for water splitting into  $\text{H}_2$  and  $\text{O}_2$  [18, 19], degradation of MB under UV light [14], and as an excellent electro-chemical Li insertion material as a negative electrode for Li ion batteries [20, 21]. A simple successive  $\text{Na}^+ / \text{Li}^+ / \text{H}^+$  ion exchange of  $\text{Na}_2\text{Ti}_6\text{O}_{13}$  produces the hexatitanate  $\text{H}_2\text{Ti}_6\text{O}_{13}$  [22]. In contrast,  $\text{Li}_2\text{Ti}_6\text{O}_{13}$  can easily be obtained from  $\text{Na}_2\text{Ti}_6\text{O}_{13}$  with complete  $\text{Na}^+ / \text{Li}^+$  ion exchange with a retained Ti – O skeleton structure [23-26]. The series of visible-light driven photocatalysts were prepared by simple ion exchange and solid-state methods by replacing both the cation ( $\text{Cu}^{2+} / \text{Ag}^+$ ) and the anion ( $\text{N}^{3-}$ ) into the  $\text{Na}_2\text{Ti}_6\text{O}_{13}$  (NTO) [27].

The framework structure of  $\text{Na}_2\text{Ti}_6\text{O}_{13}$  consists of zigzag chains of triple edge-shared  $\text{TiO}_6$  octahedra. All three  $\text{TiO}_6$  octahedra are distorted and the individual Ti – O distance is within 1.745(2) – 2.243(2) Å. However, for the three Ti sites the bond valence sums are reported as 4.18, 4.11 and 4.14 for the Ti1, Ti2 and Ti3 sites respectively. These values corresponded well to the formal valence of +4 for the Ti. It can be concluded that the distortion of these  $\text{TiO}_6$  octahedra is essential for the construction of the  $(\text{Ti}_6\text{O}_{13})^{2-}$  framework in  $\text{Na}_2\text{Ti}_6\text{O}_{13}$  structure. Therefore, a rigid and open frame is made of nearly rectangular tunnels consisting of 3 (edge-shared)  $\times$  1 (vertex-shared)  $\text{TiO}_6$  octahedra, whose interstitial sites are occupied by the alkali metals [25, 28] (Figure 6.1).

In this chapter, we have envisaged the new framework titanate,  $\text{Na}_{2(1-x)}\text{Fe}_x\text{Ti}_6\text{O}_{13}$ , by topotactic ion exchange method. We finally explained the crystal structure, optical and magnetic properties of  $\text{Na}_{2(1-x)}\text{Fe}_x\text{Ti}_6\text{O}_{13}$  after ion exchange with parent  $\text{Na}_2\text{Ti}_6\text{O}_{13}$ .

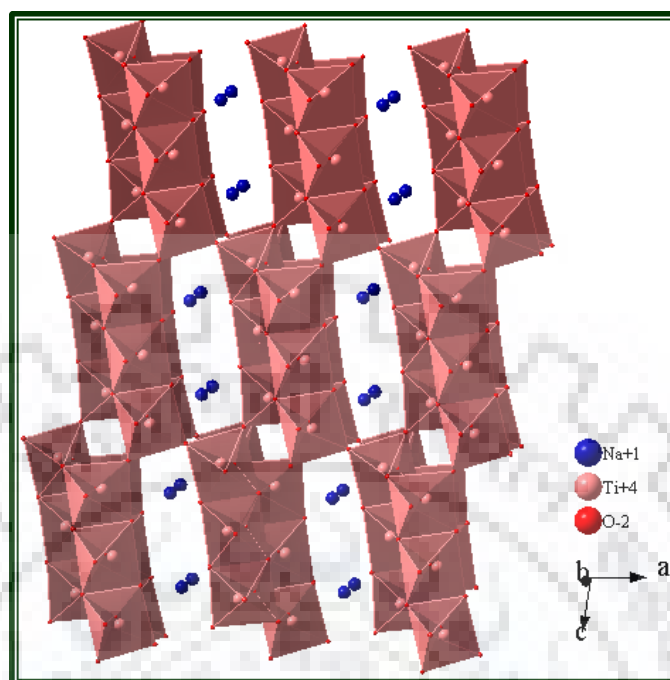


**Figure 6.1** Crystal structure of  $\text{Na}_2\text{Ti}_6\text{O}_{13}$ .

## 6.2 EXPERIMENTAL SECTION

### Materials and Synthesis

Sodium carbonate ( $\text{Na}_2\text{CO}_3$ , Sigma Aldrich,  $\geq 99.0\%$ ), and titanium dioxide ( $\text{TiO}_2$ , Sigma Aldrich, 99.8%) were used as starting materials for the synthesis of parent,  $\text{Na}_2\text{Ti}_6\text{O}_{13}$ . The reagent were used as received without any further any purification. Millipore water was used throughout the experiments and sample preparations.

The white colored  $\text{Na}_2\text{Ti}_6\text{O}_{13}$  precursor material was synthesized by following the method previously reported in the literature [25], using conventional solid-state reaction method. In a typical synthesis, stoichiometric quantities of  $\text{Na}_2\text{CO}_3$ , and  $\text{TiO}_2$  were taken in an agate mortar and ground thoroughly for nearly an hour. The ground mixture was heated at 800 °C for 40 h with an intermediate grinding.

The framework titanate,  $\text{Na}_2\text{Ti}_6\text{O}_{13}$ , thus prepared and used for subsequent ion exchange reaction with transition metal. For this, 1 g of  $\text{Na}_2\text{Ti}_6\text{O}_{13}$  precursor powder was taken into a round bottomed flask and excess amount of 0.2 M  $\text{FeCl}_2 \cdot 4\text{H}_2\text{O}$  (Alfa Aesar,  $\geq 98.0\%$ ) solution in 100 mL was added to it. The reaction mixture was magnetically stirred at 60 °C for 4 days with intermediate washing and addition of fresh 0.2 M  $\text{FeCl}_2 \cdot 4\text{H}_2\text{O}$  solution. The ion exchange reaction was carried out under Argon atmosphere. After 4 days of reaction at 60 °C, the solution was cooled and centrifuged at 8000 rpm for 5 min. The obtained product was washed with distill water for several times and dried at room temperature. The dried sample after ion exchange was mustard-yellow in color.

## 6.3 RESULTS AND DISCUSSION

### 6.3.1 P-XRD Analysis

To check the formation of the framework titanates, P-XRD patterns of  $\text{Na}_2\text{Ti}_6\text{O}_{13}$  and its ion-exchanged product,  $\text{Na}_{2(1-x)}\text{Fe}_x\text{Ti}_6\text{O}_{13}$  were recorded and presented in Figure 6.2. An analysis of P-XRD pattern of the parent ion-exchanged product  $\text{Na}_{2(1-x)}\text{Fe}_x\text{Ti}_6\text{O}_{13}$  with standard JCPDS file reported in the literature indicated formation of framework layered oxide similar to monoclinic  $\text{Na}_2\text{Ti}_6\text{O}_{13}$  (JCPDS PDF # 73-1398). Moreover, the white colored parent  $\text{Na}_2\text{Ti}_6\text{O}_{13}$  compound turns into mustard yellow after ion exchange reaction. This clearly indicates the exchange of  $\text{Na}^+$  ions by  $\text{Fe}^{2+}$  ions.

The unit cell parameters of both the parent  $\text{Na}_2\text{Ti}_6\text{O}_{13}$  and the ion exchange compounds  $\text{Na}_{2(1-x)}\text{Fe}_x\text{Ti}_6\text{O}_{13}$ , are indexed in the monoclinic  $C2/m$  space group and the lattice parameters were refined by least-square refinement of all the diffraction lines in the observed P-XRD pattern using the PROSZKI program. Least-squares refined lattice parameters of these compounds are shown in Table 6.1. The unit cell parameters of parent  $\text{Na}_2\text{Ti}_6\text{O}_{13}$  compound are in good agreement with the reported values [25]. A comparison of lattice parameters of  $\text{Na}_{2(1-x)}\text{Fe}_x\text{Ti}_6\text{O}_{13}$  with the parent  $\text{Na}_2\text{Ti}_6\text{O}_{13}$  shows a decrease in all the three lattice parameters. The Rietveld refinement of the crystal structure for  $\text{Na}_{2(1-x)}\text{Fe}_x\text{Ti}_6\text{O}_{13}$  is carried out using the P-XRD data with the help of FULLPROF program suite. The initial model for the structure refinement was constructed using the atomic coordinates of  $\text{Na}_2\text{Ti}_6\text{O}_{13}$  ( $C2/m$  space group) and the occupancies are adjusted according to the composition,  $\text{Na}_{0.02}\text{Fe}_{0.99}\text{Ti}_6\text{O}_{13}$ , as derived

from the EDX analysis. The observed, calculated and difference profiles of Rietveld refinement are shown in Figure 6.3.

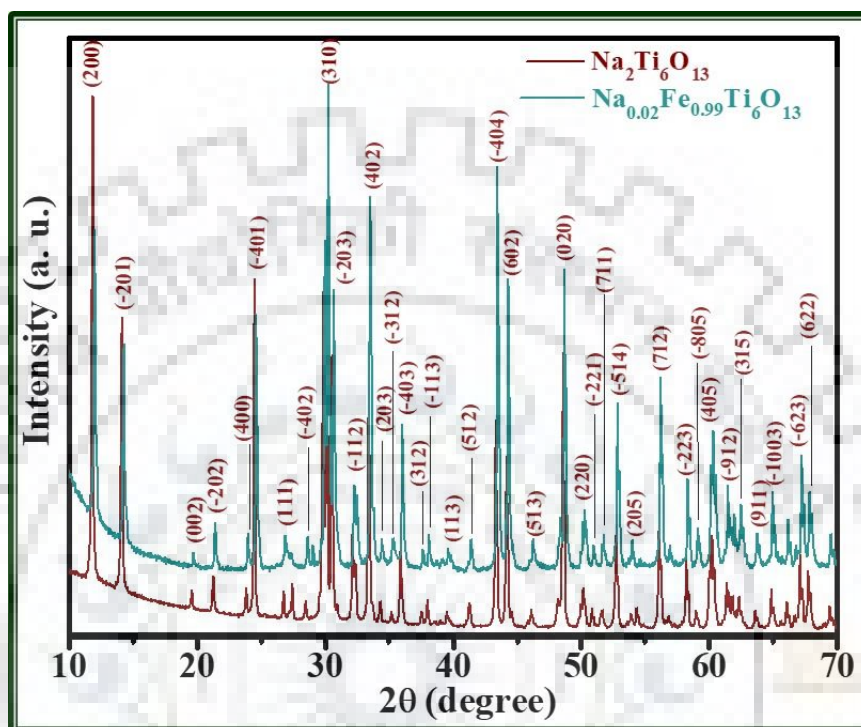


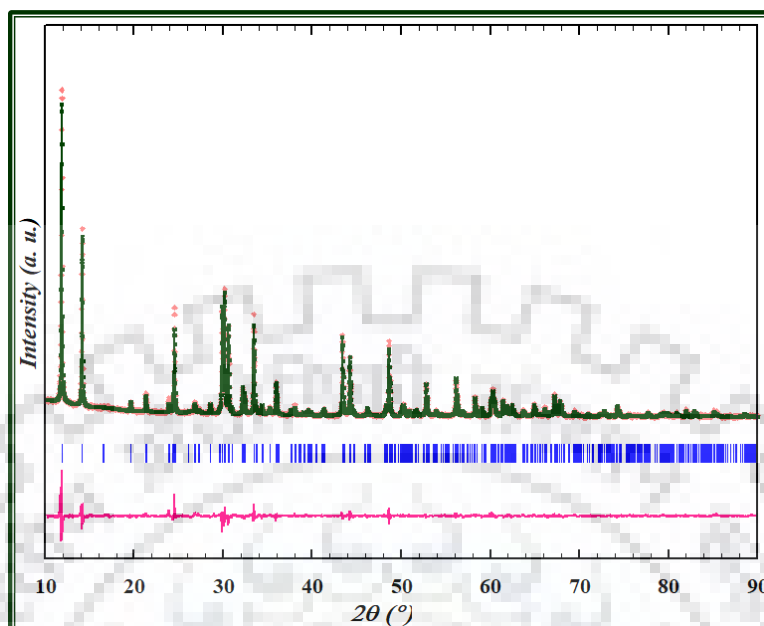
Figure 6.2 P-XRD patterns of  $\text{Na}_2\text{Ti}_6\text{O}_{13}$  and  $\text{Na}_{0.02}\text{Fe}_{0.99}\text{Ti}_6\text{O}_{13}$ .

Table 6.1 Lattice Parameters and Band Gap of  $\text{Na}_2\text{Ti}_6\text{O}_{13}$  and  $\text{Na}_{0.02}\text{Fe}_{0.99}\text{Ti}_6\text{O}_{13}$

Compound	Lattice Parameters ( $\text{\AA}$ )				Band gap ( $E_g$ ) (eV)
	$a$	$b$	$c$	$\beta$	
$\text{Na}_2\text{Ti}_6\text{O}_{13}$	15.406(4)	3.757(1)	9.297(2)	99.05(1)	3.42
$\text{Na}_{0.02}\text{Fe}_{0.99}\text{Ti}_6\text{O}_{13}$	15.087(2)	3.741(5)	9.161(1)	98.99(1)	2.08

Table 6.2 Indexed P-XRD Data for  $\text{Na}_{0.02}\text{Fe}_{0.99}\text{Ti}_6\text{O}_{13}$ 

$h k l$	$d_{\text{obs}} (\text{\AA})$	$d_{\text{calc}} (\text{\AA})$	$I_{\text{obs}}$
2 0 0	7.585	7.543	100
$\bar{2}$ 0 1	6.334	6.320	49
0 0 2	4.571	4.567	2
$\bar{2}$ 0 2	4.208	4.194	4
4 0 0	3.758	3.759	2
$\bar{4}$ 0 1	3.660	3.662	3
$\bar{4}$ 0 2	3.010	3.011	2
3 1 0	2.983	2.990	36
$\bar{2}$ 0 3	2.941	2.942	28
1 1 2	2.797	2.799	10
3 1 1	2.778	2.783	8
4 0 2	2.701	2.708	23
$\bar{6}$ 0 1	2.511	2.514	5
$\bar{4}$ 0 4	2.093	2.090	19
6 0 2	2.052	2.047	16
0 2 0	1.879	1.879	22
$\bar{5}$ 1 4	1.739	1.738	9
7 1 2	1.642	1.642	11
4 0 5	1.539	1.539	8



**Figure 6.3** Rietveld refinement of P-XRD data for  $\text{Na}_{0.02}\text{Fe}_{0.99}\text{Ti}_6\text{O}_{13}$ . Observed (+), calculated (–) and difference (at the bottom) profiles are shown. Vertical bars below the profile mark the Bragg reflection positions.

For the Rietveld structure refinement of  $\text{Na}_{0.02}\text{Fe}_{0.99}\text{Ti}_6\text{O}_{13}$  the initial model was constructed using the atomic coordinates of  $\text{Na}_2\text{Ti}_6\text{O}_{13}$  ( $C2/m$  space group) wherein  $\text{Na}^+$  completely occupy the interstitial sites of the framework titanate made up of the zigzag chain of triple edge-shared  $\text{TiO}_6$  octahedra. Figure 6.4 drawn from the refined atomic coordinates displays the triple edge-shared  $\text{TiO}_6$  octahedral zigzag chains, which are further interconnected through corners and make a tunnel and these tunnels are running parallel to the  $c$ -direction. After the ion exchange by  $\text{Fe}^{2+}$  only alternate or some sites initially occupied by  $\text{Na}^+$ , situated between the tunnels are occupied by  $\text{Fe}^{2+}$ , while others remain vacant. The observed, calculated and difference profiles of Rietveld refinement are shown in Figure 6.3. The refined atomic positions, occupancies and thermal parameters are given in Table 6.2.



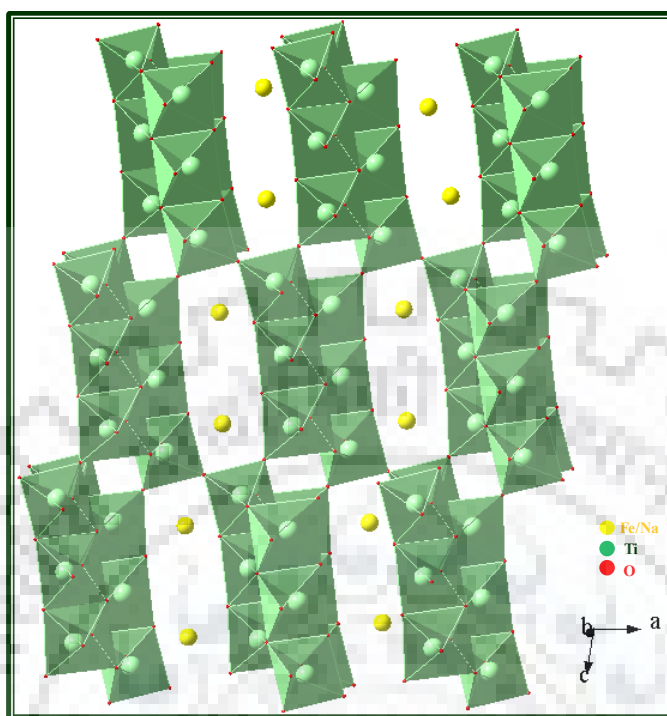


**Figure 6.4** Polyhedral representation of the structure of  $\text{Na}_{0.02}\text{Fe}_{0.99}\text{Ti}_6\text{O}_{13}$  drawn with the refined atomic coordinates. The structure shown here presents Li/Fe vacancies in an ordered fashion.

**Table 6.3 Atomic Positions, Site Occupancy and Thermal Parameters of  $\text{Na}_{0.02}\text{Fe}_{0.99}\text{Ti}_6\text{O}_{13}$**

Atom	<i>x</i>	<i>y</i>	<i>z</i>	<i>B</i> <sub>iso</sub>	Occ.
Na	0.4615(3)	0	0.2679(5)	0.0367	0.02
Fe	0.4615(3)	0	0.2679(5)	0.0367	0.99
Ti(1)	0.1151(1)	0	0.0972(3)	0.0047	2
Ti(2)	0.1700(2)	0	0.4373(3)	0.0042	2
Ti(3)	0.2273(2)	0	0.7707(3)	0.0042	2
O1	0	0	0	0.0131	1
O2	0.2394(5)	0	0.2448(9)	0.0059	2
O3	0.0722(5)	0	0.2842(9)	0.0073	2
O4	0.2969(5)	0	0.5682(1)	0.0058	2
O5	0.1257(5)	0	0.6161(9)	0.0079	2
O6	0.3524(4)	0	0.8806(9)	0.0066	2
O7	0.1622(5)	0	0.9289(1)	0.0106	2

Space group =  $C2/m$ ,  $a = 15.087(3)$  Å,  $b = 3.741(5)$  Å,  $c = 9.161(1)$  Å,  $\beta = 98.99(1)$  Å,

$V = 510.88$  Å<sup>3</sup>,  $R_{\text{Bragg}} = 5.2\%$ ,  $R_{\text{P}} = 4.7\%$ ,  $R_{\text{F}} = 5.4\%$ ,  $R_{\text{wp}} = 6.4\%$ ,  $\chi^2 = 2.8$ .

**Table 6.4 Selected Bond Lengths (Å) of  $\text{Na}_{0.02}\text{Fe}_{0.99}\text{Ti}_6\text{O}_{13}$** 

Fe – O1 (×2)	3.207(3)
Fe – O3 (×2)	2.506(3)
Fe – O5 (×2)	2.601(3)
Fe – O7 (×2)	2.993(1)
< Fe – O >	2.826
Ti1 – O1	1.829(4)
Ti1 – O2	2.123(4)
Ti1 – O3	1.946(3)
Ti1 – O6 (×2)	1.930(5)
Ti1 – O7	1.819(3)
< Ti1 – O >	1.929
Ti2 – O2	2.174(4)
Ti2 – O3	1.859(4)
Ti2 – O4	2.094(4)
Ti2 – O4 (×2)	1.941(3)
Ti2 – O5	1.854(3)
< Ti2 – O >	1.984
Ti3 – O2 (×2)	1.953(3)
Ti3 – O4	2.266(4)
Ti3 – O5	1.923(3)
Ti3 – O6	2.019(4)
Ti3 – O7	1.857(3)
< Ti3 – O >	2.003

### 6.3.2 FE-SEM and EDX Analysis

While the morphology of the parent  $\text{Na}_2\text{Ti}_6\text{O}_{13}$  and ion-exchanged product  $\text{Na}_{0.02}\text{Fe}_{0.99}\text{Ti}_6\text{O}_{13}$  are investigated by FE-SEM. The elemental composition are determined from the EDX analysis (Figure 6.5). The FE-SEM images show both plate/rod like morphology that are retained even after the ion exchange reaction. The crystallite size ranges from several hundred nanometers to few micrometers throughout the imaging area.

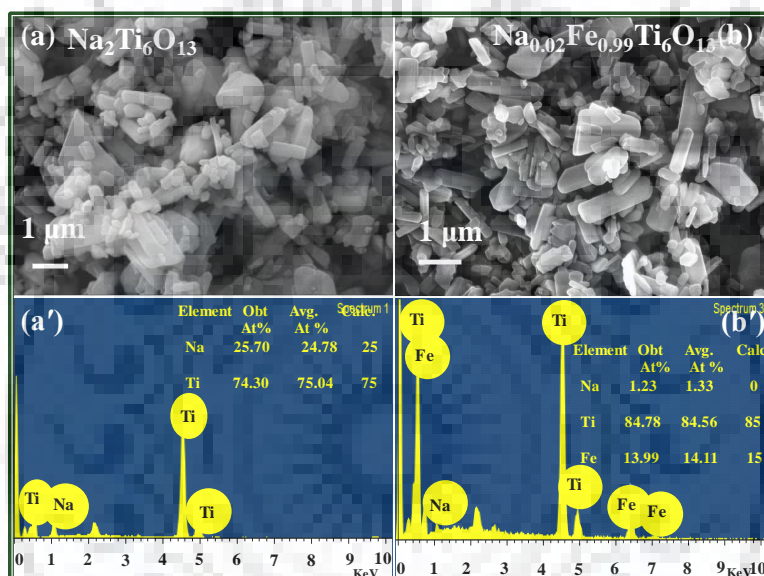


**Figure 6.5** FE-SEM and corresponding EDX data of (a, a')  $\text{Na}_2\text{Ti}_6\text{O}_{13}$  and (b, b')  $\text{Na}_{0.02}\text{Fe}_{0.99}\text{Ti}_6\text{O}_{13}$ .

### 6.3.3 HR-TEM Analysis

The crystalline nature of the ion-exchanged product,  $\text{Na}_{0.02}\text{Fe}_{0.99}\text{Ti}_6\text{O}_{13}$  is confirmed by the TEM analysis and is shown in Figure 6.6. The lattice fringes corresponds to a distance of 0.37 nm in the HR-TEM is consistent with the  $b$ -parameter of the unit cell (Figure 6.6a). The diffraction spots from the (200), (201), (400) and (401) planes can be easily recognized in the SAED pattern of the  $\text{Na}_{0.02}\text{Fe}_{0.99}\text{Ti}_6\text{O}_{13}$  compound (Figure 6.6b).

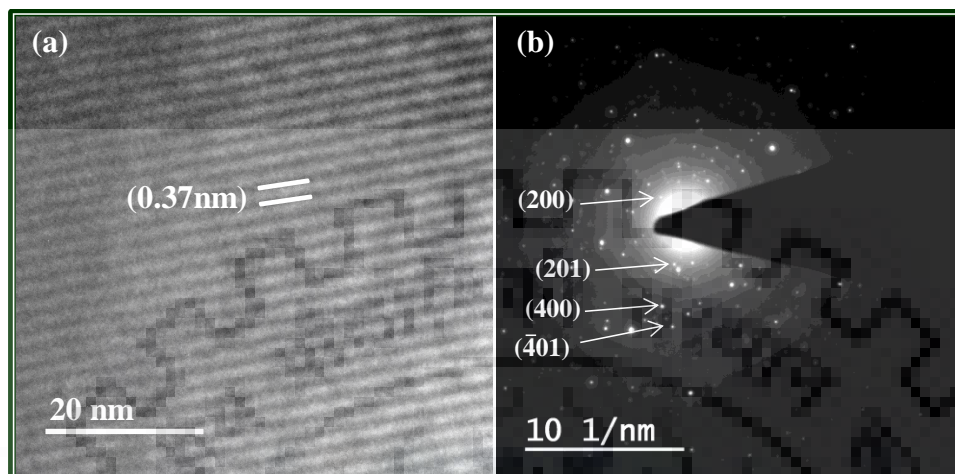


**Figure 6.6** (a) HR-TEM and (b) SAED pattern of  $\text{Na}_{0.02}\text{Fe}_{0.99}\text{Ti}_6\text{O}_{13}$ .

### 6.3.4 XPS Analysis

The XPS data (Figure 6.7) calibrated with respect to C 1s binding energy of 284.8 eV indicated Fe-2p binding energies of 723.0 and 709.7 eV corresponding to the spin-orbit coupled Fe-2p<sub>1/2</sub> and Fe-2p<sub>3/2</sub> states, respectively. This largely correspond to the presence of Fe<sup>2+</sup> in  $\text{Na}_{0.02}\text{Fe}_{0.99}\text{Ti}_6\text{O}_{13}$ . The survey spectra of  $\text{Na}_{0.02}\text{Fe}_{0.99}\text{Ti}_6\text{O}_{13}$  in Figure 6.8 shows Ti 2p peak at 459.7 eV and this is characteristic for the Ti(IV) species in the compound.

The presence of Na (1s) peak in the survey spectra indicate that the Na are not completely exchanged, as evidence in the EDX data as well.

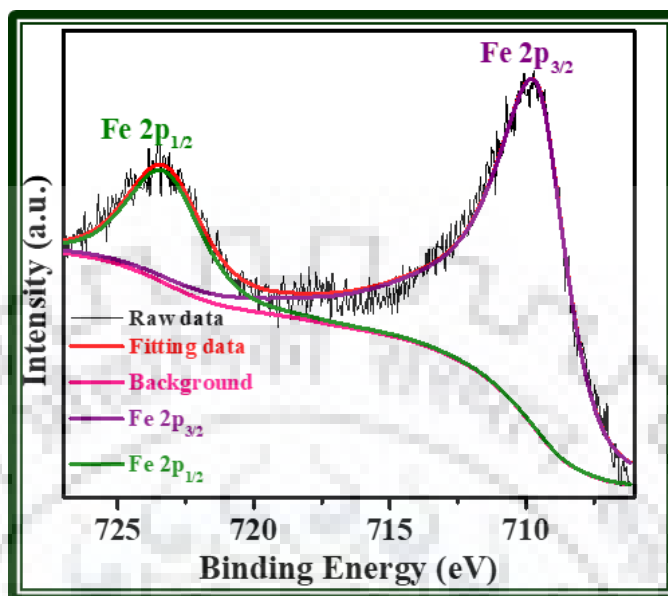


Figure 6.7 Fe-2p XPS of  $\text{Na}_{0.02}\text{Fe}_{0.99}\text{Ti}_6\text{O}_{13}$ .

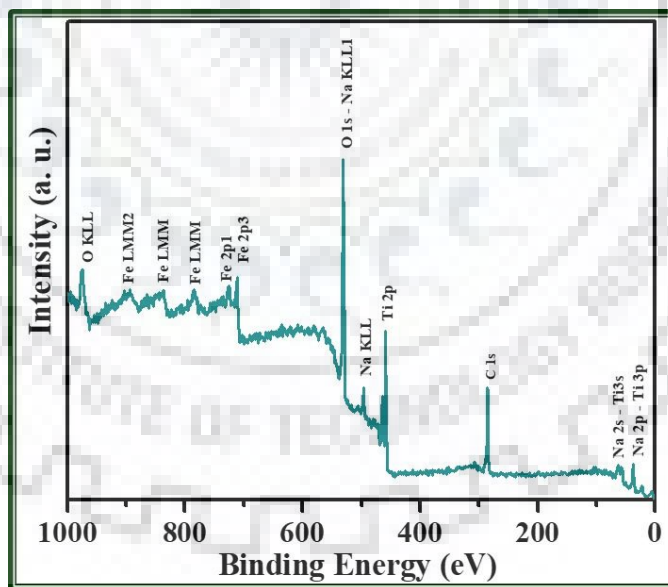
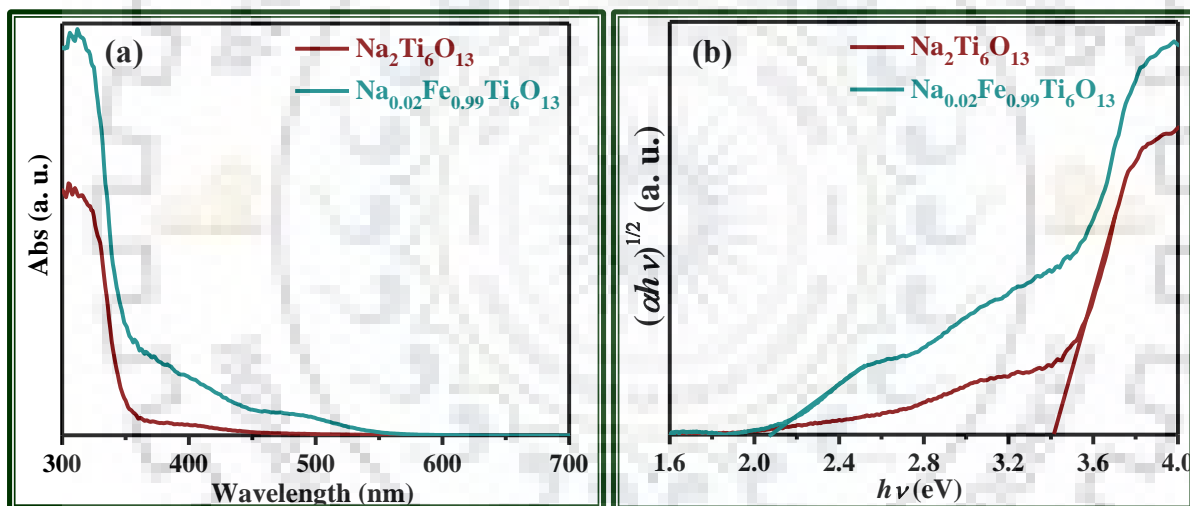


Figure 6.8 XPS survey spectra for  $\text{Na}_{0.02}\text{Fe}_{0.99}\text{Ti}_6\text{O}_{13}$ .



### 6.3.5 UV-vis DRS Analysis

Figure 6.9 portrays the UV-vis DRS data of as the synthesized  $\text{Na}_2\text{Ti}_6\text{O}_{13}$  and the ion-exchanged product,  $\text{Na}_{0.02}\text{Fe}_{0.99}\text{Ti}_6\text{O}_{13}$ . The absorption edges of parent  $\text{Na}_2\text{Ti}_6\text{O}_{13}$  compound lie in the UV region ( $\lambda < 400$  nm) and that of the ion-exchanged product in the visible region ( $\lambda > 400$  nm) (Figure 6.9(a)). This absorption data confirms that white  $\text{Na}_2\text{Ti}_6\text{O}_{13}$  is an UV-light absorber,  $\text{Na}_{0.02}\text{Fe}_{0.99}\text{Ti}_6\text{O}_{13}$  is a visible-light absorber. Figure 6.9(b) shows the Tauc plots [29,30] of  $\text{Na}_2\text{Ti}_6\text{O}_{13}$  and  $\text{Na}_{0.02}\text{Fe}_{0.99}\text{Ti}_6\text{O}_{13}$ . The calculated band gap of  $\text{Na}_2\text{Ti}_6\text{O}_{13}$  and  $\text{Na}_{0.02}\text{Fe}_{0.99}\text{Ti}_6\text{O}_{13}$  are 3.42, and 2.08 eV, respectively. The study reveals that the transition metal exchange can be a simple way for band gap engineering of UV active compound that are amenable to ion exchange reaction.



**Figure 6.9** (a) UV-vis DRS data for  $\text{Na}_{0.02}\text{Fe}_{0.99}\text{Ti}_6\text{O}_{13}$ . (b) Corresponding Tauc plot for the calculation of band gap.

### 6.3.6 Magnetic Measurement

Temperature-dependent magnetization data in a 1000 Oe applied magnetic field is collected for  $\text{Na}_{0.02}\text{Fe}_{0.99}\text{Ti}_6\text{O}_{13}$  and the data are shown in Figure 6.10. But the FC and ZFC data show paramagnetic behavior in the entire temperature range (5-300 K) without much divergence in the magnetization (Figure 6.10 (a)). The high temperature ( $\geq 150$  K) inverse

susceptibility data (inset) is indication of antiferromagnetic correlation while at low temperature the compound show pure Curie-like behavior. The absence of any hysteresis loop in the magnetization vs. field data at 300 K and 5 K show pure Curie-like paramagnetism (Figure 6.10(b)).

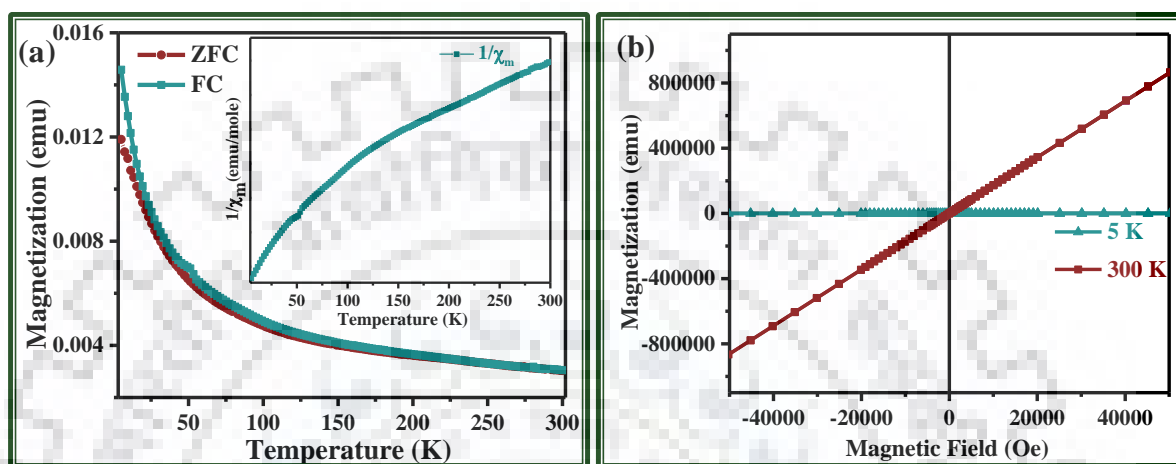


**Figure 6.10** (a) Magnetization vs. temperature and (b) magnetization vs. field data for  $\text{Na}_{0.02}\text{Fe}_{0.99}\text{Ti}_6\text{O}_{13}$ . Inset show the inverse molar susceptibility vs. temperature plot for the FC data.

**Table 6.5** Magnetic Data for  $\text{Na}_{0.02}\text{Fe}_{0.99}\text{Ti}_6\text{O}_{13}$  Calculated from the Linear Fit of the  $\chi_m^{-1}$  vs. T Plot

Compound	C (emu/mole)	$\theta$ (K)	$\mu_{\text{eff}}$ (B.M.)
$\text{Na}_{0.02}\text{Fe}_{0.99}\text{Ti}_6\text{O}_{13}$	0.9651	287.74	2.77

In summary, Na<sub>0.02</sub>Fe<sub>0.99</sub>Ti<sub>6</sub>O<sub>13</sub> was successfully prepared from Na<sub>2</sub>Ti<sub>6</sub>O<sub>13</sub> Na/Fe ion exchange in aqueous FeCl<sub>2</sub> at 60 °C under Argon atmosphere. The phase purity and chemical composition of the ion-exchanged sample was characterized by P-XRD and FE-SEM- EDX analysis. The crystal structure of Na<sub>0.02</sub>Fe<sub>0.99</sub>Ti<sub>6</sub>O<sub>13</sub> was refined by the Rietveld refinement using the P-XRD data. The basic (Ti<sub>6</sub>O<sub>13</sub>)<sup>2-</sup> framework was retained nearly unchanged from that in the parent Na<sub>2</sub>Ti<sub>6</sub>O<sub>13</sub>. The morphological homogeneity upon ion exchange was established by FE-SEM studies while the elemental compositions were determined by EDX analysis. The HR-TEM and SAED analyses further lend support on the topotactic nature of exchange by the fact that the distance between lattice fringes and indexed diffraction spots are consistent with the P-XRD data. The compound showed paramagnetic behavior down to 5 K indicating no strong magnetic correlation in the compound, which could be a manifestation of Fe being present in the tunnels of the framework structure, that are separated from each other by a large distance.

## REFERENCES

- (1) Clearfield, A. Role of Ion Exchange in Solid-State Chemistry. *Chem. Rev.* **1988**, *88*, 125–148.
- (2) Schaak R. E.; Mallouk, T. E. Perovskites by Design: A Toolbox of Solid-State Reactions. *Chem. Mater.* **2002**, *14*, 1455–1471.
- (3) Gopalakrishnan, J. Chimie Douce Approaches to the Synthesis of Metastable Oxide Materials. *Chem. Mater.* **1995**, *7*, 1265–1275.
- (4) Tsujimoto, Y.; Tassel, C.; Hayashi, N.; Watanabe, T.; Kageyama, H.; Yoshimura, K.; Takano, M.; Ceretti, M.; Ritter C.; Paulus W. Infinite-layer iron oxide with a square-planar coordination. *Nature* **2007**, *450*, 1062–1065.
- (5) Yoshida, M.; Ogata, N.; Takigawa, M.; Yamaura, J.; Ichihara, M.; Kitano, T.; Kageyama, H.; Ajiro, Y.; Yoshimura, K. Magnetic and Structural Studies of the Quasi-Two-Dimensional Spin-Gap System  $(\text{CuCl})\text{LaNb}_2\text{O}_7$ . *J. Phys. Soc. Jpn.* **2007**, *76*, 104703.
- (6) Kageyama, H.; Watanabe, T.; Tsujimoto, Y.; Kitada, A.; Sumida, Y.; Kanamori, K.; Yoshimura, K.; Hayashi, N.; Muranaka, S.; Takano, M.; Ceretti, M.; Paulus, W.; Ritter, C.; Andre, G. Spin-Ladder Iron Oxide:  $\text{Sr}_3\text{Fe}_2\text{O}_5$ . *Angew. Chem., Int. Ed.* **2008**, *47*, 5740–5745.
- (7) Machida, M.; Yabunaka, J. i.; Kijima, T. Synthesis and Photocatalytic Property of Layered Perovskite Tantalates,  $\text{RbLnTa}_2\text{O}_7$  (Ln = La, Pr, Nd, and Sm). *Chem. Mater.* **2000**, *12*, 812–817.
- (8) Gao, T.; Fjellvåg, H.; Norby, P. Raman Scattering Properties of a Protonic Titanate  $\text{H}_x\text{Ti}_{2-x/4}\square_{x/4}\text{O}_4 \cdot \text{H}_2\text{O}$  ( $\square$ , vacancy;  $x = 0.7$ ) with Lepidocrocite-Type Layered Structure. *J. Phys. Chem. B* **2008**, *112*, 9400–9405.
- (9) Kavan, L.; Kalbá, M.; Zúkalová, M.; Exnar, I.; Lorenzen, V.; Nesper, R.; Graetze, M. Lithium Storage in Nanostructured  $\text{TiO}_2$  Made by Hydrothermal Growth. *Chem. Mater.* **2004**, *16*, 477–485.
- (10) Aldon, L.; Kubiak, P.; Womes, M.; Jumas, J. C.; Olivier-Fourcade, J.; Tirado, J. L.; Corredor, J. I. Vicente, C. P. Chemical and Electrochemical Li-Insertion into the  $\text{Li}_4\text{Ti}_5\text{O}_{12}$  Spinel. *Chem. Mater.* **2004**, *16*, 5721–5725.
- (11) Li, D.; Haneda, H.; Hishita S. Ohashi, N. Visible-Light-Driven N–F–Codoped  $\text{TiO}_2$  Photocatalysts. 1. Synthesis by Spray Pyrolysis and Surface Characterization. *Chem. Mater.* **2005**, *17*, 2588–2595.
- (12) Li, D.; Haneda, H.; Hishita S. Ohashi, N. Visible-Light-Driven N–F–Codoped  $\text{TiO}_2$  Photocatalysts. 2. Optical Characterization, Photocatalysis, and Potential Application to Air Purification. *Chem. Mater.* **2005**, *17*, 2596–2602.

- (13) Prochazka, J.; Kavan, L.; Zukalova, M.; Frank, O.; Kalbac, M.; Zukal, A.; Klementova, M.; Carbone, D.; Graetzel, M. Novel Synthesis of the  $\text{TiO}_2$  (B) Multilayer Templated Films. *Chem. Mater.* **2009**, *21*, 1457–1464.
- (14) Torres-Martínez, L.; Juárez-Ramírez, I., Ángel-Sánchez, K. D.; Garza-Tovar, L.; Cruz-López, A.; Ángel, G. D. Rietveld Refinement of Sol–Gel  $\text{Na}_2\text{Ti}_6\text{O}_{13}$  and its Photocatalytic Performance on the Degradation of Methylene Blue. *J Sol Gel Sci Technol.* **2008**, *47*, 158–164.
- (15) Wang, L.; Zhang, T.; Qi, Q.; Hu, J.; Zeng, Y.; Lu, G.; Synthesis and field effect characteristics of  $\text{Na}_2\text{Ti}_3\text{O}_7$  nanowires. *Mater Lett.* **2009**, *63*, 903–904.
- (16) Li, G. L.; Wang, G. H.; Hong, J. M. Synthesis of  $\text{K}_2\text{Ti}_6\text{O}_{13}$  Whiskers by the Method of Calcinations of KF and  $\text{TiO}_2$  Mixtures. *Mater Res Bull.* **1999**, *34*, 2341–2349.
- (17) Zhao, B.; Lina, L.; He, D. Phase and Morphological Transitions of Titania/Titanate Nanostructures from an Acid to an Alkali Hydrothermal Environment. *J Mater Chem A* **2013**, *1*, 1659–1668.
- (18) Inoue, Y.; Kubokawa T.; Sato, K. Photocatalytic Activity of Alkali-Metal Titanates Combined with Ru in the Decomposition of Water. *J. Phys. Chem.* **1991**, *95*, 4059–4063.
- (19) Ogura, S.; Kohno, M.; Sato, K.; Inoue, Y. Photocatalytic Properties of (M = Na, K, Rb, Cs) with  $\text{M}_2\text{Ti}_6\text{O}_{13}$  Rectangular Tunnel and Layer Structures: Behavior of a Surface Radical Produced by UV irradiation and Photocatalytic Activity for Water Decomposition. *Phys. Chem. Chem. Phys.* **1999**, *1*, 179–183.
- (20) Dominko, R.; Baudrin, E.; Umek, P.; Arcon, D.; Gaberscek, M.; Jamnik, J. Reversible Lithium Insertion into  $\text{Na}_2\text{Ti}_6\text{O}_{13}$  Structure. *Electrochem. Commun.* **2006**, *8*, 673–677.
- (21) Dominko, R.; Dupont, L.; Gaberscek, M.; Jamnik J.; Baudrin, E. Alkali Hexatitanates— $\text{A}_2\text{Ti}_6\text{O}_{13}$  (A = Na, K) as Host Structure for Reversible Lithium Insertion. *J. Power Sources* **2007**, *174*, 1172–1176.
- (22) Pérez-Flores, J. C.; Baehtz, C.; Hoelzel, M.; Kuhn, A.; García-Alvarado, F.  $\text{H}_2\text{Ti}_6\text{O}_{13}$ , A New Protonated Titanate Prepared by  $\text{Li}^+/\text{H}^+$  Ion Exchange: Synthesis, Crystal Structure and Electrochemical Li Insertion Properties. *RSC Adv.* **2012**, *2*, 3530–3540.
- (23) England, W. A.; Goodenough, J. B.; Wiseman, P. J. Ion-Exchange Reactions of Mixed Oxides. *J. Solid State Chem.* **1983**, *49*, 289–299.
- (24) Pérez-Flores, J. C.; Kuhn A.; García-Alvarado, F. Synthesis, Structure and Electrochemical Li Insertion Behaviour of  $\text{Li}_2\text{Ti}_6\text{O}_{13}$  with the  $\text{Na}_2\text{Ti}_6\text{O}_{13}$  Tunnel-Structure. *J. Power Sources* **2011**, *196*, 1378–1385.
- (25) Kataoka, K.; Awaka, J.; Kijima, N.; Hayakawa, H.; Ohshima, K.-i.; Akimoto, J. Ion-Exchange Synthesis, Crystal Structure, and Electrochemical Properties of  $\text{Li}_2\text{Ti}_6\text{O}_{13}$ . *Chem. Mater.* **2011**, *23*, 2344–2352.

- (26) Pérez-Flores, J. C.; Kuhn, A.; García-Alvarado, F. A Structural and Electrochemical Study of  $\text{Li}_2\text{Ti}_6\text{O}_{13}$ . *Mater. Res. Soc. Symp. Proc.* **2011**, 1313.
- (27) Veldurthi, N. K.; Velchuri, R.; Pola, S.; Prasad, G.; Muniratnam, N. R.; Vithal, M. Synthesis, Characterization and Silver/Copper–Nitrogen Substitutional Effect on Visible Light Driven Photocatalytic Performance of Sodium Hexatitanate Nanostructures. *J Chem Technol Biotechnol.* **2015**, 90, 1507–1514.
- (28) Pérez-Flores, J. C.; García-Alvarado, F.; Hoelzel, M.; Sobrados, I.; Sanz, J.; Kuhn, A. Insight into the Channel Ion Distribution and Influence on the Lithium Insertion Properties of Hexatitanates  $\text{A}_2\text{Ti}_6\text{O}_{13}$  (A = Na, Li, H) as Candidates for Anode Materials in Lithium-Ion Batteries. *Dalt. Trans.* **2012**, 41, 14633–14642.
- (29) Tauc, J.; Grigorovic, R.; Vancu, A. *Phys. Status Solidi* **1966**, 15, 627–637.
- (30) Joshi, U. A.; Maggard, P. A.  $\text{CuNb}_3\text{O}_8$ : A p-Type Semiconducting Metal Oxide Photoelectrode. *J. Phys. Chem. Lett.* **2012**, 3, 1577–1581.







**CHAPTER -7**

***Conclusions and Future Prospects***



## Conclusions and Future Prospects

Transition metal oxides (TMOs) have constituted an interesting class of inorganic solids that have received considerable attention of solid-state and material chemists for the past several decades due to their diverse physicochemical properties and applications. The oxides can adopt structures that extend from rock salt, spinel, rutile, and ilmenite to perovskites and their variants. While the literature lists a wide array of transition metal oxides, many possibilities still exist with new chemical compositions and structures, which cannot be achieved by the conventional synthetic routes employing high temperatures. The routine solid-state synthesis is however very convenient and widely used for the synthesis of many functional oxides, but the number of accessible compositions is limited by the competition between thermodynamic and kinetic factors. A thermodynamically stable precursor, usually produced through a high-temperature reaction in a solid state, can be converted through soft chemical methods to a related metastable structure, which cannot be accessed by direct methods. In the last three decades, a wide variety of layered transition metal oxide and related materials, which cannot be accessible via a direct thermal synthesis, have been synthesized through soft chemical approaches including topochemical ion exchange, redox reactions, dehydration, anion substitution, acid-based response and exfoliation. In the areas of artificial photosynthesis, energy storage, optical sensing, ferroics and high- $\kappa$  dielectrics the consequences of using soft-chemistry approaches in designing functioning material are already apparent. The objective of the current study was to develop new transition metal oxides at low temperatures through topotactic ion exchange reactions. We recognized during this investigation that a topotactic ion exchange is common in layered perovskites or other structures of tunnel and framework, but rarely occur in close packed 3D structures based on all shared corners and/or edges. In the present investigation, topotactic ion exchange have been explored in three-dimensional structures based purely on corner/edge connected octahedral network in addition to a ribbon type and a framework titanate, also based on edge/corner shared  $\text{TiO}_6$  octahedra. The study has enabled transformation of a number of non-magnetic oxides into magnetic ones in addition to altering its optical property to a significant extent.

Divalent iron-exchange in a three-dimensional close-packed trirutile oxide with all octahedral coordination we report for the first time, the transition metal ion exchange in  $\alpha$ -LiNbWO<sub>6</sub> and characterization of the resulting trirutile oxide. The ion exchange with Fe<sup>II</sup> has been achieved by refluxing  $\alpha$ -LiNbWO<sub>6</sub> in an aqueous solution of FeCl<sub>2</sub>·4H<sub>2</sub>O under an argon atmosphere at 60 °C for 4 days. While a clear color changeover from white to mustard-yellow indicated the exchange of Li with Fe, intensification of the color by prolonging the reaction from 1 to 4 days clearly suggested the increased extent of exchange with time. The close resemblance of the P-XRD pattern of the ion exchanged sample with that of the parent substantiated the topotactic nature of the exchange. An ICP-OES analysis of the Fe-exchanged LiNbWO<sub>6</sub> revealed the exchange of 90% of the Li, leaving behind 10% Li in the sample. Considering 90% exchange of monovalent Li by divalent Fe, the ion-exchanged compound is formulated as Li<sub>0.1</sub>Fe<sub>0.45</sub>NbWO<sub>6</sub>. The FE-SEM analysis indicated retention of the particle morphology upon exchange and the EDX data confirmed the expected elemental ratio for Fe, Nb, and W in corroboration with the ICP-OES derived composition. The presence of lattice fringes with a periodicity of 0.932 nm as observed in the HR-TEM image conformed to the quasi-ordered trirutile phase akin to the periodicity of the (Li/Fe)O<sub>6</sub> octahedron connected to an NbO<sub>6</sub>-WO<sub>6</sub> bioctahedral unit along the *c* direction. The corresponding SAED pattern is consistent with the tetragonal crystal system, and the indexed spots are in agreement with the P-XRD data. The <sup>7</sup>Li MAS NMR spectra of LiNbWO<sub>6</sub> clearly revealed the presence of only one type of Li site, as expected. The presence of a <sup>7</sup>Li peak in the Fe exchanged sample with the same chemical shift as that of the parent is supportive of the retention of a small amount of Li without any change to its coordination environment. The XPS data indicated Fe 2p binding energies of 723.0 and 709.7 eV for spin-orbit coupled Fe 2p<sub>1/2</sub> and Fe 2p<sub>3/2</sub> states, respectively, corresponding largely to the presence of Fe<sup>2+</sup> in Li<sub>0.1</sub>Fe<sub>0.45</sub>NbWO<sub>6</sub>. As evidenced in the UV-vis DRS, Fe exchanged has clearly resulted in extension of the optical absorption edge deep into the visible region compared to its parent, only a near-UV absorber. This amounts to a significant reduction of the indirect band gap of Li<sub>0.1</sub>Fe<sub>0.45</sub>NbWO<sub>6</sub> to 1.71 eV from 3.01 eV of the parent, as estimated from the Tauc plots. The magnetic susceptibility data below 200 K indicates Curie-like paramagnetism, which arises due to the disorder of Fe at the 2*c* sites and the presence of random vacancies that keeps the Fe<sup>2+</sup> sites isolated from other neighboring Fe<sup>2+</sup> spins in the lattice. The paramagnetic moment corroborates well with the spin-only moment for high-spin Fe<sup>2+</sup>.

In our next endeavor, we explored the topotactic ion exchange in a new tri- $\alpha$ - $\text{PbO}_2$  type oxide,  $\text{LiSbWO}_6$ . The compound,  $\text{Li}_{0.08}\text{Fe}_{0.46}\text{SbWO}_6$ , is synthesized for the first time by ion exchange reaction of  $\text{LiSbWO}_6$  at 60 °C for 4 days under an argon atmosphere. The phase purity of the resulting compound and the topotactic nature of the exchange are ascertained by P-XRD analysis. The morphological homogeneity upon ion exchange and the elemental composition are determined using FE-SEM and EDX studies. The UV-vis DRS data of the iron-antimony tungstate also showed a considerable reduction of the visible band gap to 2.06 eV from  $\sim 3.02$  eV of the parent lithium-antimony tungstate. The reduction in the band gap is attributed to the formation of valence band (VB) states, primarily constituted by the overlap of Fe-3d and O-2p orbitals, which would be situated at higher energies in  $\text{Li}_{0.08}\text{Fe}_{0.46}\text{SbWO}_6$  as compared to the VB states of the parent  $\text{LiSbWO}_6$ . This upshift of VB edge and a consequent decrease in the band gap is ascribed to the extended optical absorption of  $\text{Li}_{0.08}\text{Fe}_{0.46}\text{SbWO}_6$ . The XPS data indicated Fe-2p binding energies of 723.2 and 709.6 eV for the spin-orbit coupled Fe-2p<sub>1/2</sub> and Fe-2p<sub>3/2</sub> states, respectively, corresponding to the presence of Fe<sup>2+</sup>. The observed lattice fringes in the HR-TEM image with a periodicity of 0.495 nm is in agreement with the periodicity in the *c*-direction. The SAED pattern is consistent with the orthorhombic crystal system, and the indexed spots are in agreement with the P-XRD data. The ZFC magnetization data show antiferromagnetic transition at  $\sim 20$  K. Unlike  $\text{Li}_{0.1}\text{Fe}_{0.45}\text{NbWO}_6$ , where isolated Fe<sup>2+</sup> are present, Fe(II) dimers can exist in  $\text{Li}_{0.08}\text{Fe}_{0.46}\text{SbWO}_6$  due to the presence of edge-shared chains of  $\text{LiO}_6$  octahedra running along the *c*-direction in the tri- $\alpha$ - $\text{PbO}_2$  structure. This probably is responsible for the low-temperature antiferromagnetic transition in the compound. The high temperature paramagnetic moment, however, matches well with the spin-only moment of high spin Fe<sup>2+</sup>. Further work involving neutron diffraction is necessary to understand the true nature of the the magnetic transition in this compound.

Extending our idea in developing new members of the ribbon type layered titanates, the synthesis, characterization and magnetic properties of transition metal exchanged ribbon-type layered titanates,  $\text{Na}_{0.01}\text{Mn}_{0.99}\text{Ti}_3\text{O}_7$ ,  $\text{Na}_{0.16}\text{Fe}_{0.92}\text{Ti}_3\text{O}_7$ ,  $\text{Na}_{0.14}\text{Co}_{0.93}\text{Ti}_3\text{O}_7$  and  $\text{Na}_{0.01}\text{Ni}_{0.99}\text{Ti}_3\text{O}_7$  are reported. The compounds are synthesized by ion exchange of  $\text{Na}_2\text{Ti}_3\text{O}_7$  at 60 °C for 48 hours. The close similarity of the P-XRD patterns of the resulting compounds to that with the parent and a color change over from white to orange-brown/brown/grey-

green/light green confirmed the exchange of transition metals in a topotactic fashion. The morphological homogeneity and elemental composition is established with FE-SEM and EDX studies for all the compounds. For  $\text{Na}_{0.01}\text{Ni}_{0.99}\text{Ti}_3\text{O}_7$ , in addition to the FE-SEM imaging, the TEM analysis also revealed plate-like morphology that are generally observed for oxides with ribbon/layered type structures. The HR-TEM showed clear lattice fringes with interfringe spacing of 0.390 nm, which is consistent with the  $b$ -parameter of the monoclinic unit cell. The SAED pattern is also indexable in the monoclinic space group and consistent with the lattice parameters obtained from the P-XRD data. UV-vis DRS study confirmed the presence of visible band gaps for all the compounds ranging from 1.99 - 2.86 eV. The Mn compound,  $\text{Na}_{0.01}\text{Mn}_{0.99}\text{Ti}_3\text{O}_7$ , shows antiferromagnetic transition at 32 K, while the rise in susceptibility at  $\sim 8$  K is probably due to a ferrimagnetic correlation between the  $\text{Mn}^{2+}$  and  $\text{Mn}^{3+}$  spins that may arise due to spin canting. Similar antiferromagnetic transition is also observed in the Ni compound but the low temperature feature is absent. The M-H data for Mn and Ni at low temperatures (5 and 30 K for Mn and 5 K for Ni) showed hysteretic behavior which is a signature of ferrimagnetism possibly arising out of the spin canting. On the contrary, the corresponding Fe and Co compounds showed paramagnetic behaviors throughout the entire temperature range (5 – 300 K). It will be interesting to further explore the origin of magnetic transitions in these compounds through variable temperature neutron diffraction experiments.

Finally, in our effort to synthesize new framework titanate, we explored the synthesis, characterization and magnetic properties of a new framework titanate,  $\text{Na}_{0.01}\text{Fe}_{0.99}\text{Ti}_6\text{O}_{13}$ .  $\text{Na}_{0.01}\text{Fe}_{0.99}\text{Ti}_6\text{O}_{13}$  is prepared by ion exchange reaction between  $\text{Na}_2\text{Ti}_6\text{O}_{13}$  and  $\text{FeCl}_2 \cdot 4\text{H}_2\text{O}$  in aqueous medium at 60 °C under continuous stirring for 4 days.  $\text{Na}_{0.01}\text{Fe}_{0.99}\text{Ti}_6\text{O}_{13}$  has a light yellow-orange color. The P-XRD pattern indicated that the ion-exchanged product retained the layered framework structure of the parent. The morphology and elemental ratios were characterized by FE-SEM and EDX analysis, respectively. As prepared  $\text{Na}_2\text{Ti}_6\text{O}_{13}$  and the ion-exchanged compound showed plate-like morphology, often seen and expected in layered type of oxides. The elemental ratios obtained from EDX analysis, both on spot and area basis are in good agreement with the nominal compositions. UV-vis DRS data revealed that  $\text{Na}_{0.01}\text{Fe}_{0.99}\text{Ti}_6\text{O}_{13}$  is a visible light active semiconductor with band gap of 2.05 eV. The magnetization data indicates paramagnetic character of the compound.



In summary, topotactic reactions such as, ion exchange, intercalation and deintercalation offer effective routes for the preparation of new compounds under mild conditions. The use of such methods is especially interesting due to their ability to direct the placement and connectivities of cations and/or anions in the final product. Ion exchange method have been exploited to synthesize a series of metastable transition metal oxides with close-packed three-dimensional trirutile and tri  $\alpha$ - $\text{PbO}_2$  type structures, in addition to a ribbon-type and a framework layered structure. These results reveal that simple topotactic reactions can be applied for the construction of metal-anion arrays for a number of transition metals and structures. The effectiveness of this approach is noteworthy as none of them could be prepared by a direct solid-state reaction method. It is expected that the continued development of such synthetic strategies will eventually result in a general set of methodologies for the conscious design and preparation of intricate structural arrangements. This would be especially significant to the development of so-called “rational design” of materials for applications in various technologies including electronics, magnetic and ceramics.

The present work may potentially be extended for the topotactic ion exchange of various other structure types especially including those of three-dimensional ones, which were mostly outside the scope of ion exchange so far. This may lead to the development of new oxides, phosphates, halides, and chalcogenides as well by topotactic routes. Moreover, other solvent systems may also be explored especially those including the organic ones for ion exchange of oxides containing redox sensitive cations. Lastly, realizing the importance of recent works on layered oxide hetero-interfaces and their architectures for various technological applications, and ion exchange in colloidal nanocrystals, the present work may offer opportunities in building novel architectures of 3D close packed ordered or quasi-ordered oxides in the bulk, nanocrystals as well as in thin films through ion exchange.